Timing of exhumation of the eastern Central Alps from zircon and apatite (U-Th)/He thermochronology (Graubünden, Switzerland)

By

Sarah Lynn Evans

B.S., University of North Carolina, Chapel Hill, 2008

Submitted to the graduate degree program in Geology
and the Graduate Faculty of the University of Kansas
in partial fulfillment of the requirements
for the degree of Master of Science.

_____

Daniel F. Stockli (Chairperson)

_____

Andreas Möller

_____

David Fowle

Date Defended: November 30, 2011

The Thesis Committee for Sarah Lynn Evans

certifies that this is the approved version of the following thesis:

Timing of exhumation of the eastern Central Alps from zircon and apatite (U-Th)/He thermochronology (Graubünden, Switzerland)

_____

Daniel F. Stockli (Chairperson)

Date Approved: December 13, 2011

ABSTRACT

Timing of exhumation of the eastern Central Alps from zircon and apatite (U-Th)/He thermochronology (Graubünden, Switzerland)

By

Sarah Lynn Evans
Department of Geology
University of Kansas

The structurally complex eastern Central Alps, located in eastern Switzerland and adjacent areas, have helped constrain the timing and kinematics of deformation during the Alpine orogeny. Several regional and orogenic scale studies have established a well-defined structural evolution of the eastern Central Alps; however, the low-temperature cooling history of the region remains relatively unconstrained. An understanding of this cooling history may elucidate mechanisms for exhumation of the region and evaluate orogenic scale models for the timing and nature of exhumation within the mountain belt. This study presents new low-temperature zircon and apatite (U-Th)/He age data from the Austroalpine and Penninic nappes of the eastern Central Alps that reveals a three stage cooling history for the region. These data, combined with inverse time-temperature modeling, provide cooling rates for the three phase history. Slow cooling at rates of ~1-10 °C/m.y. through the zircon HePRZ (~200-140 °C) are recorded in the Austroalpine Silvretta, Campo-Grosina, and Err nappes during the Eocene from ~52 to 36 Ma. This period of cooling is related to exhumation resulting from north directed thrusting associated with continental collision. A second stage of rapid cooling at rates of 10-50 °C/m.y. from ~36 to 21 Ma, are recorded by zircon and apatite (U-Th)/He age data from the Bernina and Corvatsch Austroalpine nappes, and zircon (U-Th)/He age data from Penninic units exposed in the Engadine Window. This period of relatively rapid cooling and exhumation is likely a response to a combination of backthrusting along the Insubric Line and crustal duplexing at depth. A final

period of cooling and exhumation is recorded only in the Silvretta Austroalpine nappe and Penninic units exposed in the Engadine Window at ~16 Ma. This period of cooling and exhumation is likely a result of uplift along the oblique left-lateral Engadine Line. The overall cooling history of the eastern Central Alps shows that the western exposure of the orogenic lid behaved as a rigid to semi-rigid block during continental collision and continued convergence until the Engadine Line affected the region in the Miocene. The three phase cooling history constrained by this low-temperature thermochronometric data contributes to the growing body of evidence for episodic cooling and apparent exhumation of the Alpine orogen.

DEDICATION

To my family, for without you I would be lost.

ACKNOWLEDGEMENTS

Funding for this research was provided in part by a Geological Society of America Grants-in-aid, Sigma Xi and University of Kansas Department of Geology summer scholarship.

I am extremely grateful for the input and guidance from my advisor Dr. Daniel Stockli on the development, implementation and completion of this project; further, I would like to thank him for being especially understanding during the evolution of my project from its initial conception to its eventual form. I would also like to thank him for letting me learn and grow as a scientist during my time at Kansas, even though it meant some (costly) mistakes.

I would like to extend my appreciation to my committee members, Dr. Andreas Möller and Dr. Dave Fowle, for their input and direction. I also need to thank several individuals who have made the logistics of field work possible and enjoyable including Dr. Daniel Stockli, Dr. Gianreto Manatschal, Dr. Othmar Müntener, Dr. Geoffroy Mohn, Emmanuel Masini, Joseph Miller, Dr. Paul Kenward, and Hilde and Fritz Stöckli.

Implementation and understanding of the laser-ablation section of this project would not have been possible without the help and patient guidance of Dr. Andreas Möller, Jeffrey Oalmann and Joseph Miller. I would like to also extend my appreciation to Dr. Doug Walker and Dr. Roman Kitslitsyn for all of their help and assistance in laboratory work, and thank them for reminding me that no, I was not in fact dying of non-existent HF burns.

Without the support, guidance, discussion, and instruction of my fellow lab mates over the years I could not have accomplished this, so thank you. I would also like to extend my gratitude to my various officemates for sharing the space so equitably, and my special thanks to my current officemates for being there to answer the random questions, listen to my ridiculous

music and help to play hide-the-ninja. I also want to thank Kathryn Hoffmeister, Joseph Miller and Kurt Sundell for reading initial drafts of this thesis.

Finally, I want to send my heart felt thank you to Joe, my family and all my friends for their love, kindness, and encouragement-without you none of this would be possible.

TABLE OF CONTENTS

	Page
TITLE PAGE	i
ACCEPTANCE PAGE	ii
ABSTRACT	iii
DEDICATION	v
ACKNOWLEDGEMENTS	vi
TABLE OF CONTENTS	viii
LIST OF FIGURES AND TABLES	xi
1. INTRODUCTION	14
2. GEOLOGIC SETTING	15
2.1 General Alpine Terminology	15
2.2 Regional Geologic Setting	16
2.2.1 Passive Margin Development	16
2.2.2 Cretaceous Alpine Orogeny	17
2.2.3 Tertiary Alpine Orogeny	19
3. SAMPLING STRATEGY AND PREVIOUS WORK	22
3.1 Sampling Strategy	22
3.2 Previous Low-Temperature Thermochronologic Studies	23
4. (U-Th)/He ANALYSES	24

4.1 Zircon (U-Th)/He Methodology 24

4.2 Apatite (U-Th)/He Methodology 28

4.3 (U-Th)/He Results 29

4.3.1 Silvretta (U-Th)/He Analyses 29

4.3.2 Campo and Grosina (U-Th)/He Analyses 30

4.3.3 Bernina (U-Th)/He Analyses 31

4.3.4 Julier (U-Th)/He Analyses 32

4.3.5 Err (U-Th)/He Analyses 32

4.3.6 Corvatsch (U-Th)/He Analyses 33

4.3.7 Engadine Window (U-Th)/He Analyses 33

5. PARENT ISOTOPE ZONATION IN ZIRCON GRAINS FROM THE SILVRETTA NAPPE 34

5.1 Depth-profiling Methodology 35

5.2 Comparison of Depth-profiling and Zircon (U-Th)/He Age Results 35

5.3 CL Imaging and Parent Isotope Zonation Patterns 38

6. (U-Th)/He INVERSE THERMAL MODELING 39

6.1 Modeling Methodology 39

6.2 Modeling Constraints 41

6.3 (U-Th)/He Inverse Modeling Results 42

7. INTERPRETATION OF (U-Th)/He ANALYSES AND THERMAL MODELING 45

7.1 Timing of Cooling and Exhumation of the Austroalpine nappes 45

7.2 Timing of Cooling and Exhumation of the Penninic nappes 47

7.3 Cooling and Apparent Exhumation rates of the Austroalpine nappes 48

7.4 Cooling and Apparent Exhumation rates of the Penninic nappes 49

7.5 Estimation of Magnitude of Total Exhumation 50

8. DISCUSSION 50

8.1 Mechanisms for Cooling and Exhumation 50

8.1.1 North Directed Thrusting 51

8.1.2 Slab break-off, Backthrusting and Crustal Duplexing 51

8.1.3 Engadine Line 54

8.2 Rigidity of Orogenic Lid 55

8.3 Hinterland Exhumation and Foreland Basin Interaction 56

9. CONCLUSIONS 58

REFERENCES CITED 61

APPENDIX A: REPLICATE ZIRCON AND APATITE (U-Th)/He ANALYSES 118

APPENDIX B: LASER ABLATION DEPTH-PROFILES 127

APPENDIX C: CL IMAGES OF LASER ABLATED ZIRCON GRAINS 202

APPENDIX D: U-Pb AGE DATA OF SILVRETTA NAPPE 224

LIST OF FIGURES AND TABLES

FIGURES **Page**

Figure 1. Geologic map of study area with sample locations 72

Figure 2. Plate reconstructions of the Alpine realm 74

Figure 3. Schematic cross section of Adriatic passive margin 76

Figure 4. Age-elevation plots 78

Figure 5. Err nappe (U-Th)/He data plots 80

Figure 6. Categorization of laser ablation depth-profiles 82

Figure 7. Depth-profiled zircon (U-Th)/He ages 84

Figure 8. Interpretation of Silvretta zircon (U-Th)/He ages 86

Figure 9. Compilation of CL images of Silvretta zircon grains 88

Figure 10. Thermal model of Campo-Grosina nappes 90

Figure 11. Thermal model of Bernina nappe 92

Figure 12. Thermal model of Err nappe 94

Figure 13. Thermal model of Corvatsch nappe 96

Figure 14. Thermal model of Engadine Window 98

Figure 15. Summary of modeled cooling histories 100

Figure 16. Post-D2 thermal structure 102

Figure 17. Summary plot of zircon and apatite (U-Th)/He ages and deformation phases 104

Figure 18. Cross sections from the Eocene to the Miocene 106

Figure 19. Block diagrams for exhumation mechanisms 108

Figure 20. Sediment yield curve for the foreland basins of the Alps 110

TABLES **Page**

Table 1. Average zircon (U-Th)/He ages 112

Table 2. Average apatite (U-Th)/He ages 113

Table 3. Replicate zircon (U-Th)/He ages of the Err nappe 114

Table 4. Replicate zircon (U-Th)/He ages of the Silvretta vertical transect 116

APPENDIX A

Table A. Replicate zircon (U-Th)/He ages 119

Table B. Replicate apatite (U-Th)/He ages 124

APPENDIX D

Table C. U-Pb age data of the Silvretta nappe 225

Page intentionally left blank.

1. Introduction

Recent work in the Alps has focused on understanding the tectonic, metamorphic, and thermal evolution of the Alpine orogeny using geophysical, geochronologic, and thermochronologic techniques, as well as palinspastic reconstructions (e.g., Hurford et al., 1989; Froitzheim et al., 1996; Schmid et al., 1996; Frisch et al., 2000; Handy and Oberhänsli, 2004; Schmid et al., 2004; Bousquet et al., 2008; Stampfli and Hochard, 2009; Handy et al., 2010; Berger et al., 2011). The structurally complex eastern Central Alps have been well-studied using these techniques, with a particular focus placed on the boundary between the Austroalpine and Penninic nappes and the surrounding region. Studies in this region have contributed to the knowledge of the timing and kinematics of deformation in the Alpine orogen (e.g., Froitzheim et al., 1994 and references therein), and the area has become a terrestrial analogue for the magma-poor rift margin model (e.g., Manatschal et al., 2007; Manatschal and Müntener, 2009 and references therein). The combined findings of these recent studies have established a well-defined structural evolution of the eastern Central Alps; however, very few studies have focused on the low-temperature thermal evolution of the Austroalpine and Penninic nappes exposed in the region.

Low-temperature thermochronometric techniques (i.e., zircon and apatite fission track, and zircon and apatite (U-Th)/He) are particularly useful tools for the study of orogenic settings and are used to quantify a variety of processes related to orogenesis (e.g., Reiners and Brandon, 2006 and references therein). These low-temperature thermochronometric methods have been used in the Alpine orogen to quantify erosion rates, and the timing and rates of exhumation of upper to mid-crustal rocks (e.g. Hurford et al., 1989 and references therein; Bernet et al., 2001; Kuhlemann et al., 2006; Carrapa, 2009, etc.). However, there is a current lack of low-

temperature thermochronologic data for portions of the Alpine orogen. Eastern Switzerland and the adjacent areas are particularly lacking in low-temperature thermochronometric data. To address the deficiency, this study integrates apatite and zircon (U-Th)/He thermochronometry to investigate the thermal evolution of the western-most exposures of the Austroalpine units and Penninic units exposed in the Engadine Window (Figure 1).

The zircon and apatite (U-Th)/He age data from this study are interpreted through inverse modeling of time-temperature histories to provide constraints on the timing, rates of cooling and apparent exhumation, as well as determine possible mechanisms of exhumation during the Tertiary Alpine orogeny. Further, the cooling and apparent exhumation rates determined from inverse modeling of the zircon and apatite (U-Th)/He data are used to elucidate the thermal structure of the region from the Eocene to Miocene during the Alpine orogeny, and to comment on the amount of eroded sediment deposited in the foreland basins during the Oligocene. The timing, degree and nature of exhumation of this region during the Alpine orogeny constrained by low-temperature thermochronology may indicate episodic exhumation of this region of the orogen during the Neogene.

2. Geologic Setting

2.1 General Alpine Terminology

The present day Alps are a doubly-vergent orogen that formed during the Late Cretaceous to Miocene as a result of the closure of multiple ocean basins and the continental collision between Europe and Adria, a promontory of the African plate (for a review see Trümpy, 1980; Schmid et al., 1996, 2004; Handy et al., 2010; Figure 2). The north- and west-vergent Alps are separated from the south-vergent Southern Alps along the Periadriatic Fault Zone (PAFZ; Schmid et al., 1989). The Alpine chain north of the PAFZ has a complex

tectonometamorphic evolution and is divided into several sub-sections that roughly correlate to their paleogeographic positions prior to the Alpine orogeny: (1) Austroalpine units derived from the Adriatic microcontinent composed of poly-metamorphosed crystalline basement and detached to semi-detached sedimentary (Paleozoic to Cenozoic) cover, (2) Penninic units, consisting of the distal portions of the Adriatic and European margins and the intervening units derived from the Alpine Tethys including ophiolitic sequences, Mesozoic to Cenozoic sediments, and continental basement units of the Briançonnais, (3) Helvetic and Ultrahelvetic units, derived from the proximal European margin, broadly consisting of platform carbonate sequences and flysch deposits, and finally (4) Northern Alpine Foreland Basin (NAFB) units, comprised of flysch and molasse sequences (Trümpy, 1980; Schmid et al., 1996; 2004).

2.2 Regional Geologic Setting

The study area is located just east of the present-day boundary between the Penninic and Austroalpine nappes in eastern Switzerland and this study focuses on the thermal evolution of several Austroalpine and Penninic nappes (Figure 1; see section 4.3.1-4.3.7 for more detailed sample location descriptions). To better understand the context of the thermal evolution of the region, a well characterized tectonometamorphic history of the area must be examined. For a general review of the geologic history of the greater Alpine orogen the reader is referred to review papers of Trümpy (1980), Schmid et al. (1996; 2004), and Handy et al. (2010).

2.2.1 Passive Margin Development

The geologic history of this region is quite complex, and has metamorphism and deformation associated with both orogenic and extensional events in the Paleozoic (Trümpy, 1980; von Quadt et al., 1994; Neubauer and Handler, 2000 and references therein). Following Paleozoic deformation, this area was the site of magma-poor continental rifting during the

Jurassic and evolved into a hyper-extended rift margin located on the northwest edge of Adria, facing the developing N-Alpine Tethys (Froitzheim and Manatschal, 1996; Manatschal and Müntener, 2009; Mohn et al., 2010; Figure 2a, 2b). This episode of rifting significantly thinned portions of the future Austroalpine nappes. As a result, they have been divided into three categories based on their positions within the Jurassic rift margin: (1) Upper Austroalpine units (i.e., Silvretta, Ortler, Ela) which represent the proximal portion of the passive Adriatic margin, (2) Middle Austroalpine units (i.e., Campo-Grosina) which constitute the severely extended middle crustal rocks exposed in the "necking zone", or zone of strain localization, within the passive margin, and (3) Lower Austroalpine units (i.e., Bernina-Julier, Err-Corvatsch) exposed in the distal passive margin, which have experienced extreme thinning from low-angle normal faulting (Mohn et al., 2010; Figure 3). The Penninic Tasna nappe exposed in the Engadine Window (Figure 1) also represents a fossil ocean-continent transition (OCT) (Florineth and Froitzheim, 1994; Manatschal et al., 2006). However, the exact paleogeographic location of this OCT is still a matter of debate (Florineth and Froitzheim, 1994; Manatschal et al., 2006; Manatschal and Müntener, 2009). Currently, the preferred position of the Tasna nappe is located within the Briançonnais as a conjugate margin to the Adriatic margin described above (Manatschal and Müntener, 2009). The other Penninic units sampled in this study, the Ramosch zone and Bündnerschiefer within the Engadine Window, are also derived from the N-Alpine Tethys (Florineth and Froitzheim, 1994).

2.2.2 Cretaceous Alpine Orogeny

Subsequent to the development of the passive margins in the region, the area was deformed during the Cretaceous to Miocene Alpine orogeny (Figure 2b-e). The timing and kinematics of the Alpine orogeny have been well documented (Schmid and Froitzheim, 1993;

Froitzheim et al., 1994; Handy et al., 1996), and the general deformational phases described by Froitzheim et al. (1994) will be employed in this paper to discuss the evolution of the study area.

The first episode of deformation associated with the Alpine orogeny within the study area is characterized by top-to-the-west thrusts (D1: Trupchun phase of Froitzheim et al., 1994; Figure 2c) that imbricate the former northwestern passive margin of Adria (i.e., Austroalpine units) from about 90 to 80 Ma (Froitzheim et al., 1994 and references therein; Handy et al., 1996). The timing of this deformational phase is based on the youngest sediments deposited in the Ortler nappe that are cut by D1 thrust faults (Froitzheim et al., 1994). The age of this period of deformation is also constrained by the formation ages of white mica in the Err nappe associated with D1 microstructures (Handy et al., 1996). The metamorphic conditions of the Austroalpine nappes in the area vary during this time period, but are generally between greenschist and anchizonal conditions (Handy et al., 1996 and references therein; Mohn et al., 2010).

The D1 period of west directed thrusting is followed by a period of deformation defined by top-to-the-east normal faults (D2: Ducan-Ela phase of Froitzheim et al., 1994) from about 79 to 67 Ma (Figure 2d; Handy et al., 1996 and references therein). The kinematics of these east directed normal faults (i.e., Ducan, Corvatsch, Fuorcla-Surlej, etc.) have been attributed to orogenic collapse (e.g., Platt, 1986; Schmid et al., 1996) or possibly to extension in the hanging wall of active southward subduction of the N-Alpine Tethys below Adria (e.g., Handy et al., 1996). The metamorphic conditions during the D2 period of extensional exhumation have a temperature range of 250-450 °C, similar to the greenschist and anchizonal conditions of D1 deformation (Handy et al., 1996). There is however a decrease in pressure from the peak estimates of 800-900 MPa during D1 to 400-500 MPa for portions of the Austroalpine units (the

Err nappe) during D2, as expected for a period of extensional exhumation (Handy et al., 1996).

2.2.3 Tertiary Alpine Orogeny

The D2 period of extension marks the end of Cretaceous Alpine orogenic (Eoalpine) deformation within the study area (Froitzheim et al., 1994). Following the Cretaceous, the assembled Austroalpine nappe stack or "orogenic lid" acts as a rigid to semi-rigid block with little internal deformation during subsequent tectonic events (e.g., Laubscher, 1983). The deformation associated with the Tertiary Alpine orogeny commenced in the Paleocene with continued subduction of the Alpine Tethys below Adria, and is followed by continental collision between Europe and Adria from the Eocene to Miocene (Froitzheim et al., 1994; Schmid et al., 1996, 2004; Handy et al., 2010).

Following the Cretaceous Eoalpine episode, deformation within the study area is characterized by north directed thrusting and E to SE-striking folding of the previously assembled Austroalpine nappe stack (D3: Blaisun phase of Froitzheim et al., 1994; Schmid et al., 1996; Figure 2e). The timing of north directed thrusting during the Eocene is constrained by biostratigraphic dating of the youngest sediments in the greater North Penninic Flysch deposited in the N-Alpine Tethys (Ziegler, 1956 in Froitzheim et al., 1994). Following the deposition of these sediments, north directed thrusting carries the orogenic lid, composed of the rigid to semi-rigid Austroalpine nappe stack and the Penninic Platta and Malenco-Forno units accreted during the Cretaceous, as a coherent block an estimated 75 km to the north (Laubscher, 1983; Froitzheim et al., 1994; Schmid et al., 1996). Internal deformation of the orogenic lid during D3 deformation is not pervasive in the study region, and is characterized by only minor thrust faults (Handy et al., 1996) and meter to kilometer scale upright folding (Froitzheim et al., 1994). Temperature conditions during D3 deformation within the Lower Austroalpine Err nappe are

estimated to be 150-250°C based on dynamic calcite recrystallization (Handy et al., 1996).

At a larger scale during the D3 period of deformation, the Penninic units of the Alpine Tethys and distal European margin were either completely subducted or accreted to Adria. The high-pressure metamorphism of Penninic and distal European units results from subduction of crustal material below Adria, and the timing of metamorphism ranges from 46-35 Ma (e.g., Gebauer, 1996; Challandes et al., 2003; Wiederkehr et al., 2009, etc.). Within the Bündnerschiefer of the study area, a Penninic unit exposed in the Engadine Window, the timing of high pressure greenschist facies metamorphism associated with subduction has been dated by *in situ* $^{40}Ar/^{39}Ar$ of white micas to 41.23±1.22 Ma (Wiederkehr et al., 2009).

As the Penninic units and distal portions of Europe were accreted or subducted below Adria the subduction zone became increasingly congested with down-going material, and as a result of contrasting buoyancy forces and changes in the convergence direction of Europe and Adria, the subducting slab foundered below the Central and Eastern Alps (von Blanckenburg and Davies, 1995; Handy et al., 2010). Exact timing of slab break-off is controversial, and estimates range from 45-40 Ma (von Blanckenburg and Davies, 1995; Schmid et al., 1996) to 32-30 Ma (Sinclair, 1997). Slab break-off and subsequent mantle upwelling may have resulted in both the uplift of the overlying crust as well as magmatism (i.e., Periadriatic intrusions; von Blanckenburg and Davies, 1995; Schmid et al., 1996). Further, slab break-off may be the cause for the switch from an underfilled to overfilled Northern Alpine Foreland basin (Sinclair, 1997). Currently there is no conclusive evidence to support a particular model for the timing of slab break-off (Handy et al., 2010).

Following the D3 period of north directed thrusting that culminated in the closure of the N-Alpine Tethys, the study area underwent a short period of syn-collisional E-W extension (D4:

Turba phase of Froitzheim et al., 1994). The D4 period of top-to-the-east extension did not penetratively deform the rigid to semi-rigid orogenic lid. Instead, the majority of deformation was localized along the Turba mylonite, a structure with top-to-the-east sense of shear, located immediately to the west of the study area along the Austroalpine-Penninic tectonic boundary (Froitzheim et al., 1994; Nievergelt et al., 1996). Motion along the Turba mylonite occurred between 45 to 30 Ma, based on formation ages of foliation within the footwall of the fault and truncation of the structure by the 30.13±0.17 Ma Bergell granodiorite (Nievergelt et al., 1996; von Blanckenburg, 1992). However, based on the timing of previous periods of deformation (i.e., D3), Nievergelt et al. (1996) suggested movement along the Turba mylonite probably occurred in the early Oligocene.

After the D4 period of extension, the study area underwent N-S shortening from continued convergence of Adria and Europe during the Oligocene (D5: Domleschg phase of Froitzheim et al., 1994). Within the study area, this period of deformation (D5) is characterized by NE striking folds (Froitzheim et al., 1994; Handy et al., 1996). Handy et al. (1996) postulate subanchizonal metamorphic conditions for the Err nappe during D5 folding. The intrusion of the Bergell tonalite at 31.88±0.09 Ma and granodiorite at 30.13±0.17 Ma, presently exposed in the SE portion of the study area, is concurrent with D5 deformation within the study region (von Blanckenburg, 1992). Backthrusting of the Central Alps over the Southern Alps along the Insubric Line also occurs during the D5 period of deformation. The timing of backthrusting is supported by the synmagmatic deformation of the Bergell pluton associated with movement along the Insubric Line (e.g., Schmid et al., 1996). Backthrusting along the Insubric Line likely commenced prior to the intrusion of the Bergell pluton and D5 deformation (Schmid et al., 1996). The exact timing of the movement prior to the Bergell intrusion is poorly constrained

(e.g., Schmid et al., 1996), but may be as early as 34 Ma and continue as late as 20 Ma (see Figure 2 from Berger et al., 2011).

The final period of deformation (D6) within the study area is characterized by brittle movement along the Engadine Line, aoccurring roughly from the late Oligocene to the middle Miocene (Engadine Line phase of Schmid et al., 1996). The Engadine Line is an oblique sinistral strike-slip fault that strikes NE and cross-cuts the Austroalpine nappes of the study area (Schmid and Froitzheim, 1993). The structure causes relative uplift of NW block near the Engadine Window, purely left lateral strike-slip motion near Samedan, Switzerland, and relative uplift of the SE block near the Bergell intrusion (Schmid and Froitzheim, 1993). The amount of vertical displacement along the Engadine Line near the Engadine Window is estimated at a minimum of 3 km and a maximum of 6 km (Schmid and Froitzheim, 1993). This uplift is thought to be responsible for the formation of the Engadine Window through updoming and unroofing of overlying Austroalpine units (Schmid and Haas, 1989; Schmid and Froitzheim, 1993). The timing of movement along the Engadine Line is poorly constrained, but it must postdate the intrusion of the Bergell grandodiorite at 30.13±0.17 Ma, since the structure cross-cuts the contact aureole of the intrusion (Schmid and Froitzheim, 1993).

3. Sampling Strategy and Previous Work

3.1 Sampling Strategy

To determine the low-temperature thermal history of the region, 66 samples from vertical transects and individual sites were collected throughout the study area. Surface samples were collected and analyzed from an assortment of variably deformed orthogneisses, paragneisses, metamorphosed intrusives and metasediments of the Austroalpine and Penninic units exposed in the region. Sample locations were selected for greatest possible vertical relief and tectonic

position within the Alpine nappe stack. Single surface samples were collected away from main vertical transects where it was necessary to increase the vertical spread in elevation of samples within a tectonic unit. The sampling targets for this study include the Upper Austroalpine (Silvretta), the Middle Austroalpine (Campo-Grosina), the Lower Austroalpine (Bernina-Julier, Err-Corvatsch) and the Penninic units (Tasna, Ramosch zone, Bündnerschiefer).

3.2 Previous Low-Temperature Thermochronologic Studies

The majority of previous thermochronologic studies of the region have focused on the high temperature evolution of the region due to metamorphism related to Paleozoic events (i.e., Variscan orogeny) and the lower temperature (greenschist facies) metamorphism during the Cretaceous (Eoalpine) and Tertiary Alpine orogeny (e.g., Spillman and Büchi, 1993; Handy et al., 1996; Bousquet et al., 2008; Wiederkehr et al., 2009). To our knowledge, lower temperature (i.e., <300 °C) studies of the Alpine orogeny in this region have been restricted to zircon and apatite fission track studies of the Silvretta nappe (Flisch, 1986; Hurford et al., 1989).

The low-temperature fission track study of the Silvretta nappe by Flisch (1986) and later summarized and interpreted by Hurford et al. (1989) indicates a three stage exhumation history of the nappe during the Alpine orogeny. Zircon fission track (ZFT) ages were interpreted to reflect two populations, a set of mixed ages and a set of fully reset ages ranging from ~110-61 Ma (Hurford et al., 1989). Apatite fission track ages (AFT) from the nappe range from ~26 to 12 Ma (Flisch, 1986 in Hurford et al., 1989). Based on these analyses, the Silvretta nappe underwent three phases of cooling following maximum Alpine metamorphic temperatures during the Cretaceous: (1) a general updoming of the nappe between 110-35 Ma, resulting in cooling below 225±25 °C before 60 Ma, (2) homogeneous uplift of the nappe from 35 Ma to 2 Ma, with a ~0.1 mm/year exhumation rate in the Oligocene and (3) an eastward tilting of the nappe

sometime after 2 Ma (Hurford et al., 1989). Based on the ZFT and AFT data, as well as modern day measurements, Hurford et al. (1989) postulate a 30 °C/km geothermal gradient for the Silvretta nappe during the Alpine orogen. This low-temperature study provides a basis of comparison for new zircon and apatite (U-Th)/He ages from this study for the Silvretta nappe.

4. (U-Th)/He Analyses

Zircon and, when possible, apatite (U-Th) /He analyses were completed for each sample collected. The (U-Th)/He thermochronometric technique is based on the retention of alpha particles (He nuclei), as a function of temperature, within a mineral grain during the radioactive decay of ^{238}U, ^{235}U, ^{232}Th and ^{147}Sm (e.g., Zeitler et al., 1987; Wolf et al., 1996; Reiners, 2005). Possible ejection of high energy alpha particles from the outer ~20 μm of mineral grains occurs and is corrected for through a statistical approach based on mineralogical characteristics (i.e., F_T correction; Farley et al., 1996; Farley, 2002). For a more specific discussion of the zircon and apatite (U-Th)/He techniques please see below (section 4.1 and 4.2).

All samples collected underwent standard mineral separation techniques and were analyzed at the Isotope Geochronology Laboratory of the University of Kansas following procedures for apatite described by Stockli et al. (2000) and House et al. (2000), and zircon procedures described by Wolfe and Stockli (2010).

4.1 Zircon (U-Th)/He Methodology

The zircon (U-Th)/He low-temperature thermochronometer offers a robust and routinely used technique for understanding the thermal history of a variety of rock types (e.g. Farley, 2002; Reiners et al., 2002; Tagami et al., 2003; Reiners et al., 2004; Reiners, 2005; Stockli, 2005; Blondes et al., 2007; Lee et al., 2011). Closure temperatures ranging from ~175-193 °C are estimated for the zircon (U-Th)/He system, based on 10 °C/m.y. cooling rate and ~40-100 μm

zircon half width (Reiners, 2005; Wolfe and Stockli, 2010). Although the closure temperature represents the temperature below which the majority of helium is fully retained within the crystal, helium is partially retained within the zircon between 140 and 200°C (zircon HePRZ) based on empirical studies from exhumed fault blocks (Reiners et al., 2002; Tagami et al., 2003; Stockli, 2005) and an *in situ* borehole study (Wolfe and Stockli, 2010). Assuming a geothermal gradient of 30 °C/km, the zircon HePRZ corresponds to depths between 4.6 and 6.6 km in the crust.

Helium retentivity within zircons has been recognized to decrease as a function of several factors other than temperature and these include radiation damage and grain size (e.g. Reiners, 2005). To date, radiation damage has been shown to only affect helium diffusivity characteristics within zircons with alpha dosages, a proxy for radiation damage, of ≥2-4 x 10^{18} α/g (Nasdala et al., 2004; Reiners, 2005). This study will build on this established relationship between radiation damage and a decrease in helium retentivity, but instead use effective uranium concentration ($[U]_e$ =[U]+[Th]0.235+[Sm]0.005) as a proxy for radiation damage (e.g., Shuster et al., 2006). Zircon grain helium retention, and therefore closure temperature, has also been recognized as grain size dependent. Grains with a smaller equivalent spherical radius (ESR), a proxy for grain size, are less retentive and grains with larger ESR are more retentive (Reiners, 2005). The effect of grain size on helium retention is readily observed in samples that have slowly cooled through a zircon HePRZ. A positive correlation between ESR and zircon helium age, and a negative correlation between $[U]_e$ and zircon helium age are useful for documenting slow cooling and residence of zircon grains within the HePRZ (Stockli et al., 2010).

The standard alpha-ejection (F_T) correction assumes a homogenous parent isotope distribution when accounting for the amount of ^{4}He daughter product lost due to alpha-ejection

(e.g., Farley et al., 1996). The alpha stopping distance within zircon is ~20 μm, and as a result the alpha-ejection correction accounts for the daughter product lost in the outer 20 μm of the mineral grain (Farley et al., 1996; Hourigan et al., 2005). However, zonation of parent isotopes within zircon crystals is a common feature, and in some cases the outer 20 μm may have higher or lower parent isotope concentrations in comparison to the rest of grain (Hourigan et al., 2005). In the case of high parent isotope concentrations in the outer 20 μm of the mineral grain, the standard alpha-ejection correction will underestimate the amount of ^{4}He daughter product lost due to alpha-ejection (Reiners et al., 2004; Hourigan et al., 2005). This under correction and the relative contrast between rim and core concentrations, will cause He ages calculated using the standard F_T correction to be too young (Reiners et al., 2004; Hourigan et al., 2005). Even rim thicknesses of only one or two microns with high parent isotope concentrations may produce inaccurate ages (Reiners et al., 2004; Hourigan et al., 2005). The opposite scenario is true for mineral grains with low parent isotope concentrations within the outer 20 μm of the mineral grains (Reiners et al., 2004; Hourigan et al., 2005). The standard F_T correction will overestimate the amount of ^{4}He daughter product lost due to alpha-ejection, which will result in the calculation of erroneously old ages (Reiners et al., 2004; Hourigan et al., 2005). The most erroneous age calculations occur when the thickness of the low parent isotope rim is approximately that of the alpha stopping distance (Reiners, 2005). Inaccurate ages due to zonation may be detected through the over-dispersion of helium ages from multiple single grain analyses for a single sample analyzed (Reiners, 2005). Although, this technique does not preclude a single systematic zonation within a sample, if multiple single grain helium ages are in good agreement zonation is probably not affecting the helium ages (Reiners, 2005). Hourigan et al. (2005) has shown that the determination of U and Th concentrations within a grain prior to

helium age analysis through laser ablation-inductively coupled mass spectrometry (LA-ICPMS) depth-profiling allows the calculation of individualized F_T corrections to determine accurate helium ages within zoned zircons. For zircon samples within this study that exhibit parent isotope zonation, LA-ICP-MS depth-profiling was completed to determine populations of 1D (one-dimensional) U and Th zonation patterns. The observed populations have been used to semi-quantitatively determine accurate zircon helium ages and are discussed below (section 5).

All zircon (U-Th)/He analyses were performed on mineral separates hand-picked for their euhedral morphology, size (>60 μm) and absence of numerous inclusions. Selected zircon single grain aliquots were imaged and measured to complete the F_T correction (e.g., Farley et al., 1996; Farley 2002). These imaged grains were then placed within Pt foil. The Pt wrapped grains were analyzed for ^{4}He within a high-vacuum noble gas extraction line and heated using either a Nd:YAG or diode laser, at temperatures of ~1290 °C for ten minutes. All aliquots were subsequently reheated until 99% of He had been extracted. All released gas was spiked with ^{3}He and analyzed using a quadropole mass spectrometer to determine ^{4}He concentrations. Following gas extraction, aliquots were removed from Pt foil and spiked using an enriched ^{235}U, ^{232}Th, ^{230}Th and ^{149}Sm tracer calibrated against a gravimetric standard solution of 1 ppb U, Th and Sm. Aliquots were then dissolved using standard zircon pressure vessel dissolution techniques first in an HF-HNO_3 solution and subsequently in HCl. Following final dissolution in HCl, aliquots were dried, reconstituted in HNO_3, and diluted to a 5% HNO_3 concentration for analysis of U, Th, and Sm isotopes using either a VG PQII or Thermo Element2 inductively coupled mass spectrometer (ICP-MS). All aliquots have been corrected for alpha-ejection using techniques described by Farley (2002) and Farley et al. (1996). Analytical uncertainties quoted are 8% (2σ) from the reproducibility of internal lab standards. Where the standard deviation of replicate

analyses is greater than the standard error, the larger standard deviation (1σ) is quoted as error (see Appendix A, Table A for comparison of error). Mean ages of multiple samples are quoted with the standard deviation of all replicate analyses of the averaged samples.

4.2 Apatite (U-Th)/He Methodology

Apatite (U-Th)/He thermochronometry is perhaps the most widely used of the multiple (U-Th)/He thermochronometers and has been applied to a variety of geologic settings (e.g. House et al., 1997; 2000; Stockli et al., 2000; Farley and Stockli, 2002; Ehlers and Farley, 2003; Stockli, 2005; Biswas et al., 2007, etc.) The apatite (U-Th)/He thermochronometer has a nominal closure temperature of ~70 °C (based on 10 °C/m.y. cooling rates) and a HePRZ between ~40-80°C (Wolf et al., 1996; 1998; House et al., 1999; Stockli et al., 2000). As a result, the apatite (U-Th)/He technique is an effective method for study of the upper crust, and the apatite HePRZ corresponds to depths of 1.3 to 2.7 km, assuming a 30 °C/km geothermal gradient.

Work by Shuster et al. (2006), and later Flowers et al. (2009), illustrates the link between increased helium retentivity within apatites with increased radiation damage accumulation. Flowers et al. (2009) developed the Radiation Damage Accumulation and Annealing Model (RDAAM), and used this to quantitatively assess the increase in helium retentivity within apatite. The RDAAM is used in this study when modeling apatite helium ages for more accurate inverse models. Grain size may also affect the retention of helium within apatite crystals, similar to effects described above for zircons. However, no correlation between apatite age and grain size is observed within our data set. Zonation of parent isotopes is possible within apatite crystals (e.g., Boyce and Hodges, 2005), and therefore may also affect apatite helium ages. Apatite (U-Th)/He ages of this study have relatively reproducible ages of replicate analyses, suggesting the samples are not strongly enough zoned with respect to U, Th, or Sm to produce significant

effects.

The selection of apatite (U-Th)/He aliquots for analysis was based on the euhedral morphology, size (>60 μm), and total absence of inclusions or cracks. Apatite aliquots were imaged, measured to calculate the F_T correction (Farley et al., 1996) and placed within Pt foil. Helium was extracted using a similar process described for zircon, by a diode laser at a temperature of ~990 °C for five minutes. Following analysis of ^{4}He, aliquots were dissolved in an HNO_3-based enriched ^{235}U, ^{232}Th, ^{230}Th and ^{149}Sm tracer calibrated against a gravimetric standard solution of 1 ppb U, Th and Sm. All aliquots were diluted to 5% HNO_3 concentration and parent isotopes were analyzed using a Thermo Element2 ICP-MS. Apatite ages were corrected for alpha-ejection (Farley et al., 1996) and quote an uncertainty of 6% (2σ) based on reproducibility of internal lab standards. If the standard deviation of replicate analyses is greater than the standard error, the larger standard deviation (1σ) is quoted as error (for comparison of error see Appendix A, Table B). In cases of mean ages of multiple samples, the error quoted is the standard deviation of the aliquot ages used to calculate the mean age.

4.3 (U-Th)/He Results

Sixty-six samples from the study area were analyzed using the zircon (U-Th)/He technique and 34 of these were analyzed using the apatite (U-Th)/He technique. All ages reported are averages of replicate analyses unless otherwise noted (Table 1 and 2). The discrepancy in the total number of zircon and apatite ages is due to the lack of suitable apatite grains from samples based on selection criteria described above. The results are presented roughly in order from highest to lowest tectonic units sampled within the region.

4.3.1 Silvretta (U-Th)/He Analyses

Samples collected within the basement rocks of the Silvretta nappe are from a nearly

vertical transect with ~1200 m spread in elevation located near the Swiss-Austrian border, and a single sample was collected from the Silvretta basement rocks exposed near the bottom of the Engadine valley near Zernez, Switzerland (Figure 1; Table 1 and 2).

The vertical transect records some of the oldest zircon (U-Th)/He ages in the study area; however, these ages are over dispersed, most likely due to inhomogeneous distribution of parent isotopes. The over-dispersion was semi-quantitatively corrected for through zircon helium dating of depth-profiled grains from three samples (10SL03, 05 and 09) spaced evenly throughout the transect. Laser-ablation depth-profiling allowed for the 1D quantification of parent distribution within the outer 18 μm of the zircon grains. The 1D zonation patterns were used to identify problematic zircon helium age populations and to determine the "true" helium age of the Silvretta vertical transect (see section 5). Within the vertical transect, zircon helium ages range from 31-86 Ma, with individual samples exhibiting large standard deviations of replicate analyses (Figure 4a; Table 1 and 4).

Apatite analyses of nine samples (10SL01-09) from the vertical transect yielded reproducible apatite helium ages that range between 19.4±1.2 to 13.1±3.4 Ma (Figure 4a; Table 2). These ages are elevation invariant, with an arithmetic mean age for all replicate analyses of 15.8±2.9 Ma. Several samples are slightly unreproducible (larger standard deviations than standard error) and this may be related to unrecognized inclusions, cracks or irregular morphologies of the analyzed grains.

A single sample (09EN01) within the Silvretta nappe collected near Zernez, Switzerland yielded a reproducible zircon helium age of 31.8±1.9 Ma (Figure 4a; Table 1). Due to the lack of suitable apatite grains, no apatite helium age analyses were conducted on this sample.

4.3.2 Campo-Grosina (U-Th)/He Analyses

A seven sample transect with an elevation spread of ~1100 m was collected in the Eita Valley, Italy across the Grosina and Campo tectonic contact (Figure 1). Samples were collected in each unit from a variety of rock types (paragneisses, orthogneisses or pegamatites). Only zircon (U-Th)/He analyses were completed for these samples due to lack of inclusion-free apatite grains. Most of the zircon helium ages are elevation invariant, ranging from 30.4±1.8 to 37.8±8.9 Ma with a mean of 35.6±5.9 Ma (Figure 4b; Table 1). There is poor zircon helium age reproducibility in several samples, illustrated by large standard deviations of replicate analyses. Possible causes of over-dispersion include inhomogeneous parent isotope distribution, cracks, numerous inclusion and irregular grain morphologies. Reproducible older ages of 52.2±4.2 Ma and 46.6±5.3 Ma are recorded by two samples taken from the Grosina nappe at the highest elevations within the transect (Figure 4b; Table 1), and these ages were excluded from calculation of the mean age. A possible explanation for these reproducibly older ages is residence within a zircon HePRZ (see section 6.3).

4.3.3 Bernina (U-Th)/He Analyses

The Bernina nappe was sampled through a six sample vertical transect in Val da Fain (08BP04, 05, 09, 10, 11, 12) and three individual samples (08BP01, 03, 06) collected along the road from Pontresina to Poschiavo, Switzerland (Figure 1). All nine samples yielded zircon helium ages, and five of these also yielded apatite helium ages. Zircon helium ages are elevation invariant with some minor scatter, with a mean age of all replicate analyses of 35.6±3.8 Ma (Table 1; Figure 4c). The apatite ages range from 26.8±4.1 to 16.9±1.9 Ma and generally young with decrease in elevation (Table 2; Figure 4c). Due to over-dispersion of these apatite helium ages and the resulting large standard deviations of sample ages, this observation must be treated with caution. The most likely explanations for the non-reproducibility of apatite helium ages of

several samples, especially 08BP01, 08BP03, and 08BP11, are unrecognized U- or Th-rich inclusions, irregular grain morphologies, or fast He diffusion pathways (i.e., cracks).

4.3.4 Julier (U-Th)/He Analyses

A single sample of the Julier granite of the Julier nappe was collected at the summit of Julier Pass, Switzerland (Figure 1). This Julier granite sample yielded a reproducible zircon helium age of 37.8±3.0 Ma and is identical to the Bernina zircon helium ages within error (Figure 4c; Table 1). It was not possible to date this sample using apatite given the absence of inclusion-free grains.

4.3.5 Err (U-Th)/He Analyses

The Err nappe was sampled through two vertical transects (08ED, 10ED and 08PN samples) and three individual samples (08FA samples). One vertical transect is located within the Albula granite and stretches from directly below the Jurassic-aged Err detachment to Val Bever, a total elevation range of ~550 m. The other vertical transect was collected in both Saluver metasediments and the Albula granite near Piz Nair and encompasses an elevation range of ~500 m. The other three samples were collected from a preserved portion of the Err nappe overlying the Platta nappe in Val d'Err (Figure 1).

The zircon helium ages are unreproducible within both vertical transects and a single sample from Val d'Err (08FA05). The overall zircon helium ages range from ~119 to ~24 Ma (Table 3; Figure 5a). Replicate analyses for each sample show a positive correlation between zircon helium age and ESR (Figure 5b). The replicate analyses also show a negative correlation between zircon helium age and effective uranium concentration (Figure 5c). Based on these correlations, aliquot ages within single samples may be best explained by residence within a paleo-zircon HePRZ (e.g., Farley et al., 1996; Shuster et al., 2006; Stockli et al., 2010).

Seven apatite helium ages within the Err detachment vertical transect were completed and these data are relatively elevation invariant, with a single highly reproducible younger sample (10ED01; Table 2; Figure 4d). This highly reproducible younger sample was excluded from the calculation of the mean age of the transect. The mean age of the samples that agree within error from the transect is 23.8±3.3 Ma. Only three samples from the vertical transect located near Piz Nair (08PN03, 04, 05) yielded apatite helium ages, and these ages are also elevation invariant with a mean age of 24.8±4.7 Ma (Table 2; Figure 4d). The mean ages of both transects agree within error.

The other two individual samples from Val d'Err have a small elevation spread of ~30 m. Zircon helium ages of these samples are internally reproducible and yield ages of 37.9±6.5 and 44.9±8.0 Ma. Apatite helium analyses were not performed due to a lack of inclusion-free grains.

4.3.6 Corvatsch (U-Th)/He Analyses

A vertical transect of eight samples spanning ~600 m was collected from the metamorphosed felsic instrusive body and slivers of metasediments exposed within the Corvatsch nappe (Figure 1). All eight samples were analyzed for zircon helium ages and five for apatite helium ages. The zircon helium ages of the Corvatsch nappe are elevation invariant with a mean age of 31.1±4.1 Ma (Table 1; Figure 4e). The apatite helium ages range from 23.5±2.5 to 19.0±2.3 Ma. All of the apatite helium ages agree within error and give a mean age of 23.0±6.6 Ma (Table 2; Figure 4e).

4.3.7 Engadine Window (U-Th)/He Analyses

Nine samples were collected from the Engadine Window from three units: (1) the Tasna nappe, a unit of lightly metamorphosed continental basement and metasediments, (2) the Ramosch zone, an ophiolite sequence composed of serpentinite, metabasalts, metagabbros,

metasediments and slices of continental basement, and (3) the Bündnerschiefer, a unit of both metasediments and metabasalts (Florineth and Froitzheim, 1994; Figure 1).

Nine of the samples yielded relatively elevation invariant zircon helium ages with a mean of 29.6±5.6 Ma (Table 1; Figure 4f). Apatite ages from five samples (08TS04, 05, 08, 09, 11) show a decrease in age with elevation and the ages range from 15.8±8.4 to 7.1±2.1 Ma (Table 2; Figure 4f). However, it is important to note these apatite helium ages were slightly unreproducible, so any observed age-elevation trends must be treated with caution. The over-dispersion of the apatite helium ages is likely due to unrecognized radioactive inclusions, cracks or irregular grain morphologies.

5. Parent Isotope Zonation in Zircon Grains from the Silvretta Nappe

Laser ablation depth-profiling in conjunction with CL imaging was completed to determine the degree and nature of zoning of parent isotopes (U and Th) in zircon grains of the Silvretta vertical transect. Approximately 25 grains, from three samples (10SL03, 05, 09) spaced evenly through the vertical transect, were selected based on the criteria described above for helium dating for analysis using laser ablation depth-profiling. Unknown zircon grains and an unzoned internal standard (GJ1; Jackson et al., 2004) were ablated using a 193 nm Photon Machines Excimer Laser. Intensity (counts per second; CPS) of U and Th of the ablated material was measured with a Thermo Element2 ICP-MS. Nine to ten grains per sample were subsequently dated using the (U-Th)/He technique to semi-quantitatively determine the effect of parent isotope zonation on helium age. All analyses were conducted at the Isotope Geochemistry Laboratory of the University of Kansas. Cathodoluminescence (CL) imaging was completed on the remaining laser-ablated grains at the Microscopy Analytical Imaging Laboratory at the

University of Kansas on a LEO 1550 Field Emission Scanning Electron Microscope, to qualitatively determine the 2D parent isotope zoning patterns.

5.1 Depth-profiling Methodology

Unknown Silvretta zircon grains were placed onto double-sided tape on a 2.54 cm diameter epoxy plug and loaded into the sample cell of the Photon Machines Excimer laser for depth-profiling. Each unknown was ablated for 30 seconds, at an ablation rate of ~0.6 μm/sec, a fluency of 3.02 J/cm^2, and a laser repetition rate of 10 Hz. The depth of each laser ablation profile was ~18 μm, and was previously determined from calibration on GJ1 zircon standards at 3.02 J/cm^2 fluency. Concentrations of U and Th were determined from the measured CPS for ^{238}U and ^{232}Th. The calculation of concentrations from the raw intensity data (CPS) was based on three assumptions: (1) the down-hole intensity decrease from the increasing matrix-effects during ablation is linear, (2) the average down-hole intensity loss correction factor calculated for the standard GJ1 analyses is applicable to unknowns, and (3) the average concentration of U and Th in GJ1 is 230 and 15 ppm, respectively (Jackson et al., 2004). Based on these assumptions, the average concentration of the standard was used to determine the intensity of raw signal for one ppm of U and Th. This calculated value was then used to determine the concentrations of U and Th in the unknowns using their down-hole fractionation corrected intensities. The concentration profiles were plotted against depth, calculated using the known ablation rate, to determine the 1D pattern of U and Th zonation within each grain.

5.2 Comparison of Depth-profiling and Zircon (U-Th)/He Age Results

The 1D parent isotope zonation patterns determined from LA-ICP-MS depth-profiling were separated into five categories (Figure 6) and these categories are used to semi-quantitatively assess the effects of zonation on the accuracy of the zircon helium ages. For

simplification the pattern of U concentrations in the laser ablation depth-profiles were used to define each category. Since U and Th often behave similarly within the grains, this simplification is justifiable although there are some exceptions (i.e., Figure 6a and 6c). Despite the uncoupled behavior of U and Th, the categories are still reasonable as U contributes the majority of the daughter product to the system (e.g., Shuster et al., 2006). Therefore, zonation of this radioactive parent has the greatest effect on the zircon helium ages.

The five categories of parent zonation patterns and representative depth-profiles are presented in Figure 6. The five categories are defined as: (1) nearly homogeneous uranium distribution (Figure 6a), (2) relatively high U concentration within a rim and core zone (Figure 6b), (3) a U rim concentration at least five times greater than the U concentration of the rest of the depth profile (Figure 6c), (4) a U rim concentration less than five times greater than the rest of the depth profile (Figure 6d), and (5) a single relatively high U concentration zone within the interior of the grain (Figure 6e). The defined zonation categories were then used to filter the measured zircon helium ages from nine to ten depth-profiled grains from each sample (Figure 7). It is important to note that there appears to be no correlation between a particular sample and its recorded zircon helium ages, even when filtered by zonation characteristics (Figure 7). The lack of correlation suggests elevation within the transect has no control on helium age (i.e., elevation invariant ages), and the over-dispersion of ages is completely controlled by the degree and nature of parent isotope zonation within individual zircon grains.

The first category of nearly homogenous parent isotope distribution likely records the true zircon helium age for the transect, as the standard alpha-ejection correction applied to this category does not erroneously estimate the bulk retentivity of the zircon grains (Hourigan et al., 2005). The two zircon helium ages defined as type 1 are in excellent agreement, supporting the

claim that this is the "correct" zircon helium age of the transect. The second category of relatively high rim and core parent isotope concentrations shows a scatter of zircon helium ages that range from ~58 to 32 Ma. Three out of six grains within this category fall within the semi-quantitatively defined zircon helium age based on category 1. This agreement may be a result of some counterbalance between the influence of the rim and core concentrations on the calculated F_T correction. The third category consists of five zircon helium ages that range from ~44 to 33 Ma and four out of five grains in the category record systematically too young ages. These erroneously young helium ages are expected for zircon grains with rims of U concentrations that are a factor of five or greater than the rest of the depth profile (Hourigan et al., 2005). The fourth category is also defined by relatively high U concentration rims, however these depth-profiles show less than a factor of five concentration increase compared to the rest of the profile. Nine zircon helium ages fall into this category and range from ~48-32 Ma. As expected for a high parent concentration overgrowth most of the helium ages within this category are too young when compared to category 1 (e.g., Hourigan et al., 2005), although three ages have similar ages to category 1. The depth-profiles of the grains that are in agreement with category 1 show no discernable difference when compared to the others of category 4. It is possible these "correct" helium ages result from a low parent isotope concentration core not captured by the shallow depth-profiles that counterbalances the high concentration of the rims. The fifth category consists of six zircon helium ages that range from ~53-36 Ma. Several of the grains within this category are in agreement with the zircon helium age of category 1 despite relatively high U concentration zones within the outer 20 μm of the grain. The agreement of many of the zircon helium ages in this category with the defined zircon helium age is likely due to the diminishing

influence of high concentration zones on the overall bulk retentivity when located further within the zircon grains (Hourigan et al., 2005).

The semi-quantitatively defined zircon helium age determined from the depth-profiled grains is now used as the zircon (U-Th)/He age of the Silvretta vertical transect, since age dispersion within the transect can be solely attributed to parent isotope zonation (Figure 8). This corrected zircon helium age of ~47 Ma for the Silvretta transect agrees with the known cooling history of the Silvretta nappe interpreted from fission track data (Figure 8; Hurford et al., 1989).

5.3 CL Imaging and Parent Isotope Zonation Patterns

To better understand the qualitative 2D parent isotope zonation patterns within the depth-profiled grains and to confirm the relevance of the defined zonation categories, grey-scale CL imaging was completed on 15 to 16 grains from each sample. The CL images qualitatively display the U and Th concentrations through the intensity of brightness of the grey-scale image. Within the CL images there is an inverse relationship between brightness intensity and U and Th concentration (i.e., dark regions represent higher U and Th concentrations). Nasdala et al. (2003) attributes this correlation to increased radiation damage resulting in decreased crystallinity and hence decreased luminescence in zones with high U and Th concentrations.

Representative CL images for the grains imaged are compiled in Figure 9. These images illustrate the lack of a single systematic zonation pattern within the zircon grains. However, the imagery does show several recurring characteristics of the zonation patterns. Many zircon grains appear to have inherited cores, which vary from irregular to subhedral morphologies and have either high or low U and Th concentrations (i.e., Figure 9a, 9f, 9j). Some zircon grains display relatively concentric zoning (i.e., Figure 9b, 9d, 9l), whereas others have no concentric zoning (i.e., Figure 9g, 9i, 9k). Several grains also exhibit high U and Th overgrowths within 20 μm of

the grain boundary and relatively high U and Th zones within the tips of the grains (i.e., 9g, 9h). The majority of the grains have a thin low U and Th overgrowth zone (i.e., 9c, 9e, 9h). Nonconcentric zoning and relatively high U and Th tips typically produce the most erroneous and systematically young (U-Th)/He ages (Hourigan et al., 2005). The zonation characteristics of the zircon grains based on the CL imagery are well represented in the categories used to qualitatively assess the Silvretta zircon (U-Th)/He ages. Notably, the low U and Th cores of the CL imagery are not seen in the defined categories, and this is the result of the relatively shallow (~18 μm) laser-ablation pit depths used in this study. The low U and Th cores of grains may also explain the too old zircon helium ages from Silvretta not accounted for in the depth-profiled grains (e.g., Hourigan et al., 2005; Figure 8).

6. (U-Th)/He Inverse Thermal Modeling

6.1 Modeling Methodology

Inverse modeling of the presented zircon and apatite (U-Th)/He analyses was completed using the numerical modeling software, Helium Modeling Package (HeMP; Hager and Stockli, 2009), to quantify the cooling history of the study region during the Alpine orogeny. The HeMP software package allows for the modeling of 1D vertical transects of multiple (U-Th)/He thermochronometers through the generation of random thermal histories within pre-defined time-temperature constraints and a selected range of geothermal gradients (Hager and Stockli, 2009; Lee et al., 2011). These generated thermal histories are simulated for each sample in a vertical transect based on input sample spacing and user-defined range of geothermal gradients. These simulated ages are then compared with measured helium ages using the goodness of fit algorithm described by Ketcham et al. (2000) and Ketcham (2005) to determine “acceptable” and “good” fits. Helium diffusion parameters used to calculate ages are described by Reiners (2005) for

zircon, and the RDAAM model and diffusion kinetics described by Flowers et al. (2009) for apatite (Lee et al., 2011). Standard alpha-ejection corrections were applied to all (U-Th)/He ages used for the modeling. All randomly generated thermal paths were allowed five nodes between defined time-temperature constraints to allow for sufficient complexity in the thermal histories generated.

Vertical transects from Campo-Grosina, Bernina, Corvatsch and the Engadine Window were modeled using apatite and zircon (U-Th)/He ages and errors presented in Figure 4. Zircon (U-Th)/He ages of the Err detachment vertical transect are over-dispersed due to residence in a zircon HePRZ. In order to model this transect, the average zircon helium age of replicate analyses with standard error (8%) were used in conjunction with the apatite helium ages. The Silvretta and Piz Nair vertical transects were excluded from modeling based on very uncertain zircon helium average ages that would produce unreliable modeling results. Fortunately, the time-temperature history for the Piz Nair vertical transect is likely similar to the Err detachment transect because of their proximity within the same nappe. The time-temperature history of the Silvretta vertical transect may be estimated based on several thermochronometers (see section 6.2).

In some cases, apatite data was absent for a given sample. In order to utilize the zircon data of the sample in the modeling software, a placeholder apatite age was created. These place holder samples were created by averaging the replicate apatite ages of the next higher and next lower elevation. The standard deviation of these averaged ages was used as the error for the created apatite age. If the placeholder sample was the highest or lowest sample within a vertical transect, the closest apatite data was used to create the placeholder, and the age error used was the standard deviation of the original apatite age. Where the standard deviations of placeholders

were less than 2.5, two standard deviations were employed for modeling the vertical transects. This error increase was implemented to prevent results of the models from being controlled by the created placeholder ages. These placeholder ages did not affect the modeled results and instead simply allowed for modeling of the vertical transects.

6.2 Modeling Constraints

The inverse models of time-temperature histories for the zircon and apatite (U-Th)/He vertical transects were completed using independently known time-temperature constraints and a reasonable geothermal gradient range. Two time-temperature constraints were imposed on all of the inverse modeling of the vertical transects.

Austroalpine units exposed in the study region are known to have reached peak Alpine metamorphic conditions of anchizonal to greenschist facies during the Cretaceous (e.g., Froitzheim et al., 1994 and references therein; Handy et al., 1996; Handy and Oberhänsli, 2004). As a result, the temperature constraints used for the Austroalpine units is a maximum of 350 °C and minimum of 250 °C. The initial time constraints used for the Austroalpine units is based on the end of Eoalpine deformation in the Cretaceous in the region around 65 Ma (e.g., Froitzheim et al., 1994; Handy et al., 1996). The boundaries of this initial time-temperature constraint agree with the known thermal history of the Silvretta nappe based on zircon fission track data (i.e., cooling below 225±25 °C; Hurford et al., 1989). The final time-constraint used is the mean annual surface temperature at the time of collection (~10 °C).

Penninic units of the study region underwent well documented high-pressure/low-temperature metamorphism in the Eocene (e.g., Bousquet et al., 2008; Wiederkehr et al., 2009). As a result, the initial time-temperature constraint for the samples modeled in the Engadine Window is 40 Ma, based on the youngest ages of high-pressure metamorphism in the

Bündnerschiefer (Wiederkehr et al., 2009). The initial temperature constraints used were based on the Bousquet et al. (2008) estimations of peak metamorphic conditions at ~350°C for the Engadine Window, and for the program inputs this is a range from 400-300°C. This broad time-temperature constraint allows for all geologically plausible initial conditions for the Penninic units modeled. The mean annual surface temperature (~10 °C) at time of collection was used for the final time-temperature constraint.

The selected geothermal gradients range from 15 °C/km to 50 °C/km and encompass reasonable geothermal gradients for an active orogen. The geothermal gradient estimated from previous ZFT and AFT work in the Silvretta nappe is 30 °C/km (Hurford et al., 1989).

6.3 (U-Th)/He Inverse Modeling Results

Numerical modeling using the HeMP software was completed to quantify cooling histories, cooling rates, and apparent exhumation rates during the Tertiary Alpine orogeny. The modeled vertical transect results and interpretations are presented in descending order through the Tertiary Alpine nappe stack. Modeling results are presented assuming a geothermal gradient of 30 °C/km based on the conclusions from previous ZFT and AFT interpretations, and the modern day geothermal gradient of the area (Hurford et al., 1989). The inverse modeling results for acceptable and when possible good fit time-temperature histories for each transect are presented in figures 10 through 14. For each model a preferred time-temperature history was chosen based on a visual inspection of the distribution of either good or acceptable fits. All models yielded either good or acceptable fits. The Campo-Grosina, Bernina, and Corvatsch models all required a single outlier data pair to obtain model fits. The Engadine Window required no outlier data pairs and the Err transect required two outlier data pairs.

The Campo-Grosina time-temperature model is only based on zircon (U-Th)/He ages and as a result the modeled time-temperature histories are relatively unconstrained above 200 °C and below 140 °C (Figure 10). Based on the zircon (U-Th)/He ages, the modeled time-temperature histories exhibit a protracted cooling history through the zircon PRZ from about 51 Ma to 40 Ma. The cooling rate at this time is between 5 to 10 °C/m.y., and assuming a 30 °C/km geothermal gradient the cooling rate translates to an apparent exhumation rate of 0.2-0.3 mm/yr. The good fit time-temperature histories of this model support the interpretation previously proposed that the upper portion of the transect records slow cooling through the zircon HePRZ (see section 4.3.2).

Modeled time-temperature histories for samples from the Bernina nappe are based on zircon and apatite (U-Th)/He data (Figure 11). The initial portion of the modeled time-temperature histories are relatively unconstrained, as the oldest zircon (U-Th)/He data point used for modeling is ~39 Ma. The model is well constrained based on the zircon and apatite age data from ~39 until ~17 Ma, the age of the youngest apatite data. During this time period the preferred time-temperature history has a cooling rate of >10 and <20 °C/m.y. This range of cooling rates translates to an apparent exhumation of rate range of 0.3 to 0.7 mm/yr between ~39 to 17 Ma. After ~17 Ma the model is no longer constrained by input data.

The Err detachment vertical transect was modeled based on zircon and apatite (U-Th)/He data (Figure 12). The modeled time-temperature histories are relatively well constrained from ~49-38 Ma (zircon (U-Th)/He data) and from ~26-16 Ma (apatite (U-Th)/He data). Based on the preferred time-temperature history of the modeling results, this vertical transect cooled slowly through the zircon HePRZ ~49 to ~37 Ma at a rate of 1 to 5 °C/m.y. The range of cooling rates converts to apparent exhumation rates of 0.03 to 0.2 mm/yr. Following this period of protracted

cooling through the zircon HePRZ, the cooling rate of the Err vertical transect is relatively unconstrained until ~26-21 Ma. From ~26-21 Ma the cooling rate increases to ~10-20 °C/m.y. This range of cooling rates translates to apparent exhumation rates of ~0.3-0.7 mm/yr. The onset of this increase in cooling rate may be somewhat obscured by the lack of data between earlier zircon (U-Th)/He data and the younger apatite (U-Th)/He ages. The preferred modeled time-temperature history substantiates the earlier interpretation of residence within the zircon HePRZ based on zircon (U-Th)/He age-ESR and $[U]_e$ plots (Figure 5b, and c) of samples from the Err nappe (see section 4.3.5).

Time-temperature histories modeled for the Corvatsch vertical transect were based on both zircon and apatite (U-Th)/He age data and this model is well constrained from ~36 to 19 Ma (Figure 13). Prior to the oldest and after the youngest (U-Th)/He input ages the modeled time-temperature history is relatively unconstrained. The preferred modeled time-temperature history shows a cooling rate of ~20 °C/m.y. from ~31 to 24 Ma. The apparent exhumation rate based on the cooling rate is ~0.7 mm/yr. This modeled time-temperature history is similar to the Bernina vertical transect, however the rates of cooling and apparent exhumation of the Corvatsch vertical transect are higher.

The Penninic nappes of the Engadine Window are modeled based on zircon and apatite (U-Th)/He age data. The modeled time-temperature histories are well constrained from ~35 to 7 Ma based on input (U-Th)/He age data. The preferred modeled time-temperature history shows an increased period of cooling from ~29 to 21 Ma, with a cooling rate of ~50 °C/m.y. This cooling rate translates to an apparent exhumation rate of ~1.7 mm/yr for the 8 Ma timespan. Following this period of rapid cooling, the time-temperature history indicates a decrease in

cooling rate to between 1 and 5 °C/m.y. beginning at 21 Ma until present. This cooling rate is equivalent to an apparent exhumation rate of 0.03-0.2 mm/yr.

7. Interpretation of (U-Th)/He Analyses and Thermal Modeling

7.1 Timing of Cooling and Exhumation of the Austroalpine nappes

The timing of cooling and exhumation of the Austroalpine nappes during the Alpine orogeny is recorded by the zircon and apatite (U-Th)/He thermochronometers. The oldest cooling ages recorded are zircon (U-Th)/He ages of the Silvretta, Campo-Grosina and Err nappes. Based on zircon (U-Th)/He age-elevation plot of the Campo-Grosina (Figure 4b), and zircon (U-Th)/He age-ESR and zircon (U-Th)/He age-$[U]_e$ plots of the Err nappe (Figure 5b and c), these vertical transects slowly cooled through the zircon HePRZ. This interpretation is supported by the inverse time-temperature modeling of these data sets (section 6.3). Based on modeled time-temperature histories the Campo-Grosina and Err nappes, protracted cooling through the zircon HePRZ ocurred from ~51 to 37 Ma (Figure 15). The oldest fully reset zircon (U-Th)/He ages of the Err nappe are located in Val d'Err, at ~45 and ~37 Ma (Table 1). These fully reset ages are slightly over-dispersed but agree within uncertainty with the modeled end of slow cooling of the Err nappe.

The Silvretta vertical transect, located within the northern portion of the study area, records a depth-profiled corrected zircon (U-Th)/He age of ~47 Ma. Based on the current data it is impossible to determine if this age is fully or partially reset. The semi-quantitatively corrected zircon helium age combined with ZFT and AFT data of Hurford et al. (1989) and the apatite (U-Th)/He data from this study allows for the development of a tentative cooling history of the Silvretta vertical transect (Figure 15). Based on this time-temperature history, the vertical transect has undergone slow cooling through the zircon HePRZ from ~52 to 36 Ma, similar to

the time-temperature histories of the Campo-Grosina and Err transects. Although this time-temperature history may not be valid for the entire nappe since a sample from the Silvretta nappe within the Engadine valley records a fully reset zircon (U-Th)/He age of ~32 Ma. However, this tentative cooling history does agree with the previously published cooling history of the nappe by Hurford et al. (1989).

Cooling below the 140 °C isotherm recorded in the Bernina-Julier and Corvatsch nappes postdates the protracted cooling through the zircon HePRZ by the Campo-Grosina, Err, and possibly Silvretta nappes. The Bernina-Julier and Corvatsch transects all cooled relatively quickly through the zircon HePRZ as shown by their elevation invariant zircon (U-Th)/He age-elevation plots. The Bernina samples and the sample from the Julier slice, record slightly older ages of cooling than the Corvatsch vertical transect. The Bernina vertical transect and associated samples record cooling through the zircon thermal sensitivity window at ~36 Ma, and the Julier sample at approximately the same time, ~38 Ma. The Corvatsch vertical transect records cooling of zircon at ~31 Ma. This distribution of ages suggests either differential cooling of the nappe stack, or a deeper paleo-depth of the Corvatsch vertical transect.

The apatite (U-Th)/He system records similar timing of cooling through the apatite thermal sensitivity window (~80-40 °C) in all the sampled Austroalpine nappes of the southern portion of the study area. The mean apatite (U-Th)/He ages from the Bernina, Err/Piz Nair and Corvatsch sample sites all agree within uncertainty at ~23 Ma. The Silvretta nappe of the northern portion of the study area records a younger apatite (U-Th)/He mean age at ~16 Ma (Figure 15). The older ages in the south and younger age in the north suggest a different mechanism for cooling through the apatite (U-Th)/He thermal sensitivity window at each of the localities.

The constraints on the temporal and spatial distribution of cooling histories allow the thermal structure of the Austroalpine nappe stack of the study area to be determined for the Eocene through the early Miocene. The location and timing of cooling through the zircon HePRZ for Err and Campo-Grosina allow for a 1D determination of the paleo 140 °C and 200 °C isotherms during the Eocene (Figure 16). The timing of cooling through the zircon HePRZ recorded by the Bernina, Julier, Val d'Err and Corvatsch samples all substantiate the location of these paleo-isotherms and attest to the longevity of this thermal regime, at least 20 m.y. These paleo-isotherms cross-cut the older D1 and D2 structures of the cross section, indicating thermal equilibration of the nappe stack following Eoalpine deformation. The cooling history of the Silvretta nappe suggests a similar thermal regime was present in the northern portion of the study area for at least the Eocene and possibly into the Oligocene.

The apatite (U-Th)/He data show the Austroalpine nappes of the southern and northern portions of the study area experienced different onests of cooling through the apatite thermal sensitivity window. The diachronous nature of cooling suggests either different thermal regimes or different mechanisms were driving cooling in the north and south during the late Oligocene and early Miocene.

7.2 Timing of Cooling and Exhumation of the Penninic nappes

The timing of cooling and exhumation of the Penninic nappes exposed in the Engadine Window is recorded by the zircon and apatite (U-Th)/He thermochronometers. The three Penninic units sampled in the Engadine Window record similar zircon (U-Th)/He cooling ages at ~30 Ma. This age is similar to the timing of cooling of the Corvatsch vertical transect of the southern portion of the study area. The apatite (U-Th)/He cooling ages show a trend of younger ages with lower elevations and these range from ~16 to 7 Ma. The oldest apatite (U-Th)/He age

of the transect is similar to the age recorded in the Silvretta, suggesting a similar thermal regime between the Austroalpine nappe and the Penninic units exposed within the window.

7.3 Cooling and Apparent Exhumation Rates of the Austroalpine nappes

The preferred time-temperature histories based on inverse modeling of zircon and apatite (U-Th)/He ages for the Austroalpine nappes show a three stage cooling history (Figure 15). The rate of cooling and apparent exhumation for these stages can be determined from the preferred model time-temperature histories. The first stage from ~51 to 36 Ma, recorded by zircon (U-Th)/He data of the Silvretta, Campo-Grosina and Err nappes, is characterized by slow cooling. The cooling rates of this phase are greater than 1 but less than 10 °C/m.y. and have corresponding apparent exhumation rates of greater than 0.03 and less than 0.3 mm/yr. The second stage begins at ~36 Ma and extends at the latest to ~21 Ma. This phase is recorded by the zircon and apatite (U-Th)/He age data of Bernina and Corvatsch, and the apatite (U-Th)/He age data of Err/Piz Nair. Cooling rates between 10-20 °C/m.y. and apparent exhumation rates of 0.3-0.7 mm/yr are recorded in this second phase of cooling. The range of cooling rates from the time-temperature histories may indicate a general increase in cooling rates from the late Eocene through the early Oligocene. Following this period of increased cooling and exhumation rates, the Bernina, Err and Corvatsch time-temperature histories indicate a decrease in cooling rate to greater than 1 but less than 10 °C/m.y. These cooling rates correspond to apparent exhumation rates of greater than 0.03 and less than 0.3 mm/yr, and these rates extend until present. It should be noted the data do not constrain the cooling and apparent exhumation rates well during the third stage. However, the modeled apparent exhumation rate agrees with present-day erosion estimates (Hergarten et al., 2010).

The Silvretta nappe only shows a similar cooling history to the Austroalpine nappes of the southern portion of the field area from ~52 to ~36 Ma. Following this time period the cooling rate determined through the tentative time-temperature reconstruction is steady at ~1-5°C/m.y., with a corresponding apparent exhumation rate of ~0.2-0.03 mm/yr. Based on the tentative cooling history, the cooling rate determined for the Silvretta nappe at ~16 Ma is ~10°C/m.y., with an apparent exhumation rate of ~0.3 mm/yr. This period of rapid cooling is reflected in the elevation invariant apatite (U-Th)/He ages of the ~1200 m vertical transect. After ~16 Ma, the cooling rate of the Silvretta nappe is slower, at ~1-5°C/m.y., with a corresponding apparent exhumation rate of ~0.2-0.03 mm/yr. This rate of apparent exhumation is in good agreement with the Oligocene to Quaternary uplift rates determined from the AFT study (Hurford et al., 1989).

7.4 Cooling and Apparent Exhumation Rates of the Penninic nappes

The preferred time-temperature history based on inverse modeling of the Penninic nappes exposed in the Engadine Window shows a relatively well constrained two-stage cooling history beginning at ~29 Ma (Figure 15). The first stage of cooling from ~29 to 26 Ma is rapid, with a cooling rate of ~50 °C/m.y. and apparent exhumation rate of ~1.7 mm/yr. This cooling rate and apparent exhumation rate is the highest for any samples recorded in this study. This increased cooling rate may indicate a continued increase in cooling rates from the late Eocene into the Oligocene for the study area (section 7.3). Following the period of rapid cooling, cooling rates decrease to ~1-5 °C/m.y., translating to apparent exhumation rates of ~0.03-0.2 mm/yr. This second period has comparable rates of cooling to the overlying Silvretta nappe, suggesting a single mechanism for the cooling of both units. The apparent rate of exhumation is in agreement

with present-day erosion rate estimates (Hergarten et al., 2010), as well as uplift rates determined from AFT in the Silvretta nappe (Hurford et al., 1989).

7.5 Estimation of Magnitude of Exhumation

Based on the location of the paleo 200 °C isotherm (section 7.1; Figure 16), and its current exposure at the surface, it is possible to place a minimum estimate on the total magnitude of exhumation of the Austroalpine nappes since the Eocene. Assuming a geothermal gradient of 30 °C/km, the paleo 200 °C isotherm corresponds to a paleodepth, and minimum amount of exhumation, of 6.6 km since the Eocene. It is also clear that the some samples of Silvretta (Engadine valley sample), Bernina-Julier, Val d'Err and Corvatsch resided at some depth below the 200 °C isotherm. As a result, 6.6 km likely underestimates the total magnitude of exhumation of the Austroalpine nappes for the Eocene to present. A minimum estimate of 6.6 km for total exhumation also applies to the Penninic nappes exposed in the Engadine Window. However, this estimate is only valid for exhumation since the late Eocene to early Oligocene based on the timing of cooling through the paleo 200 °C isotherm recorded by the zircon (U-Th)/He ages.

8. Discussion

8.1 Mechanisms for Cooling and Exhumation

The zircon and apatite (U-Th)/He thermochronometers record cooling of the study area from the Eocene to late Miocene. The cooling history of the Austroalpine nappes is better constrained in the southern portion of the study area, whereas the cooling of the Silvretta nappe in the northern portion of the study area is more tentative. The Penninic nappes of the southern portion of the Engadine Window have a well constrained cooling history based on the zircon and apatite thermochronometers, and inverse time-temperature modeling.

The (U-Th)/He data of the Austroalpine nappes in the southern part of the study area record slow cooling through the zircon HePRZ during the Eocene, more rapid cooling in the late Eocene to the Miocene, and a final period of slow cooling until the present. The cooling history recorded in the northern portion of the study area (Silvretta nappe and Engadine Window) is somewhat similar, with slow cooling in the Eocene, rapid cooling in the early Oligocene, and is dissimilar based on later cooling through the apatite thermal sensitivity window in the Miocene. The timing of cooling recorded by these thermochronometers can be related to the general deformation periods defined for the study region, and possible kinematic mechanisms may be inferred for the minimum 6.6 km of exhumation of the crust (see section 7.5).

8.1.1 North Directed Thrusting

The slow cooling of Campo-Grosina, Silvretta and Err nappes in the Eocene occurs during the D3 period of deformation (Figure 15; Figure 17). This period of deformation is associated with continental collision between Europe and Adria, and is defined by north directed thrusting of the orogenic lid as a coherent block approximately 75 km to the north (Figure 18; Laubscher, 1983; Froitzheim et al., 1994; Schmid et al., 1996). The protracted cooling through the zircon HePRZ may result from slow, but progressive exhumation of the orogenic lid as it is thrust to the north. However, it is not possible to rule out that the slow cooling through the zircon HePRZ is a result of relaxation of isotherms following continental collision during the Eocene.

8.1.2 Slab break-off, Backthrusting and Crustal Duplexing

Following the first phase of slow cooling, a period of increased cooling rates occurs from ~36 Ma until ~21 Ma. This period of increased cooling rates occurs during the end of D3 deformation, through D4 and into the D6 deformational phase of the study area (Froitzheim et al., 1994). The period from ~36-21 Ma is recorded in the zircon and apatite helium ages of the

Bernina and Corvatsch transects, the apatite helium ages of the Err nappe, and the zircon helium ages of the Penninic nappes exposed in the Engadine Window (Figure 15; Figure 17). Interestingly, with the exception of the Turba mylonite, located further to the west, there are no large structures that cross-cut the nappe stack during this period of rapid cooling (Froitzheim et al., 1994). Further, the only penetrative deformation seen in the nappe stack during this period is meter to kilometer scale upright folding and minor thrust faults (Froitzheim et al., 1994; Handy et al., 1996). Therefore, the increased cooling and apparent exhumation rates recorded in the Bernina-Julier, Err-Corvatsch, and Penninic nappes must result from exhumation due to either deeper or more regional scale structures. Throughout this period several possible indirect mechanisms for cooling and exhumation of the sampled areas occurred including: (1) break-off of the subducting slab below Adria, resulting in uplift of the overlying crust due to mantle upwelling (von Blanckenburg and Davies, 1995; Sinclair, 1997), (2) backthrusting of the orogenic lid along the Insubric Line (e.g., Schmid et al., 1996), and (3) crustal duplexing of Penninic nappes, European upper crust, and Helvetic nappes beneath the Austroalpine and Penninic units of the study area (e.g., Schmid et al., 1996; Hitz, 1996; Berger et al. 2011). The timing of these three mechanisms compared to the cooling history of the study area is summarized in Figure 17. Based on the correlation of timing between increased cooling rates (~36-21 Ma) and each tectonic mechanism, it is somewhat difficult to determine the cause of crustal exhumation in the study area. However, the proposed timings of slab break-off at either 45-40 Ma (von Blanckenburg and Davies, 1995), or 32-30 Ma (Sinclair, 1997), appears to be either too early (45-40 Ma) or too late (32-30 Ma) to cause the observed increase in cooling rates due to asthenospheric upwelling (Figure 17). The other two tectonic mechanisms, subjacent crustal duplexing and backthrusting along the Insubric Line, are in better agreement with the

time span of increased cooling and apparent exhumation rates. Although, the timing of crustal duplexing of the underlying Penninic units and European margin from ~45-31 Ma (Zapport and Ferrara phase reviewed in Berger et al., 2011) may not be of sufficient duration (Figure 17). However, crustal duplexing of the more inboard Helvetic nappes underlying the study area (e.g., Hitz, 1996) may continue later into the Oligocene (e.g., Berger et al., 2011) and could explain the sustained cooling rates until ~21 Ma. The timing of backthrusting along the Insubric Line has no well-defined upper age constraint (see section 2.2.3). Backthrusting of the orogenic lid may begin as early as 34 Ma, and displacement along the structure may continue as late as 20 Ma (see Figure 2 of Berger et al., 2011). This time span for movement along the Insubric Line is in agreement with the period of increased cooling rates (Figure 17). Based solely on the duration of each tectonic mechanism, the most likely cause of exhumation of the study area from ~36-21 Ma is backthrusting along the Insubric Line.

The spatial distribution and the onset of higher cooling rates of the individual vertical transects may provide further evidence for a specific tectonic mechanism. The period of increased cooling rates is first recorded in the Austroalpine Bernina and Corvatsch vertical transects located in the southern part of the study area. The highest rates of cooling and apparent exhumation are recorded in the structurally deepest Penninic samples located in the northern portion of the study area. These observations may suggest subjacent duplexing as a likely mechanism, since crustal duplexing at depth generally progressed from the south to the north (e.g., Schmid et al., 1996; Berger et al., 2011; Figure 18). However, crustal duplexing alone would also suggest the majority of exhumation would be confined to the northern portion of the study area (Figure 19). In contrast, if backthrusting along the Insubric Line is solely responsible for the increase in cooling and apparent exhumation rates from ~36-21 Ma, the greatest

exhumation should be observed closest to the structure in southern part of the study area (Figure 19). Instead a similar amount of exhumation is observed in the Penninic samples in the north. Therefore, neither backthrusting nor crustal duplexing alone are likely to produce the spatial distribution of cooling rates and exhumation amounts observed. A combination of crustal duplexing below the Austroalpine and Penninic units and backthrusting along the Insubric Line is more likely to create the relatively uniform exhumation of the region from ~36-21 Ma (Figure 19).

Based on the timing of the three tectonic mechanisms it seems most likely that backthrusting along the Insubric Line caused the observed period of increased cooling and apparent exhumation rates from ~36-21 Ma. Alternatively, based on the spatial distribution and magnitude of exhumation from individual transects it seems more plausible that crustal duplexing at depth and backthrusting are responsible for this period of cooling and exhumation (Figure 19). The relatively uniform nature of the exhumation, flat lying isotherms (see section 7.5), and synchronous timing, suggests a combination of the two tectonic mechanisms resulted in the increased cooling rates from the late Eocene to the Miocene.

8.1.3 Engadine Line

The localized younger period of cooling from ~16-7 Ma, recorded by apatite (U-Th)/He data of the Silvretta and Engadine Window suggests another, more localized mechanism for this period of cooling and exhumation. The rate of cooling at ~16 Ma, recorded by the Silvretta vertical transect, must have been relatively rapid since the apatite (U-Th)/He age-elevation plots for the ~1200 m transect are elevation invariant. The underlying Penninic nappes of the Engadine Window, spanning ~1100 m, record a similar onset at ~16 Ma, but continue to cool

until ~7 Ma, recorded in the lowest elevation sample. This suggests a decrease in cooling rates through time as the structurally lower Penninic nappes were exhumed.

The Engadine Line, an oblique left-lateral strike-slip fault, is responsible for the formation of the Engadine Window through updoming and unroofing of the overlying Austroalpine nappes (i.e., Silvretta; Schmid and Froitzheim, 1993). Uplift (northwest side up) along the structure near the SW terminus of the window is estimated between 3 and 6 km (Schmid and Froitzheim, 1993). However, the timing of movement along the Engadine Line is only constrained by a cross-cutting relationship with the contact aureole of the Bergell intrusion, and therefore must post-date the intrusion of the Bergell granodiorite at 30.13±0.17 Ma (von Blanckenburg, 1992; Schmid and Froitzheim, 1993). It is possible that the relatively rapid cooling recorded at ~16 Ma in the Silvretta vertical transect and upper elevations of the Engadine Window samples is a response to exhumation along the Engadine Line. The more protracted cooling from ~16-7 Ma recorded by the Engadine Window samples may result from slower cooling caused by erosional unroofing of the window following movement along the structure. The Engadine Line is a regional structure that would seemingly affect the exhumation of the Austroalpine nappes of the southern portion of the study area. However, the structure had purely left-lateral strike-slip motion in the vicinity of these samples during the Miocene and would cause little to no cooling of the stack due to slip along the fault (Schmid and Froitzheim, 1993).

8.2 Rigidity of Orogenic Lid

The Austroalpine nappes of this study are the western exposure of the orogenic lid (e.g., Laubscher, 1983). The preferred cooling histories of the Austroalpine nappes show that the orogenic lid experienced a similar cooling history throughout the study area from the Eocene to Oligocene. Only the Silvretta nappe records a younger cooling history in the Miocene related to

brittle movement along the Engadine Line. This suggests the orogenic lid largely behaved as a rigid to semi-rigid block during deformation and exhumation associated with N-S convergence of Adria and Europe. The relatively flat lying isotherms (Figure 16) inferred, based on the distribution of zircon (U-Th)/He ages of the region, suggests that large scale backfolding of the study area did not occur. Instead, the study area was exhumed as a coherent mass until the movement along the Engadine Line in the Miocene. This inference from the cooling histories of the study area is in good agreement with the lack of structural evidence for penetrative deformation during this time period (e.g., Froitzheim et al., 1994; Handy et al., 1996).

8.3 Hinterland Exhumation and Foreland Basin Interaction

The zircon and apatite (U-Th)/He age data from our study area, located within the hinterland of the Alpine orogen, show a period of increased cooling rates and apparent exhumation rates from ~36 to ~21 Ma. The exhumation of this volumetrically significant portion of the orogen must have had some effect on the amount of sediment deposited within the associated foreland basins.

During the period of increased cooling rates observed in the study area, the Northern Alpine Foreland Basin (pro-foreland) shifted from an underfilled to an overfilled basin, at approximately 33-30 Ma (Sinclair, 1997). The coincidence between the observed increase in cooling rates in our study area, and the increase of basin fill (e.g., Sinclair, 1997) suggests that this phenomenon is not confined to the eastern Central Alps. Further, evidence from a detrital thermochronologic study of the pro-foreland of the Western Alps suggests the hinterland was undergoing a period of increased exhumation between 38 and 36 Ma (Carrapa, 2009). The detrital study (Carrapa, 2009) and basin fill study (Sinclair, 1997) suggests that our observed increase in cooling rates and exhumation may represent a regional scale increase. Depending on

paleo-erosion rates, a regional scale increase in cooling and exhumation indicates that the Alpine orogen may have experienced episodic exhumation (e.g., Kuhlemann et al., 2006; Carrapa, 2009) instead of steady-state exhumation as proposed by Bernet et al. (2001; 2009).

The sediment yield curve (Figure 20), originally developed by Kuhlemann et al. (2001), associated with our study region suggests a period of rapid exhumation from 30-28 Ma. Kuhlemann et al. (2001) attribute this increase in sediment yield to exhumation associated with continental collision and slab break-off (e.g., Schmid et al., 1996; Sinclair, 1997). However, the data from this study show that at least a portion of the Alpine orogen was undergoing exhumation prior to 30 Ma. The record of this exhumation is not reflected in the sediment yield curve. An estimated 18,000 km^3 of sediment from our study area was delivered to the foreland basins from the study area before ~26 Ma. This estimate is based on ~4500 km^2 spatial extent of samples (Figure 1), and ~4 km exhumation of the samples before ~25 Ma. The ~4 km of exhumation is based on the cooling of the Bernina, Corvatsch, and Engadine Window samples from below 200 °C beginning at ~36 Ma to ~80 °C by ~26 Ma (Figure 15), assuming a 30 °C/km geothermal gradient. This amount of exhumation, or removal of overburden, corresponds to a minimum sediment flux of ~1,800 km^3/m.y from ~36-26 Ma. However, if the 4 km of exhumation occurred over only 5 m.y., then a maximum sediment flux of ~3,600 km^3/m.y. from ~36-31 Ma would be recorded (Figure 20).

Based on the data of this study alone, the sediment yield curve (Figure 20) for the late Eocene to early Oligocene is incorrect. Kuhlemann et al. (2001) acknowledges the Oligocene sediment budget may be inaccurate due to sediment recycling from thrust dissection and cannibalism of the foreland basin deposits during continental collision. Cooling ages similar to this period of rapid cooling are the dominant detrital zircon (U-Th)/He ages of the Northern

Alpine Foreland Basin (NAFB) deposits (Miller et al., 2011). This dominant cooling age signal suggests that recycling of older basin deposits occurred into younger NAFB deposits. Further, there is evidence from other studies (e.g., Sinclair, 1997; Carrapa, 2009) suggesting this period of exhumation is not confined to the eastern Central Alps. This further suggests that the early Oligocene portion of the sediment budget is severely underestimated not only for the Eastern Alps sediment curve, but possibly the Western and Central Alps as well.

9. Conclusions

Zircon and apatite (U-Th)/He thermochronology of the Austroalpine and Penninic units of Eastern Switzerland and adjacent areas were used to determine the cooling history of the region. The overall cooling history of the study area shows the region behaved as a rigid to semi-rigid block during continental collision and continued convergence until the Engadine Line affected the nappe stack in the Miocene. The cooling history of this specific region has broader implications for the current model of steady state exhumation and the sediment budget developed for the Alpine orogen.

Slow cooling through the zircon HePRZ is recorded throughout the Austroalpine nappes of the study area during the Eocene from ~52 to 36 Ma. This first period of cooling is a result of exhumation of the study area by north directed thrusting associated with the onset of continental collision between Adria and Europe. Previously the timing of continental collision within this area was constrained by the age of the youngest sediments deposited within the N-Alpine Tethys (e.g., Froitzheim et al., 1994). These new data offer further evidence for the proposed timing of continental collision. Further, the relatively uniform cooling of the Austroalpine units of the study area is further evidence for the coherent nature of north directed thrusting (e.g., Laubscher, 1983).

A second period of rapid cooling is recorded in both Austroalpine and Penninic units of the study area from ~36 to 21 Ma. This period of rapid cooling and exhumation may be a result of backthrusting along the Insubric Line, crustal duplexing at depth, or some interplay between these mechanisms. The timing of backthrusting and crustal duplexing at depth is consistent with exhumation due to either mechanism for the second period of cooling. However, we propose that a combination of these mechanisms is necessary to produce the observed vertical exhumation of the study area as a coherent mass. Further, the relatively uniform nature of exhumation in the study area suggests that exhumation caused by south-vergent backfolding is not a dominant mechanism for exhumation, as observed in other regions of the Alpine orogen (e.g., Southern Steep Belt).

The estimated sediment flux during this second cooling period, ~1800-3600 km^3/m.y., indicates the late Eocene to early Oligocene sediment budget for the eastern Alps underestimates true sediment yield by ~800 km^3/m.y. Further, detrital studies from the pro-foreland documents a similarly timed increase in the exhumation rates as this study (Carrapa, 2009; Miller et al., 2011). These studies suggest the hinterland exhumation is more aerially extensive, and that recycling of older deposits into younger deposits has occurred (Carrapa, 2009; Miller et al., 2011). Therefore, the sediment yield curve may underestimate the late Eocene to early Oligocene sediment budget for the entire Alpine orogen by much more than ~800 km^3/m.y.

A third and final period of cooling and exhumation, beginning at ~16 Ma is recorded only locally within in the northern portion of the study area. This period of cooling is a result of vertical exhumation along the oblique left-lateral Engadine Line. Previously, the timing of movement of the Engadine Line was only loosely constrained based on a cross-cutting relationship with the Bergell granodiorite's contact aureole (e.g., Schmid and Froitzheim, 1993).

The period of cooling recorded in the apatite (U-Th)/He ages of the Silvretta and Engadine Window samples better constrains movement along the structure, and indicates activity at ~16 Ma. Continued cooling was recorded within the Engadine Window until ~7 Ma, and is likely a result of erosional exhumation of the updomed window.

Finally, the timing and degree of exhumation of the eastern Central Alps presented in this study contributes to the growing body of evidence for temporally episodic exhumation of the Alpine orogen. The three stage cooling history of this study indicates apparent exhumation rates fluctuated during the Tertiary Alpine orogen, which is in direct contrast to the steady-state exhumation hypothesis. The data of this study, in conjunction with evidence from the Carrapa (2009) study, clearly indicates the temporally episodic nature of exhumation was aerially extensive. Ultimately, the data from this study area helps to challenge the steady-state exhumation hypothesis, and indicates episodic exhumation of a portion of the Alpine orogen occurred in the Tertiary.

References

Anonymous, 2005, Geologische Karte der Schweiz, 1:500,000. Bundesamt für Landestopographie, Bern

Berger, A., Schmid, S. M., Engi, M., Bousquet, R., and Wiederkehr, M., 2011, Mechanisms of mass and heat transport during Barrovian metamorphism: A discussion based on field evidence from the Central Alps (Switzerland/northern Italy): Tectonics, v. 30, p. TC1007.

Bernet, M., Zattin, M., Garver, J. I., Brandon, M. T., and Vance, J. A., 2001, Steady-state exhumation of the European Alps: Geology, v. 29, p. 35-38.

Bernet, M., Brandon, M., Garver, J., Balestieri, M., Ventura, B., and Zattin, M., 2009, Exhuming the Alps through time: clues from detrital zircon fission track thermochronology: Basin Research, v. 21, p. 781-798.

Blondes, M. S., Reiners, P. W., Edwards, B. R., and Biscontini, A., 2007, Dating young basalt eruptions by (U-Th)/He on xenolithic zircons: Geology, v. 35, p. 17-20.

Biswas, S., Coutand, I., Grujic, D., Hager, C., and Stockli, D., 2007, Exhumation uplift of the Shillong plateau and its influence on the eastern Himalayas: New constraints from apatite and zircon (U-Th-[Sm])/He and apatite fission track analyses: Tectonics, v. 26, TC6013.

Bousquet, R., Oberhänsli, R., Goffé, B., Wiederkehr, M., Koller, F., Schmid, S. M., Schuster, R., Engi, M., Berger, A., and Martinotti, G., 2008, Metamorphism of metasediments at the scale of an orogen: a key to the Tertiary geodynamic evolution of the Alps *in* Siegesmund, S., Fügenschuh, B., and Froitzheim, N. (eds) Tectonic Aspects of the Alpine-Dinaride-Carpathian System: Geological Society, London, Special Publications, v. 298, p. 393-411.

Boyce, J., and Hodges, K., 2005, U and Th zoning in Cerro de Mercado (Durango, Mexico)

fluorapatite: Insights regarding the impact of recoil redistribution of radiogenic ^{4}He on (U-Th)/He thermochronology: Chemical Geology, v. 219, p. 261-274.

Carrapa, B., 2009, Tracing exhumation and orogenic wedge dynamics in the European Alps with detrital thermochronology: Geology, v. 37, p. 1127-1130.

Challandes, N., Marquer, D., and Villa, I., 2003, Dating the evolution of C–S microstructures: a combined ^{39}Ar/^{40}Ar step-heating and UV laserprobe analysis of the Alpine Roffna shear zone: Chemical Geology, v. 197, p. 3-19.

Dumitru, T. A., 2000, Fission-track geochronology *in* Noller, J.S., Sowers, J.M., Lettis, W.R. (eds.), 2000, Quaternary Geochronology: methods and applications. Washington: American Geophysical Union, p. 131-155.

Dunkl, I., Mikes, T., Frei, D., Gerdes, A., and von Eynatten, H., 2009, PepiAge v.1, available from http://www.sediment.uni-goettingen.de/staff/dunkl/software/pepi-age.html

Ehlers, T., and Farley, K., 2003, Apatite (U-Th)/He thermochronometry: methods and applications to problems in tectonic and surface processes: Earth and Planetary Science Letters, v. 206, p. 1-14.

Farley, K., 2002, (U-Th)/He Dating: Techniques, Calibrations, and Applications: Reviews in Mineralogy and Geochemistry, v. 47, p. 819-844.

Farley, K., and Stockli, D., 2002, (U-Th)/He Dating of Phosphates: Apatite, Monazite, and Xenotime: Reviews in Mineralogy and Geochemistry, v. 48, p. 559-577.

Farley, K., Wolf, R., and Silver, L., 1996, The effects of long alpha-stopping distances on (U-Th)/He ages: Geochimica et Cosmochimica Acta, v. 60, p. 4223-4229.

Florineth, D., and Froitzheim, N., 1994, Transition from continental to oceanic basement in the Tasna nappe (Engadine Window, Graubünden, Switzerland): evidence for Early

Cretaceous opening of the Valais ocean: Schweizerische Mineralogische und Petrographische Mitteilungen, v. 74, p. 437–448.

Flisch, M., 1986, Die Hebungsgeschichte der oberostalpinen Silvretta-Decke seit der mittleren Kreide: Bull. Ver. Schweiz. Pet.-Geol. Ing, v. 53, p. 23-49.

Flowers, R., Ketcham, R., Shuster, D., and Farley, K., 2009, Apatite (U-Th)/He thermochronometry using a radiation damage accumulation and annealing model: Geochimica et Cosmochimica Acta, v. 73, p. 2347-2365.

Frisch, W., Dunkl, I., and Kuhlemann, J., 2000, Post-collisional orogen-parallel large-scale extension in the Eastern Alps: Tectonophysics, v. 327, p. 239-265.

Froitzheim, N., and Manatschal, G., 1996, Kinematics of Jurassic rifting, mantle exhumation, and passive-margin formation in the Austroalpine and Penninic nappes (eastern Switzerland): Geological Society of America Bulletin, v. 108, p. 1120-1133.

Froitzheim, N., Schmid, S. M., and Conti, P., 1994, Repeated change from crustal shortening to orogen-parallel extension in the Austroalpine units of Graubünden: Eclogae Geologicae Helvetiae, v. 87, p. 559-612.

Froitzheim, N., Schmid, S. M., and Frey, M., 1996, Mesozoic paleogeography and the timing of eclogite-facies metamorphism in the Alps: A working hypothesis: Eclogae Geologicae Helvetiae, v. 89, p. 81-110.

Gebauer, D., 1996, A P-T-t path for an (Ultra?-) high-pressure ultramafic/mafic rock-association and its felsic country-rocks based on SHRIMP-dating of magmatic and metamorphic zircon domains. Example: Alpe Arami (Central Swiss Alps): Geophysical Monograph-American Geophysical Union, v. 95, p. 307-330.

Hager, C., Stockli, D.F., 2009, A new MATLAB©-based helium modeling package (“HeMP”)

for thermal history recovery from single and multi-thermochronometer (U-Th)/He data and data arrays: Geological Society of America Abstracts with Programs, v. 41, p. 487.

Handy, M. R., Herwegh, M., Kamber, B. S., Tietz, R., and Villa, I., 1996, Geochronologic, petrologic and kinematic constraints on the evolution of the Err-Platta boundary, part of a fossil continent-ocean suture in the Alps (eastern Switzerland): Schweizerische Mineralogische und Petrographische Mitteilungen, v. 76, p. 453-474.

Handy, M., and Oberhänsli, R., 2004, Age map of the metamorphic structure of the Alps—tectonic interpretation and outstanding problems: Mitteilungen der Österreichischen Mineralogischen Gesellschaft, v. 149, p. 97-121.

Handy, M. R., Schmid, S. M., Bousquet, R., Kissling, E., and Bernoulli, D., 2010, Reconciling plate-tectonic reconstructions of Alpine Tethys with the geological--geophysical record of spreading and subduction in the Alps: Earth Science Reviews, v. 102, p. 121-158.

Hergarten, S., Wagner, T., and Stüwe, K., 2010, Age and Prematurity of the Alps Derived from Topography: Earth and Planetary Science Letters, v. 297, p. 453-460.

Hitz, L., 1996, The deep structure of the Engadine Window: Evidence from deep seismic data: Eclogae Geologicae Helvetiae, v. 89, p. 657-676.

Hourigan, J. K., Reiners, P. W., and Brandon, M. T., 2005, U-Th zonation-dependent alpha ejection in (U-Th)/He chronometry: Geochimica et Cosmochimica Acta, v. 69, p. 3349-3365.

House, M., Farley, K., and Stockli, D., 2000, Helium chronometry of apatite and titanite using Nd-YAG laser heating: Earth and Planetary Science Letters, v. 183, p. 365-368.

House, M., Wernicke, B., Farley, K., and Dumitru, T., 1997, Cenozoic thermal evolution of the central Sierra Nevada, California, from (U-Th)/He thermochronometry: Earth and

Planetary Science Letters, v. 151, p. 167-179.

House, M. A., Farley, K. A., and Kohn, B. P., 1999, An empirical test of helium diffusion in apatite: borehole data from the Otway basin, Australia: Earth and Planetary Science Letters, v. 170, p. 463-474.

Hurford, A., Flisch, M., and Jäger, E., 1989, Unravelling the thermo-tectonic evolution of the Alps: a contribution from fission track analysis and mica dating *in* Coward, M. P., Dietrich, D, and Park, R. G. (eds), 1989, Alpine Tectonics, Geological Society Special Publication No. 45, p. 153-171.

Jackson, S. E., Pearson, N. J., Griffin, W. L., and Belousova, E. A., 2004, The application of laser ablation-inductively coupled plasma-mass spectrometry to in situ U-Pb zircon geochronology: Chemical Geology, v. 211, p. 47-69.

Jarvis, A., Reuter, H., Nelson, A., and Guevara, E., 2008, Hole-filled seamless SRTM data V4, International Centre for Tropical Agriculture (CIAT), available from http://srtm.csi.cgiar.org.

Ketcham, R. A., 2005, Forward and inverse modeling of low-temperature thermochronometry data *in* Reiners, P.W. and Ehlers, T.A. (eds), Low-Temperature Thermochronology: Techniques, Interpretations, and Applications, v. 58, p. 411-448.

Ketcham, R. A., Donelick, R. A., and Donelick, M. B., 2000, AFTSolve: A program for multi-kinetic modeling of apatite fission-track data: Geological Materials Research, v. 2, p. 1-32.

Kuhlemann, J., Frisch, W., Dunkl, I., and Szekely, B., 2001, Quantifying tectonic versus erosive denudation by the sediment budget: The Miocene core complexes of the Alps: Tectonophysics, v. 330, p. 1-23.

Kuhlemann, J., Dunkl, I., Brugel, A., Spiegel, C., and Frisch, W., 2006, From source terrains of the Eastern Alps to the Molasse Basin: Detrital record of non-steady-state exhumation: Tectonophysics, v. 413, p. 301-316.

Laubscher, H., 1983, Detachment, shear and compression in the central Alps: Contributions to the tectonics and geophysics of mountain chains: Geological Society of America Memoir, v. 158, p. 191–211.

Lee, J., Hager, C., Wallis, S. R., Stockli, D. F., Whitehouse, M. J., Aoya, M., and Wang, Y., 2011, Middle to late Miocene extremely rapid exhumation and thermal reequilibration in the Kung Co rift, southern Tibet: Tectonics, v. 30, p. TC2007.

Manatschal, G., Engström, A., Desmurs, L., Schaltegger, U., Cosca, M., Müntener, O., and Bernoulli, D., 2006, What is the tectono-metamorphic evolution of continental break-up: The example of the Tasna Ocean-Continent Transition: Journal of Structural Geology, v. 28, p. 1849-1869.

Manatschal, G., and Müntener, O., 2009, A type sequence across an ancient magma-poor ocean-continent transition: the example of the western Alpine Tethys ophiolites: Tectonophysics, v. 473, p. 4-19.

Manatschal, G., Müntener, O., Lavier, L., Minshull, T., and Péron-Pinvidic, G., 2007, Observations from the Alpine Tethys and Iberia–Newfoundland margins pertinent to the interpretation of continental breakup: Geological Society, London, Special Publications, v. 282, p. 291-324.

Miller, J., Stockli, D., Möller, A., Oalmann, J., 2011, Zircon U-Pb-He double dating of Northern Alpine Foreland Basin, Switzerland: Implications for orogenic dynamics and subsidence: Geologic Society of America Abstracts with Programs, v. 43, p. 654.

Mohn, G., Manatschal, G., Masini, E., and Müntener, O., 2010, Rift-related inheritance in orogens: a case study from the Austroalpine nappes in Central Alps (SE-Switzerland and N-Italy): International Journal of Earth Sciences, p. 1-25.

Nasdala, L., Zhang, M., Kempe, U., Panczer, G., Gaft, M., Andrut, M., and Plotze, M., 2003, Spectroscopic methods applied to zircon *in* Hanchar J.M, and Hoskin, P.W.O. (eds), Reviews in Mineralogy and Geochemistry, v. 53, p. 427-467.

Nasdala, L., Reiners, P., Garver, J., Kennedy, A., Stern, R., Balan, E., and Wirth, R., 2004, Incomplete retention of radiation damage in zircon from Sri Lanka: American Mineralogist, v. 89, p. 219-231.

Neubauer, F., and Handler, R., 2000, Variscan orogeny in the Eastern Alps and Bohemian Massif: How do these units correlate: Mitteilungen Österreichische Geologische Gesellschaft, v. 92, p. 35-59.

Nievergelt, P., Liniger, M., Froitzheim, N., and Mählmann, R. F., 1996, Early to mid Tertiary crustal extension in the Central Alps: The Turba mylonite zone (eastern Switzerland): Tectonics, v. 15, p. 329-340.

Peters, T., 2005, Blatt Nr. 1257 St.Moritz. - Geol. Atlas der Schweiz 1:25'000, Karte 118, mit Erlaüterungen. Bundesamt für Wasser und Geologie, Bern

Platt, J., 1986, Dynamics of orogenic wedges and the uplift of high-pressure metamorphic rocks: Geological Society of America Bulletin, v. 97, p. 1037-1053.

Reiners, P., 2005, Zircon (U-Th)/He thermochronometry *in* Reiners, P.W. and Ehlers, T.A. (eds), Low-Temperature Thermochronology: Techniques, Interpretations, and Applications, v. 58, p. 151-179.

Reiners, P., Farley, K., and Hickes, H., 2002, He diffusion and (U-Th)/He thermochronometry of

zircon: initial results from Fish Canyon Tuff and Gold Butte: Tectonophysics, v. 349, p. 297-308.

Reiners, P., Spell, T., Nicolescu, S., and Zanetti, K., 2004, Zircon (U-Th)/He thermochronometry: He diffusion and comparisons with $^{40}Ar/^{39}Ar$ dating: Geochimica Et Cosmochimica Acta, v. 68, p. 1857-1887.

Reiners, P. W., and Brandon, M. T., 2006, Using Thermochronology to Understand Orogenic Erosion: Annual Review of Earth and Planetary Sciences, v. 34, p. 419-466.

Schmid, S., Aebli, H., Heller, F., and Zingg, A., 1989, The role of the Periadriatic Line in the tectonic evolution of the Alps *in* Coward, M. P., Dietrich, D, and Park, R. G. (eds), 1989, Alpine Tectonics, Geological Society Special Publication, p. 153-171.

Schmid, S., and Haas, R., 1989, Transition from near-surface thrusting to intrabasement decollement, Schlinig Thrust, Eastern Alps: Tectonics, v. 8, p. 697-718.

Schmid, S., and Froitzheim, N., 1993, Oblique slip and block rotation along the Engadine Line: Eclogae Geologicae Helvetiae, v. 86, p. 569-593.

Schmid, S., Pfiffner, O., Froitzheim, N., Schönborn, G., and Kissling, E., 1996, Geophysical-geological transect and tectonic evolution of the Swiss-Italian Alps: Tectonics, v. 15, p. 1036-1064.

Schmid, S. M., Fügenschuh, B., Kissling, E., and Schuster, R., 2004, Tectonic map and overall architecture of the Alpine orogen: Eclogae Geologicae Helvetiae, v. 97, p. 93-117.

Shuster, D. L., Flowers, R. M., and Farley, K. A., 2006, The influence of natural radiation damage on helium diffusion kinetics in apatite: Earth and Planetary Science Letters, v. 249, p. 148-161.

Sinclair, H., 1997, Flysch to molasse transition in peripheral foreland basins: The role of the

passive margin versus slab breakoff: Geology, v. 25, p. 1123-1126.

Spillmann, P., and Büchi, H., 1993, The pre-Alpine basement of the lower Austroalpine nappes in the Bernina massif (Grisons, Switzerland; Valtellina, Italy): Pre-Mesozoic Geology in the Alps. Springer-Verlag, Berlin, p. 457–467.

Stampfli, G. M., and Hochard, C., 2009, Plate tectonics of the Alpine realm: Geological Society, London, Special Publications, *in* Murphy, J. B., Keppie, J. D. and Hynes, A. J. (eds) Ancient Orogens and Modern Analogues. Geological Society, London, Special Publications, v. 327, p. 89–111.

Steiger, R., and Jäger, E., 1977, Subcommission on geochronology: convention on the use of decay constants in geo-and cosmochronology: Earth and Planetary Science Letters, v. 36, p. 359-362.

Stockli, D. F., 2005, Application of low-temperature thermochronometry to extensional tectonic settings, *in* Reiners, P.W. and Ehlers, T.A. (eds), Low-Temperature Thermochronology: Techniques, Interpretations, and Applications, v. 58, p. 411-448.

Stockli, D. F., Farley, K. A., and Dumitru, T. A., 2000, Calibration of the apatite (U-Th)/He thermochronometer on an exhumed fault block, White Mountains, California: Geology, v. 28, p. 983-986.

Stockli, D. F., Wolfe, M. R., Pujols, E. J., Goldsmith, A., Ghorbal, B., 2010, The good, the bad, and the metamict – Bulk He diffusion and radiation damage in zircon and impact on zircon (U-Th)/He thermochronometry: Thermo2010 Conference Abstract, v. 2, p.51

Tagami, T., Farley, K., and Stockli, D., 2003, (U-Th)/He geochronology of single zircon grains of known Tertiary eruption age: Earth and Planetary Science Letters, v. 207, p. 57-67.

Tagami, T., and Dumitru, T. A., 1996, Provenance and thermal history of the Franciscan

accretionary complex: Constraints from zircon fission track thermochronology: Journal of Geophysical Research, v. 101, p. 11353-11364.

Trümpy, R., Bernoulli, D., Grunenfelder, M., Koppel, M., Muller, S., and V., T., 1980, Geology of Switzerland, a guidebook. Part A Schweiz Geol Kommission, Basel, Wepf., 104 p.

von Blackenburg, F., 1992, Combined high-precision chronometry and geochemical tracing using accessory minerals: applied to the Central-Alpine Bergell intrusion (central Europe): Chemical Geology, v. 100, p. 19-40.

von Blanckenburg, F., and Davies, J. H., 1995, Slab breakoff: A model for syncollisional magmatism and tectonics in the Alps: Tectonics, v. 14, p. 120-131.

von Quadt, A., Grünenfelder, M., and Büchi, H., 1994, U-Pb zircon ages from igneous rocks of the Bernina nappe system (Grisons, Switzerland): Schweizerische Mineralogische und Petrographische Mitteilungen, v. 74, p. 373–382.

Wiederkehr, M., Sudo, M., Bousquet, R., Berger, A., and Schmid, S. M., 2009, Alpine orogenic evolution from subduction to collisional thermal overprint: The 40Ar/39Ar age constraints from the Valaisan Ocean, central Alps: Tectonics, v. 28, p. TC6009.

Willett, S., 2010, Late Neogene Erosion of the Alps: A Climate Driver?: Annual Review of Earth and Planetary Sciences, v. 38, p. 411-437.

Wolf, R. A., Farley, K. A., and Silver, L. T., 1996, Helium diffusion and low-temperature thermochronometry of apatite: Geochimica Et Cosmochimica Acta, v. 60, p. 4231-4240.

Wolf, R., Farley, K., and Kass, D., 1998, Modeling of the temperature sensitivity of the apatite (U-Th)/He thermochronometer: Chemical Geology, v. 148, p. 105-114.

Wolfe, M. R., and Stockli, D. F., 2010, Zircon (U-Th)/He thermochronometry in the KTB drill hole, Germany, and its implications for bulk He diffusion kinetics in zircon: Earth and

Planetary Science Letters, v. 295, p. 69-82.

Zeitler, P., Herczeg, A., McDougall, I., and Honda, M., 1987, U-Th-He dating of apatite: A potential thermochronometer: Geochimica et Cosmochimica Acta, v. 51, p. 2865-2868.

Ziegler, W., 1956, Geologische Studien in den Flyschgebieten des Oberhalbsteins (Graubünden): Eclogae Geologicae Helvetiae, v. 49, p. 1-78.

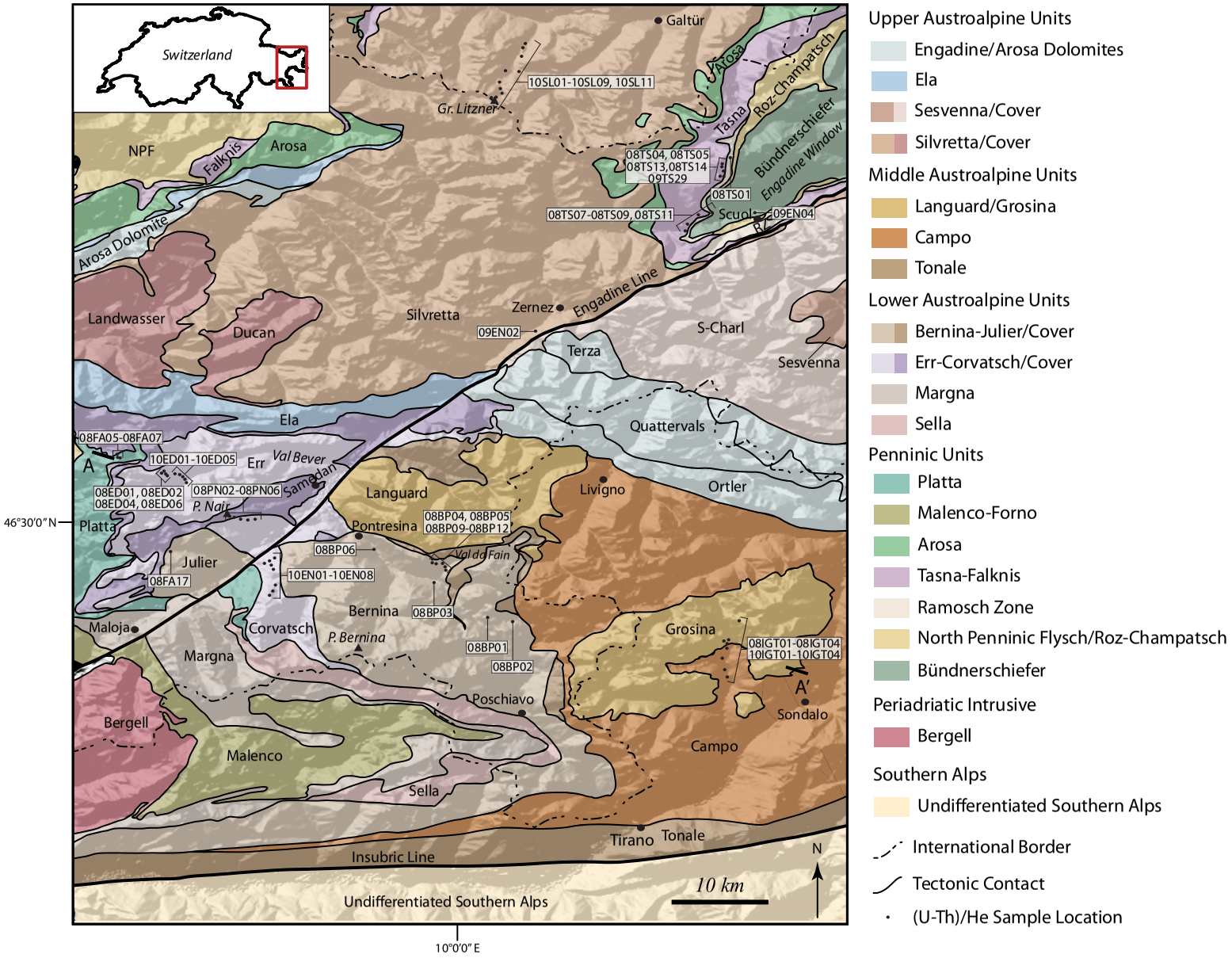
Switzerland
Galtür
10SL01-10SL09, 10SL11
Gr. Litzner
Arosa
Tasna
Roz-Champatsch
Bündnerschiefer
Engadine Window
NPF
Falknis
Arosa
08TS04, 08TS05
08TS13,08TS14
09TS29
08TS01
08TS07-08TS09, 08TS11
Scuol
09EN04
Arosa Dolomite
Engadine Line
Zernez
09EN02
Landwasser
Ducan
Silvretta
S-Charl
Terza
Sesvenna
Ela
Quattervals
08FA05-08FA07
10ED01-10ED05
Err
Val Bever
Samaden
08ED01, 08ED02
08ED04, 08ED06
08PN02-08PN06
P. Nair
Languard
Livigno
Ortler
Platta
Pontresina
08BP04, 08BP05
08BP09-08BP12
08BP06
Val da Fain
Julier
08FA17
10EN01-10EN08
Bernina
08BP03
Maloja
Corvatsch
P. Bernina
Grosina
08IGT01-08IGT04
10IGT01-10IGT04
Margna
08BP01
08BP02
Poschiavo
Sondalo
Bergell
Malenco
Campo
Sella
Tirano
Tonale
Insubric Line
Undifferentiated Southern Alps
10 km
N
A
A'
46°30'0" N
10°0'0" E
Upper Austroalpine Units
Engadine/Arosa Dolomites
Ela
Sesvenna/Cover
Silvretta/Cover
Middle Austroalpine Units
Languard/Grosina
Campo
Tonale
Lower Austroalpine Units
Bernina-Julier/Cover
Err-Corvatsch/Cover
Margna
Sella
Penninic Units
Platta
Malenco-Forno
Arosa
Tasna-Falknis
Ramosch Zone
North Penninic Flysch/Roz-Champatsch
Bündnerschiefer
Periadriatic Intrusive
Bergell
Southern Alps
Undifferentiated Southern Alps
International Border
Tectonic Contact
(U-Th)/He Sample Location

Figure 1. Tectonic map of the study region based on maps of Mohn et al. (2010), Tectonic Map of Switzerland (2005), Peters (2005) and Froitzheim et al. (1994). Tectonic units are displayed over a hillshade produced from 90 m SRTM data (Shuttle Radar Topography Mission; processing completed by Jarvis et al., 2008). Small inset map indicates location of study area in Switzerland. Locations and sample names of (U-Th)/He analyses are indicated by black circles and white labels. For the geographic coordinates of sample locations see Table 1, 2 and 3. The A -A' indicates the location of Figure 15 cross section.

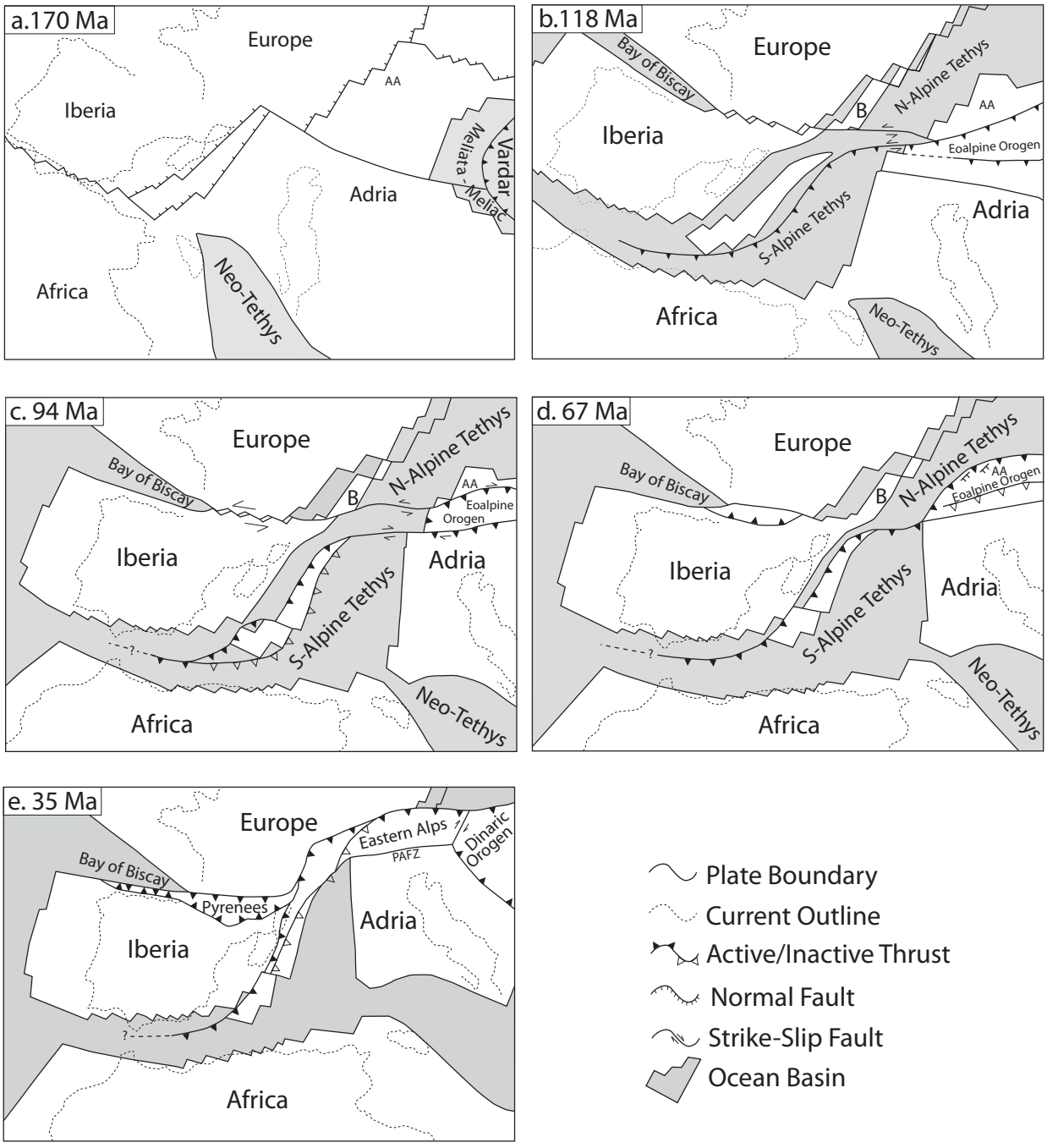
a.170 Ma
Europe
Iberia
AA
Adria
Vardar
Meliata - Meliac
Africa
Neo-Tethys
b.118 Ma
Bay of Biscay
Europe
N-Alpine Tethys
B
AA
Iberia
Eoalpine Orogen
Adria
S-Alpine Tethys
Africa
Neo-Tethys
c. 94 Ma
Europe
N-Alpine Tethys
Bay of Biscay
B
AA
Eoalpine Orogen
Iberia
Adria
S-Alpine Tethys
Africa
Neo-Tethys
d. 67 Ma
Europe
N-Alpine Tethys
Bay of Biscay
B
AA
Eoalpine Orogen
Iberia
Adria
S-Alpine Tethys
Africa
Neo-Tethys
e. 35 Ma
Europe
Eastern Alps
Dinaric Orogen
PAFZ
Bay of Biscay
Pyrenees
Adria
Iberia
Africa
Plate Boundary
Current Outline
Active/Inactive Thrust
Normal Fault
Strike-Slip Fault
Ocean Basin

Figure 2. Plate reconstructions of the greater Alpine realm, modified from Handy et al. (2010), for (a) the Jurassic, (b) the Aptian, (c) the Cenomanian, (d) the Maastrichtian, and (e) the Oligocene. Abbreviations used in the figure are: AA-Austroalpine, B-Briançonnais, PAFZ-Periadriatic Fault Zone.

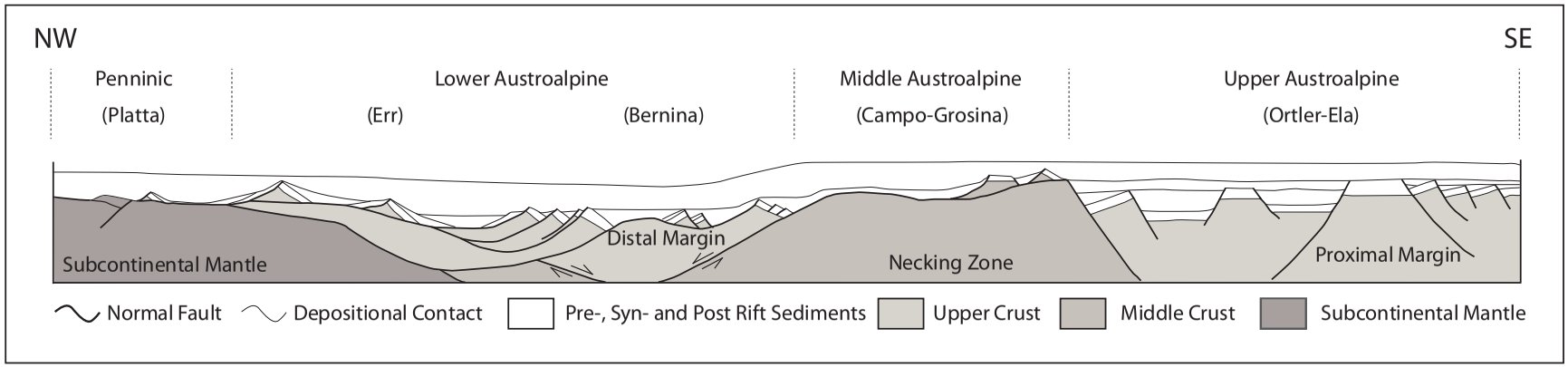
NW
SE
Penninic
(Platta)
Lower Austroalpine
(Err)
(Bernina)
Middle Austroalpine
(Campo-Grosina)
Upper Austroalpine
(Ortler-Ela)
Subcontinental Mantle
Distal Margin
Necking Zone
Proximal Margin
Normal Fault
Depositional Contact
Pre-, Syn- and Post Rift Sediments
Upper Crust
Middle Crust
Subcontinental Mantle

Figure 3. Schematic cross section through the northwestern passive margin of Adria during the Jurassic prior to the Alpine orogeny, modified from Mohn et al. (2010). Note degree of thinning increases from Upper Austroalpine to Lower Austroalpine units.

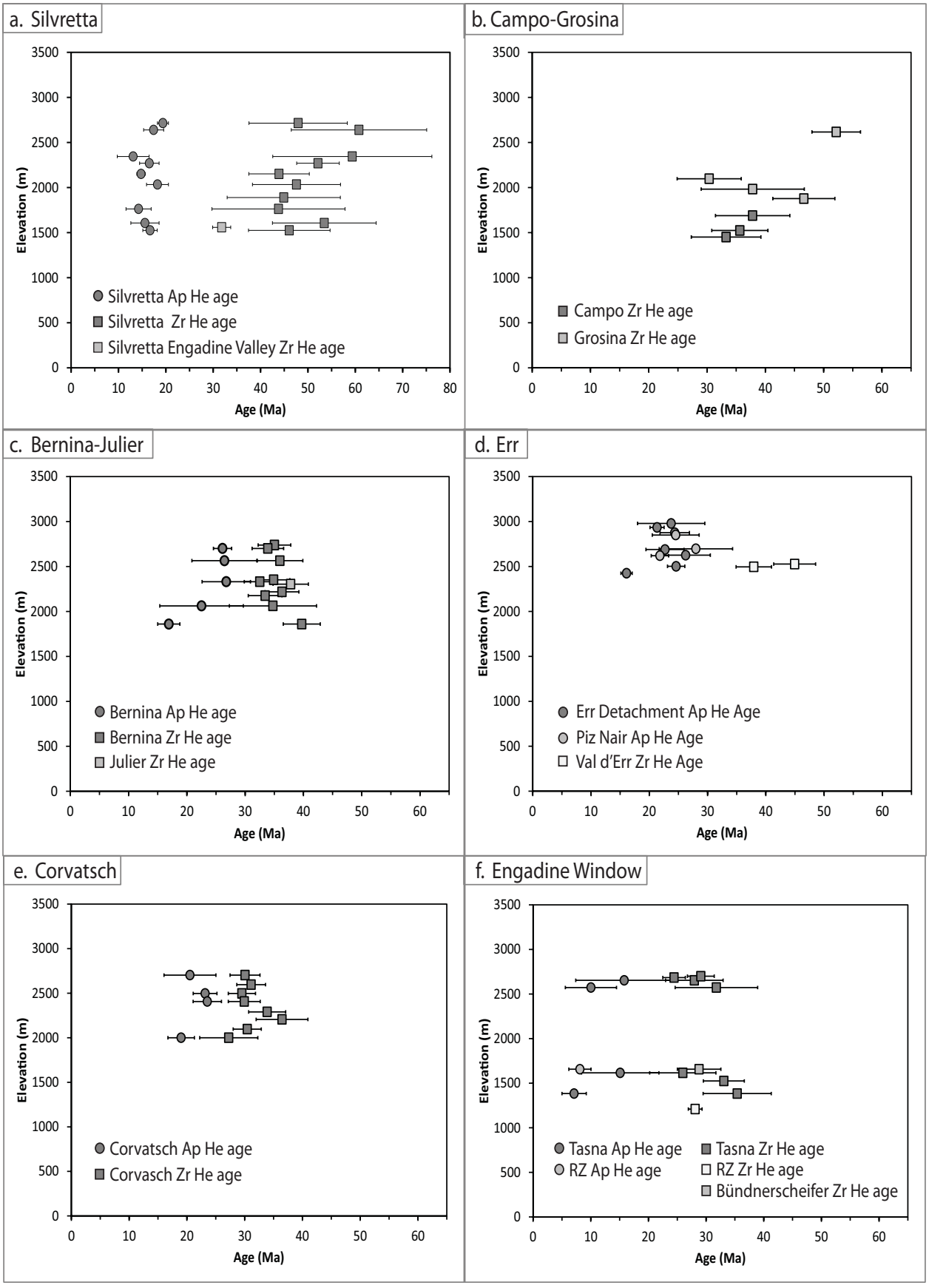
a. Silvretta
Elevation (m)
Age (Ma)
Silvretta Ap He age
Silvretta Zr He age
Silvretta Engadine Valley Zr He age
b. Campo-Grosina
Campo Zr He age
Grosina Zr He age
c. Bernina-Julier
Bernina Ap He age
Bernina Zr He age
Julier Zr He age
d. Err
Err Detachment Ap He Age
Piz Nair Ap He Age
Val d'Err Zr He Age
e. Corvatsch
Corvatsch Ap He age
Corvasch Zr He age
f. Engadine Window
Tasna Ap He age
Tasna Zr He age
RZ Ap He age
RZ Zr He age
Bündnerscheifer Zr He age

Figure 4. Age-elevation plots of averaged zircon and apatite (U-Th)/He analyses. All errors shown are the greater of either standard error (apatite: 6%, zircon: 8%, 2σ) or standard deviation of replicate analyses (1σ). For complete information of the data plotted and number of replicate analyses used to calculate sample ages see Table 1 and 2. For all replicate analyses performed see Tables A and B in Appendix A.

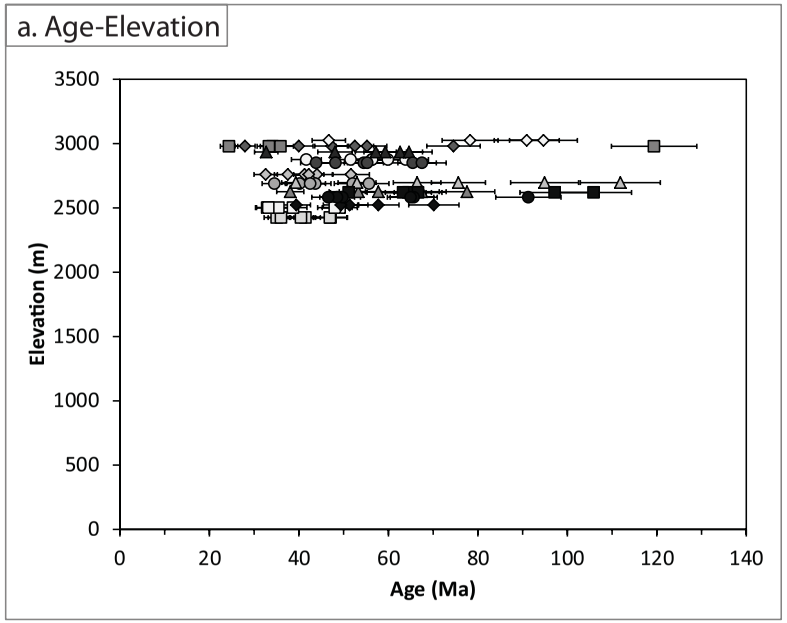
a. Age-Elevation
Elevation (m)
Age (Ma)
0
500
1000
1500
2000
2500
3000
3500
0
20
40
60
80
100
120
140

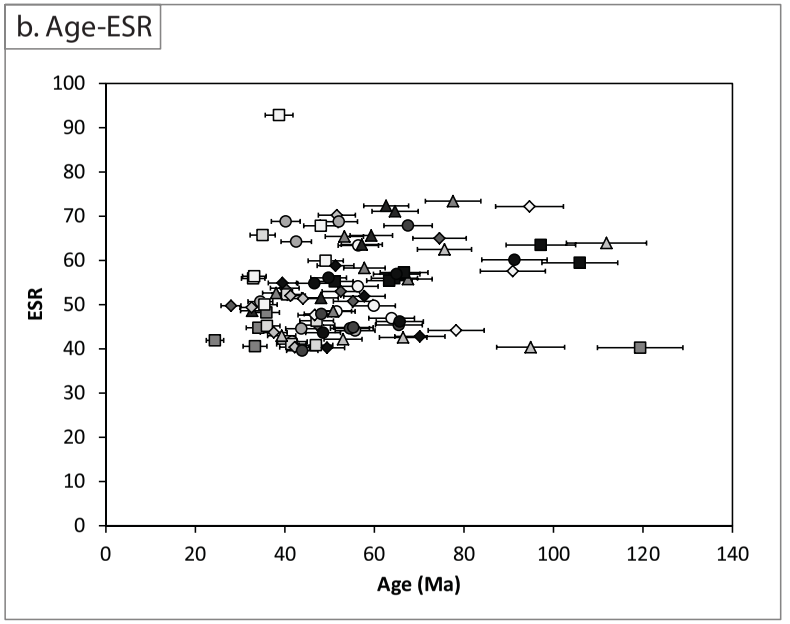
b. Age-ESR
ESR
Age (Ma)
0
10
20
30
40
50
60
70
80
90
100
0
20
40
60
80
100
120
140

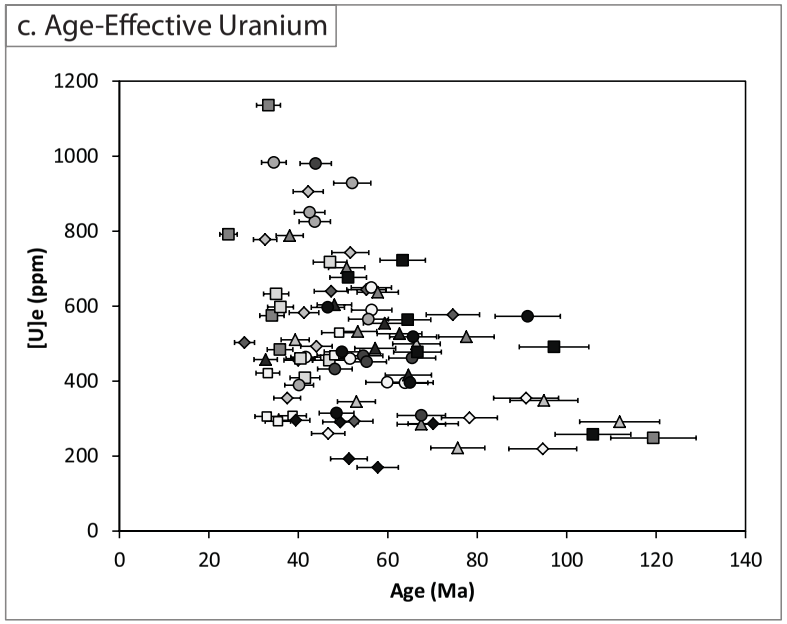
c. Age-Effective Uranium
[U]e (ppm)
Age (Ma)
0
200
400
600
800
1000
1200
0
20
40
60
80
100
120
140

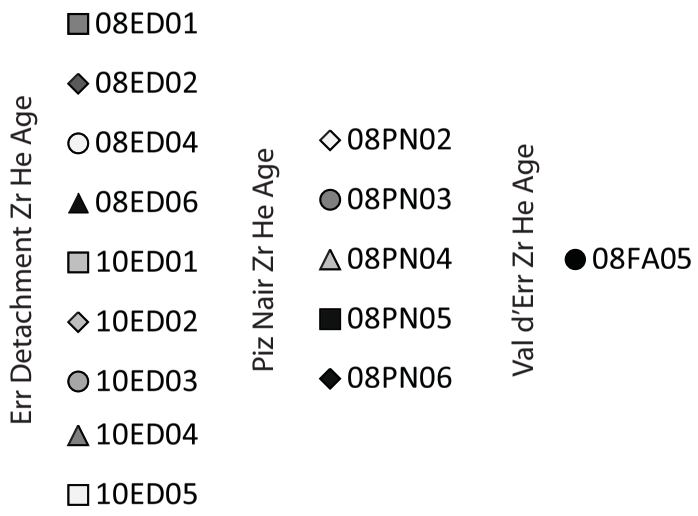
Err Detachment Zr He Age
08ED01
08ED02
08ED04
08ED06
10ED01
10ED02
10ED03
10ED04
10ED05
Piz Nair Zr He Age
08PN02
08PN03
08PN04
08PN05
08PN06
Val d'Err Zr He Age
08FA05

Figure 5. Plots of individual zircon (U-Th)/He analyses from the Err nappe. All data plotted is reported in Table 3. Errors quoted are standard error (8%; 2σ). (a) Age-elevation plot illustrates the total spread of zircon helium ages recorded by each sample. (b) Age-ESR (equivalent spherical radius, a proxy for grain size) plot exhibits the positive correlation within individual samples between size and grain age. (c) Age-effective uranium concentration plot showing a negative correlation within individual samples between effective uranium concentration, a proxy for radiation damage (e.g., Shuster et al., 2006; $[U]_e$ =[U]+[Th]0.235+[Sm]0.005), and helium age. This correlation is suggestive of a link between increased radiation damage and decreased helium retentivity within zircon grains (Nasdala et al., 2004; Reiners, 2005; Stockli et al., 2010). Note samples with a small spread in effective uranium concentration do not show this trend. These correlations between age-ESR and age-$[U]_e$ suggest protracted cooling through the zircon PRZ for the Err nappe.

a. Category 1

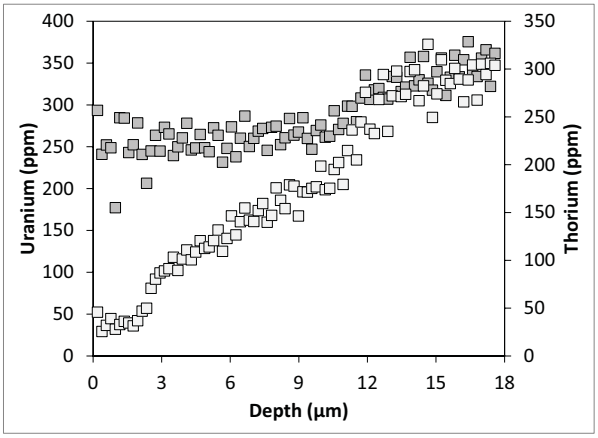

b. Category 2

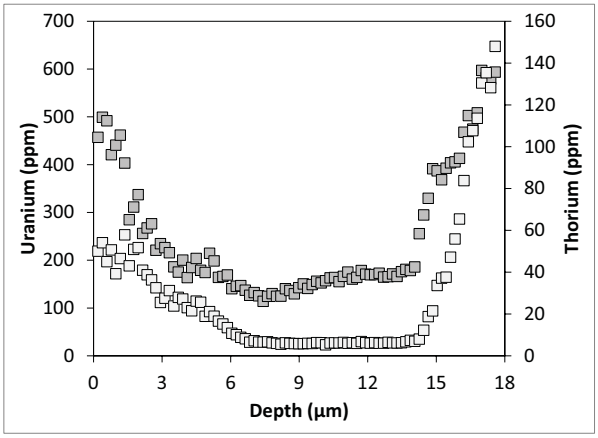

c. Category 3

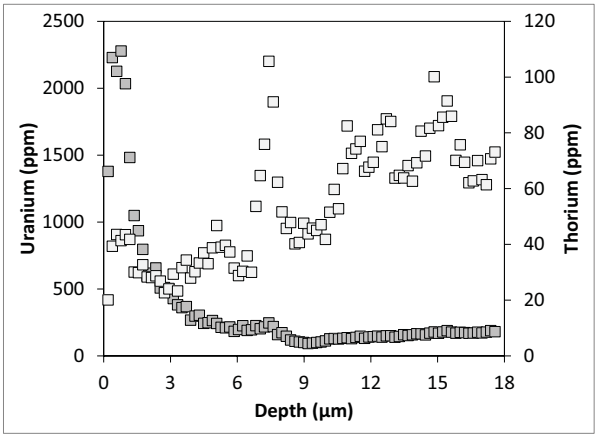

d. Category 4

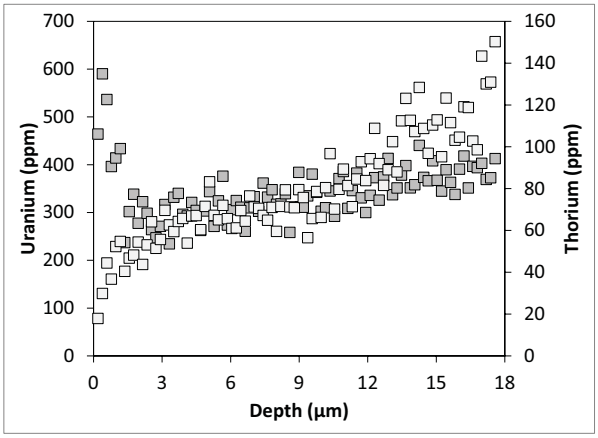

e. Category 5

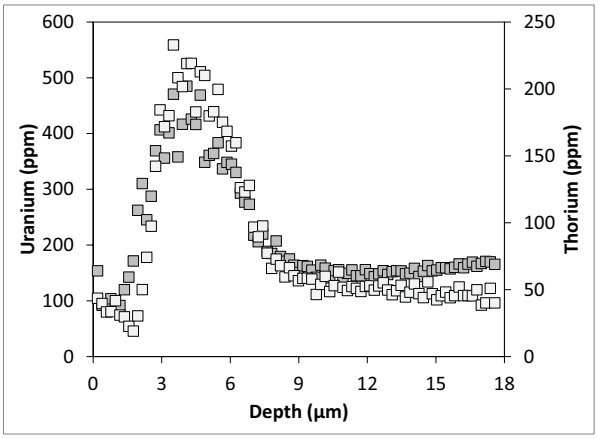

Uranium Concentration

Thorium Concentration

Figure 6. Representative laser ablation depth-profiles of U and Th concentration for defined categories. Categories are defined based on the U concentration pattern. (a) Category 1 is defined as nearly homogeneous U concentration distribution. Note decoupled behavior of Th and U in this profile. This category also contains another depth-profile with coupled behavior of Th and U (see Appendix B). (b) Category 2 comprises depth-profiles that exhibit both a relatively high U concentration overgrowth, as well as a high U concentration zone within the interior of the grain. (c) Category 3 encompasses depth-profiles with a single high U concentration overgrowth with a relative concentration five times the remainder of the depth-profile. (d) Category 4 is defined by a high U concentration overgrowth less than five times greater than the rest of the depth-profile. (e) Category 5 includes depth profiles that have a single zone of high U concentration within the interior of the grain.

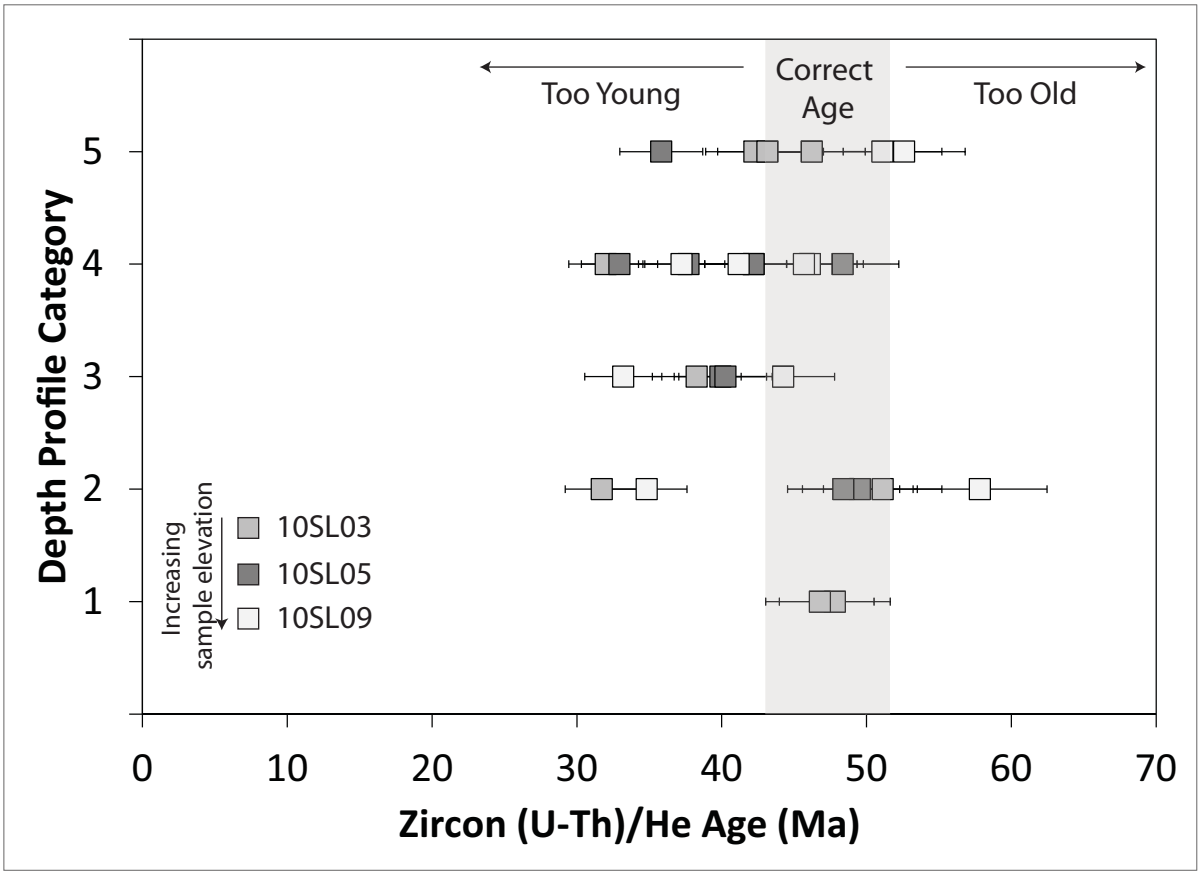
Too Young
Correct Age
Too Old
Depth Profile Category
5
4
3
2
1
Increasing sample elevation
10SL03
10SL05
10SL09
0
10
20
30
40
50
60
70
Zircon (U-Th)/He Age (Ma)

Figure 7. Plot of zircon (U-Th)/He ages when filtered using zonation categories of Figure 6. The correct zircon (U-Th)/He age bar is based on the zircon helium ages of grains within the first category of nearly homogeneous U distribution. Erroneously young ages are recorded by zircon grains sorted into categories 2-5, and these young zircon helium ages are a result of an underestimate of daughter loss by the standard alpha-ejection correction (Hourigan et al., 2005). Only one aliquot records an erroneously old zircon (U-Th)/He age, which may be explained through unaccounted for loss of parent during analysis (i.e., physically lost portion of grain) or an unseen high U or Th core (Hourigan et al., 2005). Note there is no correlation between individual samples and categorized zircon (U-Th)/He age, which suggests that the age is not elevation dependent.

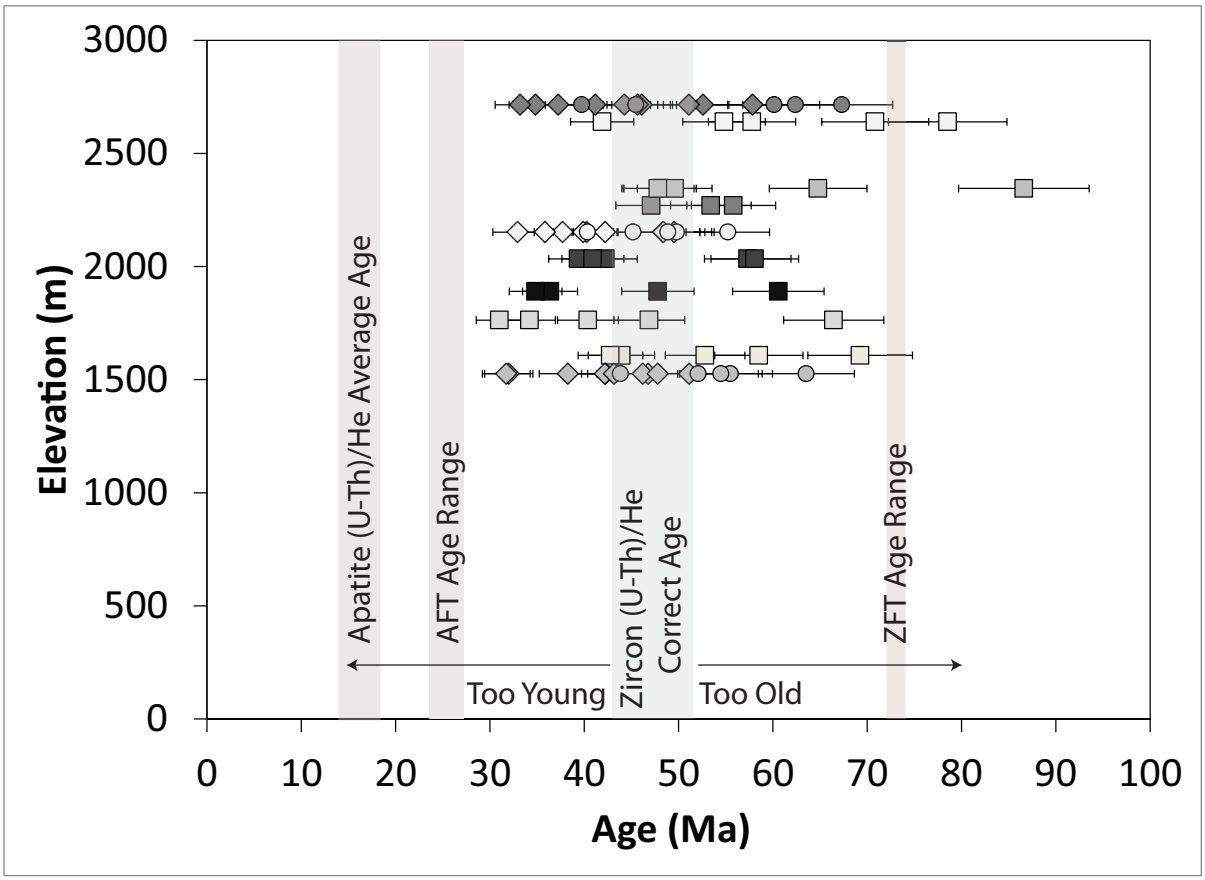
3000
2500
2000
1500
1000
500
0
Elevation (m)
0
10
20
30
40
50
60
70
80
90
100
Age (Ma)
Apatite (U-Th)/He Average Age
AFT Age Range
Zircon (U-Th)/He Correct Age
ZFT Age Range
Too Young
Too Old

Figure 8. Age-elevation plot of all aliquot zircon (U-Th)/He ages analyzed for the Silvretta nappe vertical transect. Diamonds indicate grains depth-profiled before zircon (U-Th)/He analysis. Circles indicate aliquots that were analyzed only using standard zircon (U-Th)/He techniques from the three samples chosen for laser-ablation depth profiling. Squares indicate all other zircon (U-Th)/He aliquot analyses. All error bars shown are 8% (2σ). Apatite fission track (AFT) and zircon fission track (ZFT) age ranges are those reported by Hurford et al. (1989) for the northeastern portion of the Silvretta nappe. Replicate zircon (U-Th)/He ages that fall within the ZFT age range are clearly too old based on the higher thermally sensitivity of the ZFT thermochronometer (total annealing of fission tracks at temperatures >310 °C; Tagami and Dumitru, 1996). The average apatite (U-Th)/He age from this study (see figure 4a), and AFT ages (total annealing of fission tracks at temperatures >110-125 °C; Dumitru, 2000) are younger than the zircon replicate ages as expected. The correct zircon (U-Th)/He age bar was determined through the semi-quantitative analysis of parent isotope zonation and recorded zircon helium age (see text for discussion).

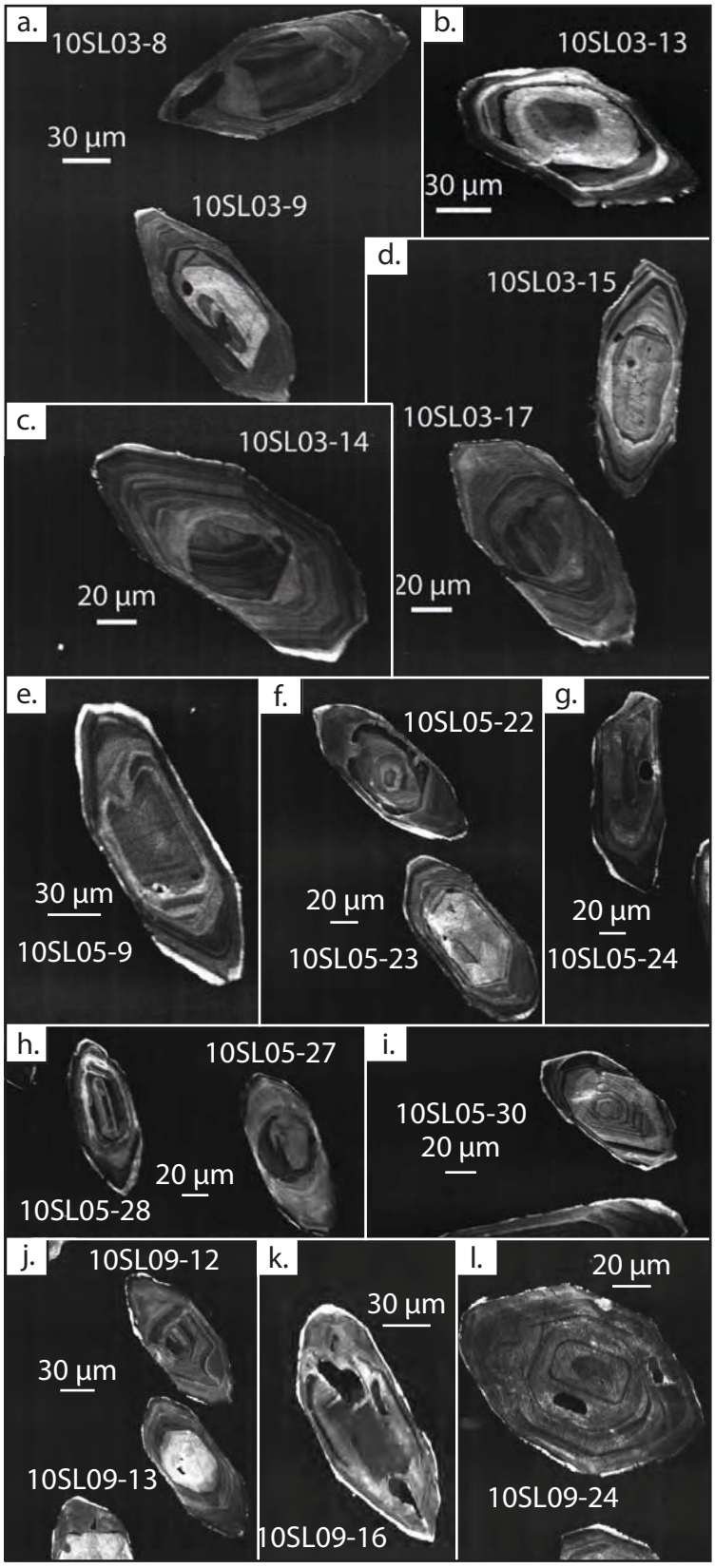
a.
10SL03-8
30 µm
10SL03-9
b.
10SL03-13
30 µm
d.
10SL03-15
10SL03-17
20 µm
c.
10SL03-14
20 µm
e.
30 µm
10SL05-9
f.
10SL05-22
20 µm
10SL05-23
g.
20 µm
10SL05-24
h.
10SL05-27
20 µm
10SL05-28
i.
10SL05-30
20 µm
j.
10SL09-12
30 µm
10SL09-13
k.
30 µm
10SL09-16
l.
20 µm
10SL09-24

Figure 9. Compilation of CL images from the three samples chosen from the Silvretta vertical transect for laser ablation depth-profiling. Note grains are complexly zoned and several show zones of high U and Th concentrations within the outer 20 μm of the grain. This type of zoning is known to cause erroneously young (U-Th)/He ages (Hourgian et al., 2005).

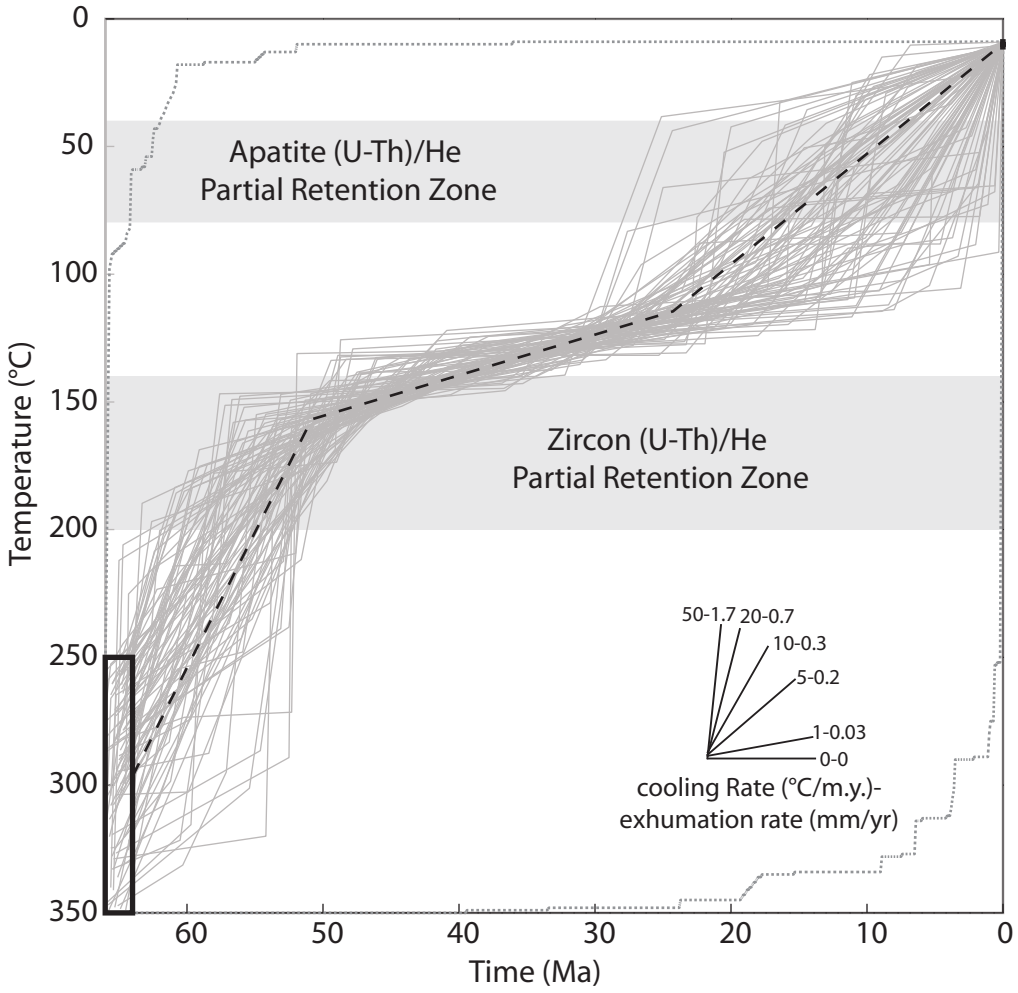
0
50
100
150
200
250
300
350
Temperature (°C)
Apatite (U-Th)/He
Partial Retention Zone
Zircon (U-Th)/He
Partial Retention Zone
50-1.7
20-0.7
10-0.3
5-0.2
1-0.03
0-0
cooling Rate (°C/m.y.)-
exhumation rate (mm/yr)
60
50
40
30
20
10
0
Time (Ma)

Figure 10. HeMP inverse model time-temperature history paths generated for the Campo-Grosina vertical transect using a 30 °C/km geothermal gradient and allowing for a single outlier data pair. This geothermal gradient was chosen based on work by Hurford et al. (1989). Cooling rate and exhumation rate curves are based on the assumed geothermal gradient. Ninety-two good fit time-temperature curves were found by this model and are depicted in grey. Dashed grey lines indicate range of 100,000 random time-temperature curves tested by the model. The black boxes indicate modeling constraints based on temperature estimates by Handy et al. (1996) for the ending of the D2 period of deformation and mean annual surface temperature. The black dashed line indicates preferred cooling history. Note only zircon (U-Th)/He ages were used for modeling. As a result, the cooling history below 140° C is unconstrained and may not be representative of the true cooling history of the Campo and Grosina nappes.

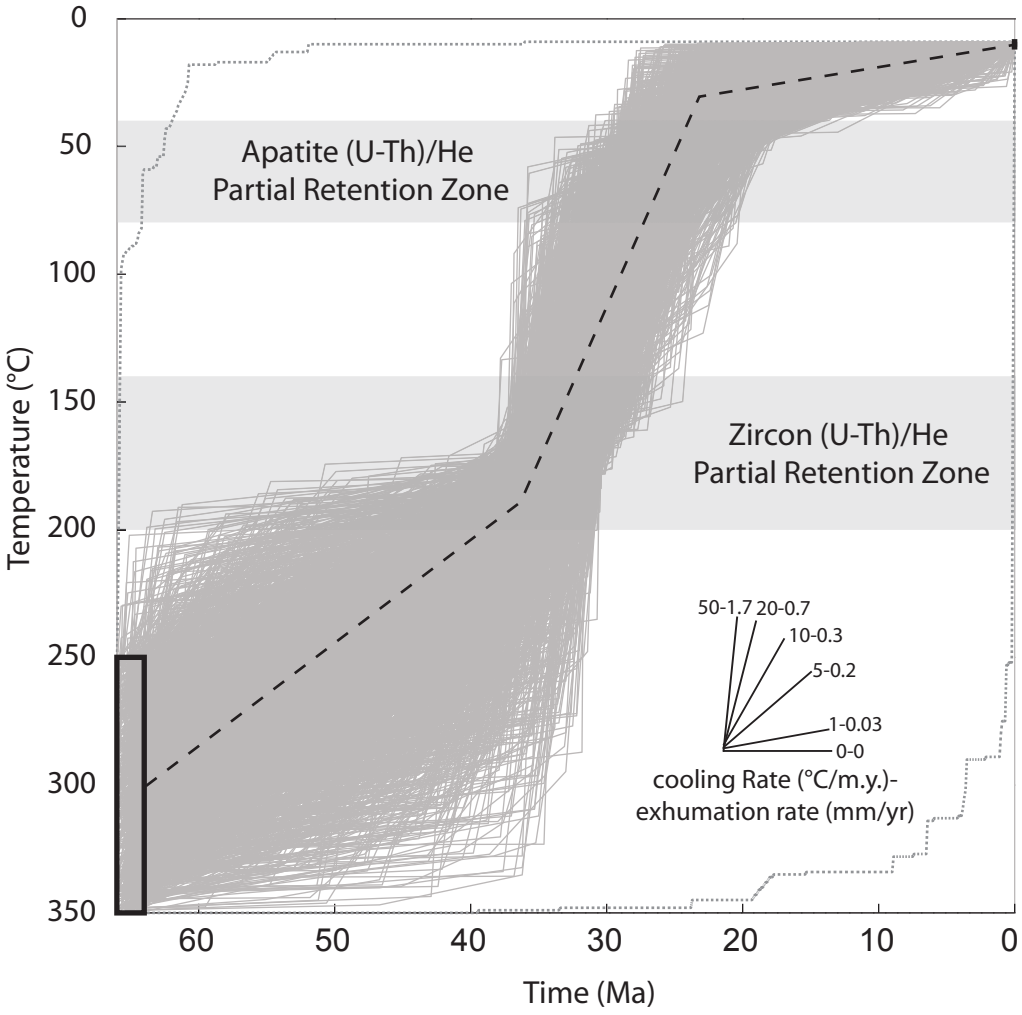
0
50
100
150
200
250
300
350
Temperature (°C)
Apatite (U-Th)/He
Partial Retention Zone
Zircon (U-Th)/He
Partial Retention Zone
50-1.7
20-0.7
10-0.3
5-0.2
1-0.03
0-0
cooling Rate (°C/m.y.)-
exhumation rate (mm/yr)
60
50
40
30
20
10
0
Time (Ma)

Figure 11. HeMP inverse model time-temperature history paths generated for the Bernina vertical transect using a 30 °C/km geothermal gradient and allowing for a single outlier data pair. This geothermal gradient was chosen based on work by Hurford et al. (1989). Cooling rate and exhumation rate curves are based on the assumed geothermal gradient. The inverse model found 1715 acceptable fits and these curves are depicted in grey. Dashed grey lines indicate range of 100,000 random time-temperature curves tested by the model. The black dashed line indicates preferred cooling history. The black boxes indicate modeling constraints based on temperature estimates by Handy et al. (1996) for the ending of the D2 period of deformation and mean annual surface temperature.

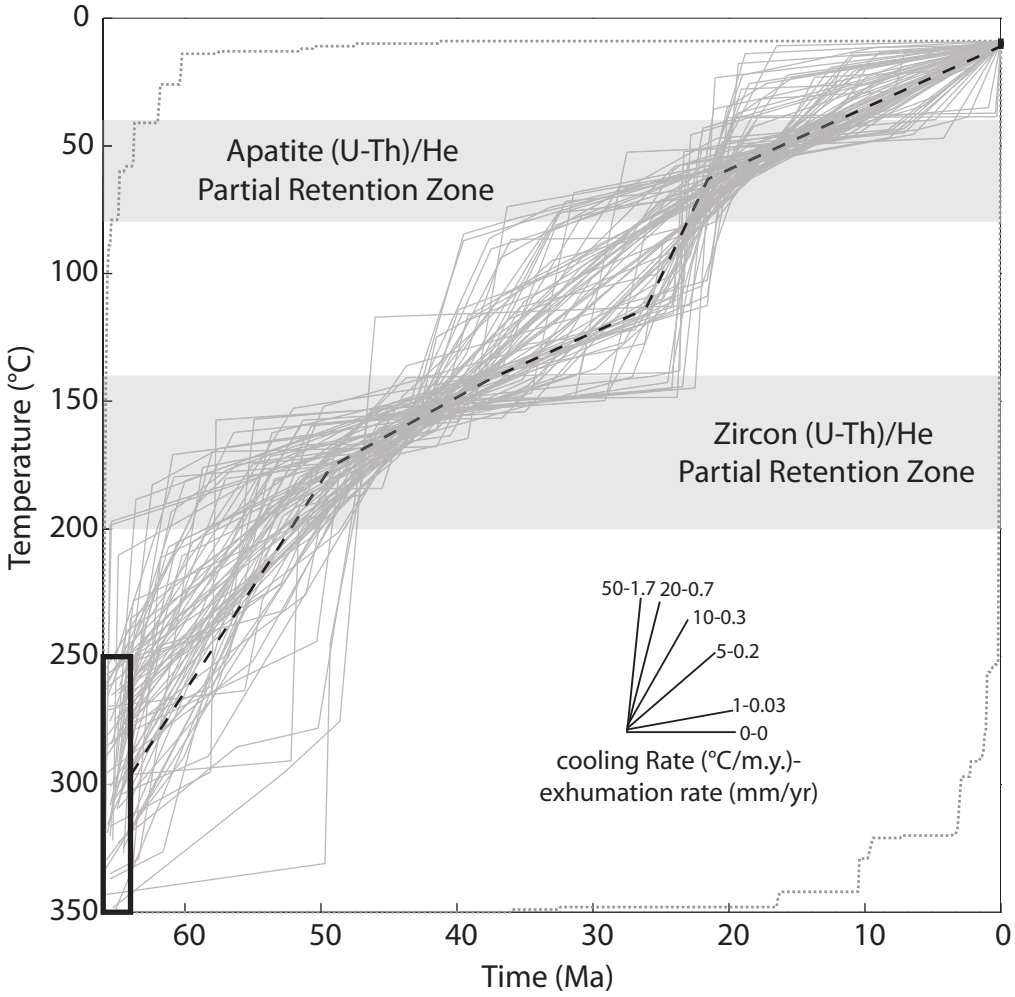
0
50
100
150
200
250
300
350
Temperature (°C)
Apatite (U-Th)/He
Partial Retention Zone
Zircon (U-Th)/He
Partial Retention Zone
50-1.7
20-0.7
10-0.3
5-0.2
1-0.03
0-0
cooling Rate (°C/m.y.)-
exhumation rate (mm/yr)
60
50
40
30
20
10
0
Time (Ma)

Figure 12. HeMP inverse model time-temperature history paths generated for the Err detachment vertical transect using a 30 °C/km geothermal gradient and allowing for a two outlier data pairs. This geothermal gradient was chosen based on work by Hurford et al. (1989). Cooling rate and exhumation rate curves are based on the assumed geothermal gradient. The inverse model found 81 acceptable fits and these curves are depicted in grey. Dashed grey lines indicate range of 100,000 random time-temperature curves tested by the model. The black dashed line indicates preferred cooling history. The black boxes indicate modeling constraints based on temperature estimates by Handy et al. (1996) for the ending of the D2 period of deformation and mean annual surface temperature. Note zircon (U-Th)/He ages used to model this transect are average ages of replicate analyses of the Err detachment transect; replicate analyses are depicted in figure 5a.

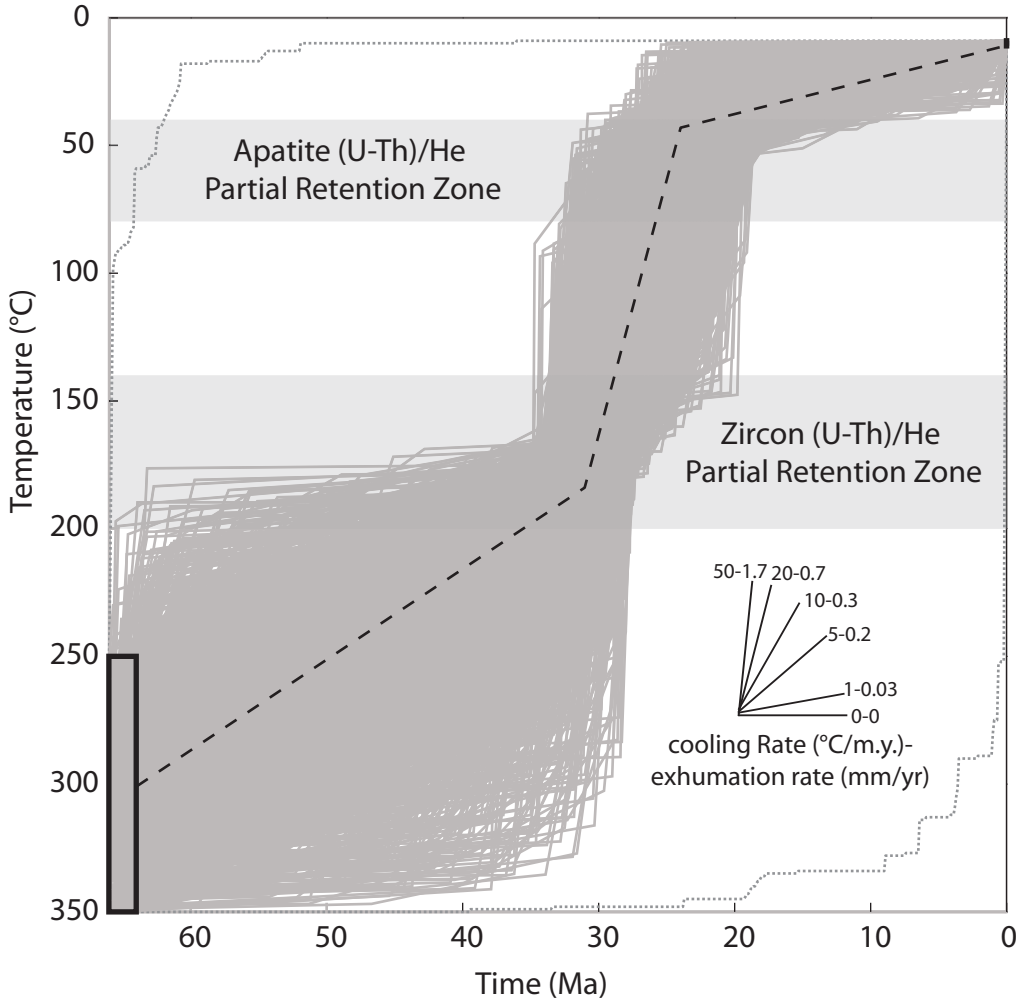
Apatite (U-Th)/He
Partial Retention Zone
Zircon (U-Th)/He
Partial Retention Zone
50-1.7
20-0.7
10-0.3
5-0.2
1-0.03
0-0
cooling Rate (°C/m.y.)-
exhumation rate (mm/yr)
Temperature (°C)
Time (Ma)
0
50
100
150
200
250
300
350
60
50
40
30
20
10
0

Figure 13. HeMP inverse model time-temperature history paths generated for the Corvatsch vertical transect using a 30 °C/km geothermal gradient and allowing for a single outlier data pair. This geothermal gradient was chosen based on work by Hurford et al. (1989). Cooling rate and exhumation rate curves are based on the assumed geothermal gradient. The inverse model found 1705 acceptable fits and these curves are depicted in grey. Dashed grey lines indicate range of 100,000 random time-temperature curves tested by the model. The black dashed line indicates preferred cooling history. The black boxes indicate modeling constraints based on temperature estimates by Handy et al. (1996) for the ending of the D2 period of deformation and mean annual surface temperature.

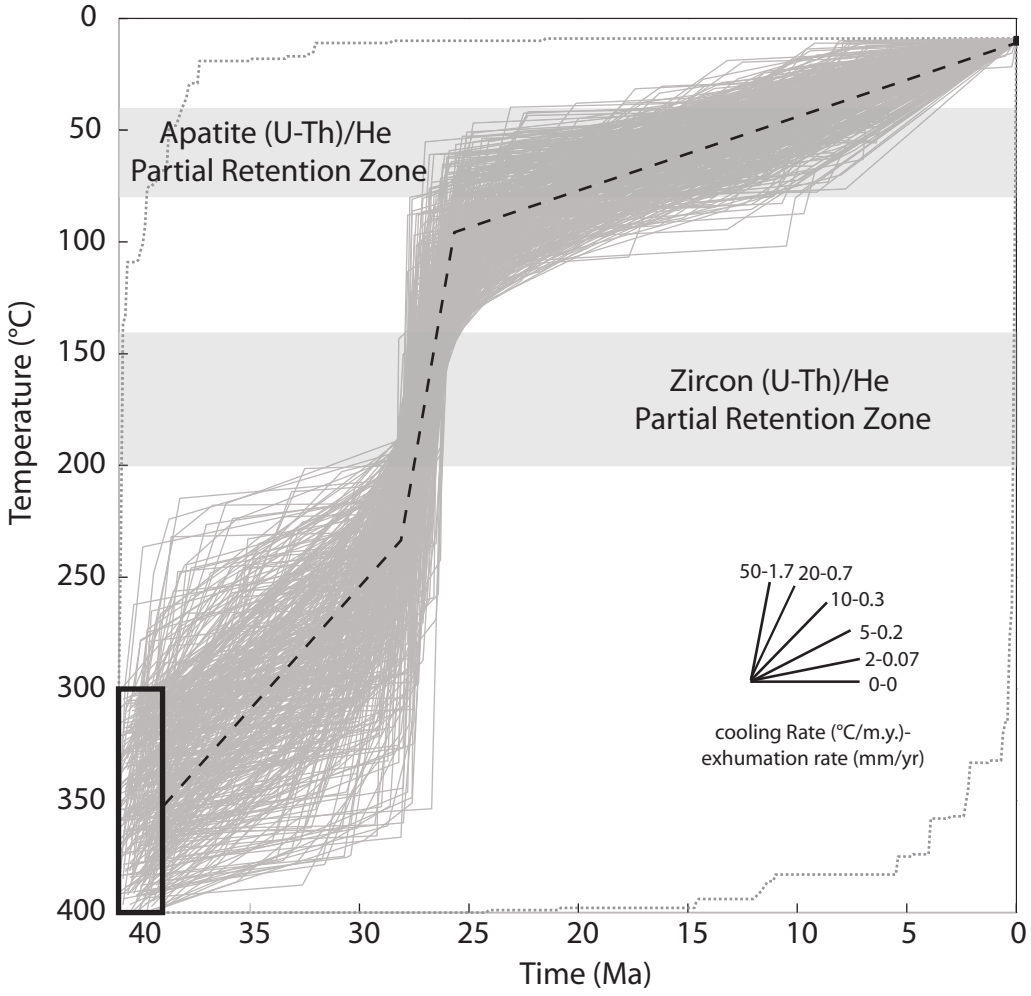
Apatite (U-Th)/He
Partial Retention Zone
Zircon (U-Th)/He
Partial Retention Zone
50-1.7
20-0.7
10-0.3
5-0.2
2-0.07
0-0
cooling Rate (°C/m.y.)-
exhumation rate (mm/yr)
Temperature (°C)
Time (Ma)
0
50
100
150
200
250
300
350
400
40
35
30
25
20
15
10
5
0

Figure 14. HeMP inverse model time-temperature history paths generated for the Engadine window samples using a 30 °C/km geothermal gradient and allowing no outlier data pair. This geothermal gradient was chosen based on work by Hurford et al. (1989). Cooling rate and exhumation rate curves are based on the assumed geothermal gradient. The inverse model found 399 acceptable fits and these curves are depicted in grey. Dashed grey lines indicate range of 100,000 random time-temperature curves tested by the model. The black dashed line indicates preferred cooling history. The black box indicates modeling constraints based on temperature estimates by Bousquet et al. (2008) for high-pressure greenschist metamorphism within the Bündnerscheifer, and timing constraints from *in situ* $^{40}Ar/^{39}Ar$ dating of white mica associated with the high-pressure greenschist metamorphism of the Bündnerscheifer (Wiederkehr et al., 2009).

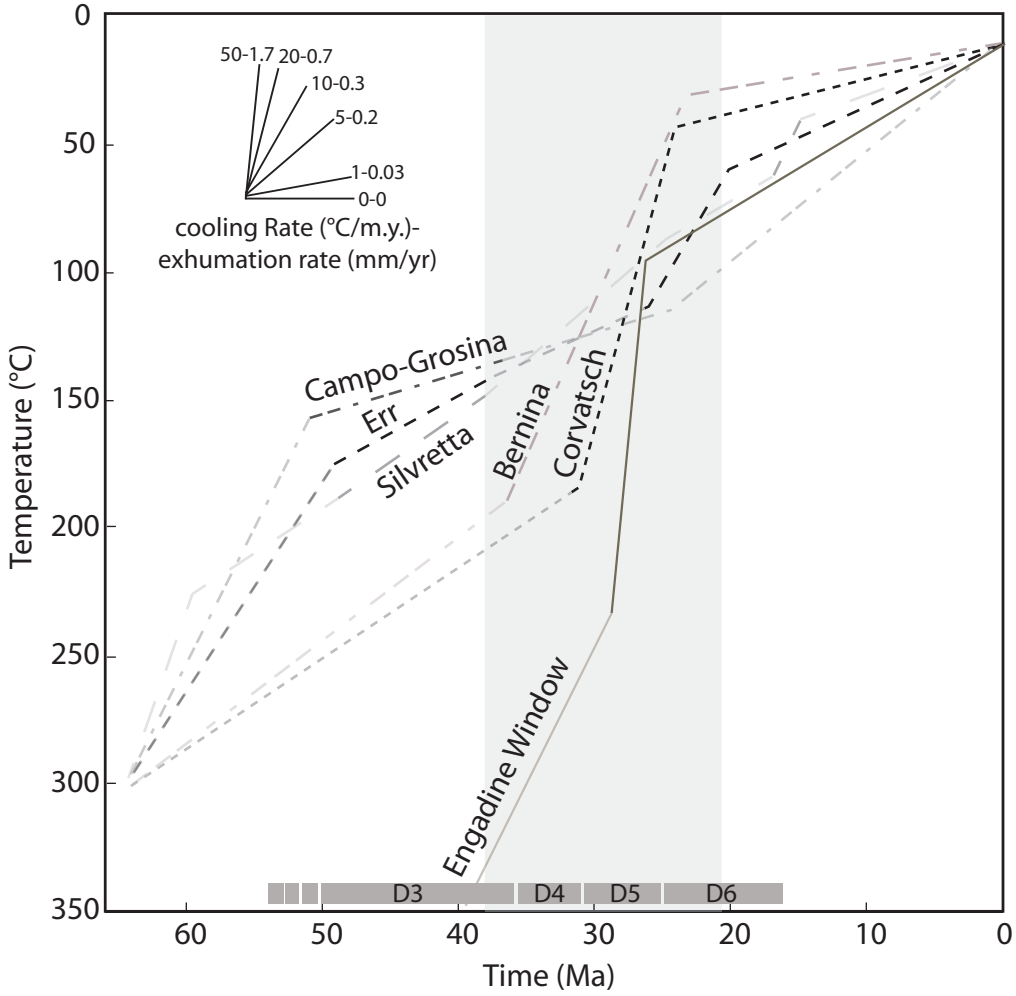
0
50
100
150
200
250
300
350
Temperature (°C)
60
50
40
30
20
10
0
Time (Ma)
50-1.7
20-0.7
10-0.3
5-0.2
1-0.03
0-0
cooling Rate (°C/m.y.)-
exhumation rate (mm/yr)
Campo-Grosina
Err
Silvretta
Bernina
Corvatsch
Engadine Window
D3
D4
D5
D6

Figure 15. A compilation of the preferred cooling histories based on the inverse modeling of the Austroalpine and Penninic (Engadine Window, solid line) (U-Th)/He data. The transparent portions of the cooling histories are considered relatively unconstrained by the data. The Silvretta cooling history curve was determined based on ZFT ages, corrected zircon (U-Th)/He age, AFT ages, and the apatite (U-Th)/He ages of the Silvretta nappe (i.e., the Silvretta time-temperature history is not derived from inverse modeling). Cooling rate and exhumation rate curves are based on a 30 °C/km geothermal gradient. Three general stages of cooling can be determined for the Austroalpine and Penninc nappe stack based on this graphical summary: (1) relatively slow cooling rates from ~52 Ma to ~36 Ma, (2) a period of increased cooling rates from ~36 Ma to ~21 Ma, and (3) decreased, and the slowest cooling rates of the nappe stack from ~21 Ma to present. Note, for the Silvretta nappe a period of rapid cooling is documented based on the apatite (U-Th)/He ages at ~16 Ma. Darker grey bars along the bottom of the graph indicate the defined deformational periods of the study region from Schmid and Froitzheim (1993), Froitzheim et al. (1994) and Schmid et al. (1996).

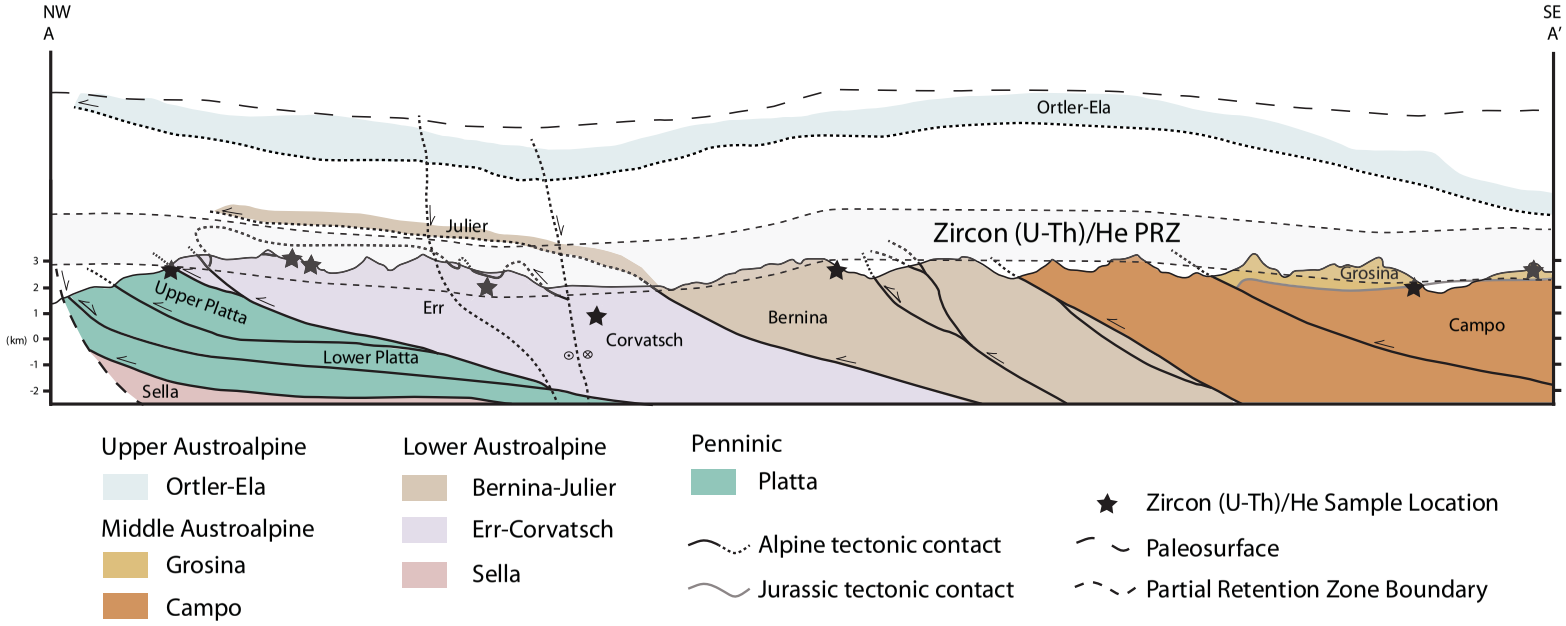
NW
A
SE
A'
Ortler-Ela
Julier
Zircon (U-Th)/He PRZ
Upper Platta
Err
Corvatsch
Bernina
Grosina
Campo
Lower Platta
Sella
(km)
3
2
1
0
-1
-2
Upper Austroalpine
Ortler-Ela
Middle Austroalpine
Grosina
Campo
Lower Austroalpine
Bernina-Julier
Err-Corvatsch
Sella
Penninic
Platta
Alpine tectonic contact
Jurassic tectonic contact
Zircon (U-Th)/He Sample Location
Paleosurface
Partial Retention Zone Boundary

Figure 16. A simplified cross section of the Austroalpine nappe stack for the southern portion of the study area modified from Mohn et al. (2010). The cross section depicts the interpreted location of the post-D2 zircon (U-Th)/He HePRZ and paleo-surface. The interpretation assumes a geothermal gradient of 30 °C/km, which corresponds to a 2 km thick zircon HePRZ ranging from depths of 4.6 to 6.6 km. The location of the cross section line is shown in Figure 1 as A-A'. Note the Julier nappe slice projects into the paleo HePRZ, however the zircon (U-Th)/He age shows no evidence of prolonged residence within the zircon HePRZ. This discrepancy may be explained through a slight southward plunge of the nappes south of the cross section line. A slight southward plunge has been described in cross sections of the Err nappe by Handy et al. (1996).

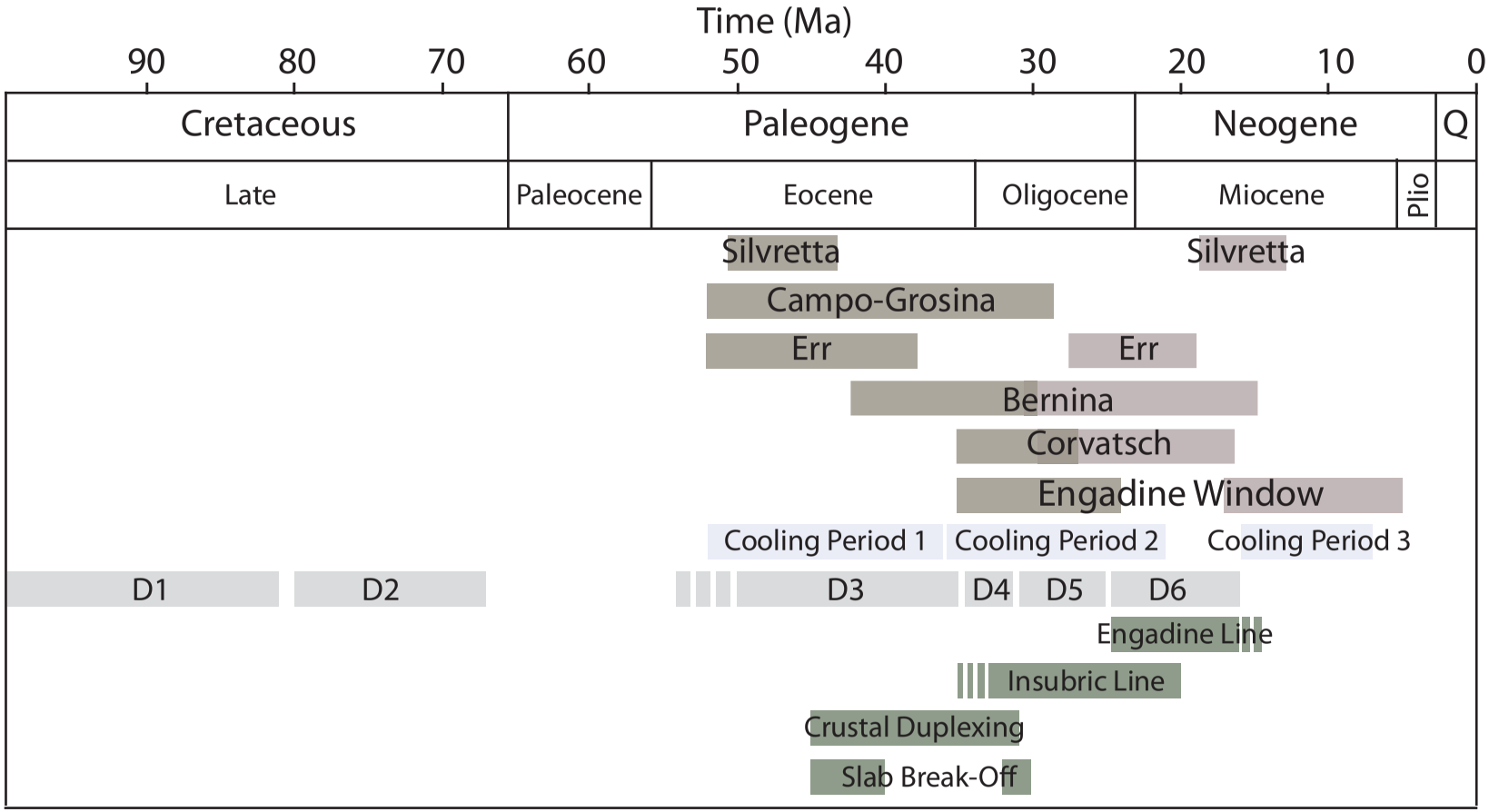
Time (Ma)
90
80
70
60
50
40
30
20
10
0
Cretaceous
Paleogene
Neogene
Q
Late
Paleocene
Eocene
Oligocene
Miocene
Plio
Silvretta
Silvretta
Campo-Grosina
Err
Err
Bernina
Corvatsch
Engadine Window
Cooling Period 1
Cooling Period 2
Cooling Period 3
D1
D2
D3
D4
D5
D6
Engadine Line
Insubric Line
Crustal Duplexing
Slab Break-Off

Figure 17. Summary of apatite and zircon (U-Th)/He ages from the study area, cooling periods of the study area, deformation periods and the timing of possible tectonic mechanisms for exhumation of the region. Dark grey bars represent zircon (U-Th)/He ages. For the Silvretta nappe the age range shown is the semi-quantitatively corrected zircon (U-Th)/He age with standard error (8%). The Bernina, Corvatsch and Engadine Window dark grey bars show the mean zircon (U-Th)/He ages of the nappes with the standard deviation of the averaged ages. For the Campo-Grosina and Err nappes the grey bar depicts the timing of cooling through the zircon PRZ constrained by modeled time-temperature histories (Figure 10 and 12). For Campo-Grosina the mean age of fully reset zircon (U-Th)/He analyses is also indicated by the grey bar. Lavender bars indicate the apatite (U-Th)/He age ranges. The Silvretta, Bernina, Err, Corvatsch and Engadine Window apatite ages are the mean and standard deviation of replicate analyses. The Err mean age for apatite was calculated based on the average of all replicate analyses from both the Piz Nair and Err detachment vertical transects (excluding sample 10ED01). Light blue bars illustrate the three stage cooling history for the region. Light grey bars indicate the span of deformation periods in the study region from Schmid and Froitzheim (1993), Froitzheim et al. (1994) and Schmid et al. (1996). Green bars show the timing of the tectonic mechanisms discussed in section 8.1.2 and 8.1.3 that may be responsible for exhumation of the study region (von Blanckenburg and Davies, 1995; Schmid and Froitzheim, 1993; Schmid et al., 1996; Sinclair, 1997; Berger et al., 2011).

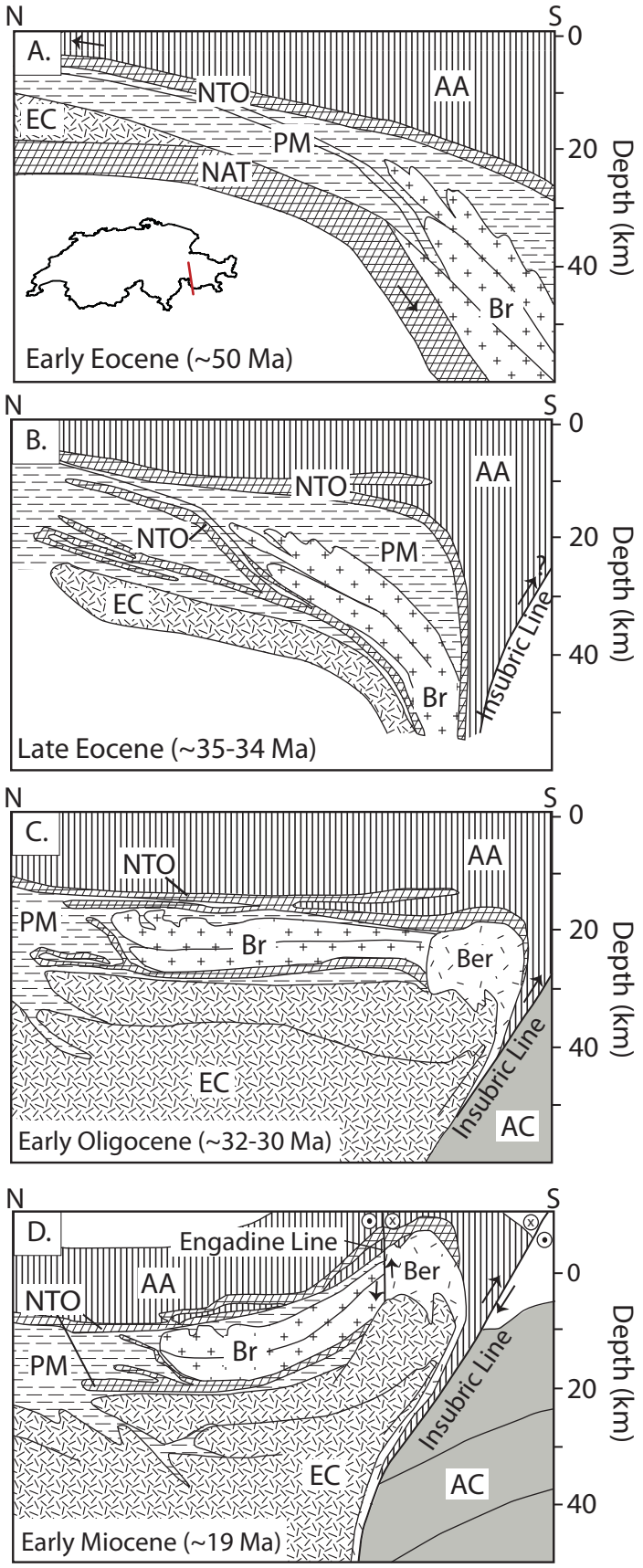
N
S
A.
NTO
AA
EC
PM
NAT
Br
Early Eocene (~50 Ma)
0
20
40
Depth (km)
B.
NTO
NTO
AA
PM
EC
Br
Insubric Line
Late Eocene (~35-34 Ma)
C.
NTO
AA
PM
Br
Ber
EC
Insubric Line
AC
Early Oligocene (~32-30 Ma)
D.
Engadine Line
Ber
AA
NTO
Br
PM
Insubric Line
EC
AC
Early Miocene (~19 Ma)

Figure 18. Cross sections of the Central Alps from the Eocene to the Miocene (see inset for location; all cross sections are modified from Schmid et al., 1996). Abbreviations used to label units include: AA-Austroalpine units, Br-Briançonnais, PM-Penninic metasediments (including Bündnerschiefer and Valais sediments), NAT-North Alpine Tethys crust, NTO-North Alpine Tethys ophiolite, Ber-Bergell intrusion, EC-European crust and AC-Adriatic crust. a) This cross section depicts the north directed thrusting of the Austroalpine units in the Eocene and subduction of the N-Alpine Tethys below the Adriatic plate. b) In the late Eocene movement along the Insubric line may have begun to backthrust Austroalpine units to the south, and crustal duplexing below the Austroalpine units has initiated. c) The intrusion of the Bergell tonalite and granodiorite occurs in the early Oligocene. Backthrusting along the Insubric line and crustal duplexing at depth continues into the Oligocene. d) In the early Miocene the oblique left-lateral Engadine line deforms the units of the orogenic lid, and causes relative uplift of the SE block near the Bergell. In the northern portion of the study area the NW block (relative to the Engadine line) is also uplifted and forms the Engadine window (not shown in the cross section line).

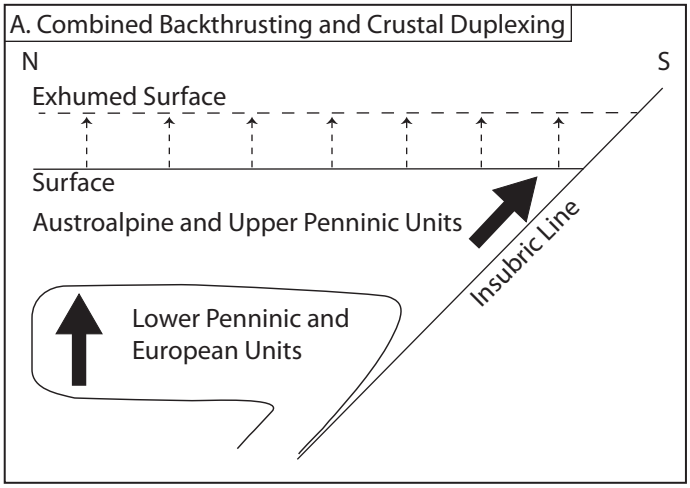
A. Combined Backthrusting and Crustal Duplexing
N
S
Exhumed Surface
Surface
Austroalpine and Upper Penninic Units
Insubric Line
Lower Penninic and
European Units

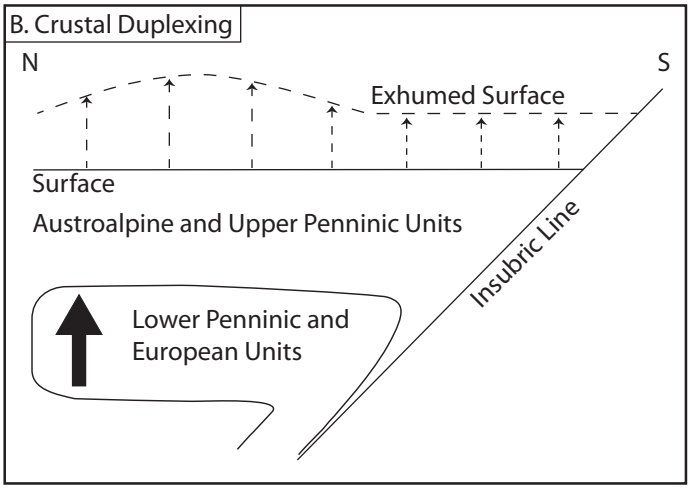
B. Crustal Duplexing
N
S
Exhumed Surface
Surface
Austroalpine and Upper Penninic Units
Insubric Line
Lower Penninic and
European Units

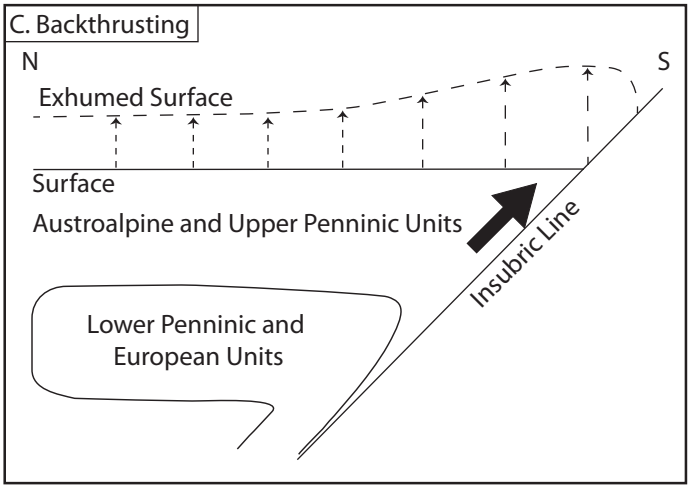
C. Backthrusting
N
S
Exhumed Surface
Surface
Austroalpine and Upper Penninic Units
Insubric Line
Lower Penninic and
European Units

Figure 19. Schematic block diagrams illustrating the spatial distribution of exhumation of units along a north-south cross section through the study area from ~36-21 Ma. Solid arrows indicate the general direction of exhumation due to crustal duplexing and backthrusting along the Insubric Line. Dashed arrows indicate the resulting relative magnitudes of exhumation of the Austroalpine and Penninic units of the study area. (A) The resulting magnitude of exhumation from the combination of the tectonic mechanisms. The combination of these mechanisms results in relatively uniform exhumation of the region. This model is most similar to the observed cooling and exhumation history of the study area from ~36-21 Ma (see text for discussion). (B) A conceptual model of exhumation of the orogenic lid by crustal duplexing. Note the greater amount of exhumation is predicted for the northern portion of the study area. (C) The resulting exhumation of the cross section from only backthrusting along the Insubric Line. In this scenario the largest amount of exhumation in the study area would be located closest to the Insubric Line.

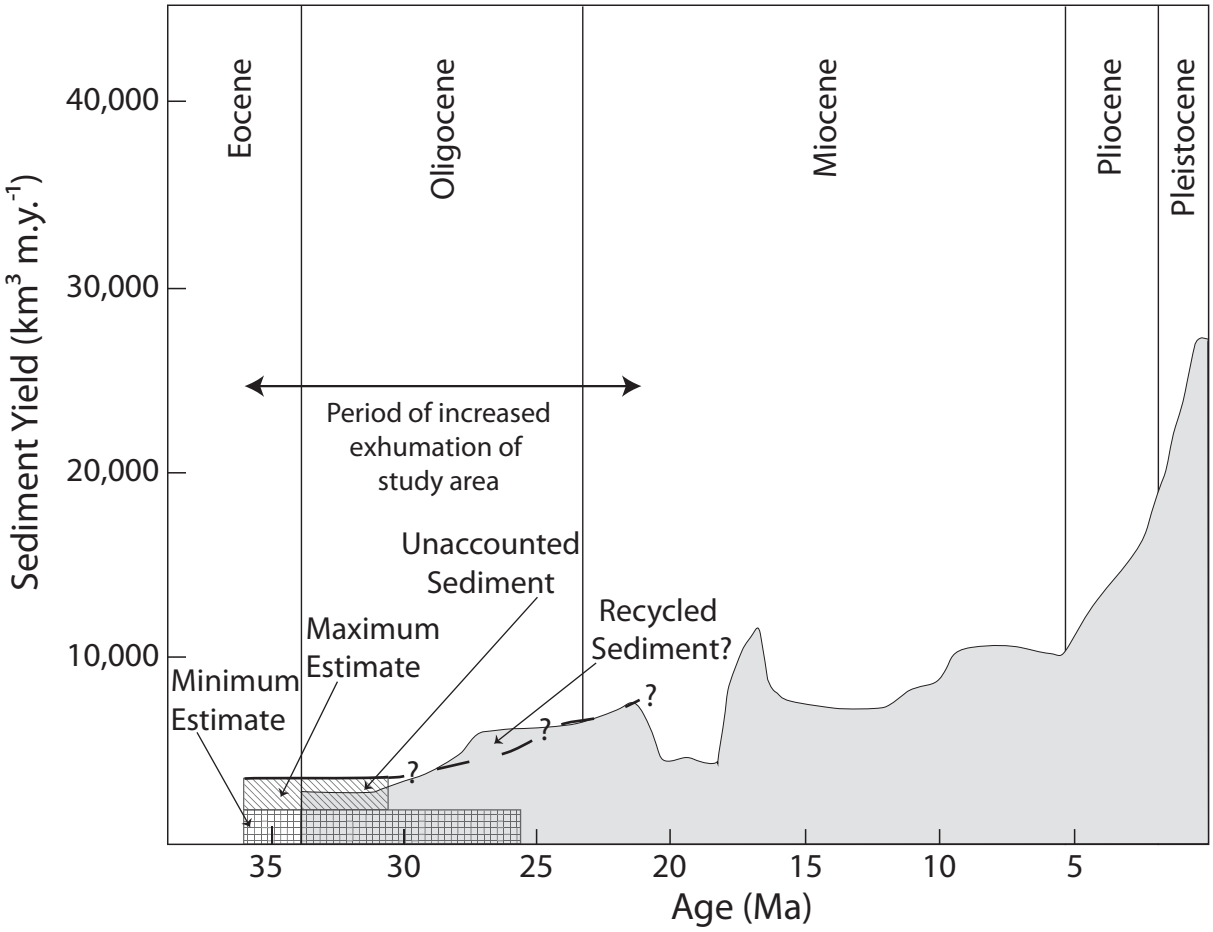
Eocene
Oligocene
Miocene
Pliocene
Pleistocene
40,000
30,000
20,000
10,000
Sediment Yield (km3 m.y.-1)
Period of increased exhumation of study area
Unaccounted Sediment
Maximum Estimate
Minimum Estimate
Recycled Sediment?
?
?
?
35
30
25
20
15
10
5
Age (Ma)

Figure 20. The light gray region indicates the sediment yield curve for the Eastern, eastern Central, and eastern Southern Alps modified from Willet (2010). Note the timing of cooling and increased exhumation of the study area coincides with an increase in sediment yield in the basins. However, the major pulse in sediment deposition is younger than the onset of exhumation within the study area. The region of diagonal hatches indicates the maximum amount of sediment yield for the study area, based on the minimum amount of time for exhumation of the units of this study to ~80 °C. The cross hatched region indicates the minimum amount of sediment yield from the study area, based on the maximum amount of time for exhumation of the units of this study to ~80 °C. The discrepancy between the sediment yield of this study and the current yield curve prior to ~ 31 Ma may result from unrecognized sediment recycling into younger basin deposits (see text for discussion).

1. Table of Average Zircon (U-Th)/He Analyses

Sample	Latitude (N) (degrees)[a]	Longitude (E) (degrees)[a]	Elevation (meters)	Age (Ma)[b]	Std. Error (±2σ, Ma)[c]	Std. Dev. (±1σ, Ma)[d]	U (ppm)[b]	Th (ppm)[b]	Sm (ppm)[b]	$[U]_e$ (ppm)[e]	Th/U[b]	He (nmol/g)[b]	Mass (µg)[b]	Ft[b]	ESR (µm)[b]	Replicate Analyses[f]
Silvretta nappe																
10SL01	46.9428	10.0608	1607	53.5	4.3	11.0	288.7	45.7	1.3	299.2	0.2	64.6	6.3	0.8	49.6	5
10SL02	46.9350	10.0595	1763	43.8	3.5	14.0	198.9	40.7	0.8	208.3	0.2	39.4	6.0	0.8	46.4	5
10SL03	46.9457	10.0626	1526	46.1	3.7	8.6	313.3	72.5	0.9	330.0	0.2	63.8	7.6	0.8	50.7	15
10SL04	46.9214	10.0442	2034	47.6	3.8	9.3	238.0	35.5	0.7	246.2	0.2	51.6	9.2	0.8	54.1	5
10SL05	46.9109	10.0401	2152	43.9	3.5	6.4	363.8	52.3	0.7	375.9	0.2	68.0	9.5	0.8	54.5	14
10SL06	46.9042	10.0399	2270	52.1	4.2	4.5	292.5	45.6	0.9	303.0	0.2	65.2	5.9	0.8	47.1	3
10SL07	46.9002	10.0414	2345	59.4	4.7	16.8	172.0	92.5	0.6	193.3	0.6	46.7	8.6	0.8	54.5	5
10SL08	46.8944	10.0321	2640	60.8	4.9	14.3	316.6	87.1	1.1	336.7	0.3	85.5	6.3	0.8	47.5	5
10SL09	46.8935	10.0308	2715	47.9	3.8	10.4	274.2	56.0	1.0	287.1	0.2	57.0	7.6	0.8	50.7	15
10SL11	46.9220	10.0578	1890	44.9	3.6	11.9	308.4	54.5	0.9	321.0	0.2	63.5	7.7	0.8	51.4	4
09EN01	46.6773	10.0726	1559	31.8	1.9	1.5	199.9	57.1	0.5	213.0	0.3	26.3	3.8	0.7	40.9	3
Grosina nappe																
08IGT01	46.4082	10.2633	2617	52.2	4.2	2.6	478.0	102.3	1.2	501.6	0.2	108.4	6.4	0.8	48.8	3
08IGT02	46.3869	10.2534	1878	46.6	3.7	5.3	389.5	50.8	1.1	401.2	0.2	74.0	6.6	0.8	48.5	5
10IGT01	46.3877	10.2497	2098	33.5	2.0	5.5	1410.8	126.3	9.4	1439.9	0.1	187.5	3.1	0.7	36.3	2
10IGT02	46.3877	10.2539	1983	37.8	2.3	8.9	156.5	63.2	0.7	171.0	0.4	26.6	4.0	0.7	41.0	3
Campo nappe																
08IGT03	46.3858	10.2527	1853	30.7	2.5	3.0	299.9	46.2	2.1	310.5	0.2	31.2	1.4	0.6	29.2	3
08IGT04	46.3628	10.2494	1524	35.6	2.9	4.8	211.7	41.2	0.8	221.2	0.2	32.5	4.5	0.7	41.4	5
10IGT03	46.3733	10.2471	1689	37.8	2.6	6.4	196.2	57.8	1.8	209.5	0.4	32.9	4.2	0.7	44.1	5
10IGT04	46.3555	10.2516	1451	33.3	2.7	6.0	188.8	73.7	0.7	205.7	0.4	28.0	6.8	0.8	48.7	3
Bernina nappe																
08BP01	46.4108	10.0277	2331	32.5	2.6	2.7	265.7	48.7	0.5	276.9	0.2	38.1	6.6	0.8	51.8	3
08BP03	46.4436	9.9776	2062	34.8	2.8	7.5	249.7	45.7	0.7	260.2	0.2	35.2	5.7	0.8	47.7	4
08BP04	46.4553	9.9897	2176	33.4	2.7	2.9	137.4	35.5	0.7	145.6	0.2	22.2	25.4	0.9	82.6	4[g]
08BP05	46.4577	9.9884	2218	36.3	2.9	1.2	170.5	41.6	0.7	180.0	0.2	27.3	7.4	0.8	50.1	3
08BP06	46.4750	9.9238	1860	39.7	3.2	2.8	450.2	156.8	1.0	486.3	0.3	81.0	9.5	0.8	53.7	6
08BP09	46.4648	9.9774	2739	35.0	2.8	0.3	210.3	42.6	0.6	220.1	0.2	30.7	5.3	0.7	43.4	3
08BP10	46.4632	9.9779	2701	33.9	2.7	0.9	124.0	33.6	0.2	131.7	0.3	19.0	8.2	0.8	56.2	3
08BP11	46.4621	9.9796	2565	36.0	2.9	3.9	260.0	53.7	0.8	272.3	0.2	39.5	6.0	0.8	47.5	4
08BP12	46.4610	9.9858	2352	34.9	2.8	0.7	265.1	55.1	0.6	277.8	0.2	41.1	8.6	0.8	56.1	3
Julier nappe																
08FA17	46.4727	9.7290	2304	37.8	3.0	2.8	335.2	120.3	0.9	362.9	0.4	56.1	6.2	0.8	48.5	5
Err nappe																
08FA06	46.5635	9.6820	2496	37.9	3.0	6.5	448.0	70.4	0.5	464.2	0.2	69.6	7.3	0.8	51.1	5
08FA07	46.5660	9.6816	2527	44.9	3.6	8.0	316.3	48.1	0.5	327.4	0.2	62.9	10.6	0.8	56.1	4
Corvatsch nappe																
10EN01	46.4320	9.8246	2703	30.1	2.4	2.6	470.0	148.1	1.1	504.1	0.3	66.3	15.6	0.8	65.5	3
10EN02	46.4361	9.8280	2596	31.1	2.5	1.6	376.8	118.9	2.6	404.1	0.3	52.4	5.9	0.8	50.5	3
10EN03	46.4408	9.8303	2497	29.5	2.4	0.4	363.1	120.7	0.9	390.9	0.3	47.0	4.5	0.8	46.9	3
10EN04	46.4570	9.8273	2407	29.9	2.4	2.8	401.3	204.0	1.1	448.2	0.5	53.7	3.5	0.7	43.9	3
10EN05	46.4594	9.8260	2290	33.9	2.7	3.2	369.9	133.1	1.1	400.6	0.4	54.7	5.9	0.8	48.3	5[g]
10EN06	46.4658	9.8287	2206	36.5	2.9	4.5	335.5	136.0	1.2	366.8	0.4	52.9	5.9	0.8	49.4	4
10EN07	46.4640	9.8249	2097	30.4	2.4	0.4	388.5	125.1	0.7	417.3	0.3	51.2	4.1	0.7	46.0	3
10EN08	46.4626	9.8202	2000	27.2	1.9	5.0	496.3	310.4	0.9	567.7	0.7	62.2	6.8	0.8	50.2	5
Engadine Window (Penninic nappes)																
08TS04	46.8227	10.2465	2654	28.0	2.2	5.0	182.8	28.7	0.2	189.4	0.2	22.6	6.1	0.8	49.5	4
08TS05	46.8230	10.2492	2573	31.8	2.5	7.2	223.5	27.7	0.2	229.9	0.1	30.4	5.0	0.8	46.8	5
08TS07	46.7783	10.2144	1525	33.1	2.6	3.5	231.8	77.5	0.3	249.6	0.4	32.7	4.6	0.7	45.0	4
08TS08	46.7723	10.2132	1384	35.4	2.8	5.9	239.7	84.8	0.4	259.2	0.4	38.4	5.9	0.8	48.7	5
08TS09	46.7861	10.2243	1616	26.0	2.1	5.7	477.2	279.9	1.8	541.7	0.6	53.3	5.9	0.8	49.7	6
08TS11	46.7885	10.2398	1657	28.8	2.3	4.6	179.6	33.0	0.1	187.2	0.2	20.7	2.7	0.7	39.1	3
08TS13	46.8326	10.2469	2700	29.1	2.3	2.3	386.5	69.2	0.0	402.5	0.3	48.6	3.9	0.7	43.8	3
08TS14	46.8321	10.2476	2685	24.4	2.0	0.9	177.7	66.3	0.0	192.9	0.5	18.2	3.8	0.7	43.8	3
09EN04	46.7886	10.2776	1210	28.1	2.2	1.2	350.9	50.5	1.0	362.6	0.1	40.5	4.6	0.7	44.5	3

[a]WGS datum 1984

[b]Mean value of included replicate analyses; see Auxiliary Material A for all replicate analyses

[c]Standard error of 8% (2σ) based on reproducibility of internal lab standards

[d]Standard deviation (1σ) of included replicate analyses

[e]$[U]_e$ =[U]+[Th]0.235+[Sm]0.005 (e.g., Shuster et al., 2006)

[f]Total number of replicate analyses preformed

[g]An outlier replicate analysis was excluded from mean value calculations; see Auxiliary Material A for all replicate analyses

2. Table of Average Apatite (U-Th)/He Analyses

Sample	Latitude (N) (degrees)[a]	Longitude (E) (degrees)[a]	Elevation (meters)	Age (Ma)[b]	Std. Error (±2σ, Ma)[c]	Std. Dev. (±1σ, Ma)[d]	U (ppm)[b]	Th (ppm)[b]	Sm (ppm)[b]	$[U]_e$ (ppm)[e]	Th/U^b	He (nmol/g)[b]	Mass (µg)[b]	Ft^b	ESR (µm)[b]	Replicate Analyses[f]
Silvretta nappe																
10SL01	46.9428	10.0608	1607	15.6	0.9	3.0	18.5	6.7	34.4	20.2	0.4	1.0	1.1	0.6	36.8	3
10SL02	46.9350	10.0595	1763	14.2	0.9	2.7	21.1	7.2	26.3	22.9	0.3	1.3	1.8	0.6	41.8	3
10SL03	46.9457	10.0626	1526	16.7	1.0	1.5	39.0	7.9	31.5	41.0	0.2	2.5	2.1	0.7	44.7	3
10SL04	46.9214	10.0442	2034	18.2	1.1	2.3	36.0	6.0	34.5	37.6	0.2	2.4	1.2	0.6	37.0	5[g]
10SL05	46.9109	10.0401	2152	14.8	0.9	0.7	17.6	7.1	32.9	19.4	0.4	1.1	2.1	0.7	45.6	3[g]
10SL06	46.9042	10.0399	2270	16.5	1.0	2.1	16.5	2.2	39.1	17.2	0.1	1.0	1.6	0.7	41.3	3
10SL07	46.9002	10.0414	2345	13.1	0.8	3.4	9.1	7.4	24.7	11.0	0.9	0.5	2.2	0.7	45.3	6
10SL08	46.8944	10.0321	2640	17.4	1.0	2.1	21.4	2.2	27.9	22.1	0.1	1.3	2.1	0.7	44.3	3
10SL09	46.8935	10.0308	2715	19.4	1.2	0.6	13.6	1.5	34.8	14.1	0.1	1.0	1.6	0.7	41.5	3[g]
Bernina nappe																
08BP01	46.4108	10.0277	2331	26.8	1.6	4.1	25.4	6.5	52.7	27.2	0.3	2.8	2.9	0.7	50.9	3
08BP03	46.4436	9.9776	2062	22.5	1.4	7.2	6.9	3.3	17.7	7.7	0.4	0.7	1.3	0.6	38.1	3
08BP06	46.4750	9.9238	1860	16.9	1.0	1.9	67.7	50.3	47.4	79.5	0.8	4.3	1.1	0.6	35.9	3
08BP10	46.4632	9.9779	2701	26.1	1.6	0.1	27.4	8.1	26.6	29.4	0.3	2.4	0.9	0.6	33.2	3[g]
08BP11	46.4621	9.9796	2565	26.5	1.6	5.6	5.2	7.9	15.7	7.1	1.6	0.6	1.1	0.6	36.9	3
Err nappe																
08ED01	46.5459	9.7257	2979	23.8	1.4	5.8	52.5	21.4	85.5	57.8	0.9	4.1	1.1	0.6	35.5	3
08ED04	46.5448	9.7252	2876	24.4	1.5	2.5	37.5	4.0	69.2	38.8	0.1	3.6	2.1	0.7	45.4	3
08ED06	46.5454	9.7252	2935	21.3	1.3	1.2	89.7	15.5	81.7	93.7	0.1	6.9	1.5	0.6	39.5	3
10ED01	46.5397	9.7453	2425	16.1	1.0	0.9	40.8	5.7	27.7	42.2	0.1	2.1	0.8	0.6	32.1	3
10ED03	46.5421	9.7414	2689	22.7	1.4	3.3	55.5	31.2	105.4	63.2	0.5	5.2	1.8	0.7	42.6	3
10ED04	46.5414	9.7426	2626	26.2	1.6	4.2	84.0	16.4	86.2	88.2	0.2	7.5	3.0	0.7	46.3	3
10ED05	46.5395	9.7437	2502	24.6	1.5	1.5	91.4	2.0	60.7	92.2	0.0	8.5	2.0	0.7	44.0	3
08PN03	46.5053	9.7914	2850	24.5	1.5	4.0	18.2	20.2	67.6	23.2	1.1	2.0	1.6	0.6	39.7	3
08PN04	46.5047	9.7975	2697	28.0	1.7	6.3	13.9	14.9	63.7	17.7	1.1	1.9	1.9	0.7	43.3	3
08PN05	46.5023	9.8044	2620	21.8	1.3	1.5	19.8	19.2	66.7	24.5	1.0	1.8	1.2	0.6	36.9	3
Corvatsch nappe																
10EN01	46.4320	9.8246	2703	20.5	1.2	4.5	21.7	12.6	43.7	24.8	0.6	1.9	2.2	0.7	43.3	3
10EN03	46.4408	9.8303	2497	23.2	1.4	2.1	18.9	35.0	107.7	27.5	1.8	2.0	1.0	0.6	33.3	3[g]
10EN04	46.4570	9.8273	2407	23.5	1.4	2.5	18.1	27.6	82.7	24.8	1.5	1.9	1.1	0.6	37.0	3[g]
10EN08	46.4626	9.8202	2000	19.0	1.1	2.3	37.5	27.1	50.7	44.0	0.7	2.8	1.2	0.6	37.2	3
Engadine Window (Penninic nappes)																
08TS04	46.8227	10.2465	2654	15.8	0.9	8.4	7.9	0.9	28.7	8.2	0.1	0.5	2.5	0.7	47.4	3
08TS05	46.8230	10.2492	2573	10.0	0.6	4.4	11.2	1.8	14.8	11.7	0.2	0.4	2.1	0.7	44.4	3
08TS08	46.7723	10.2132	1384	7.1	0.4	2.1	19.9	30.8	104.0	27.5	1.6	0.6	1.0	0.6	34.9	3
08TS09	46.7861	10.2243	1616	15.1	0.9	6.7	22.2	57.1	119.0	36.0	2.7	1.4	0.9	0.6	33.6	3
08TS11	46.7885	10.2398	1657	8.1	0.5	1.9	16.7	1.9	6.9	17.2	0.1	0.5	1.8	0.7	41.6	3

[a]WGS datum 1984

[b]Mean value of included replicate analyses; see Auxiliary Material B for all replicate analyses

[c]Standard error of 6% (2σ) based on reproducibility of internal lab standards

[d]Standard deviation (1σ) of included replicate analyses

[e]$[U]_e$ =[U]+[Th]0.235+[Sm]0.005 (e.g., Shuster et al., 2006)

[f]Total number of replicate analyses preformed

[g]An outlier(s) replicate analysis was excluded from mean value calculations; see Auxiliary Material A for all replicate analyses

3. Table of Individual Zircon (U-Th)/He Analyses for the Err Nappe

Sample[a]	Age (Ma)[b]	Std. Error (±2σ, Ma)[c]	U (ppm)[b]	Th (ppm)[b]	Sm (ppm)[b]	$[U]_e$ (ppm)[d]	Th/U[b]	He (nmol/g)[b]	Mass (µg)[b]	Ft[b]	ESR (µm)[b]
Err Detachment Transect											
08ED01: 46.5459 °N, 9.7257 °E; 2979 m											
08ED01-1	24.4	2.0	742.5	212.7	2.3	791.4	0.3	75.9	3.0	0.7	41.9
08ED01-2	34.1	2.7	547.4	119.0	3.1	574.8	0.2	78.8	3.9	0.7	44.8
08ED01-3	35.9	2.9	458.3	111.9	1.1	484.0	0.2	71.4	4.8	0.8	48.2
08ED01-4	33.3	2.7	1074.4	266.6	2.0	1135.8	0.2	147.3	3.2	0.7	40.6
08ED01-5	119.4	9.6	239.4	39.3	0.0	248.4	0.2	116.0	3.7	0.7	40.3
08ED02: 46.5455 °N, 9.7222 °E; 2981 m											
08ED02-1	52.5	4.2	279.3	59.4	3.5	293.0	0.2	65.0	6.6	0.8	53.0
08ED02-2	40.0	3.2	431.6	105.2	2.1	455.8	0.2	77.3	7.2	0.8	53.7
08ED02-3	47.4	3.8	607.9	138.0	2.6	639.7	0.2	122.6	4.1	0.7	45.4
08ED02-4	28.0	2.2	475.6	118.6	2.3	503.0	0.2	58.3	5.2	0.8	49.7
08ED02-5	55.2	4.4	613.7	131.3	0.6	643.9	0.2	148.7	6.1	0.8	50.7
08ED02-6	74.6	6.0	546.2	134.9	1.8	577.2	0.2	191.1	11.7	0.8	65.0
08ED04: 46.5454 °N, 9.7252 °E; 2876 m											
08ED04-1	56.3	4.5	613.1	158.0	1.1	649.5	0.3	155.5	8.7	0.8	54.1
08ED04-2	63.9	5.1	374.9	89.1	0.6	395.5	0.2	103.2	5.7	0.8	46.9
08ED04-3	59.9	4.8	378.5	79.5	0.9	396.8	0.2	98.8	6.7	0.8	49.7
08ED04-4	56.4	4.5	559.9	128.8	1.0	589.5	0.2	146.7	14.0	0.8	63.4
08ED04-5	41.7	3.3	435.8	122.4	0.9	464.0	0.3	75.9	4.0	0.7	41.6
08ED04-6	51.6	4.1	434.2	112.3	0.9	460.1	0.3	97.8	6.1	0.8	48.5
08ED06: 46.5454 °N, 9.7252 °E; 2935 m											
08ED06-1	48.1	3.8	577.8	112.3	2.6	603.6	0.2	121.9	6.2	0.8	51.5
08ED06-2	59.3	4.7	527.8	115.1	2.5	554.3	0.2	146.0	12.8	0.8	65.6
08ED06-3	32.7	2.6	423.6	147.5	1.8	457.5	0.3	61.6	5.3	0.8	48.6
08ED06-4	62.6	5.0	505.1	92.8	0.9	526.5	0.2	149.5	16.0	0.8	72.3
08ED06-5	64.6	5.2	395.7	89.1	0.7	416.2	0.2	121.5	16.7	0.8	71.1
08ED06-6	57.2	4.6	467.1	89.0	0.4	487.6	0.2	123.1	11.6	0.8	63.6
10ED01: 46.5397 °N, 9.7453 °E; 2425 m											
10ED01-1	47.1	2.8	686.0	136.6	0.7	717.4	0.2	137.5	5.0	0.8	46.3
10ED01-2	35.0	2.1	608.2	105.9	0.7	632.6	0.2	98.4	14.7	0.8	65.7
10ED01-3	36.0	2.2	572.8	107.8	1.1	597.6	0.2	86.9	5.3	0.7	45.2
10ED01-4	41.5	3.3	391.6	74.9	0.5	408.8	0.2	66.4	3.9	0.7	41.1
10ED01-5	47.0	3.8	444.8	47.8	0.4	455.8	0.1	83.8	3.9	0.7	40.8
10ED01-6	40.5	3.2	440.6	85.5	0.7	460.3	0.2	78.5	8.0	0.8	52.3
10ED02: 46.5434 °N, 9.7380 °E; 2760 m											
10ED02-1	51.6	3.1	713.9	125.7	1.1	742.8	0.2	172.7	15.7	0.8	70.2
10ED02-2	44.1	2.6	469.0	103.6	0.9	492.9	0.2	91.0	6.5	0.8	51.4
10ED02-3	37.5	2.3	340.6	61.4	0.7	354.8	0.2	53.2	3.9	0.7	43.7
10ED02-4	41.3	3.3	570.3	53.7	0.3	582.6	0.1	101.3	9.4	0.8	52.0
10ED02-5	32.6	2.6	762.9	63.6	0.8	777.5	0.1	105.2	6.5	0.8	49.4
10ED02-6	42.2	3.4	885.6	86.9	1.3	905.6	0.1	149.1	3.6	0.7	40.4
10ED03: 46.5241 °N, 9.7414 °E; 2689 m											
10ED03-1	43.7	2.6	790.5	151.8	1.0	825.4	0.2	145.0	4.7	0.7	44.6
10ED03-2	34.5	2.1	951.2	139.1	1.3	983.2	0.1	141.8	7.0	0.8	50.7
10ED03-3	55.7	3.3	541.9	101.5	1.0	565.3	0.2	126.3	4.7	0.7	44.1
10ED03-4	52.1	4.2	891.9	157.5	1.1	928.1	0.2	216.8	17.8	0.8	68.8
10ED03-5	40.2	3.2	380.1	39.7	0.5	389.3	0.1	70.2	18.7	0.8	68.8
10ED03-6	42.5	3.4	819.8	131.6	1.5	850.1	0.2	159.9	14.5	0.8	64.2
10ED04: 46.5414 °N, 9.7426 °E; 2626 m											
10ED04-1	50.8	4.1	663.6	169.3	1.1	702.6	0.3	147.2	6.4	0.8	48.5
10ED04-2	67.5	5.4	271.2	60.8	0.7	285.2	0.2	82.5	9.6	0.8	55.8
10ED04-3	77.6	6.2	491.0	118.8	1.2	518.3	0.2	182.9	24.0	0.8	73.4
10ED04-4	38.1	3.0	748.5	172.4	1.0	788.2	0.2	126.5	8.2	0.8	52.6
10ED04-5	53.3	4.3	506.6	112.4	0.8	532.5	0.2	126.0	16.1	0.8	65.4
10ED04-6	57.8	4.6	604.4	141.9	0.9	637.0	0.2	159.3	10.9	0.8	58.3
10ED05: 46.5395 °N, 9.7437 °E; 2502 m											
10ED05-1	38.7	3.1	299.3	36.7	0.5	307.7	0.1	56.2	43.3	0.9	92.8
10ED05-2	49.1	3.9	511.1	79.7	0.5	529.5	0.2	113.4	11.5	0.8	59.9
10ED05-3	35.4	2.8	282.3	46.4	0.6	293.0	0.2	43.2	7.1	0.8	50.0
10ED05-4	48.0	3.8	450.0	82.9	0.5	469.1	0.2	100.8	17.4	0.8	67.8
10ED05-5	32.9	2.6	290.7	65.7	0.7	305.8	0.2	43.1	10.5	0.8	55.9
10ED05-6	33.2	2.7	404.4	74.1	0.7	421.5	0.2	60.0	9.6	0.8	56.4
Piz Nair Transect											
08PN02: 46.5059 °N , 9.7871 °E; 3025 m											
08PN02-1	46.7	3.7	254.5	25.4	0.5	260.3	0.1	50.0	6.4	0.8	47.6
08PN02-2	94.7	7.6	205.5	60.3	0.7	219.4	0.3	94.2	21.3	0.8	72.2
08PN02-3	78.3	6.3	283.7	80.3	0.5	302.2	0.3	94.9	4.7	0.7	44.2
08PN02-4	90.9	7.3	345.8	38.7	0.7	354.7	0.1	139.8	10.4	0.8	57.6
08PN03: 46.5053 °N , 9.7914 °E; 2850 m											
08PN03-1	48.2	3.9	409.0	101.4	0.8	432.4	0.2	85.6	5.8	0.8	47.9
08PN03-2	54.5	4.4	445.0	97.8	0.9	467.5	0.2	102.6	5.2	0.7	44.6
08PN03-3	65.5	5.2	443.8	77.8	0.2	461.7	0.2	122.5	5.2	0.7	45.4

3. Table of Individual Zircon (U-Th)/He Analyses for the Err Nappe, cont.

Sample[a]	Age (Ma)[b]	Std. Error (±2σ, Ma)[c]	U (ppm)[b]	Th (ppm)[b]	Sm (ppm)[b]	$[U]_e$ (ppm)[d]	Th/U[b]	He (nmol/g)[b]	Mass (µg)[b]	Ft[b]	ESR (µm)[b]
08PN03 cont.											
08PN03-4	67.5	5.4	295.4	57.4	1.7	308.6	0.2	93.3	16.4	0.8	67.9
08PN03-5	43.9	3.5	937.8	184.8	1.5	980.3	0.2	166.2	3.6	0.7	39.6
08PN03-6	55.3	4.4	422.6	126.1	2.4	451.6	0.3	100.5	4.9	0.7	44.8
08PN04: 46.5047 °N, 9.7975 °E; 2697 m											
08PN04-1	66.4	4.0	459.3	173.7	1.1	499.3	0.4	131.2	4.4	0.7	42.6
08PN04-2	53.0	3.2	325.2	87.6	1.1	345.3	0.3	72.2	4.0	0.7	42.2
08PN04-3	94.9	5.7	329.5	82.3	0.4	348.5	0.2	129.0	3.6	0.7	40.4
08PN04-4	39.3	3.1	481.2	125.9	1.3	510.2	0.3	79.6	4.2	0.7	43.0
08PN04-5	75.7	6.1	212.3	41.4	0.5	221.8	0.2	73.9	13.7	0.8	62.5
08PN04-6	111.8	8.9	278.3	58.2	0.4	291.7	0.2	144.8	14.6	0.8	63.9
08PN05: 46.5023 °N, 9.8044 °E; 2620 m											
08PN05-1	105.9	8.5	246.7	48.9	0.5	257.9	0.2	119.3	9.8	0.8	59.5
08PN05-2	64.5	5.2	537.3	114.8	0.8	563.7	0.2	155.9	7.9	0.8	56.0
08PN05-3	51.2	4.1	645.1	136.5	0.6	676.5	0.2	147.9	7.4	0.8	55.2
08PN05-4	97.2	7.8	467.0	105.2	0.9	491.3	0.2	211.3	13.6	0.8	63.5
08PN05-5	66.6	5.3	451.0	115.5	1.1	477.6	0.3	137.2	10.9	0.8	57.3
08PN05-6	63.3	5.1	693.5	125.6	1.6	722.4	0.2	195.9	9.6	0.8	55.4
08PN06: 46.5026 °N, 9.8114 °E; 2523 m											
08PN06-1	57.8	4.6	144.4	110.8	1.8	169.9	0.8	41.1	6.7	0.8	51.9
08PN06-2	39.4	3.2	280.4	65.8	0.5	295.6	0.2	49.7	7.0	0.8	54.9
08PN06-3	51.3	4.1	185.2	33.2	0.4	192.8	0.2	42.9	8.9	0.8	58.8
08PN06-4	49.4	4.0	276.5	63.3	0.8	291.1	0.2	55.9	4.2	0.7	40.2
08PN06-5	70.2	5.6	264.2	96.4	0.9	286.4	0.4	79.7	4.7	0.7	42.8
Val d'Err Sample											
08FA05: 46.5629 °N, 9.6821 °E; 2583 m											
08FA05-1	49.8	4.0	453.0	108.9	0.8	478.1	0.2	102.0	8.0	0.8	56.1
08FA05-2	65.7	5.3	488.1	130.5	0.8	518.1	0.3	138.4	4.4	0.8	46.2
08FA05-3	91.3	7.3	536.4	158.3	1.2	572.9	0.3	228.5	10.8	0.8	60.1
08FA05-4	48.5	3.9	300.1	63.3	0.9	314.7	0.2	61.0	3.9	0.7	43.7
08FA05-5	46.6	3.7	561.5	153.0	1.3	596.7	0.3	118.4	7.4	0.8	54.8
08FA05-6	65.0	5.2	367.2	125.6	0.6	396.1	0.3	110.7	8.2	0.8	56.9

[a]Location and elevation listed in table; WGS datum 1984

[b]Individual results for aliquot analysis

[c]Standard error of 8% (2σ) based on reproducibility of internal lab standards

[d]$[U]_e$ =[U]+[Th]0.235+[Sm]0.005 (e.g., Shuster et al., 2006)

4. Table of Replicate Silvretta Zircon (U-Th)/He Analyses

Sample[a]	Age (Ma)	Std. Error (±2σ, Ma)[b]	U (ppm)	Th (ppm)	Sm (ppm)	$[U]_e$ (ppm)[c]	Th/U	He (nmol/g)	Mass (µg)	Ft	ESR (µm)	Std. Dev. (±1σ, Ma)[d]
Silvretta nappe												
z10SL01-1	43.9	3.5	385.4	37.8	0.9	394.1	0.1	73.7	7.8	0.8	54.3	
z10SL01-2	58.5	4.7	217.0	53.0	3.7	229.3	0.2	53.6	3.8	0.7	43.7	
z10SL01-3	42.8	3.4	243.6	34.3	0.5	251.5	0.1	45.7	7.1	0.8	53.9	
z10SL01-4	69.3	5.5	217.8	41.2	0.6	227.3	0.2	65.8	7.2	0.8	50.6	
z10SL01-5	52.8	4.2	379.5	62.4	1.0	393.9	0.2	84.3	5.5	0.7	45.5	
10SL01	***53.5***	***4.3***	***288.7***	***45.7***	***1.3***	***299.2***	***0.2***	***64.6***	***6.3***	***0.8***	***49.6***	***11.0***
z10SL02-1	66.4	5.3	255.4	37.9	0.8	264.1	0.1	72.4	6.4	0.8	48.0	
z10SL02-2	34.2	2.7	111.8	35.2	0.9	119.9	0.3	16.2	4.8	0.7	42.9	
z10SL02-3	46.9	3.8	216.4	35.1	0.7	224.5	0.2	44.0	7.1	0.8	50.9	
z10SL02-4	31.0	2.5	142.3	51.0	0.9	154.1	0.4	19.5	6.5	0.8	47.1	
z10SL02-5	40.4	3.2	268.7	44.1	0.9	278.8	0.2	44.9	4.9	0.7	43.2	
10SL02	***43.8***	***3.5***	***198.9***	***40.7***	***0.8***	***208.3***	***0.2***	***39.4***	***6.0***	***0.8***	***46.4***	***14.1***
z10SL03-1	63.5	5.1	216.6	44.6	0.6	226.8	0.2	63.5	13.1	0.8	62.7	
z10SL03-2	52.1	4.2	290.3	60.0	1.1	304.1	0.2	69.9	14.1	0.8	63.4	
z10SL03-3	43.9	3.5	378.7	40.6	0.5	388.0	0.1	71.9	7.8	0.8	52.6	
z10SL03-4	55.5	4.4	296.9	53.1	2.0	309.2	0.2	73.3	9.3	0.8	55.0	
z10SL03-5	54.5	4.4	320.8	88.8	0.9	341.2	0.3	77.1	6.7	0.8	49.5	
z10SL03-6[e]	46.8	3.7	722.4	218.4	0.5	772.7	0.3	151.1	7.4	0.8	51.0	
z10SL03-7[e]	32.0	2.6	250.9	41.5	1.0	260.5	0.2	35.1	8.3	0.8	52.3	
z10SL03-11[e]	31.7	2.5	190.1	26.8	0.5	196.3	0.1	25.6	5.7	0.8	47.6	
z10SL03-12[e]	38.3	3.1	166.8	43.5	0.8	176.9	0.3	28.8	9.2	0.8	54.5	
z10SL03-16[e]	42.3	3.4	267.6	81.6	0.8	286.4	0.3	50.2	7.4	0.8	49.7	
z10SL03-19[e]	46.2	3.7	272.8	84.3	0.8	292.2	0.3	55.7	6.8	0.8	48.7	
z10SL03-21[e]	47.8	3.8	260.6	51.7	1.3	272.5	0.2	51.7	4.2	0.7	42.7	
z10SL03-23[e]	42.2	3.4	262.9	68.5	1.1	278.7	0.3	46.1	4.1	0.7	41.5	
z10SL03-24[e]	51.1	4.1	329.9	57.0	0.9	343.0	0.2	69.0	4.1	0.7	41.6	
z10SL03-28[e]	43.2	3.5	472.7	127.5	0.8	502.0	0.3	88.6	5.7	0.8	47.2	
10SL03	***46.1***	***3.7***	***313.3***	***72.5***	***0.9***	***330.0***	***0.2***	***63.8***	***7.6***	***0.8***	***50.7***	***8.6***
z10SL04-1	39.4	3.1	155.4	31.7	1.0	162.7	0.2	27.1	8.5	0.8	53.6	
z10SL04-2	57.3	4.6	225.1	30.3	0.6	232.1	0.1	57.9	11.2	0.8	59.1	
z10SL04-3	42.3	3.4	179.7	32.8	0.8	187.3	0.2	34.9	14.6	0.8	63.7	
z10SL04-4	58.1	4.6	403.5	48.1	0.5	414.6	0.1	98.8	6.1	0.8	47.2	
z10SL04-5	40.9	3.3	226.5	34.6	0.8	234.4	0.2	39.2	5.5	0.8	47.0	
10SL04	***47.6***	***3.8***	***238.0***	***35.5***	***0.7***	***246.2***	***0.2***	***51.6***	***9.2***	***0.8***	***54.1***	***9.3***
z10SL05-1	49.8	4.0	472.7	37.1	0.9	481.2	0.1	102.2	9.2	0.8	54.5	
z10SL05-2	40.3	3.2	374.7	51.6	1.1	386.6	0.1	67.1	10.1	0.8	57.0	
z10SL05-3	55.2	4.4	159.5	35.1	0.3	167.6	0.2	40.8	14.0	0.8	63.0	
z10SL05-4	48.9	3.9	156.7	47.3	0.4	167.6	0.3	34.4	7.6	0.8	52.3	
z10SL05-5	45.2	3.6	297.7	47.1	0.5	308.5	0.2	60.5	12.7	0.8	58.8	
z10SL05-7[e]	40.3	3.2	420.9	77.3	0.6	438.7	0.2	70.8	5.1	0.7	44.0	
z10SL05-10[e]	49.5	4.0	344.4	80.8	0.7	363.0	0.2	78.2	11.9	0.8	59.5	
z10SL05-11[e]	48.4	3.9	444.3	87.0	0.9	464.3	0.2	98.6	13.0	0.8	62.3	
z10SL05-14[e]	39.9	3.2	357.3	49.2	1.0	368.6	0.1	64.1	12.1	0.8	60.1	
z10SL05-15[e]	37.7	3.0	533.7	56.4	0.6	546.7	0.1	87.3	8.6	0.8	53.1	
z10SL05-18[e]	32.9	2.6	684.7	38.6	0.8	693.6	0.1	93.5	5.9	0.8	46.9	
z10SL05-19[e]	48.4	3.9	318.6	44.7	0.6	328.9	0.1	68.6	10.5	0.8	57.1	
z10SL05-25[e]	35.8	2.9	325.1	31.1	0.3	332.3	0.1	48.8	6.2	0.8	47.2	
z10SL05-26[e]	42.2	3.4	203.3	48.4	0.9	214.5	0.2	36.9	5.3	0.8	46.7	
10SL05	***43.9***	***3.5***	***363.8***	***52.3***	***0.7***	***375.9***	***0.2***	***68.0***	***9.5***	***0.8***	***54.5***	***6.4***
z10SL06-1	47.1	3.8	246.7	39.2	1.0	255.8	0.2	48.6	5.2	0.7	44.9	
z10SL06-2	55.8	4.5	291.5	49.7	0.9	303.0	0.2	67.8	4.7	0.7	44.0	
z10SL06-3	53.4	4.3	339.2	48.0	0.6	350.2	0.1	79.0	7.7	0.8	52.5	
10SL06	***52.1***	***4.2***	***292.5***	***45.6***	***0.9***	***303.0***	***0.2***	***65.2***	***5.9***	***0.8***	***47.1***	***4.5***
z10SL07-1	48.0	3.8	268.8	96.5	0.6	291.0	0.4	60.7	9.8	0.8	59.4	
z10SL07-2	49.6	4.0	194.2	117.4	0.6	221.3	0.6	47.8	11.1	0.8	60.9	
z10SL07-3	64.8	5.2	259.9	172.1	0.8	299.5	0.7	82.8	9.0	0.8	55.6	
z10SL07-4	86.6	6.9	66.1	45.7	0.4	76.6	0.7	26.8	5.5	0.7	45.9	
z10SL07-5	47.8	3.8	71.0	30.9	0.4	78.1	0.4	15.6	7.7	0.8	50.8	
10SL07	***59.4***	***4.7***	***172.0***	***92.5***	***0.6***	***193.3***	***0.6***	***46.7***	***8.6***	***0.8***	***54.5***	***16.8***
z10SL08-1	78.5	6.3	507.7	135.5	1.2	538.9	0.3	172.4	6.2	0.8	46.3	
z10SL08-2	41.9	3.4	436.0	57.3	1.6	449.2	0.1	75.4	4.8	0.7	43.8	

4. Table of Replicate Silvretta Zircon (U-Th)/He Analyses

Sample[a]	Age (Ma)	Std. Error (±2σ, Ma)[b]	U (ppm)	Th (ppm)	Sm (ppm)	$[U]_e$ (ppm)[c]	Th/U	He (nmol/g)	Mass (µg)	Ft	ESR (µm)	Std. Dev. (±1σ, Ma)[d]
Silvretta nappe, cont.												
z10SL08-3	54.8	4.4	119.2	38.0	1.0	128.0	0.3	28.2	5.1	0.7	44.8	
z10SL08-4	57.8	4.6	264.8	149.3	0.4	299.1	0.6	74.1	9.5	0.8	56.5	
z10SL08-5	70.8	5.7	255.5	55.3	1.3	268.2	0.2	77.4	5.9	0.8	46.2	
10SL08	***60.8***	***4.9***	***316.6***	***87.1***	***1.1***	***336.7***	***0.3***	***85.5***	***6.3***	***0.8***	***47.5***	***14.3***
z10SL09-1	39.7	3.2	149.7	65.3	1.5	164.8	0.4	26.8	6.2	0.8	47.5	
z10SL09-2	45.5	3.6	178.2	60.0	1.1	192.0	0.3	35.8	5.8	0.8	47.8	
z10SL09-3	67.3	5.4	195.0	33.4	0.6	202.7	0.2	58.1	8.5	0.8	54.3	
z10SL09-4	62.4	5.0	217.4	63.4	1.0	232.0	0.3	61.5	8.4	0.8	54.0	
z10SL09-5	60.2	4.8	269.0	32.2	0.9	276.4	0.1	69.6	7.3	0.8	50.6	
z10SL09-8[e]	41.2	3.3	391.9	43.5	1.4	401.9	0.1	67.2	5.4	0.8	45.6	
z10SL09-9[e]	34.8	2.8	181.3	31.8	0.8	188.6	0.2	26.8	6.0	0.8	46.7	
z10SL09-10[e]	46.1	3.7	240.5	39.7	1.1	249.6	0.2	48.4	8.1	0.8	52.0	
z10SL09-11[e]	52.6	4.2	570.9	79.4	0.9	589.2	0.1	128.3	6.7	0.8	48.8	
z10SL09-15[e]	57.8	4.6	183.0	125.7	0.8	211.9	0.7	53.6	13.4	0.8	61.9	
z10SL09-18[e]	37.2	3.0	263.4	47.8	0.7	274.4	0.2	40.9	4.7	0.7	44.0	
z10SL09-20[e]	44.2	3.5	537.3	36.6	0.5	545.7	0.1	95.1	4.3	0.7	41.4	
z10SL09-23[e]	45.7	3.66	112.4	22.7	0.7	117.6	0.20	22.7	8.62	0.78	52.95	
z10SL09-29[e]	33.2	2.7	304.9	63.3	0.5	319.5	0.2	45.5	9.6	0.8	56.5	
z10SL09-30[e]	51.1	4.1	318.4	95.0	2.0	340.3	0.3	74.8	11.6	0.8	56.9	
10SL09	***47.9***	***3.8***	***274.2***	***56.0***	***1.0***	***287.1***	***0.2***	***57.0***	***7.6***	***0.8***	***50.7***	***10.4***
z10SL11-1	36.4	2.9	170.0	24.3	0.5	175.6	0.1	27.2	9.1	0.8	54.4	
z10SL11-2	60.6	4.8	334.2	80.1	1.7	352.6	0.2	89.1	7.0	0.8	50.4	
z10SL11-3	34.8	2.8	161.4	34.7	0.6	169.4	0.2	25.4	10.8	0.8	56.9	
z10SL11-5	47.8	3.8	568.1	79.0	0.9	586.3	0.1	112.4	4.1	0.7	43.9	
10SL11	***44.9***	***3.6***	***308.4***	***54.5***	***0.9***	***321.0***	***0.2***	***63.5***	***7.7***	***0.8***	***51.4***	***12.0***

[a]For location and elevation data see Table 1

[b]Standard error of 8% (2σ) based on reproducibility of internal lab standards

[c][U]e =[U]+[Th]0.235+[Sm]0.005 (e.g., Shuster et al., 2006)

[d]Standard deviation (1σ) of replicate analyses

[e] LA-ICP-MS depth profiling also completed on zircon aliquot; see Appendix C for laser ablation depth profiles

Italics indicate mean values of replicate analyses

Appendix A: Replicate Zircon and Apatite (U-Th)/He Analyses

Replicate analyses of zircon and apatite (U-Th)/He aliquots are presented in the following tables. These tables are separated into zircon and apatite analyses, Table A and B respectively. Locations for samples reported in the tables may be found in Tables 1 and 2 of the main body of the thesis.

A. Table of Replicate Zircon (U-Th)/He Analyses

Sample[a]	Age (Ma)	Std. Error (±2σ, Ma)[b]	U (ppm)	Th (ppm)	Sm (ppm)	$[U]_e$ (ppm)[c]	Th/U	He (nmol/g)	Mass (µg)	Ft	ESR (µm)	Std. Dev. (±1σ, Ma)[d]
Silvretta nappe												
z10SL01-1	43.9	3.5	385.4	37.8	0.9	394.1	0.1	73.7	7.8	0.8	54.3	
z10SL01-2	58.5	4.7	217.0	53.0	3.7	229.3	0.2	53.6	3.8	0.7	43.7	
z10SL01-3	42.8	3.4	243.6	34.3	0.5	251.5	0.1	45.7	7.1	0.8	53.9	
z10SL01-4	69.3	5.5	217.8	41.2	0.6	227.3	0.2	65.8	7.2	0.8	50.6	
z10SL01-5	52.8	4.2	379.5	62.4	1.0	393.9	0.2	84.3	5.5	0.7	45.5	
10SL01	***53.5***	***4.3***	***288.7***	***45.7***	***1.3***	***299.2***	***0.2***	***64.6***	***6.3***	***0.8***	***49.6***	***11.0***
z10SL02-1	66.4	5.3	255.4	37.9	0.8	264.1	0.1	72.4	6.4	0.8	48.0	
z10SL02-2	34.2	2.7	111.8	35.2	0.9	119.9	0.3	16.2	4.8	0.7	42.9	
z10SL02-3	46.9	3.8	216.4	35.1	0.7	224.5	0.2	44.0	7.1	0.8	50.9	
z10SL02-4	31.0	2.5	142.3	51.0	0.9	154.1	0.4	19.5	6.5	0.8	47.1	
z10SL02-5	40.4	3.2	268.7	44.1	0.9	278.8	0.2	44.9	4.9	0.7	43.2	
10SL02	***43.8***	***3.5***	***198.9***	***40.7***	***0.8***	***208.3***	***0.2***	***39.4***	***6.0***	***0.8***	***46.4***	***14.1***
z10SL03-1	63.5	5.1	216.6	44.6	0.6	226.8	0.2	63.5	13.1	0.8	62.7	
z10SL03-2	52.1	4.2	290.3	60.0	1.1	304.1	0.2	69.9	14.1	0.8	63.4	
z10SL03-3	43.9	3.5	378.7	40.6	0.5	388.0	0.1	71.9	7.8	0.8	52.6	
z10SL03-4	55.5	4.4	296.9	53.1	2.0	309.2	0.2	73.3	9.3	0.8	55.0	
z10SL03-5	54.5	4.4	320.8	88.8	0.9	341.2	0.3	77.1	6.7	0.8	49.5	
z10SL03-6[e]	46.8	3.7	722.4	218.4	0.5	772.7	0.3	151.1	7.4	0.8	51.0	
z10SL03-7[e]	32.0	2.6	250.9	41.5	1.0	260.5	0.2	35.1	8.3	0.8	52.3	
z10SL03-11[e]	31.7	2.5	190.1	26.8	0.5	196.3	0.1	25.6	5.7	0.8	47.6	
z10SL03-12[e]	38.3	3.1	166.8	43.5	0.8	176.9	0.3	28.8	9.2	0.8	54.5	
z10SL03-16[e]	42.3	3.4	267.6	81.6	0.8	286.4	0.3	50.2	7.4	0.8	49.7	
z10SL03-19[e]	46.2	3.7	272.8	84.3	0.8	292.2	0.3	55.7	6.8	0.8	48.7	
z10SL03-21[e]	47.8	3.8	260.6	51.7	1.3	272.5	0.2	51.7	4.2	0.7	42.7	
z10SL03-23[e]	42.2	3.4	262.9	68.5	1.1	278.7	0.3	46.1	4.1	0.7	41.5	
z10SL03-24[e]	51.1	4.1	329.9	57.0	0.9	343.0	0.2	69.0	4.1	0.7	41.6	
z10SL03-28[e]	43.2	3.5	472.7	127.5	0.8	502.0	0.3	88.6	5.7	0.8	47.2	
10SL03	***46.1***	***3.7***	***313.3***	***72.5***	***0.9***	***330.0***	***0.2***	***63.8***	***7.6***	***0.8***	***50.7***	***8.6***
z10SL04-1	39.4	3.1	155.4	31.7	1.0	162.7	0.2	27.1	8.5	0.8	53.6	
z10SL04-2	57.3	4.6	225.1	30.3	0.6	232.1	0.1	57.9	11.2	0.8	59.1	
z10SL04-3	42.3	3.4	179.7	32.8	0.8	187.3	0.2	34.9	14.6	0.8	63.7	
z10SL04-4	58.1	4.6	403.5	48.1	0.5	414.6	0.1	98.8	6.1	0.8	47.2	
z10SL04-5	40.9	3.3	226.5	34.6	0.8	234.4	0.2	39.2	5.5	0.8	47.0	
10SL04	***47.6***	***3.8***	***238.0***	***35.5***	***0.7***	***246.2***	***0.2***	***51.6***	***9.2***	***0.8***	***54.1***	***9.3***
z10SL05-1	49.8	4.0	472.7	37.1	0.9	481.2	0.1	102.2	9.2	0.8	54.5	
z10SL05-2	40.3	3.2	374.7	51.6	1.1	386.6	0.1	67.1	10.1	0.8	57.0	
z10SL05-3	55.2	4.4	159.5	35.1	0.3	167.6	0.2	40.8	14.0	0.8	63.0	
z10SL05-4	48.9	3.9	156.7	47.3	0.4	167.6	0.3	34.4	7.6	0.8	52.3	
z10SL05-5	45.2	3.6	297.7	47.1	0.5	308.5	0.2	60.5	12.7	0.8	58.8	
z10SL05-7[e]	40.3	3.2	420.9	77.3	0.6	438.7	0.2	70.8	5.1	0.7	44.0	
z10SL05-10[e]	49.5	4.0	344.4	80.8	0.7	363.0	0.2	78.2	11.9	0.8	59.5	
z10SL05-11[e]	48.4	3.9	444.3	87.0	0.9	464.3	0.2	98.6	13.0	0.8	62.3	
z10SL05-14[e]	39.9	3.2	357.3	49.2	1.0	368.6	0.1	64.1	12.1	0.8	60.1	
z10SL05-15[e]	37.7	3.0	533.7	56.4	0.6	546.7	0.1	87.3	8.6	0.8	53.1	
z10SL05-18[e]	32.9	2.6	684.7	38.6	0.8	693.6	0.1	93.5	5.9	0.8	46.9	
z10SL05-19[e]	48.4	3.9	318.6	44.7	0.6	328.9	0.1	68.6	10.5	0.8	57.1	
z10SL05-25[e]	35.8	2.9	325.1	31.1	0.3	332.3	0.1	48.8	6.2	0.8	47.2	
z10SL05-26[e]	42.2	3.4	203.3	48.4	0.9	214.5	0.2	36.9	5.3	0.8	46.7	
10SL05	***43.9***	***3.5***	***363.8***	***52.3***	***0.7***	***375.9***	***0.2***	***68.0***	***9.5***	***0.8***	***54.5***	***6.4***
z10SL06-1	47.1	3.8	246.7	39.2	1.0	255.8	0.2	48.6	5.2	0.7	44.9	
z10SL06-2	55.8	4.5	291.5	49.7	0.9	303.0	0.2	67.8	4.7	0.7	44.0	
z10SL06-3	53.4	4.3	339.2	48.0	0.6	350.2	0.1	79.0	7.7	0.8	52.5	
10SL06	***52.1***	***4.2***	***292.5***	***45.6***	***0.9***	***303.0***	***0.2***	***65.2***	***5.9***	***0.8***	***47.1***	***4.5***
z10SL07-1	48.0	3.8	268.8	96.5	0.6	291.0	0.4	60.7	9.8	0.8	59.4	
z10SL07-2	49.6	4.0	194.2	117.4	0.6	221.3	0.6	47.8	11.1	0.8	60.9	
z10SL07-3	64.8	5.2	259.9	172.1	0.8	299.5	0.7	82.8	9.0	0.8	55.6	
z10SL07-4	86.6	6.9	66.1	45.7	0.4	76.6	0.7	26.8	5.5	0.7	45.9	
z10SL07-5	47.8	3.8	71.0	30.9	0.4	78.1	0.4	15.6	7.7	0.8	50.8	
10SL07	***59.4***	***4.7***	***172.0***	***92.5***	***0.6***	***193.3***	***0.6***	***46.7***	***8.6***	***0.8***	***54.5***	***16.8***
z10SL08-1	78.5	6.3	507.7	135.5	1.2	538.9	0.3	172.4	6.2	0.8	46.3	
z10SL08-2	41.9	3.4	436.0	57.3	1.6	449.2	0.1	75.4	4.8	0.7	43.8	

A. Table of Replicate Zircon (U-Th)/He Analyses, cont.

Sample[a]	Age (Ma)	Std. Error (±2σ, Ma)[b]	U (ppm)	Th (ppm)	Sm (ppm)	$[U]_e$ (ppm)[c]	Th/U	He (nmol/g)	Mass (µg)	Ft	ESR (µm)	Std. Dev. (±1σ, Ma)[d]
Silvretta nappe, cont.												
z10SL08-3	54.8	4.4	119.2	38.0	1.0	128.0	0.3	28.2	5.1	0.7	44.8	
z10SL08-4	57.8	4.6	264.8	149.3	0.4	299.1	0.6	74.1	9.5	0.8	56.5	
z10SL08-5	70.8	5.7	255.5	55.3	1.3	268.2	0.2	77.4	5.9	0.8	46.2	
10SL08	***60.8***	***4.9***	***316.6***	***87.1***	***1.1***	***336.7***	***0.3***	***85.5***	***6.3***	***0.8***	***47.5***	***14.3***
z10SL09-1	39.7	3.2	149.7	65.3	1.5	164.8	0.4	26.8	6.2	0.8	47.5	
z10SL09-2	45.5	3.6	178.2	60.0	1.1	192.0	0.3	35.8	5.8	0.8	47.8	
z10SL09-3	67.3	5.4	195.0	33.4	0.6	202.7	0.2	58.1	8.5	0.8	54.3	
z10SL09-4	62.4	5.0	217.4	63.4	1.0	232.0	0.3	61.5	8.4	0.8	54.0	
z10SL09-5	60.2	4.8	269.0	32.2	0.9	276.4	0.1	69.6	7.3	0.8	50.6	
z10SL09-8[e]	41.2	3.3	391.9	43.5	1.4	401.9	0.1	67.2	5.4	0.8	45.6	
z10SL09-9[e]	34.8	2.8	181.3	31.8	0.8	188.6	0.2	26.8	6.0	0.8	46.7	
z10SL09-10[e]	46.1	3.7	240.5	39.7	1.1	249.6	0.2	48.4	8.1	0.8	52.0	
z10SL09-11[e]	52.6	4.2	570.9	79.4	0.9	589.2	0.1	128.3	6.7	0.8	48.8	
z10SL09-15[e]	57.8	4.6	183.0	125.7	0.8	211.9	0.7	53.6	13.4	0.8	61.9	
z10SL09-18[e]	37.2	3.0	263.4	47.8	0.7	274.4	0.2	40.9	4.7	0.7	44.0	
z10SL09-20[e]	44.2	3.5	537.3	36.6	0.5	545.7	0.1	95.1	4.3	0.7	41.4	
z10SL09-23[e]	45.7	3.66	112.4	22.7	0.7	117.6	0.20	22.7	8.62	0.78	52.95	
z10SL09-29[e]	33.2	2.7	304.9	63.3	0.5	319.5	0.2	45.5	9.6	0.8	56.5	
z10SL09-30[e]	51.1	4.1	318.4	95.0	2.0	340.3	0.3	74.8	11.6	0.8	56.9	
10SL09	***47.9***	***3.8***	***274.2***	***56.0***	***1.0***	***287.1***	***0.2***	***57.0***	***7.6***	***0.8***	***50.7***	***10.4***
z10SL11-1	36.4	2.9	170.0	24.3	0.5	175.6	0.1	27.2	9.1	0.8	54.4	
z10SL11-2	60.6	4.8	334.2	80.1	1.7	352.6	0.2	89.1	7.0	0.8	50.4	
z10SL11-3	34.8	2.8	161.4	34.7	0.6	169.4	0.2	25.4	10.8	0.8	56.9	
z10SL11-5	47.8	3.8	568.1	79.0	0.9	586.3	0.1	112.4	4.1	0.7	43.9	
10SL11	***44.9***	***3.6***	***308.4***	***54.5***	***0.9***	***321.0***	***0.2***	***63.5***	***7.7***	***0.8***	***51.4***	***12.0***
z09EN01-1	31.7	1.9	122.7	32.4	0.5	130.1	0.3	15.7	2.9	0.7	38.4	
z09EN01-2	33.4	2.0	156.4	73.9	0.5	173.4	0.5	21.0	2.8	0.7	34.3	
z09EN01-3	30.3	1.8	320.6	65.0	0.6	335.5	0.2	42.2	5.8	0.8	49.9	
09EN01	***31.8***	***1.9***	***199.9***	***57.1***	***0.5***	***213.0***	***0.3***	***26.3***	***3.8***	***0.7***	***40.9***	***1.5***
Grosina nappe												
z08IGT01-1	49.4	3.9	583.3	124.8	1.0	612.0	0.2	126.4	6.8	0.8	51.0	
z08IGT01-2	52.7	4.2	289.4	71.9	0.7	306.0	0.2	63.6	4.3	0.7	42.0	
z08IGT01-3	54.4	4.4	561.3	110.3	2.0	586.7	0.2	135.1	8.1	0.8	53.2	
08IGT01	***52.2***	***4.2***	***478.0***	***102.3***	***1.2***	***501.6***	***0.2***	***108.4***	***6.4***	***0.8***	***48.8***	***2.6***
z08IGT02-1	41.0	3.3	464.3	120.9	1.5	492.1	0.3	76.9	2.4	0.7	38.3	
z08IGT02-2	48.1	3.8	311.7	40.2	1.0	321.0	0.1	61.3	3.8	0.7	42.6	
z08IGT02-3	54.5	4.4	142.9	28.5	1.4	149.4	0.2	32.2	3.2	0.7	42.1	
z08IGT02-4	42.5	3.4	158.0	27.4	0.5	164.3	0.2	31.7	18.2	0.8	73.2	
z08IGT02-5	46.8	3.7	870.6	37.2	0.9	879.1	0.0	168.0	5.3	0.8	46.1	
08IGT02	***46.6***	***3.7***	***389.5***	***50.8***	***1.1***	***401.2***	***0.2***	***74.0***	***6.6***	***0.8***	***48.5***	***5.3***
z10IGT01-1	31.2	1.9	1337.2	124.5	1.4	1365.8	0.1	169.5	4.8	0.7	43.0	
z10IGT01-2	29.6	1.8	1187.8	89.3	25.2	1208.4	0.1	135.3	2.4	0.7	37.2	
10IGT01	***30.4***	***1.8***	***1262.5***	***106.9***	***13.3***	***1287.1***	***0.1***	***152.4***	***3.6***	***0.7***	***40.1***	***1.1***
z10IGT02-1	30.3	1.8	126.2	60.8	1.3	140.2	0.5	16.5	4.0	0.7	40.8	
z10IGT02-2	47.6	2.9	237.6	96.4	0.5	259.8	0.4	47.3	3.4	0.7	38.8	
z10IGT02-3	35.6	2.1	105.6	32.5	0.3	113.1	0.3	16.0	4.6	0.7	43.3	
10IGT02	***37.8***	***2.3***	***156.5***	***63.2***	***0.7***	***171.0***	***0.4***	***26.6***	***4.0***	***0.7***	***41.0***	***8.9***
Campo nappe												
z08IGT04-1	36.3	2.9	118.1	57.0	1.2	131.2	0.5	19.0	5.6	0.7	44.4	
z08IGT04-2	32.6	2.6	165.9	10.2	0.7	168.2	0.1	21.3	4.2	0.7	40.0	
z08IGT04-3	43.7	3.5	389.2	56.3	0.9	402.2	0.1	72.6	6.4	0.8	48.7	
z08IGT04-4	31.7	2.5	130.0	35.2	1.0	138.1	0.3	17.0	3.6	0.7	40.3	
z08IGT04-5	33.9	2.7	255.4	47.6	0.5	266.3	0.2	32.8	2.4	0.7	33.8	
08IGT04	***35.6***	***2.9***	***211.7***	***41.2***	***0.8***	***221.2***	***0.2***	***32.5***	***4.5***	***0.7***	***41.4***	***4.8***
z10IGT03-1	34.6	2.1	162.2	93.6	1.6	183.8	0.6	25.4	3.7	0.7	44.1	
z10IGT03-2	36.1	2.2	103.2	55.1	3.0	115.9	0.5	17.0	4.5	0.8	47.2	
z10IGT03-3	29.7	1.8	141.1	51.5	0.7	152.9	0.4	18.5	4.4	0.8	46.5	
z10IGT03-4	44.5	3.6	306.3	40.6	2.9	315.6	0.1	55.4	4.3	0.7	41.8	
z10IGT03-5	44.1	3.5	268.2	48.2	1.0	279.3	0.2	48.2	4.1	0.7	41.0	
10IGT03	***37.8***	***2.6***	***196.2***	***57.8***	***1.8***	***209.5***	***0.4***	***32.9***	***4.2***	***0.7***	***44.1***	***6.4***
z10IGT04-1	34.8	2.8	166.7	46.7	0.9	177.5	0.3	26.5	10.3	0.8	56.8	

A. Table of Replicate Zircon (U-Th)/He Analyses, cont.

Sample[a]	Age (Ma)	Std. Error (±2σ, Ma)[b]	U (ppm)	Th (ppm)	Sm (ppm)	$[U]_e$ (ppm)[c]	Th/U	He (nmol/g)	Mass (µg)	Ft	ESR (µm)	Std. Dev. (±1σ, Ma)[d]
Campo nappe, cont.												
z10IGT04-2	26.7	2.1	197.6	25.6	0.4	203.5	0.1	22.3	5.7	0.8	47.7	
z10IGT04-3	38.3	3.1	202.0	148.7	0.8	236.2	0.7	35.3	4.3	0.7	41.5	
10IGT04	***33.3***	***2.7***	***188.8***	***73.7***	***0.7***	***205.7***	***0.4***	***28.0***	***6.8***	***0.8***	***48.7***	***6.0***
Bernina nappe												
z08BP01-1	30.4	2.4	260.2	36.5	0.2	268.6	0.1	34.8	7.6	0.8	54.6	
z08BP01-2	35.5	2.8	342.6	75.0	1.0	359.8	0.2	52.8	5.8	0.8	48.9	
z08BP01-3	31.6	2.5	194.2	34.7	0.4	202.2	0.2	26.9	6.2	0.8	52.1	
08BP01	***32.5***	***2.6***	***265.7***	***48.7***	***0.5***	***276.9***	***0.2***	***38.1***	***6.6***	***0.8***	***51.8***	***2.7***
z08BP03-1	33.4	2.7	165.8	34.8	0.5	173.8	0.2	25.3	10.1	0.8	60.6	
z08BP03-2	30.0	2.4	280.0	27.4	0.6	286.3	0.1	34.9	5.1	0.8	46.3	
z08BP03-3	45.7	3.7	181.1	67.3	0.7	196.5	0.4	36.2	4.1	0.7	45.3	
z08BP03-4	30.0	2.4	371.9	53.5	0.9	384.2	0.1	44.1	3.3	0.7	38.5	
08BP03	***34.8***	***2.8***	***249.7***	***45.7***	***0.7***	***260.2***	***0.2***	***35.2***	***5.7***	***0.8***	***47.7***	***7.5***
z08BP04-1[f]	88.6	7.1	71.3	26.5	1.3	77.4	0.4	29.7	9.0	0.8	58.6	
z08BP04-2	30.1	2.4	165.3	65.9	0.3	180.5	0.4	24.4	16.2	0.8	70.4	
z08BP04-3	34.8	2.8	82.4	15.8	1.0	86.0	0.2	13.9	25.5	0.9	84.2	
z08BP04-4	35.4	2.8	164.6	24.6	0.7	170.2	0.1	28.4	34.7	0.9	93.1	
08BP04	***33.4***	***2.7***	***137.4***	***35.5***	***0.7***	***145.6***	***0.2***	***22.2***	***25.4***	***0.9***	***82.6***	***2.9***
z08BP05-1	36.2	2.9	141.2	32.2	0.6	148.6	0.2	22.0	6.1	0.8	47.4	
z08BP05-2	35.2	2.8	164.9	33.5	0.5	172.6	0.2	25.7	9.1	0.8	53.2	
z08BP05-3	37.6	3.0	205.3	59.1	1.1	218.9	0.3	34.1	6.9	0.8	49.6	
08BP05	***36.3***	***2.9***	***170.5***	***41.6***	***0.7***	***180.0***	***0.2***	***27.3***	***7.4***	***0.8***	***50.1***	***1.2***
z08BP06-1	34.3	2.7	517.5	156.7	0.7	553.6	0.3	77.4	6.3	0.8	46.8	
z08BP06-2	40.8	3.3	520.0	179.3	1.9	561.3	0.3	92.5	5.3	0.7	45.7	
z08BP06-3	39.3	3.1	407.5	144.0	1.1	440.6	0.4	69.6	5.3	0.7	44.7	
z08BP06-4	41.4	3.3	514.0	241.9	1.2	569.7	0.5	104.1	14.4	0.8	64.5	
z08BP06-5	42.1	3.4	408.8	107.0	0.4	433.4	0.3	79.3	13.6	0.8	59.4	
z08BP06-6	40.3	3.2	333.4	111.8	0.6	359.1	0.3	63.1	11.7	0.8	60.7	
08BP06	***39.7***	***3.2***	***450.2***	***156.8***	***1.0***	***486.3***	***0.3***	***81.0***	***9.5***	***0.8***	***53.7***	***2.8***
z08BP09-1	35.2	2.8	264.1	28.1	0.3	270.5	0.1	37.8	5.3	0.7	42.6	
z08BP09-2	35.2	2.8	186.6	48.7	0.9	197.8	0.3	28.2	6.3	0.8	46.0	
z08BP09-3	34.7	2.8	180.3	50.9	0.4	192.1	0.3	26.1	4.4	0.7	41.5	
08BP09	***35.0***	***2.8***	***210.3***	***42.6***	***0.6***	***220.1***	***0.2***	***30.7***	***5.3***	***0.7***	***43.4***	***0.3***
z08BP10-1	34.4	2.8	118.4	28.2	0.2	124.9	0.2	19.1	12.6	0.8	65.9	
z08BP10-2	34.4	2.7	124.2	32.1	0.3	131.6	0.3	19.0	6.0	0.8	52.2	
z08BP10-3	32.9	2.6	129.5	40.6	0.2	138.8	0.3	19.0	5.9	0.8	50.4	
08BP10	***33.9***	***2.7***	***124.0***	***33.6***	***0.2***	***131.7***	***0.3***	***19.0***	***8.2***	***0.8***	***56.2***	***0.9***
z08BP11-1	34.0	2.7	276.6	70.5	1.0	292.9	0.3	41.0	6.3	0.8	48.4	
z08BP11-2	32.0	2.6	285.7	54.1	1.1	298.2	0.2	36.6	3.4	0.7	38.9	
z08BP11-3	41.1	3.3	220.8	39.8	0.6	230.0	0.2	40.8	10.2	0.8	57.6	
z08BP11-4	36.7	2.9	256.7	50.4	0.5	268.3	0.2	39.7	4.1	0.7	44.9	
08BP11	***36.0***	***2.9***	***260.0***	***53.7***	***0.8***	***272.3***	***0.2***	***39.5***	***6.0***	***0.8***	***47.5***	***3.9***
z08BP12-1	35.7	2.9	224.0	73.5	0.6	241.0	0.3	38.5	13.9	0.8	68.6	
z08BP12-2	34.4	2.8	277.7	49.6	0.7	289.1	0.2	40.9	5.4	0.8	48.0	
z08BP12-3	34.5	2.8	293.6	42.2	0.6	303.3	0.1	44.0	6.5	0.8	51.6	
08BP12	***34.9***	***2.8***	***265.1***	***55.1***	***0.6***	***277.8***	***0.2***	***41.1***	***8.6***	***0.8***	***56.1***	***0.7***
Julier nappe												
z08FA17-1	33.3	2.7	390.4	132.5	0.9	420.9	0.3	60.7	11.2	0.8	59.4	
z08FA17-2	38.4	3.1	372.2	161.0	0.9	409.3	0.4	65.5	5.9	0.8	50.8	
z08FA17-3	38.2	3.1	297.3	101.0	1.3	320.6	0.3	50.4	5.0	0.8	48.2	
z08FA17-4	38.0	3.0	191.3	66.2	0.6	206.6	0.3	31.5	5.1	0.7	44.5	
z08FA17-5	41.1	3.3	424.6	141.0	0.8	457.0	0.3	72.5	3.8	0.7	39.8	
08FA17	***37.8***	***3.0***	***335.2***	***120.3***	***0.9***	***362.9***	***0.4***	***56.1***	***6.2***	***0.8***	***48.5***	***2.8***
Err nappe												
z08FA06-2	38.9	3.1	321.2	48.1	0.5	332.3	0.1	55.2	9.1	0.8	55.1	
z08FA06-3	56.6	4.5	308.3	42.5	0.5	318.0	0.1	81.0	18.6	0.8	69.3	
z08FA06-4	43.5	3.5	310.5	53.1	0.5	322.7	0.2	59.1	8.6	0.8	52.4	
z08FA06-5	40.8	3.3	325.4	48.6	0.5	336.6	0.1	56.5	6.0	0.8	47.7	
08FA06	***37.9***	***3.0***	***448.0***	***70.4***	***0.5***	***464.2***	***0.2***	***69.6***	***7.3***	***0.8***	***51.1***	***6.5***
z08FA07-1	33.6	2.7	732.0	113.0	0.4	758.0	0.2	105.4	6.8	0.8	48.9	
z08FA07-2	39.0	3.1	462.0	72.9	0.3	478.8	0.2	77.2	5.5	0.8	49.0	
z08FA07-3	37.1	3.0	251.2	41.7	0.2	260.8	0.2	43.4	15.2	0.8	69.6	

A. Table of Replicate Zircon (U-Th)/He Analyses, cont.

Sample[a]	Age (Ma)	Std. Error (±2σ, Ma)[b]	U (ppm)	Th (ppm)	Sm (ppm)	$[U]_e$ (ppm)[c]	Th/U	He (nmol/g)	Mass (µg)	Ft	ESR (µm)	Std. Dev. (±1σ, Ma)[d]
Err nappe, cont.												
z08FA07-4	31.6	2.5	539.6	72.0	1.0	556.1	0.1	70.0	5.0	0.7	43.0	
z08FA07-5	48.4	3.9	255.4	52.7	0.6	267.5	0.2	52.2	4.1	0.7	44.9	
08FA07	***44.9***	***3.6***	***316.3***	***48.1***	***0.5***	***327.4***	***0.2***	***62.9***	***10.6***	***0.8***	***56.1***	***8.0***
Corvatsch nappe												
z10EN01-1	27.1	2.2	589.5	174.6	1.3	629.7	0.3	76.0	17.0	0.8	67.2	
z10EN01-2	31.4	2.5	454.0	147.4	1.0	488.0	0.3	67.7	14.2	0.8	64.9	
z10EN01-3	31.8	2.5	366.6	122.3	1.0	394.7	0.3	55.3	15.6	0.8	64.3	
10EN01	***30.1***	***2.4***	***470.0***	***148.1***	***1.1***	***504.1***	***0.3***	***66.3***	***15.6***	***0.8***	***65.5***	***2.6***
z10EN02-1	32.9	2.6	405.9	131.9	0.7	436.3	0.3	58.9	5.2	0.8	48.2	
z10EN02-2	29.8	2.4	386.7	106.4	0.9	411.2	0.3	51.2	6.5	0.8	51.3	
z10EN02-3	30.7	2.5	337.7	118.3	6.2	365.0	0.4	47.0	5.9	0.8	52.0	
10EN02	***31.1***	***2.5***	***376.8***	***118.9***	***2.6***	***404.1***	***0.3***	***52.4***	***5.9***	***0.8***	***50.5***	***1.6***
z10EN03-1	29.4	2.3	251.1	82.4	1.1	270.1	0.3	32.5	4.6	0.8	48.0	
z10EN03-2	30.0	2.4	445.8	143.3	0.6	478.8	0.3	58.6	4.5	0.8	47.3	
z10EN03-3	29.2	2.3	392.3	136.3	0.9	423.7	0.3	49.9	4.3	0.7	45.4	
10EN03	***29.5***	***2.4***	***363.1***	***120.7***	***0.9***	***390.9***	***0.3***	***47.0***	***4.5***	***0.8***	***46.9***	***0.4***
z10EN04-1	27.3	2.2	381.2	307.1	0.8	451.9	0.8	49.3	3.7	0.7	44.9	
z10EN04-2	32.8	2.6	480.6	164.2	1.4	518.4	0.3	68.0	3.6	0.7	44.2	
z10EN04-3	29.7	2.4	342.0	140.7	1.1	374.4	0.4	43.9	3.2	0.7	42.6	
10EN04	***29.9***	***2.4***	***401.3***	***204.0***	***1.1***	***448.2***	***0.5***	***53.7***	***3.5***	***0.7***	***43.9***	***2.8***
z10EN05-1[f]	60.3	4.8	311.7	146.8	1.0	345.5	0.5	81.6	3.5	0.7	41.5	
z10EN05-2	29.8	2.4	464.6	144.2	1.2	497.8	0.3	59.3	3.9	0.7	44.0	
z10EN05-3	36.0	2.9	256.6	111.6	1.5	282.3	0.4	43.2	7.2	0.8	55.2	
z10EN05-4	36.9	3.0	333.8	151.2	1.0	368.6	0.5	55.5	6.4	0.8	47.3	
z10EN05-5	32.9	2.6	424.7	125.6	0.8	453.6	0.3	60.8	6.2	0.8	46.7	
10EN05	***33.9***	***2.7***	***369.9***	***133.1***	***1.1***	***400.6***	***0.4***	***54.7***	***5.9***	***0.8***	***48.3***	***3.2***
z10EN06-1	38.3	3.1	284.1	124.7	0.7	312.8	0.4	48.3	4.1	0.7	45.5	
z10EN06-2	31.4	2.5	527.3	190.7	1.0	571.2	0.4	68.2	2.3	0.7	38.5	
z10EN06-3	34.5	2.8	266.7	128.7	2.0	296.3	0.5	41.9	4.5	0.8	48.0	
z10EN06-4	41.7	3.3	264.0	99.8	0.9	287.0	0.4	53.0	12.6	0.8	65.4	
10EN06	***36.5***	***2.9***	***335.5***	***136.0***	***1.2***	***366.8***	***0.4***	***52.9***	***5.9***	***0.8***	***49.4***	***4.5***
z10EN07-1	30.1	2.4	388.8	121.5	0.5	416.8	0.3	52.6	5.4	0.8	51.8	
z10EN07-2	30.3	2.4	511.0	158.4	0.7	547.4	0.3	65.8	3.6	0.7	43.1	
z10EN07-3	30.9	2.5	265.7	95.4	0.9	287.7	0.4	35.2	3.4	0.7	43.0	
10EN07	***30.4***	***2.4***	***388.5***	***125.1***	***0.7***	***417.3***	***0.3***	***51.2***	***4.1***	***0.7***	***46.0***	***0.4***
z10EN08-1	21.2	1.3	343.3	352.3	0.7	424.4	1.0	39.2	10.0	0.8	61.4	
z10EN08-2	33.6	2.0	268.0	325.8	0.9	343.0	1.2	47.5	5.6	0.8	49.6	
z10EN08-3	27.1	1.6	631.3	132.3	0.4	661.7	0.2	68.4	3.4	0.7	38.5	
z10EN08-4	30.7	2.5	564.4	227.1	0.9	616.6	0.4	75.0	4.3	0.7	43.3	
z10EN08-5	23.7	1.9	674.5	514.6	1.7	793.0	0.8	80.7	10.8	0.8	58.2	
10EN08	***27.2***	***1.9***	***496.3***	***310.4***	***0.9***	***567.7***	***0.7***	***62.2***	***6.8***	***0.8***	***50.2***	***5.0***
Engadine Window (Penninic nappes)												
z08TS04-1	21.0	1.7	120.2	59.4	0.0	133.9	0.5	11.4	4.5	0.7	46.6	
z08TS04-2	27.9	2.2	174.1	10.0	0.0	176.4	0.1	21.2	8.7	0.8	57.2	
z08TS04-4	30.8	2.5	220.4	26.2	0.3	226.4	0.1	28.7	5.8	0.8	48.1	
z08TS04-5	32.2	2.6	216.6	19.1	0.3	221.0	0.1	29.0	5.4	0.8	46.3	
08TS04	***28.0***	***2.2***	***182.8***	***28.7***	***0.2***	***189.4***	***0.2***	***22.6***	***6.1***	***0.8***	***49.5***	***5.0***
z08TS05-1	24.2	1.9	317.3	24.1	0.0	322.9	0.1	31.0	3.0	0.7	42.5	
z08TS05-2	28.2	2.3	166.9	29.4	0.0	173.7	0.2	20.8	6.5	0.8	54.6	
z08TS05-3	43.4	3.5	332.5	43.9	0.0	342.6	0.1	60.5	4.6	0.8	46.3	
z08TS05-4	31.7	2.5	139.3	22.8	0.4	144.6	0.2	17.9	4.0	0.7	40.6	
z08TS05-5	31.5	2.5	161.4	18.2	0.4	165.5	0.1	21.7	7.0	0.8	49.9	
08TS05	***31.8***	***2.5***	***223.5***	***27.7***	***0.2***	***229.9***	***0.1***	***30.4***	***5.0***	***0.8***	***46.8***	***7.2***
z08TS07-1	36.4	2.9	179.4	92.7	0.0	200.8	0.5	31.0	7.2	0.8	54.7	
z08TS07-2	30.5	2.4	217.1	64.4	0.0	232.0	0.3	29.4	5.8	0.8	50.0	
z08TS07-3	29.6	2.4	233.5	100.1	0.0	256.5	0.4	28.9	2.5	0.7	38.5	
z08TS07-4	35.8	2.9	297.2	52.6	1.0	309.3	0.2	41.6	3.0	0.7	36.8	
08TS07	***33.1***	***2.6***	***231.8***	***77.5***	***0.3***	***249.6***	***0.4***	***32.7***	***4.6***	***0.7***	***45.0***	***3.5***
z08TS08-1	32.3	2.6	204.2	66.3	0.0	219.4	0.3	30.1	8.0	0.8	54.9	
z08TS08-2	29.5	2.4	191.4	79.3	0.0	209.7	0.4	26.0	6.4	0.8	52.6	
z08TS08-3	45.1	3.6	295.6	101.3	0.0	319.0	0.3	59.7	5.8	0.8	49.9	
z08TS08-4	34.8	2.8	211.1	76.8	1.0	228.8	0.4	31.2	4.3	0.7	41.9	
z08TS08-5	35.3	2.8	296.2	100.2	0.8	319.3	0.3	45.1	5.2	0.7	44.3	
08TS08	***35.4***	***2.8***	***239.7***	***84.8***	***0.4***	***259.2***	***0.4***	***38.4***	***5.9***	***0.8***	***48.7***	***5.9***

A. Table of Replicate Zircon (U-Th)/He Analyses, cont.

Sample[a]	Age (Ma)	Std. Error (±2σ, Ma)[b]	U (ppm)	Th (ppm)	Sm (ppm)	$[U]_e$ (ppm)[c]	Th/U	He (nmol/g)	Mass (µg)	Ft	ESR (µm)	Std. Dev. (±1σ, Ma)[d]
Engadine window, cont.												
z08TS09-1	25.6	2.0	272.3	150.6	0.0	307.0	0.6	30.7	3.6	0.7	42.0	
z08TS09-2	36.0	2.9	204.8	95.3	0.0	226.7	0.5	34.4	6.1	0.8	53.3	
z08TS09-3	20.4	1.6	747.8	502.8	0.0	863.6	0.7	70.2	3.5	0.7	44.6	
z08TS09-4	23.9	1.9	286.6	245.8	2.0	343.2	0.9	35.9	11.5	0.8	63.2	
z08TS09-5	21.4	1.7	840.4	394.5	6.7	931.2	0.5	84.1	7.4	0.8	53.8	
z08TS09-6	28.6	2.3	511.4	290.1	2.2	578.2	0.6	64.5	3.6	0.7	41.3	
08TS09	***26.0***	***2.1***	***477.2***	***279.9***	***1.8***	***541.7***	***0.6***	***53.3***	***5.9***	***0.8***	***49.7***	***5.7***
z08TS11-2	25.3	2.0	145.7	22.7	0.0	150.9	0.2	14.9	3.1	0.7	41.0	
z08TS11-3	27.1	2.2	219.9	45.3	0.0	230.4	0.2	23.8	2.3	0.7	38.1	
z08TS11-4	34.0	2.7	173.2	31.0	0.4	180.3	0.2	23.4	2.6	0.7	38.2	
08TS11	***28.8***	***2.3***	***179.6***	***33.0***	***0.1***	***187.2***	***0.2***	***20.7***	***2.7***	***0.7***	***39.1***	***4.6***
z08TS13-1	27.5	2.2	100.7	37.2	0.0	109.2	0.4	11.9	3.9	0.7	43.3	
z08TS13-2	28.0	2.2	351.1	129.9	0.0	381.0	0.4	42.7	4.2	0.7	44.5	
z08TS13-3	31.8	2.5	707.9	40.5	0.0	717.2	0.1	91.3	3.5	0.7	43.7	
08TS13	***29.1***	***2.3***	***386.5***	***69.2***	***0.0***	***402.5***	***0.3***	***48.6***	***3.9***	***0.7***	***43.8***	***2.3***
z08TS14-1	23.9	1.9	77.5	54.6	0.0	90.1	0.7	9.1	6.7	0.8	54.4	
z08TS14-2	25.5	2.0	191.8	69.9	0.0	207.9	0.4	20.8	3.0	0.7	41.7	
z08TS14-3	24.0	1.9	263.8	74.3	0.0	280.9	0.3	24.9	1.7	0.7	35.3	
08TS14	***24.4***	***2.0***	***177.7***	***66.3***	***0.0***	***192.9***	***0.5***	***18.2***	***3.8***	***0.7***	***43.8***	***0.9***
z09EN04-1	29.5	2.4	272.6	26.0	0.2	278.6	0.1	34.6	6.3	0.8	52.0	
z09EN04-2	27.4	2.2	575.4	87.0	1.6	595.4	0.2	64.4	4.0	0.7	41.9	
z09EN04-3	27.4	2.2	204.7	38.4	1.0	213.6	0.2	22.6	3.5	0.7	39.5	
09EN04	***28.1***	***2.2***	***350.9***	***50.5***	***1.0***	***362.6***	***0.1***	***40.5***	***4.6***	***0.7***	***44.5***	***1.2***

[a]For location and elevation data see Table 1

[b]Standard error of 8% (2σ) based on reproducibility of internal lab standards

[c][U]e =[U]+[Th]0.235+[Sm]0.005 (e.g., Shuster et al., 2006)

[d]Standard deviation (1σ) of included replicate analyses

[e] LA-ICP-MS depth profiling also completed on zircon aliquot; see Appendix C for laser ablation depth profiles

[f]An outlier replicate analysis was excluded from mean value calculation and standard deviation

Italics indicate mean values of replicate analyses

B. Table of Replicate Apatite (U-Th)/He Analyses

Sample[a]	Age (Ma)	Std. Error (±2σ, Ma)[b]	U (ppm)	Th (ppm)	Sm (ppm)	$[U]_e$ (ppm)[c]	Th/U	He (nmol/g)	Mass (µg)	Ft	ESR (µm)	Std. Dev. (±1σ, Ma)[d]
Silvretta nappe												
10SL01-1	15.2	0.9	19.8	4.8	33.4	21.0	0.2	1.0	0.9	0.6	33.8	
10SL01-2	18.8	1.1	14.1	9.9	35.5	16.6	0.7	1.0	1.2	0.6	38.2	
10SL01-3	12.9	0.8	21.7	5.4	34.3	23.1	0.2	1.0	1.3	0.6	38.3	
10SL01	***15.6***	***0.9***	***18.5***	***6.7***	***34.4***	***20.2***	***0.4***	***1.0***	***1.1***	***0.6***	***36.8***	***3.0***
10SL02-1	12.9	0.8	16.3	4.6	22.5	17.4	0.3	0.8	1.4	0.6	40.2	
10SL02-2	12.5	0.8	11.1	1.6	20.6	11.5	0.1	0.5	0.8	0.6	33.3	
10SL02-3	17.3	1.0	36.0	15.4	35.7	39.7	0.4	2.7	3.0	0.7	51.8	
10SL02	***14.2***	***0.9***	***21.1***	***7.2***	***26.3***	***22.9***	***0.3***	***1.3***	***1.8***	***0.6***	***41.8***	***2.7***
10SL03-1	15.0	0.9	40.3	8.5	31.8	42.4	0.2	2.3	1.5	0.7	41.4	
10SL03-2	18.0	1.1	47.1	10.9	34.6	49.7	0.2	3.3	2.1	0.7	45.4	
10SL03-3	17.0	1.0	29.7	4.4	28.1	30.9	0.1	2.0	2.5	0.7	47.4	
10SL03	***16.7***	***1.0***	***39.0***	***7.9***	***31.5***	***41.0***	***0.2***	***2.5***	***2.1***	***0.7***	***44.7***	***1.5***
10SL04-1	19.4	1.2	27.0	8.9	42.4	29.3	0.3	1.7	0.7	0.6	32.0	
10SL04-2[e]	91.5	5.5	16.6	3.2	52.3	17.6	0.2	5.2	0.9	0.6	34.1	
10SL04-3[e]	363.3	21.8	12.7	7.4	43.4	14.6	0.6	17.5	1.0	0.6	35.3	
10SL04-4	19.8	1.2	54.4	5.1	34.7	55.7	0.1	3.8	1.4	0.6	39.3	
10SL04-5	15.6	0.9	26.7	3.8	26.3	27.7	0.1	1.5	1.4	0.6	39.6	
10SL04	***18.2***	***1.1***	***36.0***	***6.0***	***34.5***	***37.6***	***0.2***	***2.4***	***1.2***	***0.6***	***37.0***	***2.3***
10SL05-1	15.3	0.9	18.2	2.3	36.6	18.9	0.1	1.1	2.1	0.7	45.7	
10SL05-2[e]	235.7	14.1	36.7	4.0	35.8	37.8	0.1	33.4	2.2	0.7	44.6	
10SL05-3	14.3	0.9	17.0	11.9	29.1	19.9	0.7	1.0	2.2	0.7	45.6	
10SL05	***14.8***	***0.9***	***17.6***	***7.1***	***32.9***	***19.4***	***0.4***	***1.1***	***2.1***	***0.7***	***45.6***	***0.7***
10SL06-1	17.2	1.0	14.3	1.6	32.0	14.8	0.1	0.9	1.8	0.7	43.6	
10SL06-2	14.2	0.9	13.7	2.1	38.6	14.4	0.2	0.7	1.3	0.6	38.4	
10SL06-3	18.2	1.1	21.6	2.9	46.7	22.5	0.1	1.5	1.6	0.7	41.9	
10SL06	***16.5***	***1.0***	***16.5***	***2.2***	***39.1***	***17.2***	***0.1***	***1.0***	***1.6***	***0.7***	***41.3***	***2.1***
10SL07-1	12.0	0.7	8.3	11.9	25.1	11.2	1.4	0.5	2.4	0.7	47.8	
10SL07-2	11.3	0.7	8.4	9.4	24.7	10.7	1.1	0.5	3.7	0.7	55.2	
10SL07-3	18.0	1.1	10.3	2.2	25.2	10.9	0.2	0.8	3.1	0.7	50.9	
10SL07-4	8.2	0.5	8.6	17.3	19.0	12.6	2.0	0.4	1.7	0.6	41.0	
10SL07-5	14.9	0.9	8.4	1.3	28.4	8.9	0.2	0.5	1.7	0.7	42.7	
10SL07-6	14.2	0.8	10.8	2.7	26.0	11.5	0.2	0.5	0.9	0.6	34.0	
10SL07	***13.1***	***0.8***	***9.1***	***7.4***	***24.7***	***11.0***	***0.9***	***0.5***	***2.2***	***0.7***	***45.3***	***3.4***
10SL08-1	19.7	1.2	11.6	2.6	26.8	12.3	0.2	1.0	3.3	0.7	53.4	
10SL08-2	17.0	1.0	27.8	2.7	36.9	28.6	0.1	1.6	1.2	0.6	37.0	
10SL08-3	15.6	0.9	24.9	1.4	19.9	25.3	0.1	1.4	1.7	0.7	42.4	
10SL08	***17.4***	***1.0***	***21.4***	***2.2***	***27.9***	***22.1***	***0.1***	***1.3***	***2.1***	***0.7***	***44.3***	***2.1***
10SL09-1	19.0	1.1	16.4	1.6	28.9	16.9	0.1	1.2	1.7	0.7	42.1	
10SL09-2	19.8	1.2	10.8	1.3	40.8	11.3	0.1	0.8	1.5	0.7	40.9	
10SL09-3[e]	46.0	2.8	36.7	10.8	40.9	39.4	0.3	6.3	1.3	0.6	39.3	
10SL09	***19.4***	***1.2***	***13.6***	***1.5***	***34.8***	***14.1***	***0.1***	***1.0***	***1.6***	***0.7***	***41.5***	***0.6***
Bernina nappe												
08BP01-1	28.7	1.7	28.8	6.3	48.0	30.5	0.2	3.4	3.1	0.7	52.4	
08BP01-2	29.6	1.8	20.8	7.5	60.8	22.9	0.4	2.6	2.7	0.7	49.5	
08BP01-3	22.0	1.3	26.5	5.9	49.4	28.1	0.2	2.4	2.9	0.7	50.8	
08BP01	***26.8***	***1.6***	***25.4***	***6.5***	***52.7***	***27.2***	***0.3***	***2.8***	***2.9***	***0.7***	***50.9***	***4.1***

B. Table of Replicate Apatite (U-Th)/He Analyses, cont.

Sample[a]	Age (Ma)	Std. Error (±2σ, Ma)[b]	U (ppm)	Th (ppm)	Sm (ppm)	$[U]_e$ (ppm)[c]	Th/U	He (nmol/g)	Mass (µg)	Ft	ESR (µm)	Std. Dev. (±1σ, Ma)[d]
Bernina nappe cont.												
08BP03-1	30.6	1.8	9.8	6.2	25.9	11.3	0.6	1.3	2.2	0.7	46.1	
08BP03-2	16.8	1.0	6.4	1.9	11.8	6.9	0.3	0.4	0.8	0.6	32.8	
08BP03-3	20.2	1.2	4.5	1.9	15.5	5.0	0.4	0.3	1.0	0.6	35.3	
08BP03	***22.5***	***1.4***	***6.9***	***3.3***	***17.7***	***7.7***	***0.4***	***0.7***	***1.3***	***0.6***	***38.1***	***7.2***
08BP06-1	19.0	1.1	36.1	42.2	52.9	46.0	1.2	2.8	1.0	0.6	35.3	
08BP06-2	16.5	1.0	86.2	60.5	51.7	100.4	0.7	5.4	1.3	0.6	36.1	
08BP06-3	15.2	0.9	80.9	48.1	37.7	92.1	0.6	4.6	1.1	0.6	36.2	
08BP06	***16.9***	***1.0***	***67.7***	***50.3***	***47.4***	***79.5***	***0.8***	***4.3***	***1.1***	***0.6***	***35.9***	***1.9***
08BP10-1[e]	55.6	3.3	16.8	4.8	23.2	18.0	0.3	3.5	1.4	0.6	39.8	
08BP10-2	26.2	1.6	15.3	2.4	18.8	16.0	0.2	1.3	0.9	0.6	33.4	
08BP10-3	26.0	1.6	39.5	13.7	34.5	42.8	0.3	3.5	0.9	0.6	33.0	
08BP10	***26.1***	***1.6***	***27.4***	***8.1***	***26.6***	***29.4***	***0.3***	***2.4***	***0.9***	***0.6***	***33.2***	***0.1***
08BP11-1	21.2	1.3	6.6	5.4	16.1	7.9	0.8	0.5	1.1	0.6	36.5	
08BP11-2	32.4	1.9	4.3	5.3	13.6	5.6	1.2	0.6	1.1	0.6	36.0	
08BP11-3	25.8	1.5	4.8	13.1	17.2	7.9	2.7	0.7	1.3	0.6	38.1	
08BP11	***26.5***	***1.6***	***5.2***	***7.9***	***15.7***	***7.1***	***1.6***	***0.6***	***1.1***	***0.6***	***36.9***	***5.6***
Err nappe												
08ED01-1	30.4	1.8	12.3	23.8	82.4	18.2	1.9	1.7	0.9	0.6	34.0	
08ED01-2	20.6	1.2	41.5	24.7	85.9	47.6	0.6	2.8	0.6	0.5	30.0	
08ED01-3	20.3	1.2	103.6	15.9	88.2	107.7	0.2	7.9	1.7	0.7	42.5	
08ED01	***23.8***	***1.4***	***52.5***	***21.4***	***85.5***	***57.8***	***0.9***	***4.1***	***1.1***	***0.6***	***35.5***	***5.8***
08ED04-1	27.2	1.6	41.1	3.0	52.7	42.1	0.1	4.4	2.4	0.7	48.1	
08ED04-2	23.7	1.4	48.7	7.3	96.1	50.9	0.1	4.5	2.2	0.7	46.3	
08ED04-3	22.2	1.3	22.7	1.8	58.6	23.4	0.1	1.9	1.7	0.7	41.8	
08ED04	***24.4***	***1.5***	***37.5***	***4.0***	***69.2***	***38.8***	***0.1***	***3.6***	***2.1***	***0.7***	***45.4***	***2.5***
08ED06-1	20.3	1.2	26.3	2.4	50.6	27.1	0.1	1.9	1.3	0.6	39.2	
08ED06-2	22.6	1.4	71.6	11.0	80.3	74.5	0.2	6.1	1.9	0.7	42.3	
08ED06-3	21.1	1.3	171.2	33.1	114.2	179.3	0.2	12.7	1.2	0.6	36.9	
08ED06	***21.3***	***1.3***	***89.7***	***15.5***	***81.7***	***93.7***	***0.1***	***6.9***	***1.5***	***0.6***	***39.5***	***1.2***
10ED01-1	16.1	1.0	43.7	6.2	31.7	45.3	0.1	2.1	0.5	0.5	28.8	
10ED01-2	17.0	1.0	35.1	4.6	23.5	36.3	0.1	2.1	1.1	0.6	36.3	
10ED01-3	15.2	0.9	43.5	6.3	27.7	45.1	0.1	2.1	0.7	0.6	31.2	
10ED01	***16.1***	***1.0***	***40.8***	***5.7***	***27.7***	***42.2***	***0.1***	***2.1***	***0.8***	***0.6***	***32.1***	***0.9***
10ED03-1	26.0	1.6	50.4	42.2	107.0	60.6	0.8	5.9	2.4	0.7	47.3	
10ED03-2	19.4	1.2	33.9	2.7	93.8	35.0	0.1	2.4	1.5	0.7	40.1	
10ED03-3	22.7	1.4	82.2	48.8	115.5	94.0	0.6	7.4	1.5	0.6	40.3	
10ED03	***22.7***	***1.4***	***55.5***	***31.2***	***105.4***	***63.2***	***0.5***	***5.2***	***1.8***	***0.7***	***42.6***	***3.3***
10ED04-1	31.0	1.9	23.9	1.8	51.3	24.6	0.1	3.2	6.6	0.8	64.2	
10ED04-2	24.9	1.5	123.7	27.9	119.2	130.7	0.2	11.0	1.3	0.6	37.2	
10ED04-3	22.9	1.4	104.3	19.5	88.2	109.2	0.2	8.5	1.2	0.6	37.5	
10ED04	***26.2***	***1.6***	***84.0***	***16.4***	***86.2***	***88.2***	***0.2***	***7.5***	***3.0***	***0.7***	***46.3***	***4.2***
10ED05-1	25.2	1.5	75.2	1.7	52.5	75.9	0.0	6.7	1.4	0.6	39.3	
10ED05-2	25.7	1.5	120.0	2.2	66.7	120.8	0.0	12.1	3.0	0.7	51.2	
10ED05-3	22.9	1.4	79.0	2.1	62.9	79.8	0.0	6.5	1.6	0.7	41.3	
10ED05	***24.6***	***1.5***	***91.4***	***2.0***	***60.7***	***92.2***	***0.0***	***8.5***	***2.0***	***0.7***	***44.0***	***1.5***
08PN03-1	22.5	1.4	16.6	20.0	53.2	21.5	1.2	1.6	1.1	0.6	35.7	
08PN03-2	29.2	1.7	17.9	20.0	82.2	22.9	1.1	2.5	2.6	0.7	47.5	
08PN03-3	21.9	1.3	20.2	20.6	67.5	25.2	1.0	1.8	1.2	0.6	36.0	

B. Table of Replicate Apatite (U-Th)/He Analyses, cont.

Sample[a]	Age (Ma)	Std. Error (±2σ, Ma)[b]	U (ppm)	Th (ppm)	Sm (ppm)	$[U]_e$ (ppm)[c]	Th/U	He (nmol/g)	Mass (µg)	Ft	ESR (µm)	Std. Dev. (±1σ, Ma)[d]
Err nappe cont.												
08PN03	***24.5***	***1.5***	***18.2***	***20.2***	***67.6***	***23.2***	***1.1***	***2.0***	***1.6***	***0.6***	***39.7***	***4.0***
08PN04-1	35.2	2.1	20.4	21.2	73.8	25.7	1.0	3.2	1.9	0.6	41.3	
08PN04-2	23.9	1.4	8.0	8.6	72.3	10.3	1.1	0.9	1.8	0.7	43.5	
08PN04-3	24.8	1.5	13.4	14.8	44.9	17.0	1.1	1.5	2.0	0.7	45.0	
08PN04	***28.0***	***1.7***	***13.9***	***14.9***	***63.7***	***17.7***	***1.1***	***1.9***	***1.9***	***0.7***	***43.3***	***6.3***
08PN05-1	22.0	1.3	19.2	18.9	72.9	23.9	1.0	1.8	1.3	0.6	38.0	
08PN05-2	23.2	1.4	20.6	19.5	65.3	25.4	0.9	1.9	1.3	0.6	36.9	
08PN05-3	20.2	1.2	19.6	19.1	62.0	24.3	1.0	1.6	1.0	0.6	35.9	
08PN05	***21.8***	***1.3***	***19.8***	***19.2***	***66.7***	***24.5***	***1.0***	***1.8***	***1.2***	***0.6***	***36.9***	***1.5***
Corvatsch nappe												
10EN01-1	25.6	1.5	27.5	13.7	43.4	30.9	0.5	2.7	1.8	0.6	39.6	
10EN01-2	17.1	1.0	26.3	19.1	42.4	30.9	0.7	2.0	2.9	0.7	48.8	
10EN01-3	18.8	1.1	11.3	5.0	45.2	12.7	0.4	0.9	1.8	0.7	41.5	
10EN01	***20.5***	***1.2***	***21.7***	***12.6***	***43.7***	***24.8***	***0.6***	***1.9***	***2.2***	***0.7***	***43.3***	***4.5***
10EN03-1	24.6	1.5	20.2	40.1	101.8	30.0	2.0	2.3	1.1	0.6	34.7	
10EN03-2	21.7	1.3	17.5	29.9	113.6	24.9	1.7	1.6	0.8	0.5	31.8	
10EN03-3[e]	401.2	24.1	13.2	33.7	71.1	21.3	2.6	25.0	0.7	0.5	30.6	
10EN03	***23.2***	***1.4***	***18.9***	***35.0***	***107.7***	***27.5***	***1.8***	***2.0***	***1.0***	***0.6***	***33.3***	***2.1***
10EN04-1	25.3	1.5	25.3	38.4	102.9	34.6	1.5	2.8	1.0	0.6	34.9	
10EN04-2	21.8	1.3	10.8	16.9	62.5	15.0	1.6	1.1	1.3	0.6	39.0	
10EN04-3	40.6	2.4	7.9	13.7	64.4	11.4	1.7	1.7	1.9	0.6	43.0	
10EN04	***23.5***	***1.4***	***18.1***	***27.6***	***82.7***	***24.8***	***1.5***	***1.9***	***1.1***	***0.6***	***37.0***	***2.5***
10EN08-1	16.7	1.0	25.3	12.8	35.4	28.4	0.5	1.5	1.0	0.6	35.4	
10EN08-2	21.3	1.3	39.7	23.9	42.6	45.4	0.6	3.5	1.8	0.7	43.0	
10EN08-3	19.0	1.1	47.4	44.8	74.0	58.1	0.9	3.4	0.8	0.6	33.2	
10EN08	***19.0***	***1.1***	***37.5***	***27.1***	***50.7***	***44.0***	***0.7***	***2.8***	***1.2***	***0.6***	***37.2***	***2.3***
Engadine window (Penninic nappes)												
08TS04-1	11.3	0.7	8.0	1.0	21.2	8.4	0.1	0.4	2.6	0.7	49.1	
08TS04-2	25.5	1.5	8.7	1.1	43.4	9.2	0.1	0.9	2.5	0.7	47.7	
08TS04-3	10.6	0.6	6.8	0.5	21.5	7.0	0.1	0.3	2.4	0.7	45.5	
08TS04	***15.8***	***0.9***	***7.9***	***0.9***	***28.7***	***8.2***	***0.1***	***0.5***	***2.5***	***0.7***	***47.4***	***8.4***
08TS05-1	9.9	0.6	13.4	2.1	20.6	14.0	0.2	0.5	1.5	0.7	40.5	
08TS05-2	14.5	0.9	9.0	2.2	14.5	9.5	0.2	0.5	1.6	0.6	40.6	
08TS05-3	5.7	0.3	11.2	1.2	9.4	11.5	0.1	0.3	3.1	0.7	52.0	
08TS05	***10.0***	***0.6***	***11.2***	***1.8***	***14.8***	***11.7***	***0.2***	***0.4***	***2.1***	***0.7***	***44.4***	***4.4***
08TS08-1	5.5	0.3	22.6	27.2	99.0	29.4	1.2	0.5	0.9	0.6	33.7	
08TS08-2	9.5	0.6	20.4	37.2	119.5	29.5	1.8	0.9	1.0	0.6	34.8	
08TS08-3	6.4	0.4	16.6	28.0	93.4	23.5	1.7	0.5	1.2	0.6	36.1	
08TS08	***7.1***	***0.4***	***19.9***	***30.8***	***104.0***	***27.5***	***1.6***	***0.6***	***1.0***	***0.6***	***34.9***	***2.1***
08TS09-1	10.6	0.6	19.0	77.8	131.5	37.5	4.1	1.2	0.9	0.5	32.9	
08TS09-2	11.9	0.7	36.1	71.5	166.9	53.4	2.0	1.8	0.6	0.5	30.4	
08TS09-3	22.8	1.4	11.6	21.9	58.7	17.0	1.9	1.3	1.2	0.6	37.6	
08TS09	***15.1***	***0.9***	***22.2***	***57.1***	***119.0***	***36.0***	***2.7***	***1.4***	***0.9***	***0.6***	***33.6***	***6.7***
08TS11-1	6.4	0.4	4.7	0.2	4.4	4.7	0.0	0.1	2.9	0.7	49.6	
08TS11-2	7.8	0.5	16.6	2.1	7.6	17.1	0.1	0.5	1.5	0.6	39.8	
08TS11-3	10.2	0.6	28.8	3.5	8.8	29.7	0.1	1.0	1.0	0.6	35.4	
08TS11	***8.1***	***0.5***	***16.7***	***1.9***	***6.9***	***17.2***	***0.1***	***0.5***	***1.8***	***0.7***	***41.6***	***1.9***

[a]For location and elevation data see Table 2

[b]Standard error of 8% (2σ) based on reproducibility of internal lab standards

[c][U]e =[U]+[Th]0.235+[Sm]0.005 (e.g., Shuster et al., 2006)

[d]Standard deviation (1σ) of included replicate analyses

[e]An outlier replicate analysis was excluded from mean value calculation and standard deviation in Table 2

Italics indicate mean values of replicate analyses

Appendix B: Laser ablation depth-profiling

Laser ablation depth-profiling of 76 zircon grains from three samples from the Silvretta nappe (10SL03, 05, 09) was completed to determine parent isotope concentration (U and Th). All LA-ICP-MS depth profiling was completed at the University of Kansas in the Isotope Geochemistry Laboratory using a Photon Machines 193 nm Excimer Laser for sample ablation and a Thermo Element 2 ICP-MS for isotope measurements. All LA-ICP-MS depth profiles completed, except those displayed within Figure 9, are included within this appendix. See text for discussion of concentration calculations, and down-hole intensity decrease corrections.

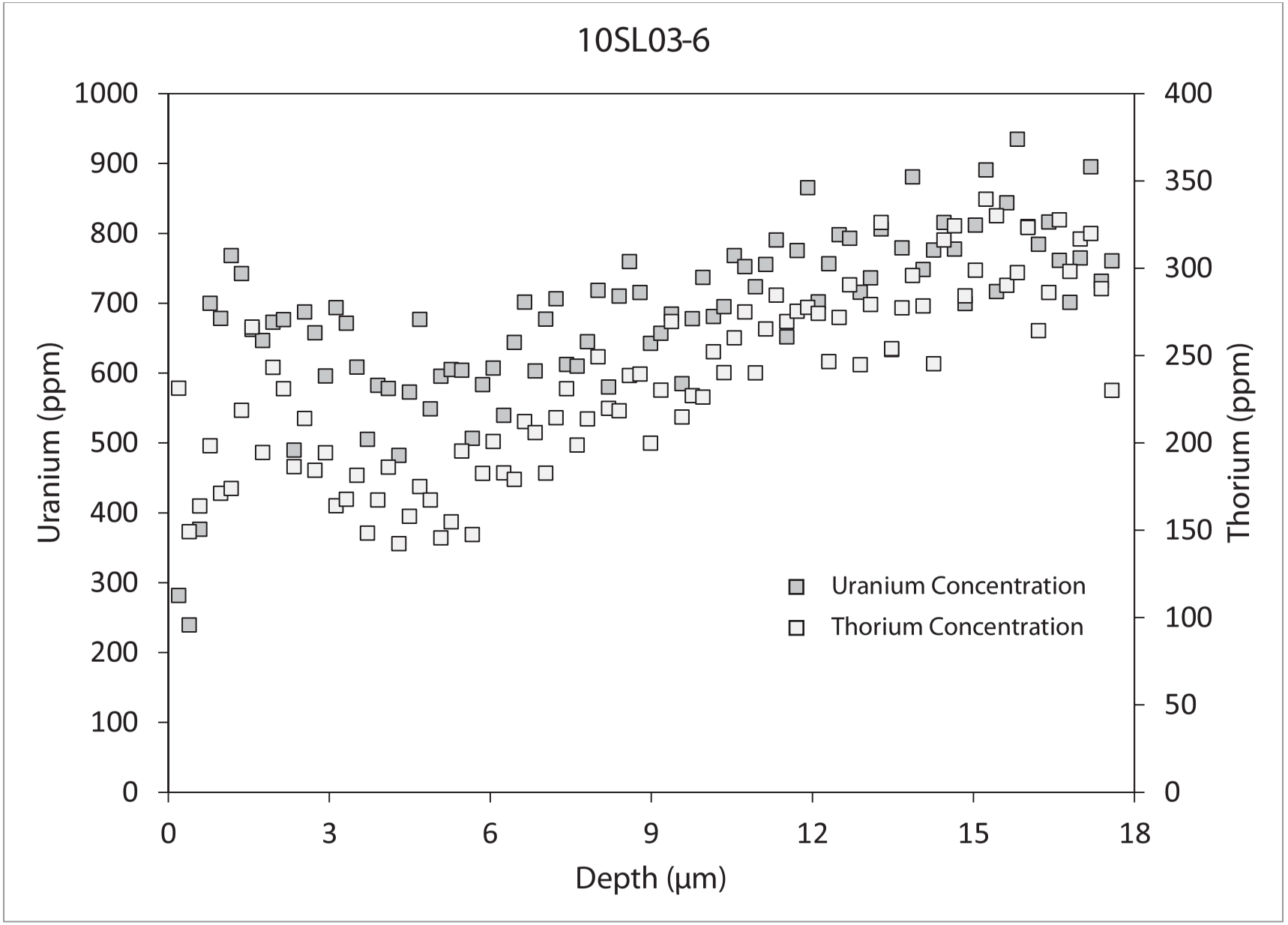
10SL03-6
Uranium (ppm)
Thorium (ppm)
Depth (µm)
Uranium Concentration
Thorium Concentration
0
100
200
300
400
500
600
700
800
900
1000
0
50
100
150
200
250
300
350
400
0
3
6
9
12
15
18

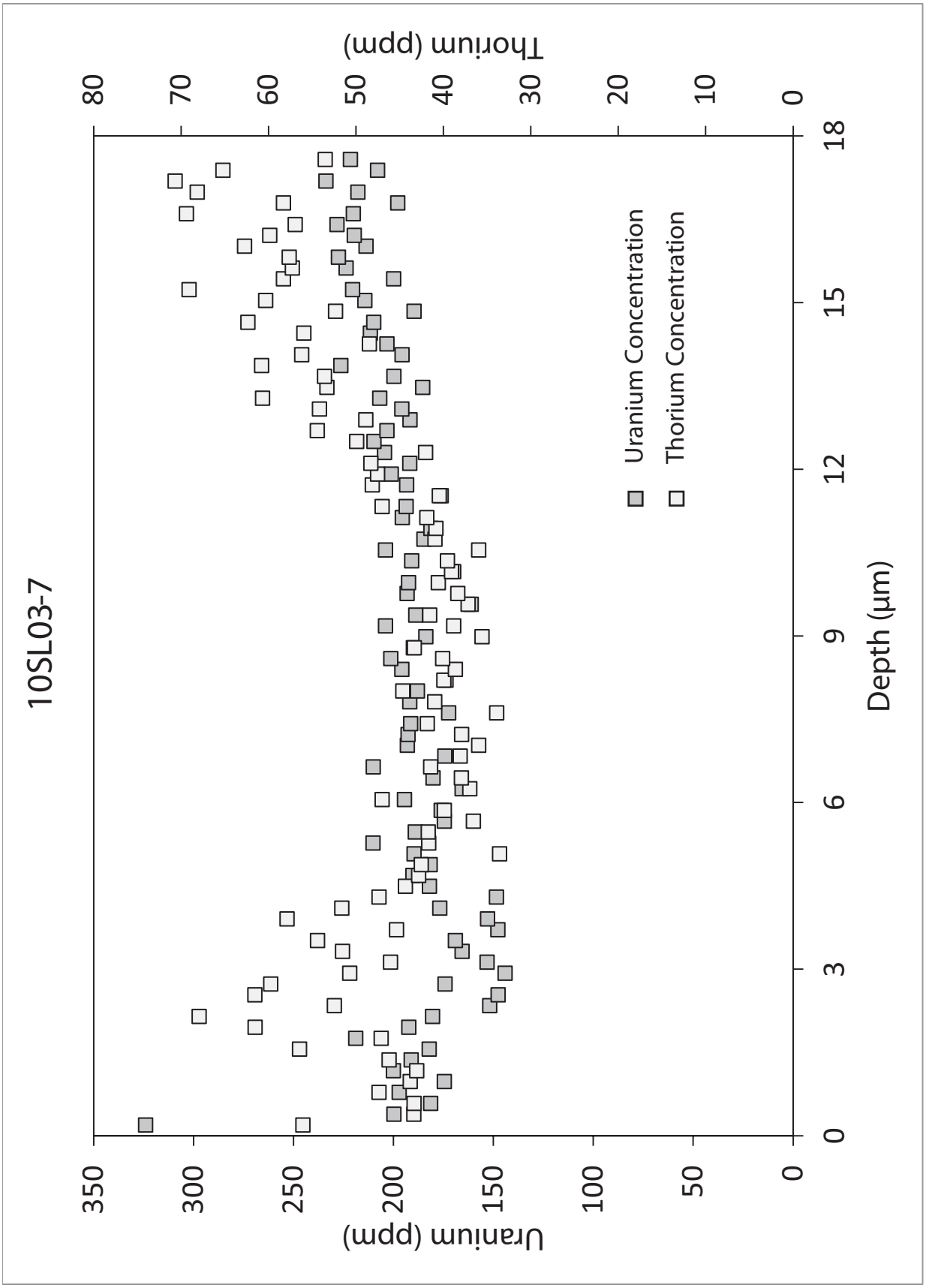
10SL03-7
Uranium (ppm)
Thorium (ppm)
Depth (µm)
Uranium Concentration
Thorium Concentration
0
50
100
150
200
250
300
350
0
10
20
30
40
50
60
70
80
0
3
6
9
12
15
18

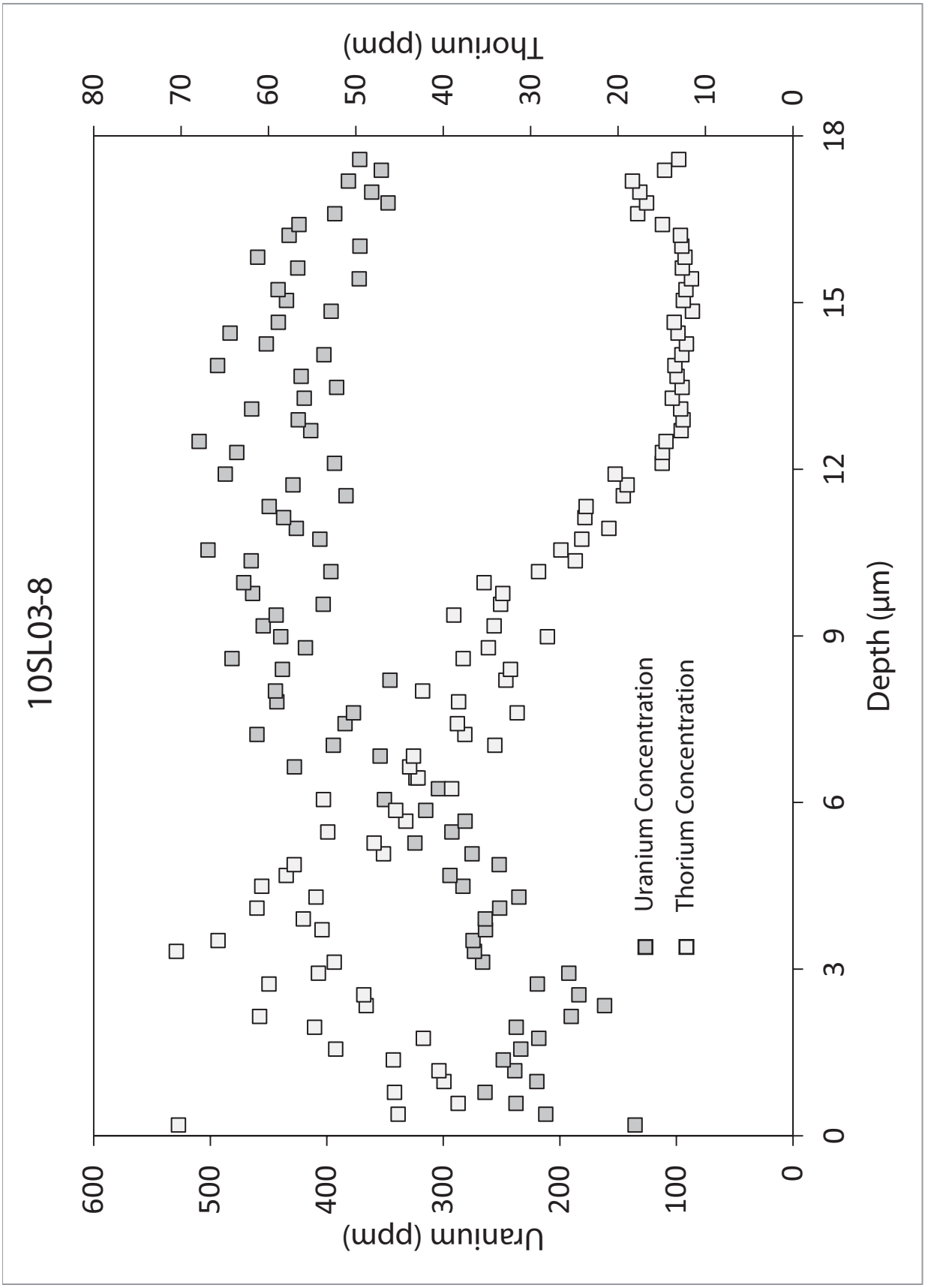
10SL03-8
Uranium (ppm)
Thorium (ppm)
Depth (µm)
Uranium Concentration
Thorium Concentration
0
100
200
300
400
500
600
0
10
20
30
40
50
60
70
80
0
3
6
9
12
15
18

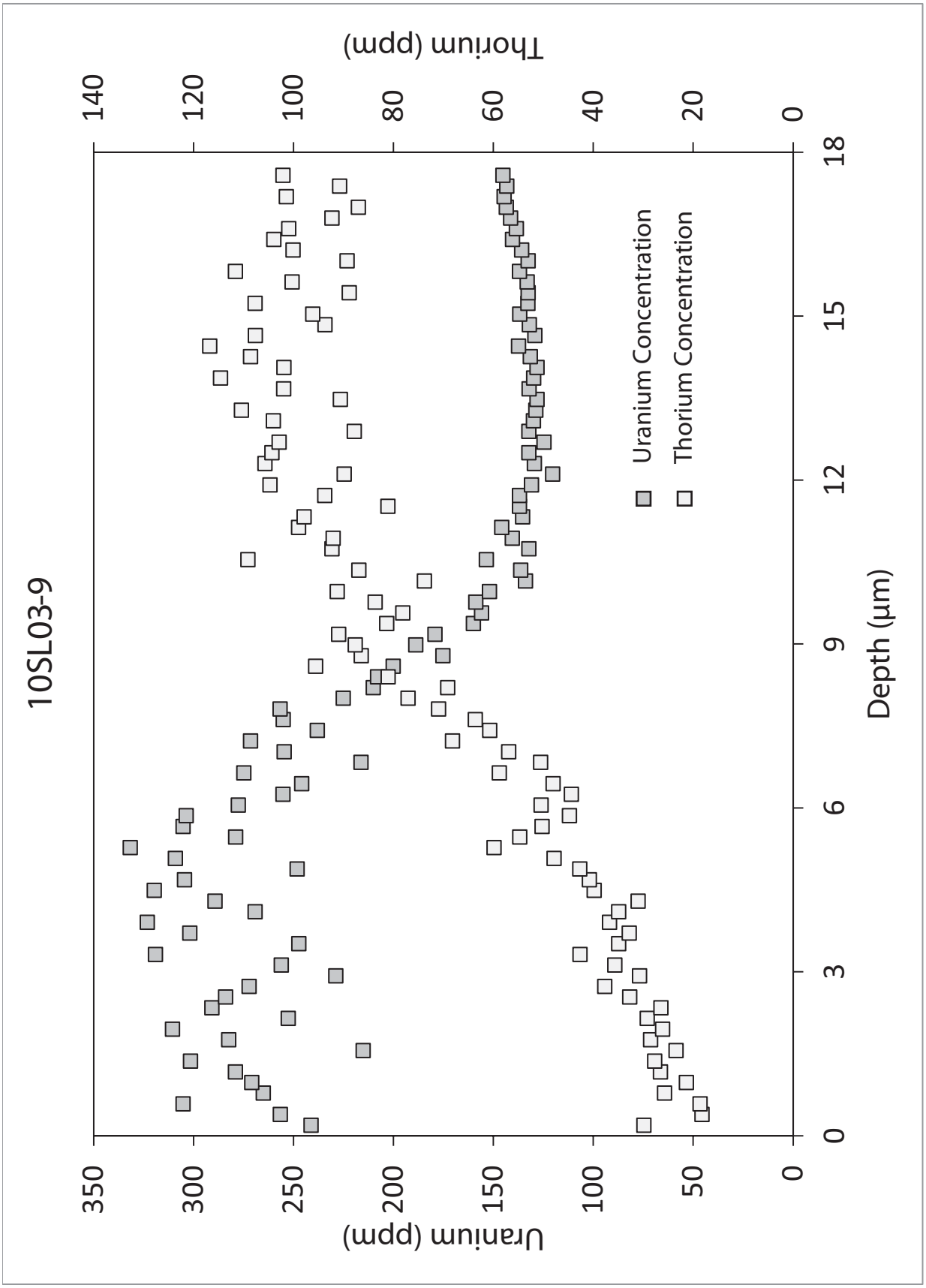
10SL03-9
Uranium (ppm)
Thorium (ppm)
Depth (µm)
Uranium Concentration
Thorium Concentration
0
50
100
150
200
250
300
350
0
20
40
60
80
100
120
140
0
3
6
9
12
15
18

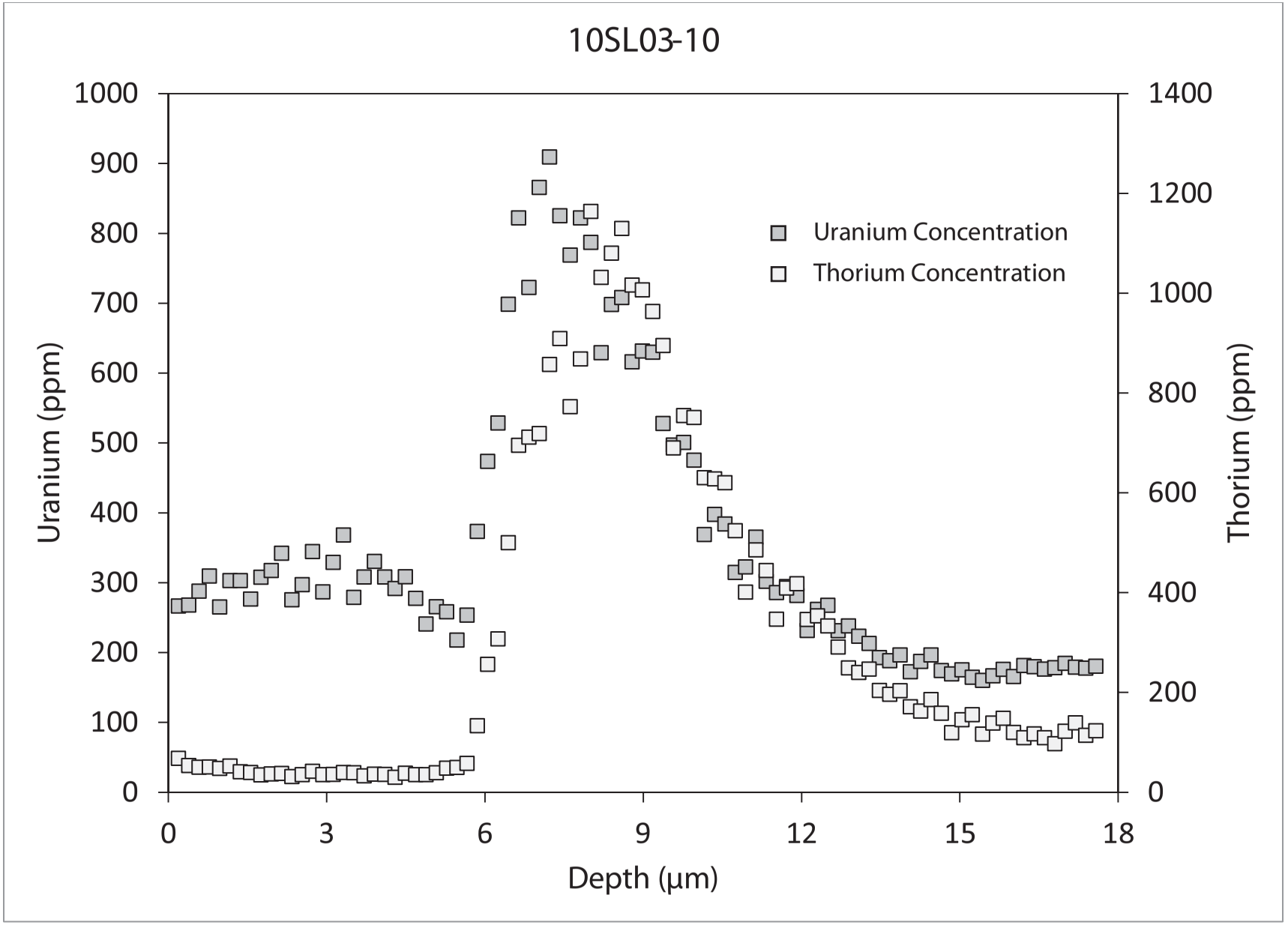
10SL03-10
Uranium Concentration
Thorium Concentration
Uranium (ppm)
Thorium (ppm)
Depth (µm)
0
100
200
300
400
500
600
700
800
900
1000
0
200
400
600
800
1000
1200
1400
0
3
6
9
12
15
18

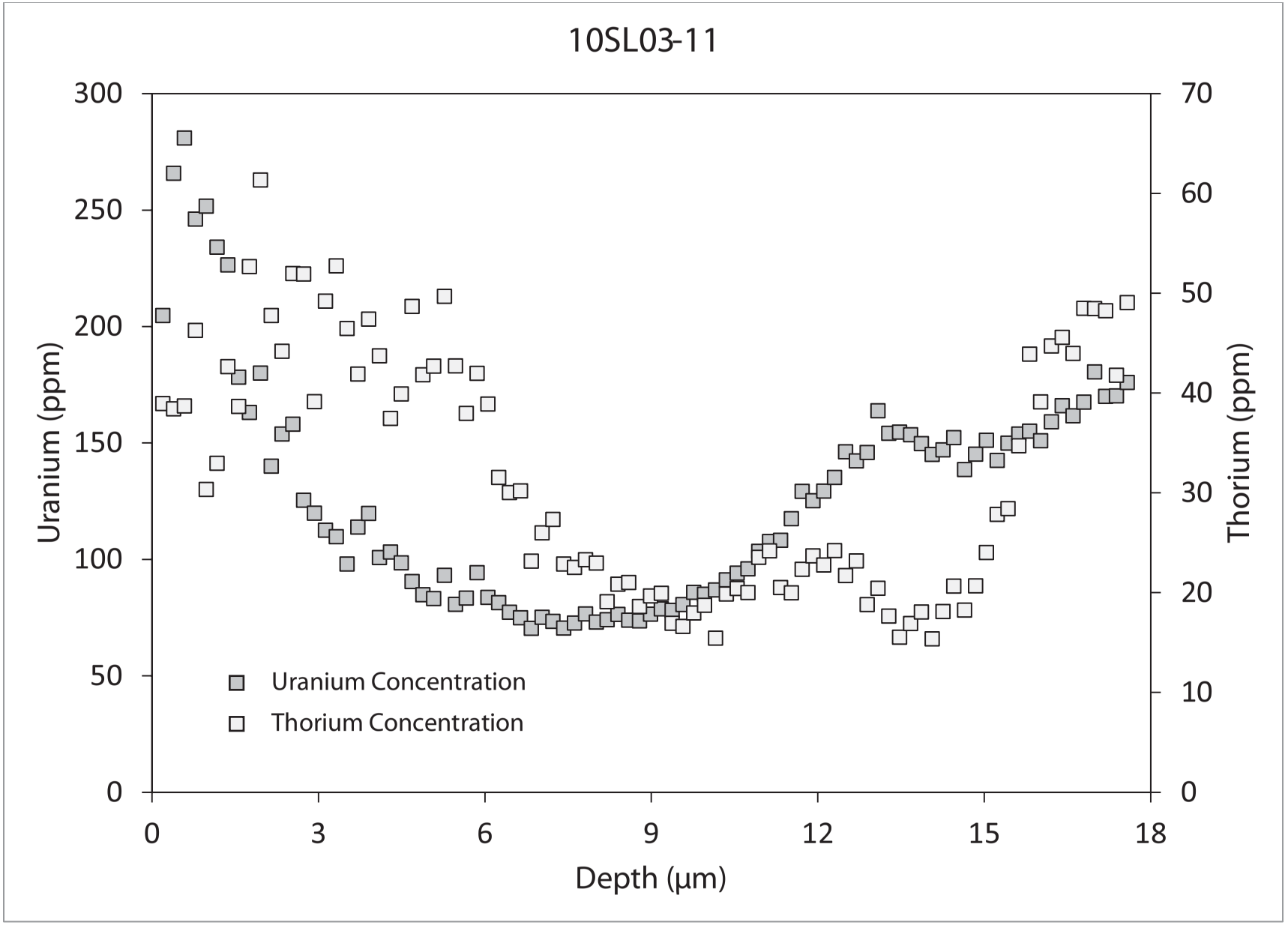
10SL03-11
Uranium (ppm)
Thorium (ppm)
Depth (µm)
Uranium Concentration
Thorium Concentration
300
250
200
150
100
50
0
70
60
50
40
30
20
10
0
0
3
6
9
12
15
18

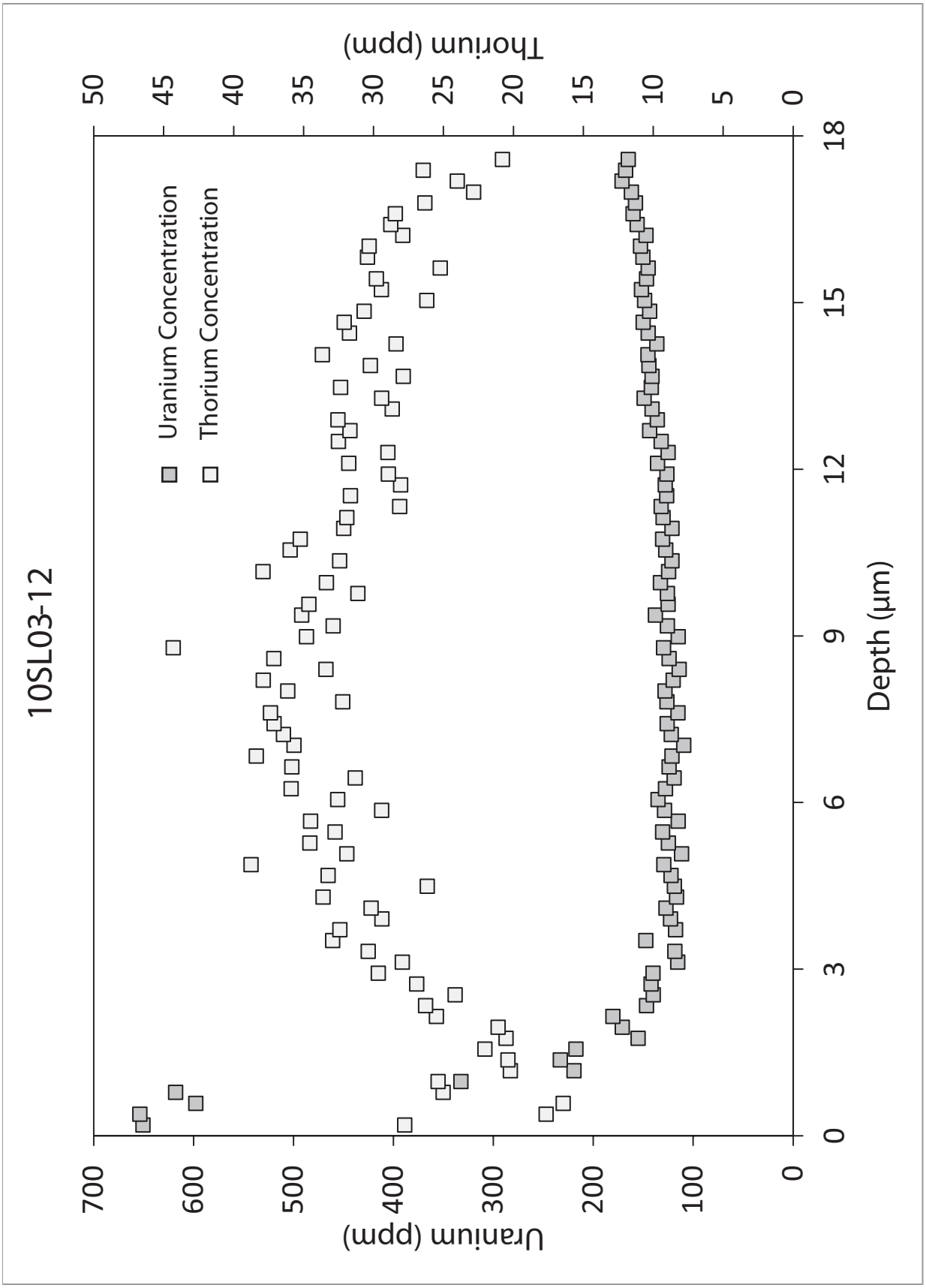
10SL03-12
Uranium Concentration
Thorium Concentration
Uranium (ppm)
Thorium (ppm)
Depth (µm)
0
100
200
300
400
500
600
700
0
5
10
15
20
25
30
35
40
45
50
0
3
6
9
12
15
18

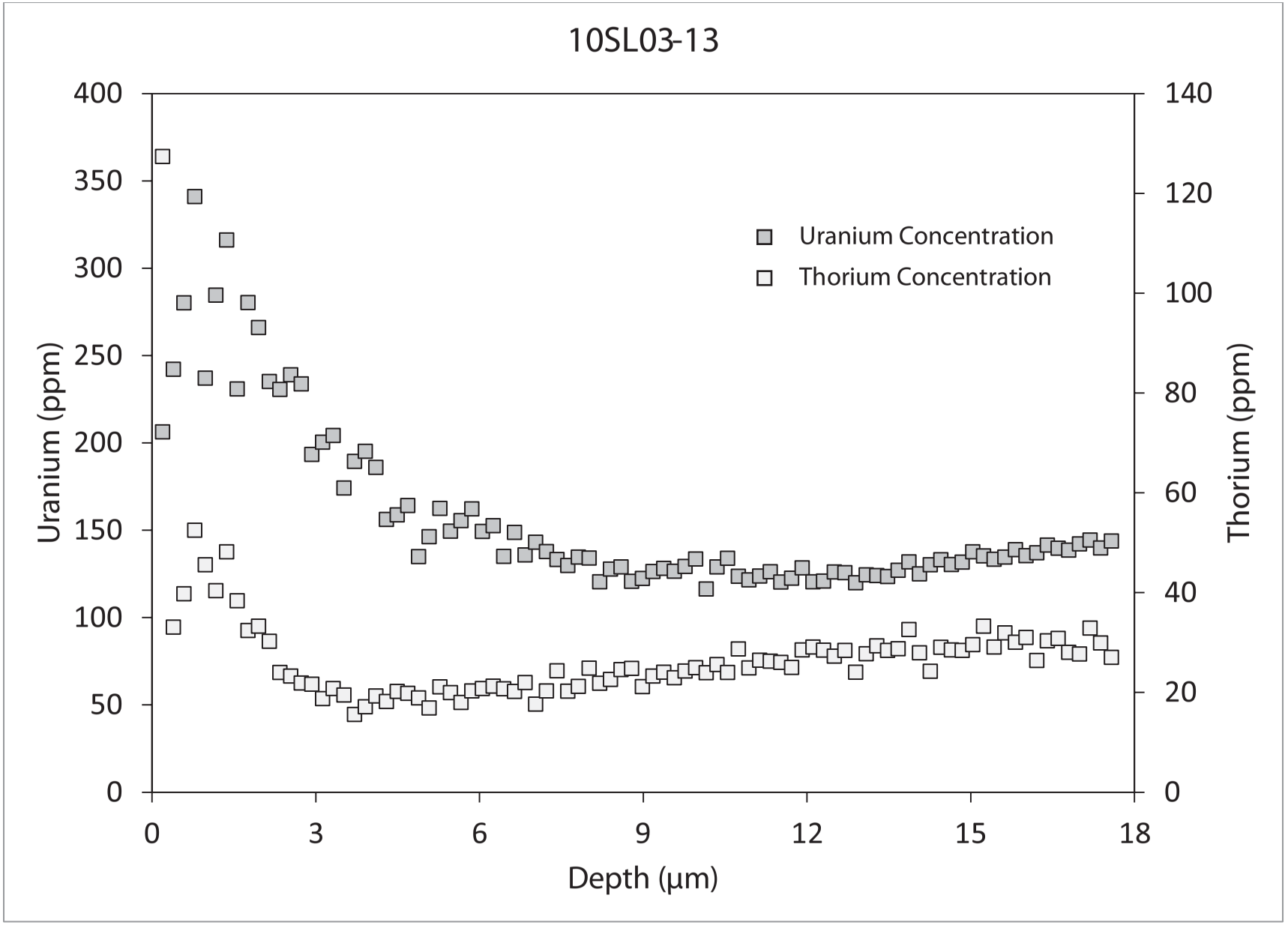
10SL03-13
Uranium Concentration
Thorium Concentration
Uranium (ppm)
Thorium (ppm)
Depth (µm)
400
350
300
250
200
150
100
50
0
140
120
100
80
60
40
20
0
0
3
6
9
12
15
18

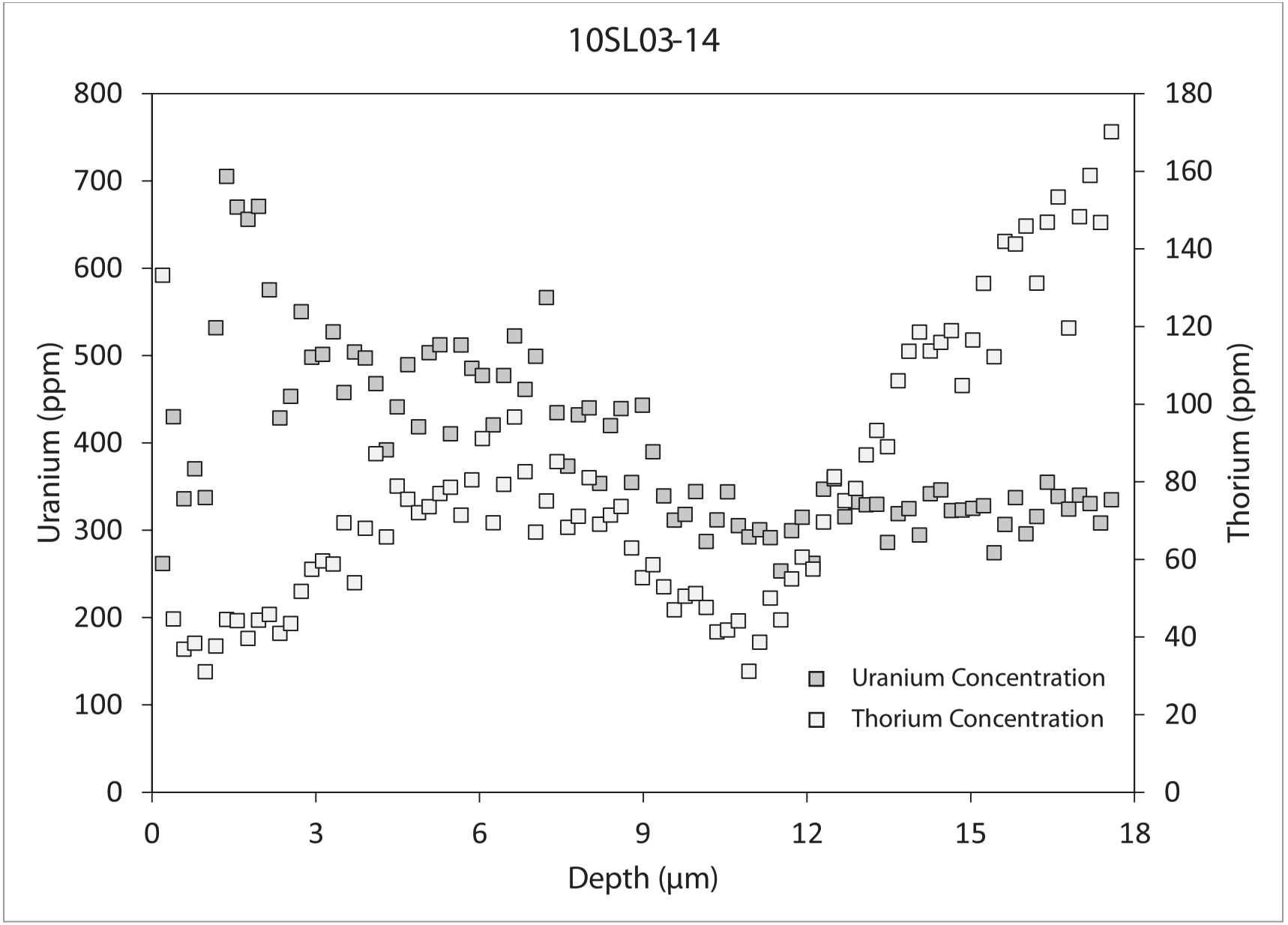
10SL03-14
Uranium (ppm)
Thorium (ppm)
Depth (µm)
Uranium Concentration
Thorium Concentration
0
100
200
300
400
500
600
700
800
0
20
40
60
80
100
120
140
160
180
0
3
6
9
12
15
18

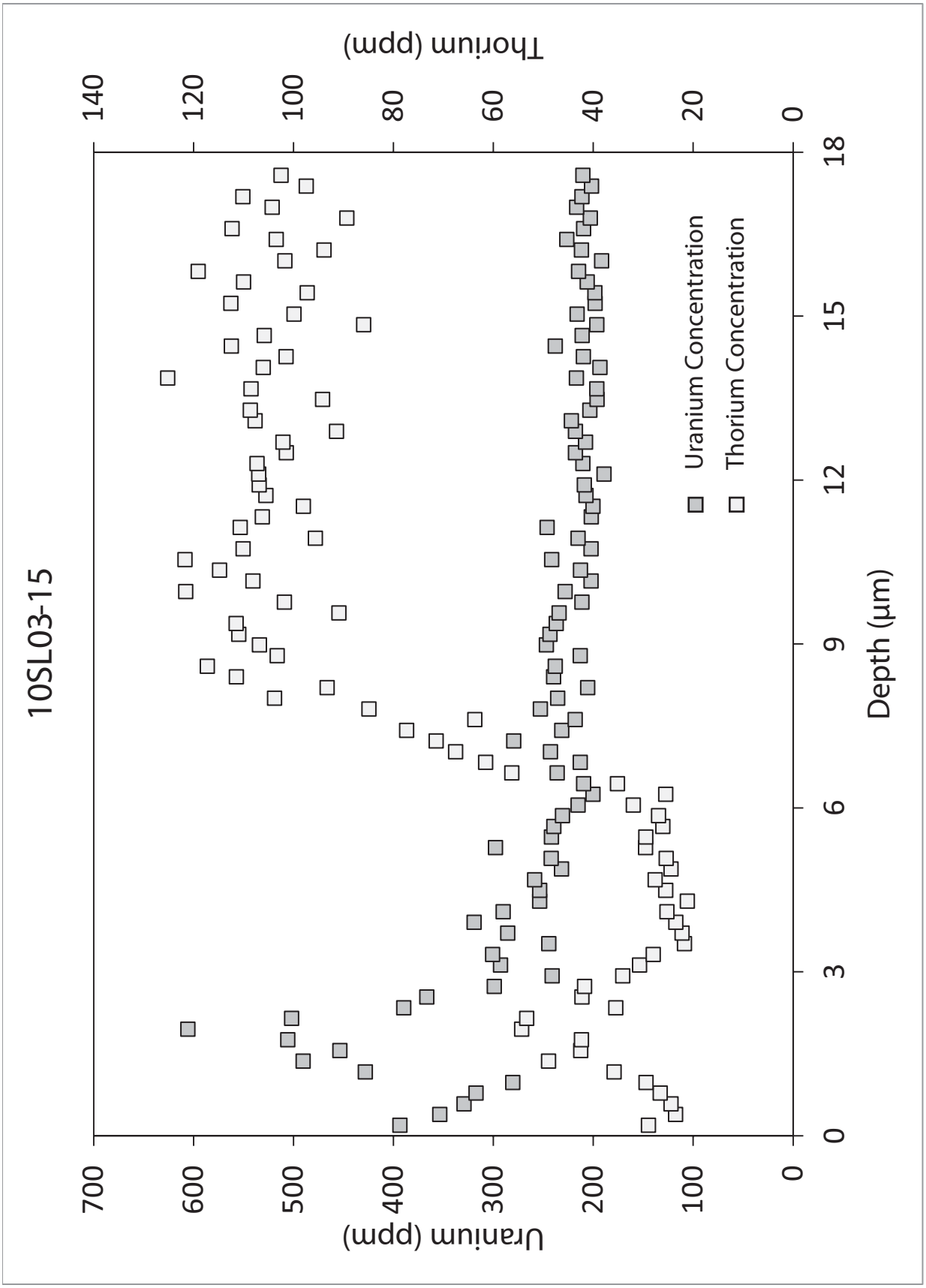
10SL03-15
Uranium (ppm)
Thorium (ppm)
Depth (µm)
Uranium Concentration
Thorium Concentration
0
100
200
300
400
500
600
700
0
20
40
60
80
100
120
140
0
3
6
9
12
15
18

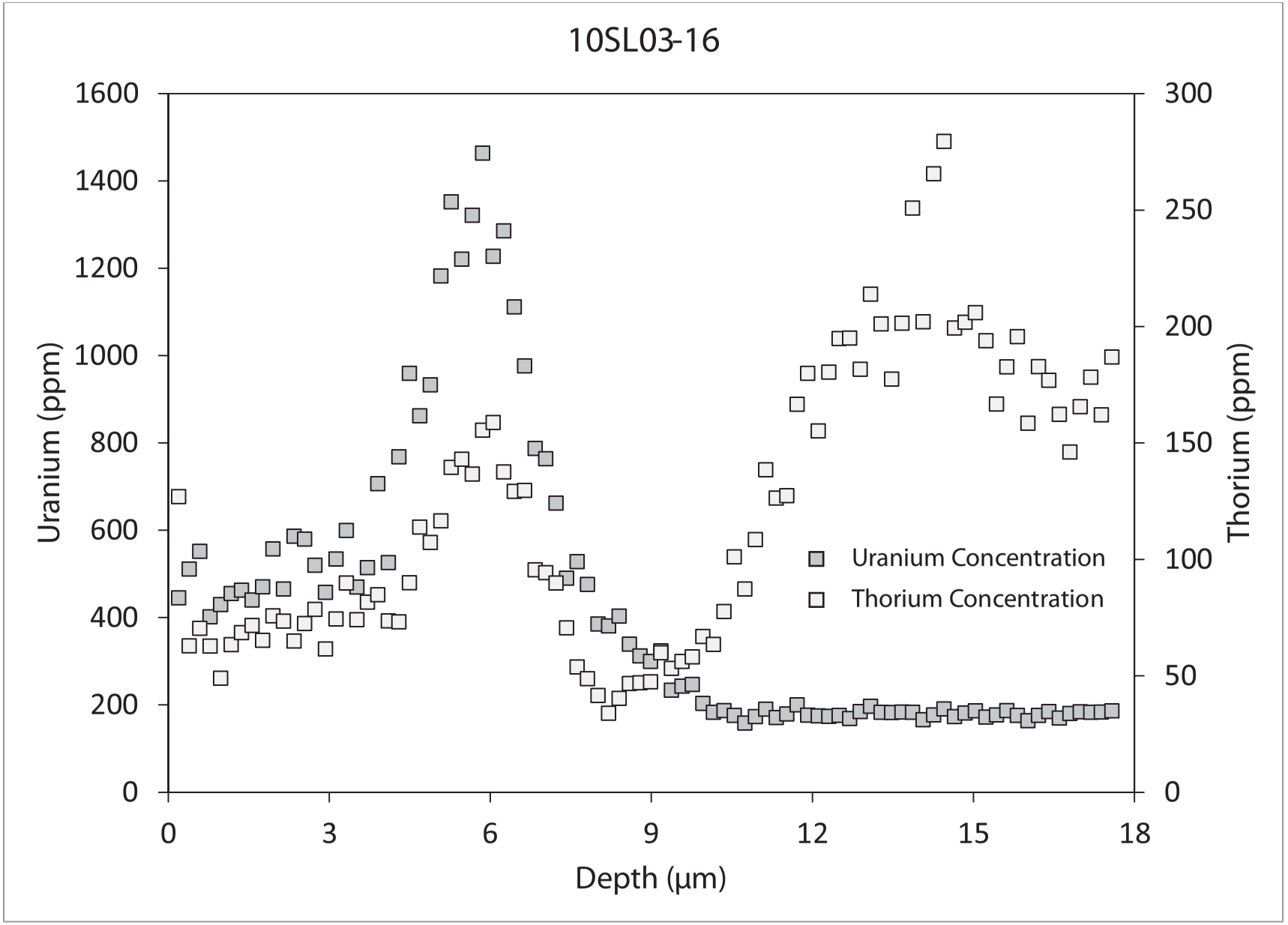
10SL03-16
Uranium (ppm)
Thorium (ppm)
Depth (µm)
Uranium Concentration
Thorium Concentration
0
200
400
600
800
1000
1200
1400
1600
0
50
100
150
200
250
300
0
3
6
9
12
15
18

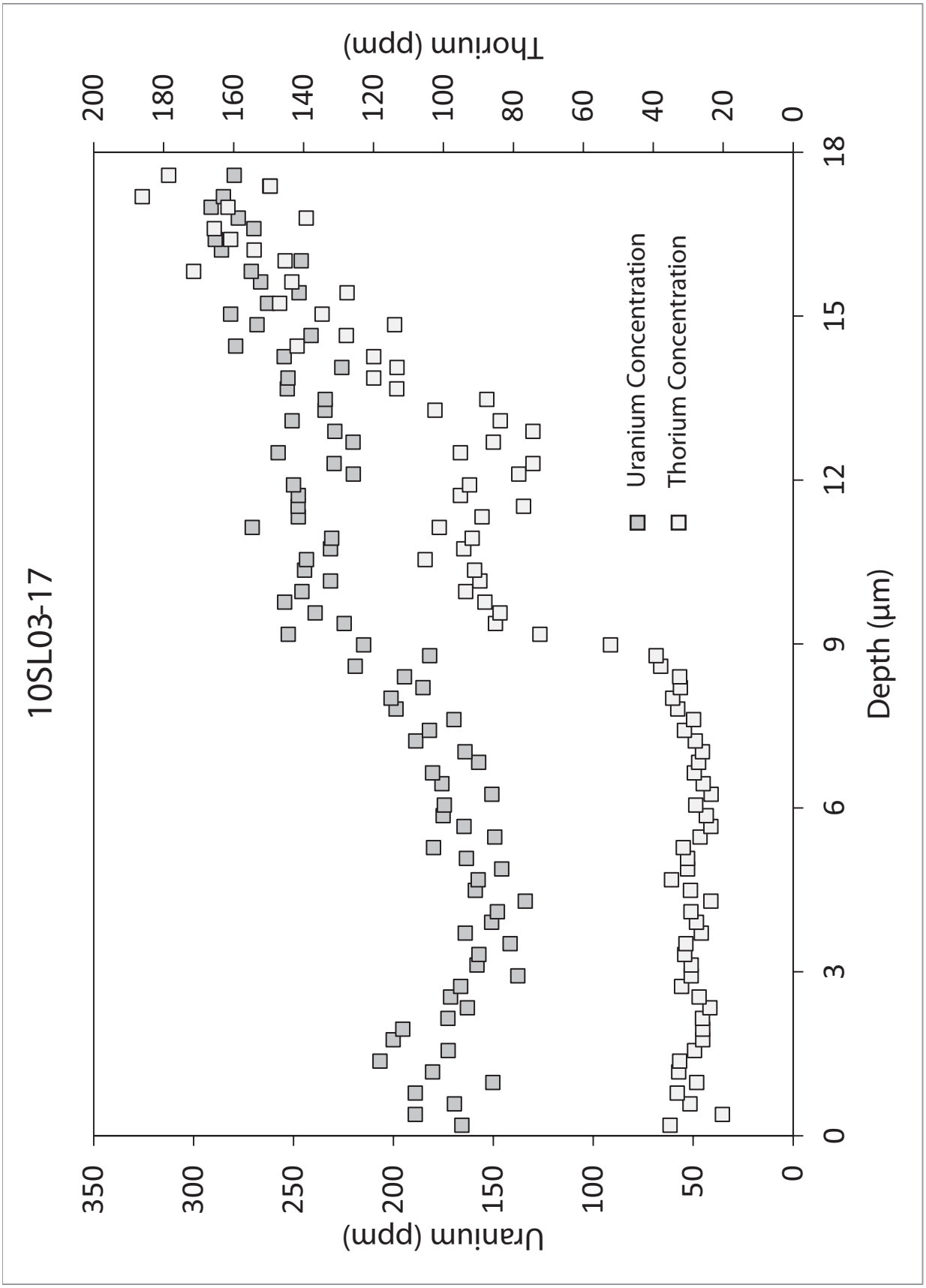
10SL03-17
Uranium (ppm)
Thorium (ppm)
Depth (µm)
Uranium Concentration
Thorium Concentration
0
50
100
150
200
250
300
350
0
20
40
60
80
100
120
140
160
180
200
0
3
6
9
12
15
18

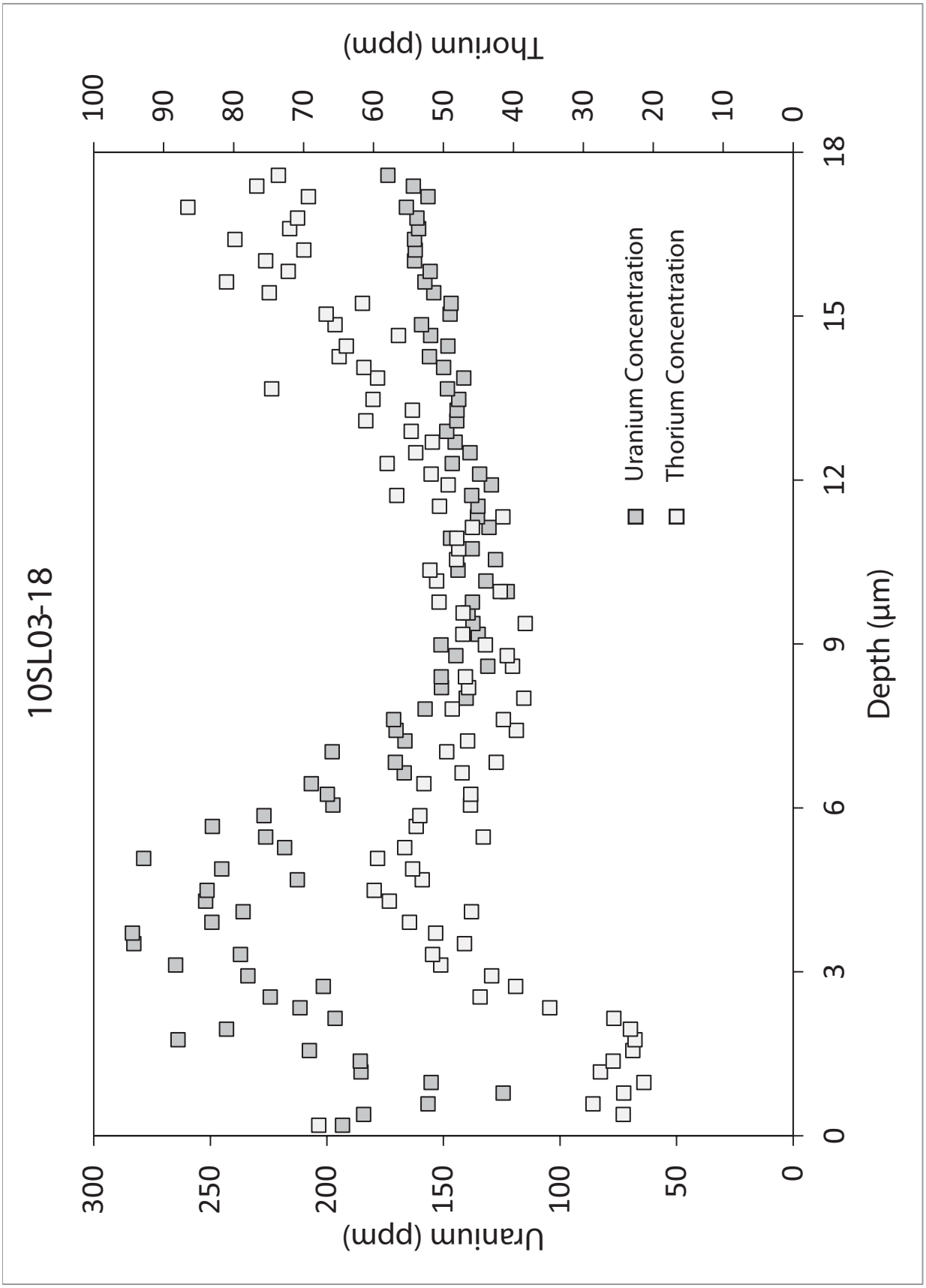
10SL03-18
Uranium (ppm)
Thorium (ppm)
Depth (µm)
Uranium Concentration
Thorium Concentration
0
50
100
150
200
250
300
0
10
20
30
40
50
60
70
80
90
100
0
3
6
9
12
15
18

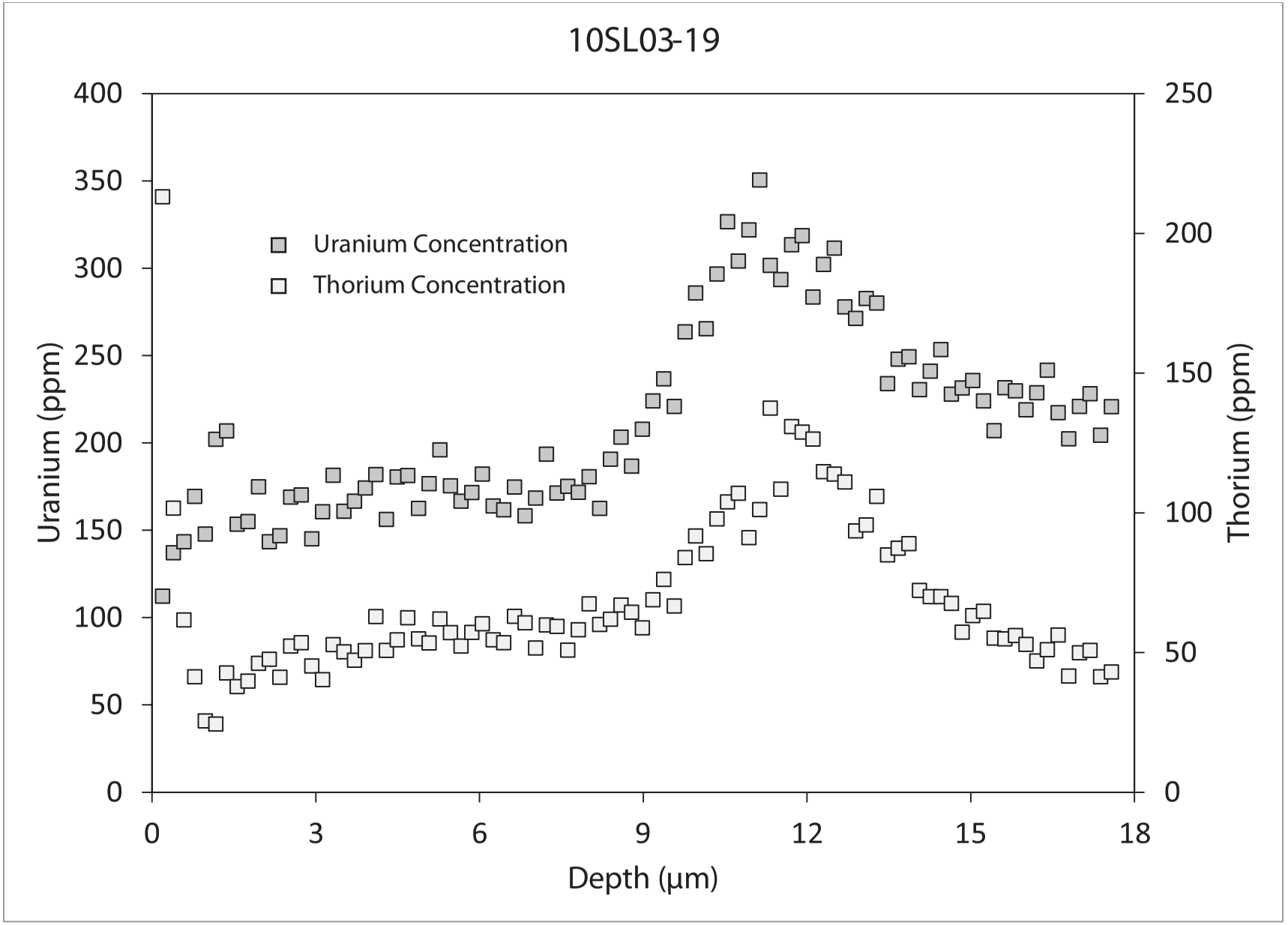
10SL03-19
Uranium Concentration
Thorium Concentration
Uranium (ppm)
Thorium (ppm)
Depth (µm)
400
350
300
250
200
150
100
50
0
250
200
150
100
50
0
0
3
6
9
12
15
18

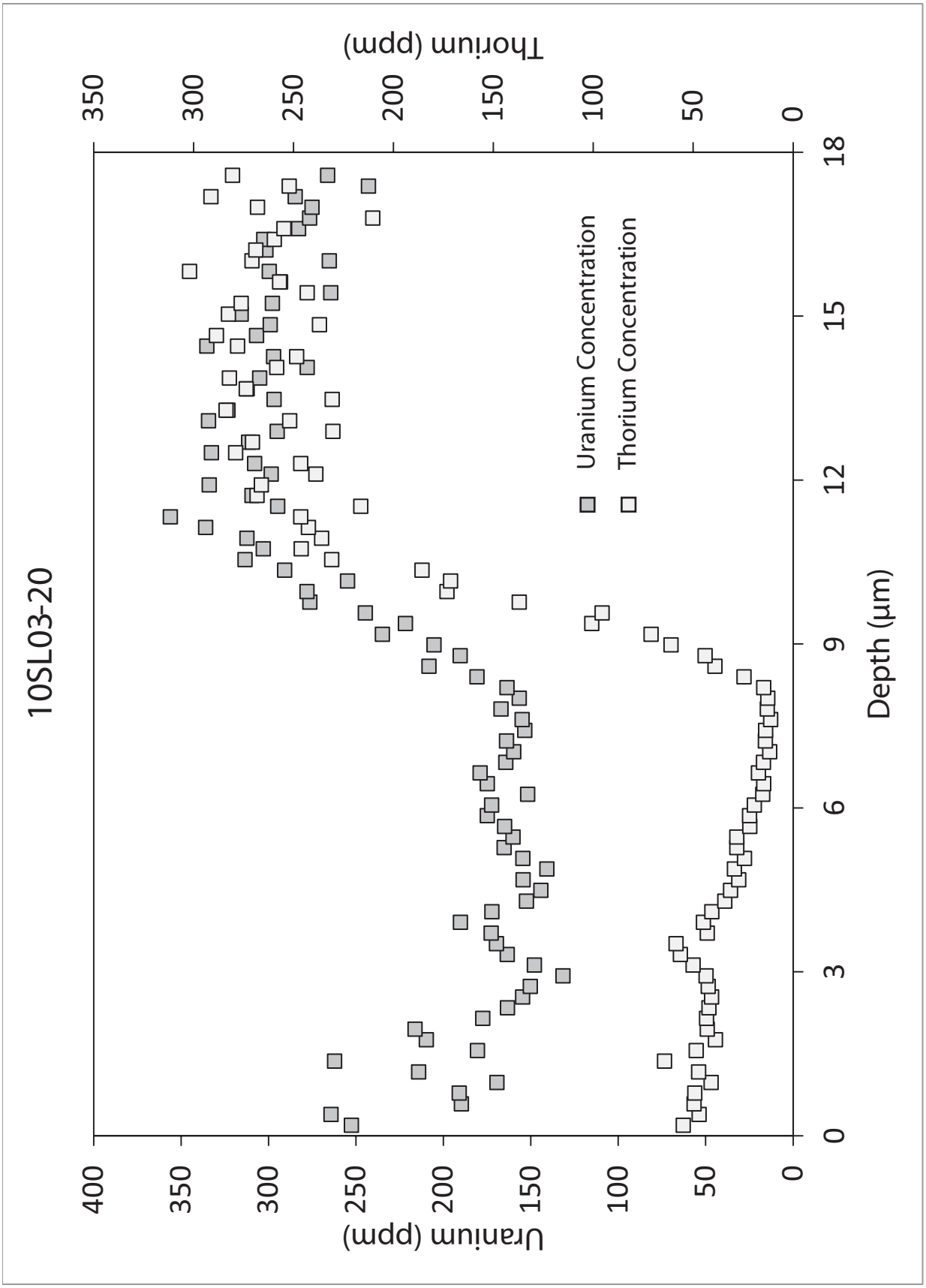
10SL03-20
Uranium (ppm)
Thorium (ppm)
Depth (µm)
Uranium Concentration
Thorium Concentration
0
50
100
150
200
250
300
350
400
0
3
6
9
12
15
18

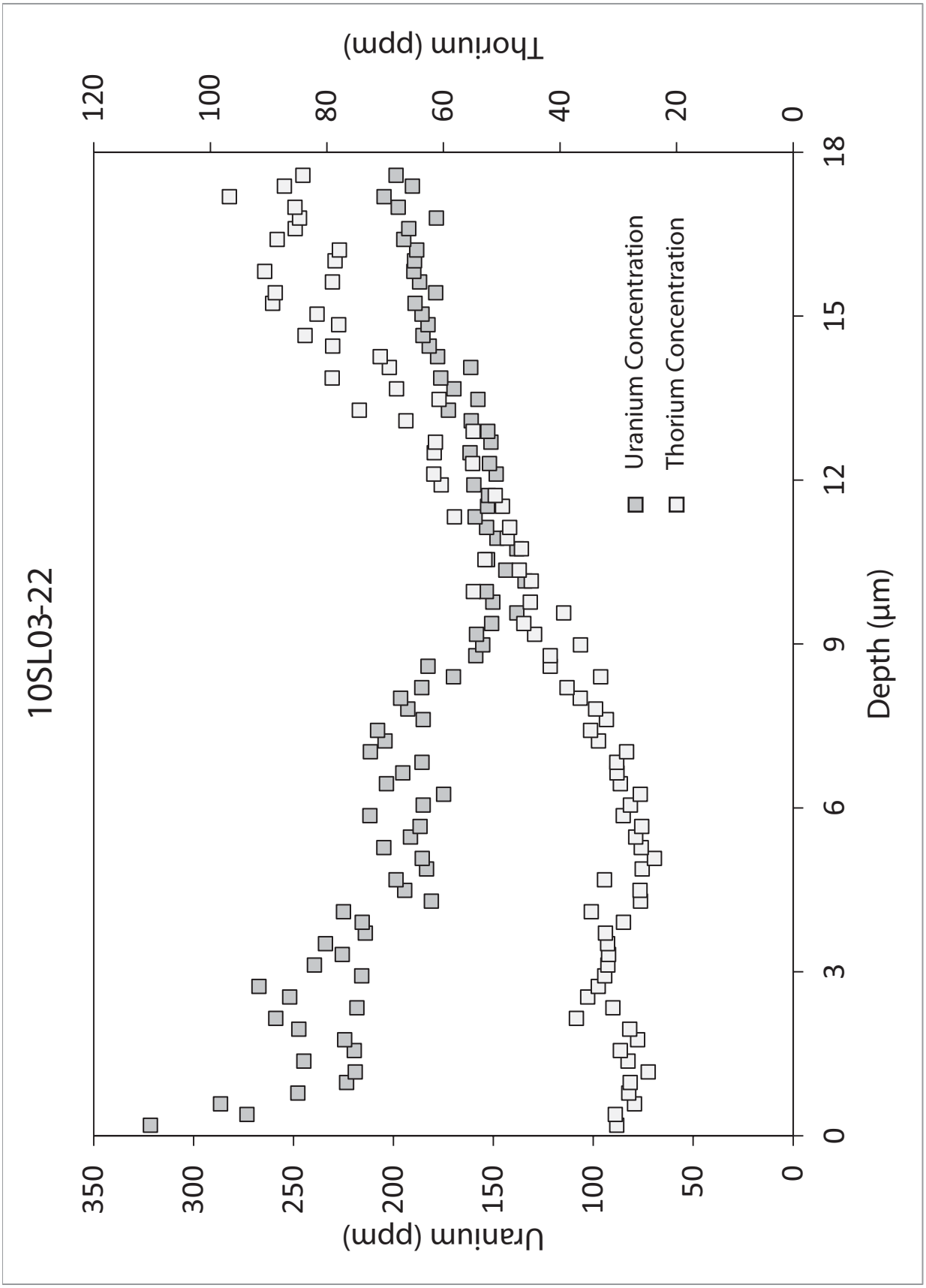
10SL03-22
Uranium (ppm)
Thorium (ppm)
Depth (µm)
Uranium Concentration
Thorium Concentration
0
50
100
150
200
250
300
350
0
20
40
60
80
100
120
0
3
6
9
12
15
18

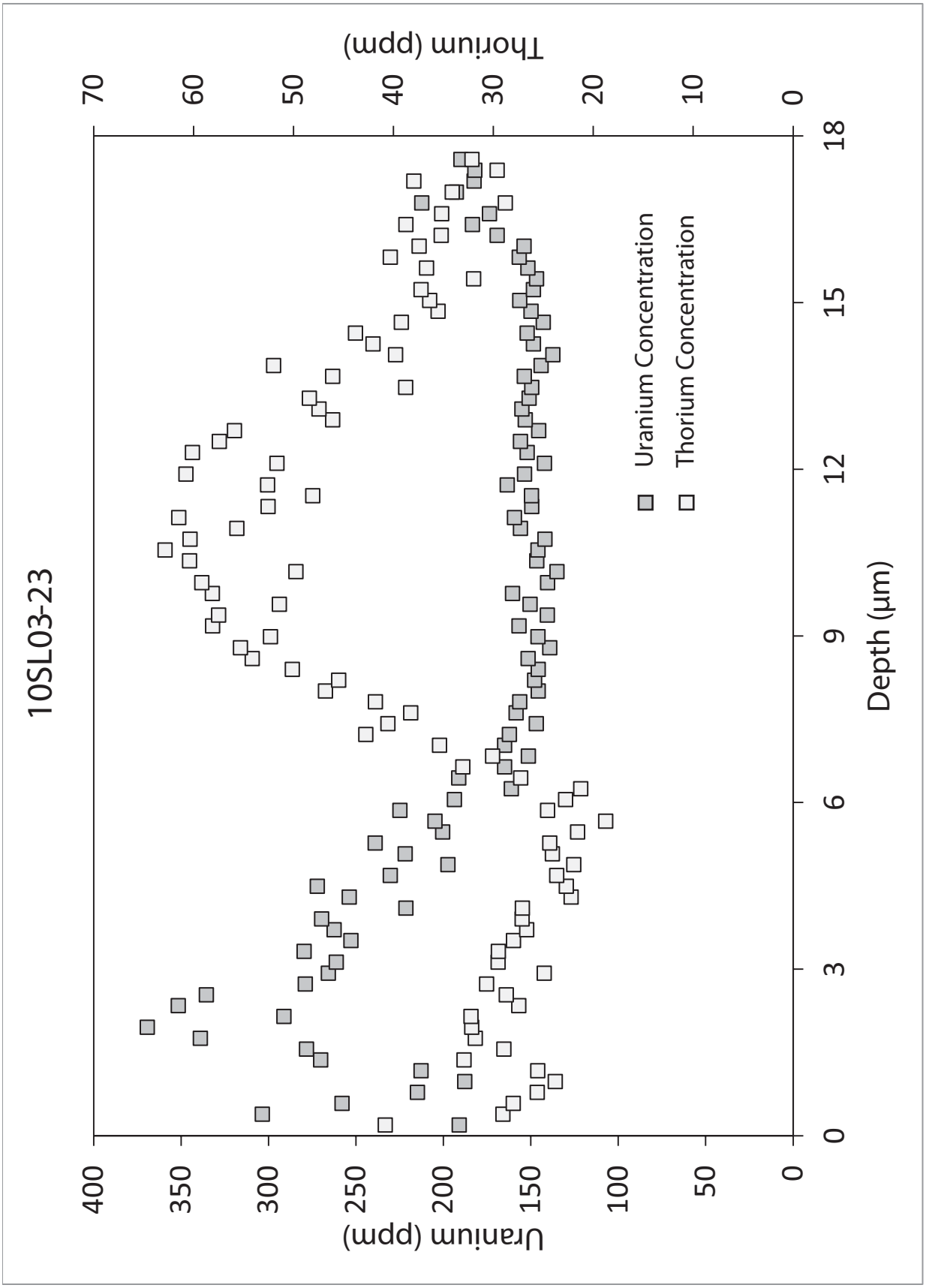
10SL03-23
Uranium (ppm)
Thorium (ppm)
Depth (µm)
Uranium Concentration
Thorium Concentration
0
50
100
150
200
250
300
350
400
0
10
20
30
40
50
60
70
0
3
6
9
12
15
18

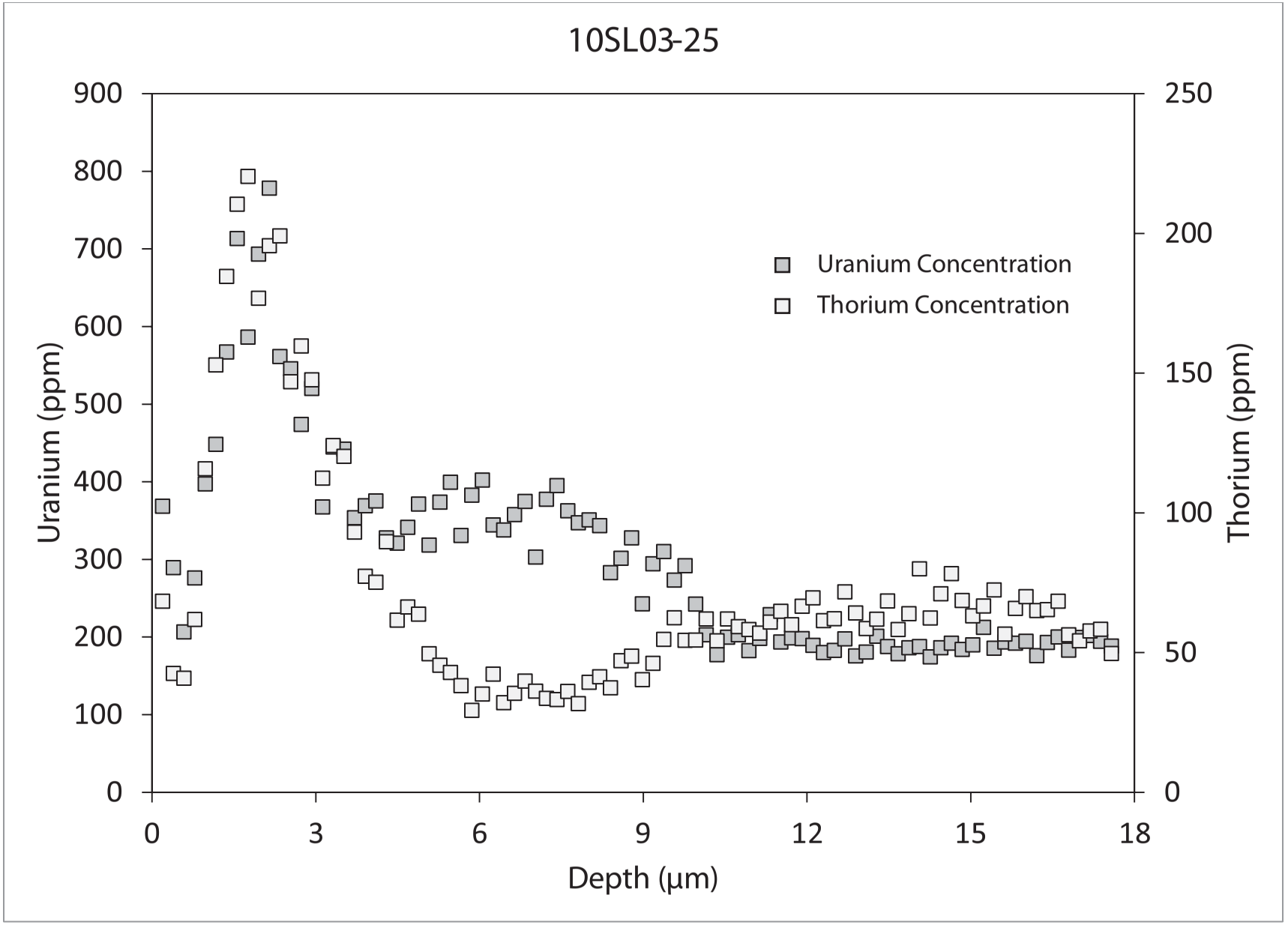
10SL03-25
Uranium Concentration
Thorium Concentration
Uranium (ppm)
Thorium (ppm)
Depth (µm)
900
800
700
600
500
400
300
200
100
0
250
200
150
100
50
0
0
3
6
9
12
15
18

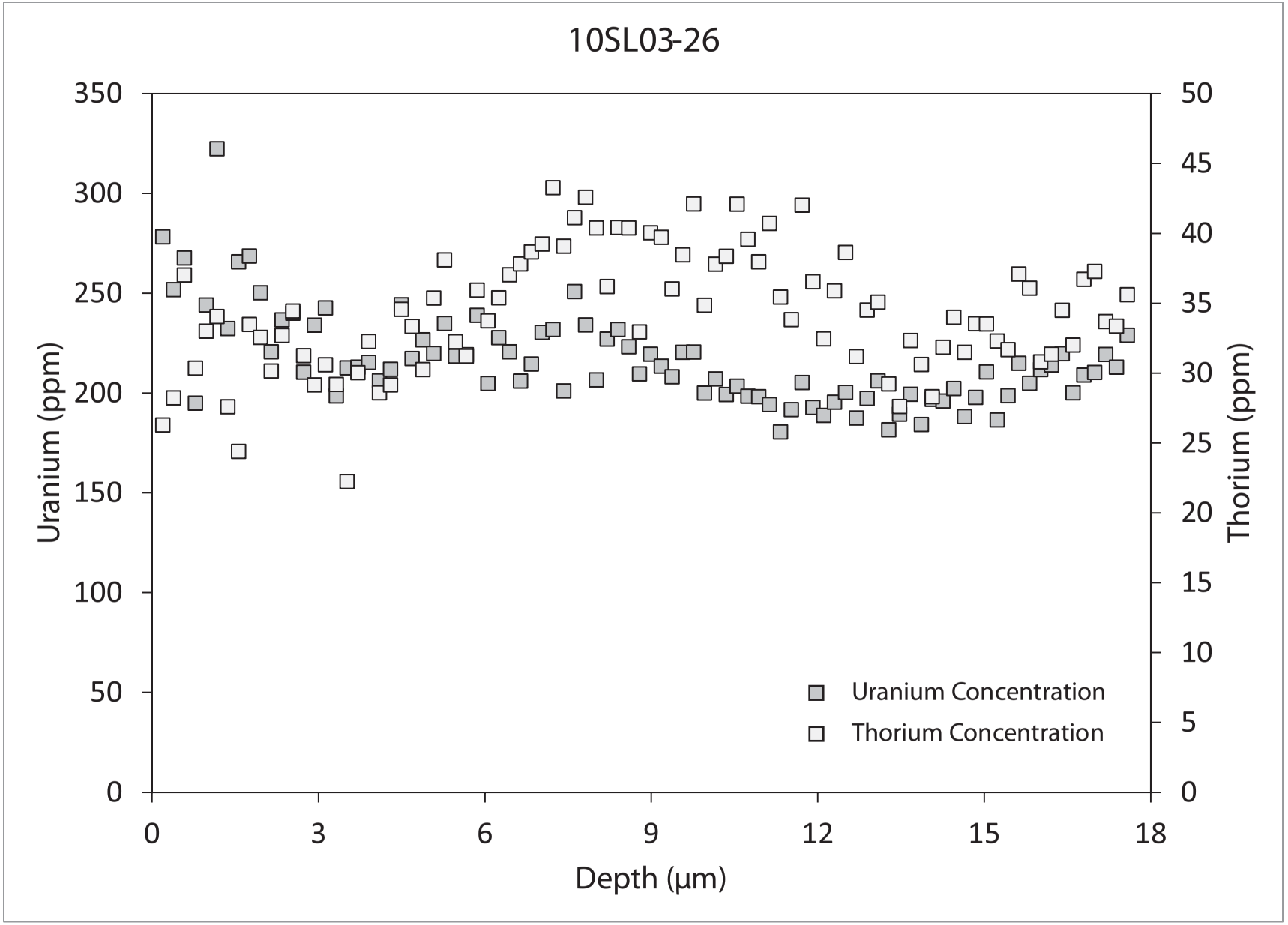
10SL03-26
Uranium (ppm)
Thorium (ppm)
Depth (µm)
Uranium Concentration
Thorium Concentration
0
50
100
150
200
250
300
350
0
5
10
15
20
25
30
35
40
45
50
0
3
6
9
12
15
18

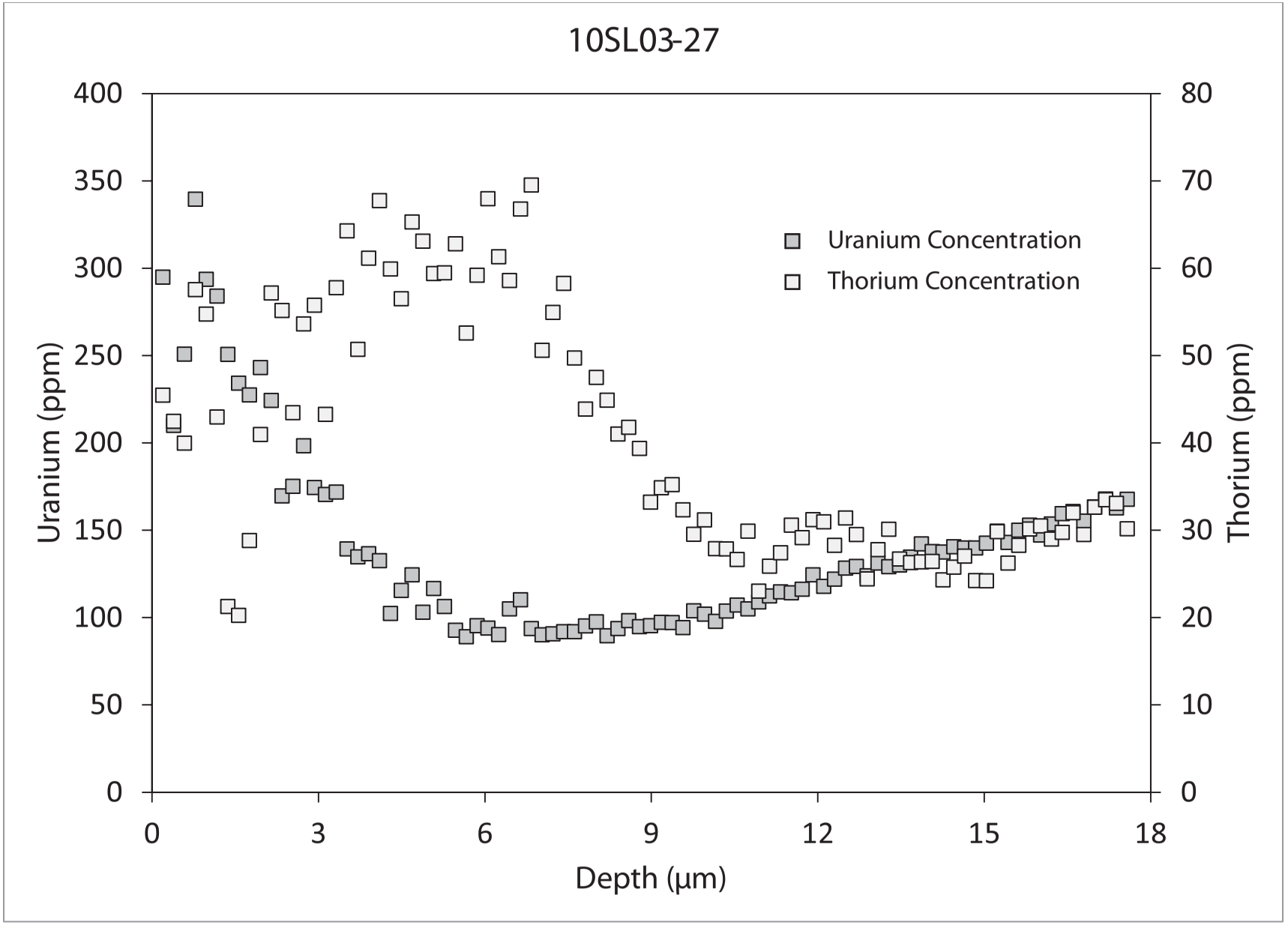
10SL03-27
Uranium Concentration
Thorium Concentration
Uranium (ppm)
Thorium (ppm)
Depth (µm)
400
350
300
250
200
150
100
50
0
80
70
60
50
40
30
20
10
0
0
3
6
9
12
15
18

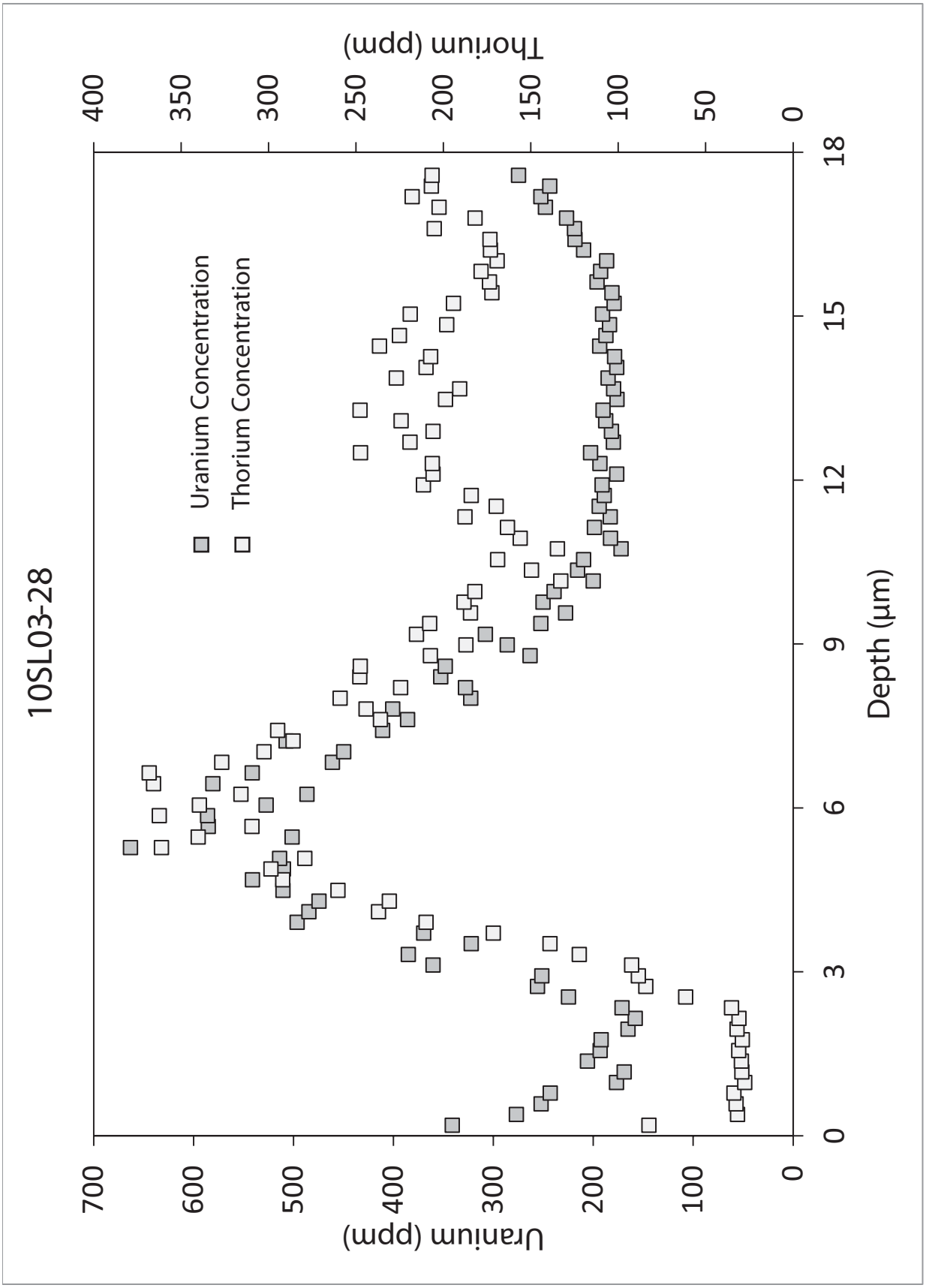
10SL03-28
Uranium Concentration
Thorium Concentration
Uranium (ppm)
Thorium (ppm)
Depth (µm)
0
100
200
300
400
500
600
700
0
50
100
150
200
250
300
350
400
0
3
6
9
12
15
18

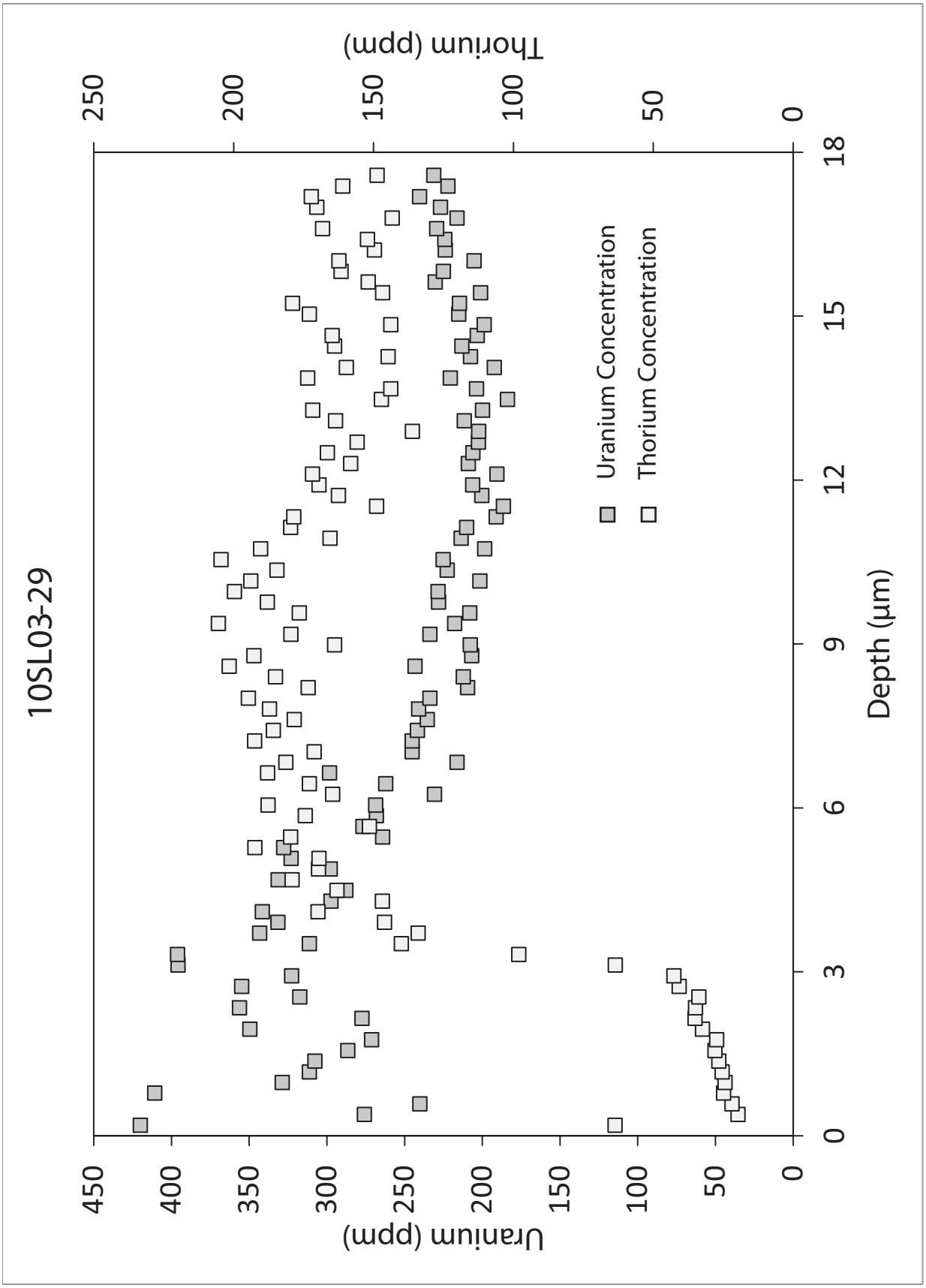
10SL03-29
Uranium (ppm)
Thorium (ppm)
Depth (µm)
Uranium Concentration
Thorium Concentration
0
50
100
150
200
250
300
350
400
450
0
3
6
9
12
15
18

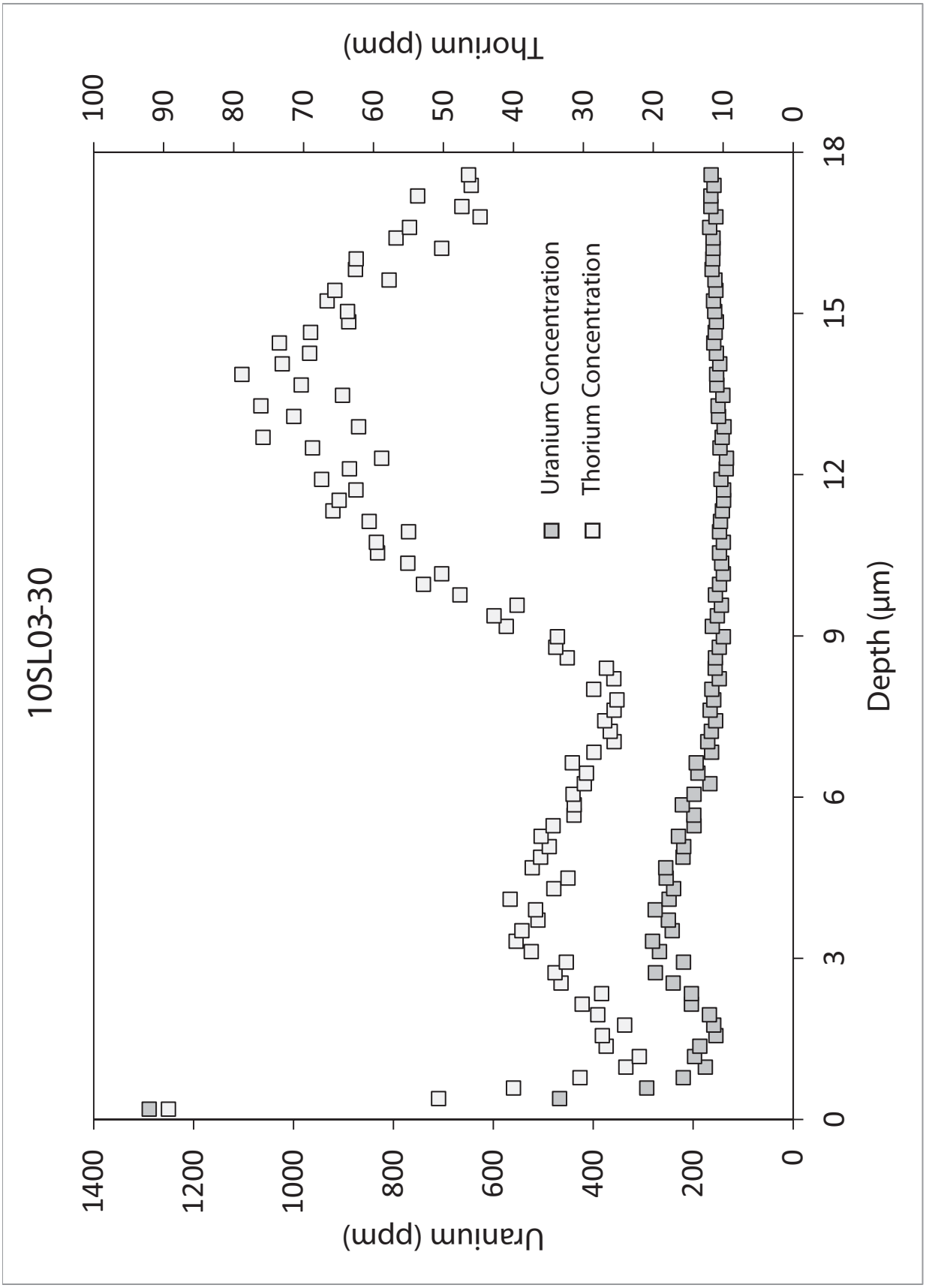
10SL03-30
Uranium (ppm)
Thorium (ppm)
Depth (µm)
Uranium Concentration
Thorium Concentration
0
200
400
600
800
1000
1200
1400
0
10
20
30
40
50
60
70
80
90
100
0
3
6
9
12
15
18

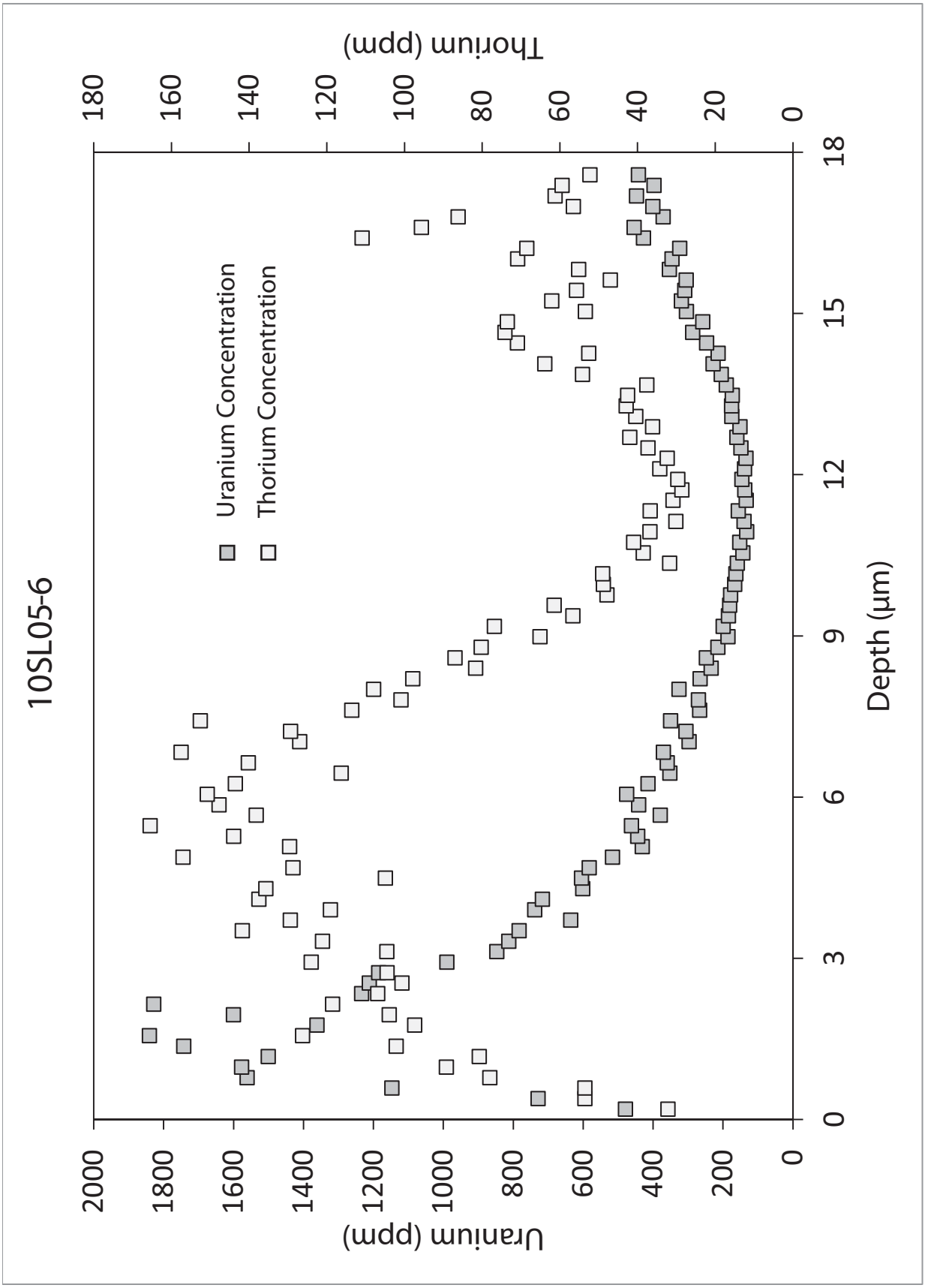
10SL05-6
Uranium Concentration
Thorium Concentration
Uranium (ppm)
Thorium (ppm)
Depth (µm)
0
200
400
600
800
1000
1200
1400
1600
1800
2000
0
20
40
60
80
100
120
140
160
180
0
3
6
9
12
15
18

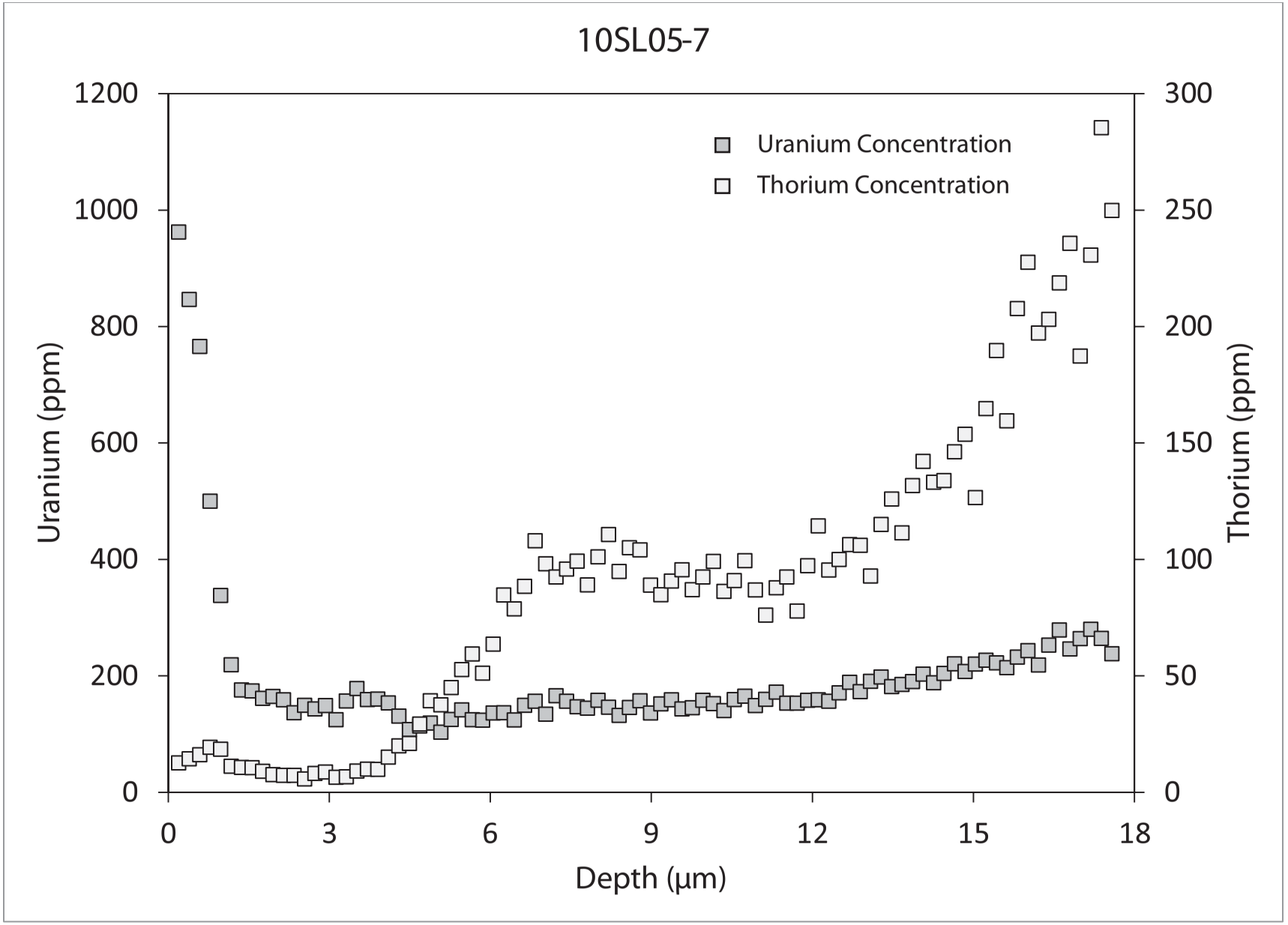
10SL05-7
Uranium Concentration
Thorium Concentration
Uranium (ppm)
Thorium (ppm)
Depth (µm)
0
200
400
600
800
1000
1200
0
50
100
150
200
250
300
0
3
6
9
12
15
18

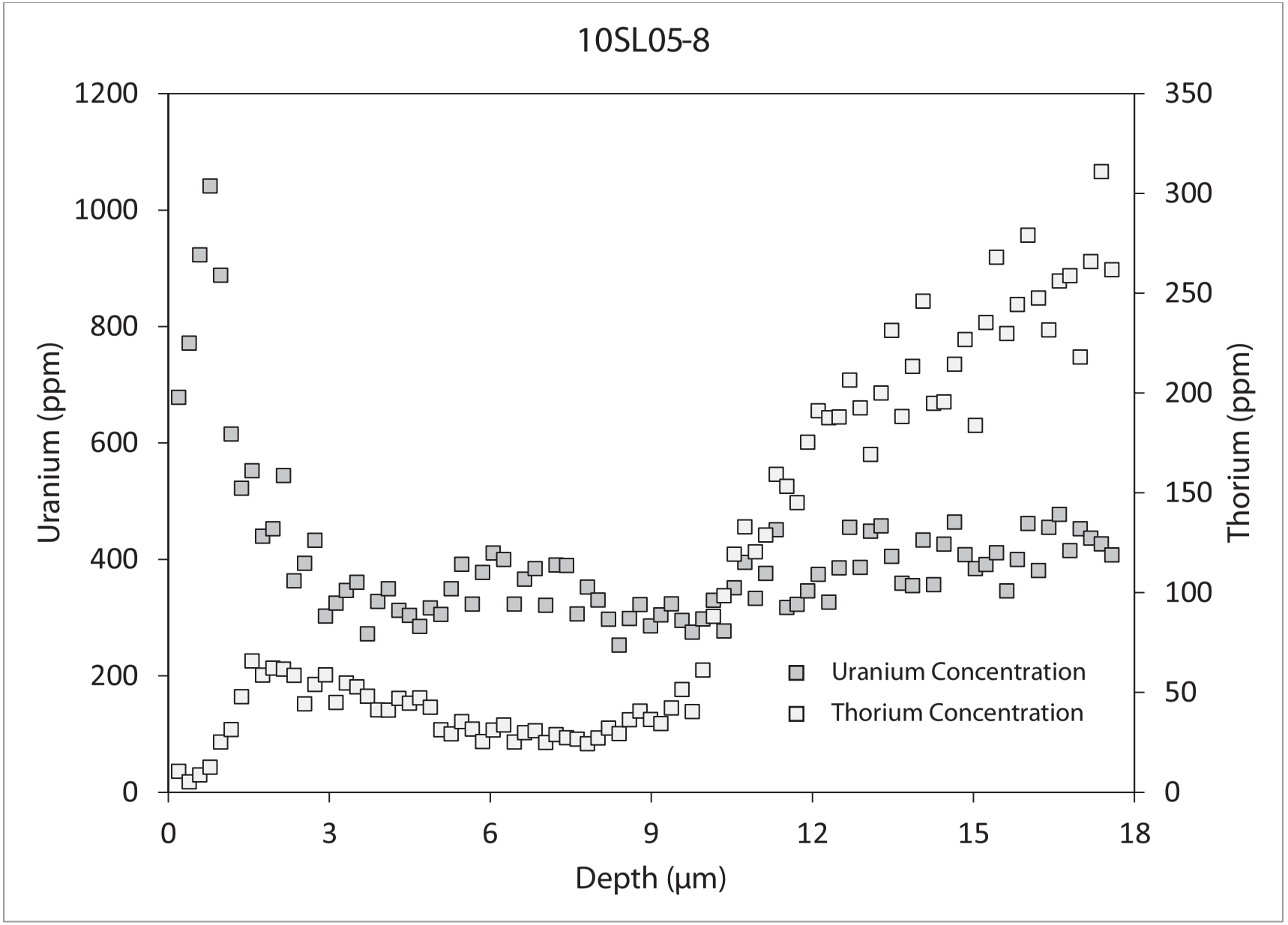
10SL05-8
Uranium (ppm)
Thorium (ppm)
Depth (µm)
Uranium Concentration
Thorium Concentration
0
200
400
600
800
1000
1200
0
50
100
150
200
250
300
350
0
3
6
9
12
15
18

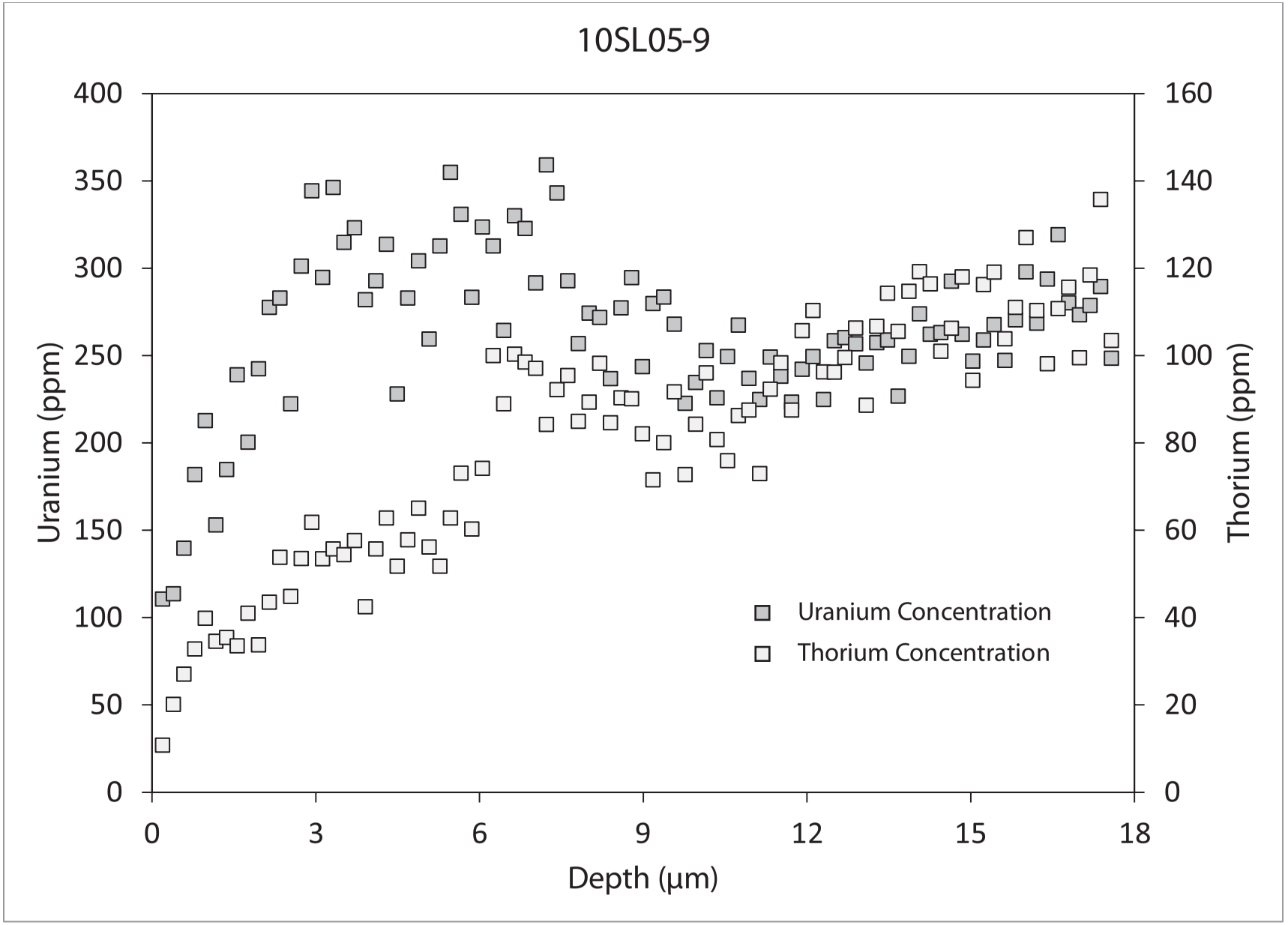
10SL05-9
Uranium (ppm)
Thorium (ppm)
Depth (µm)
Uranium Concentration
Thorium Concentration
0
50
100
150
200
250
300
350
400
0
20
40
60
80
100
120
140
160
0
3
6
9
12
15
18

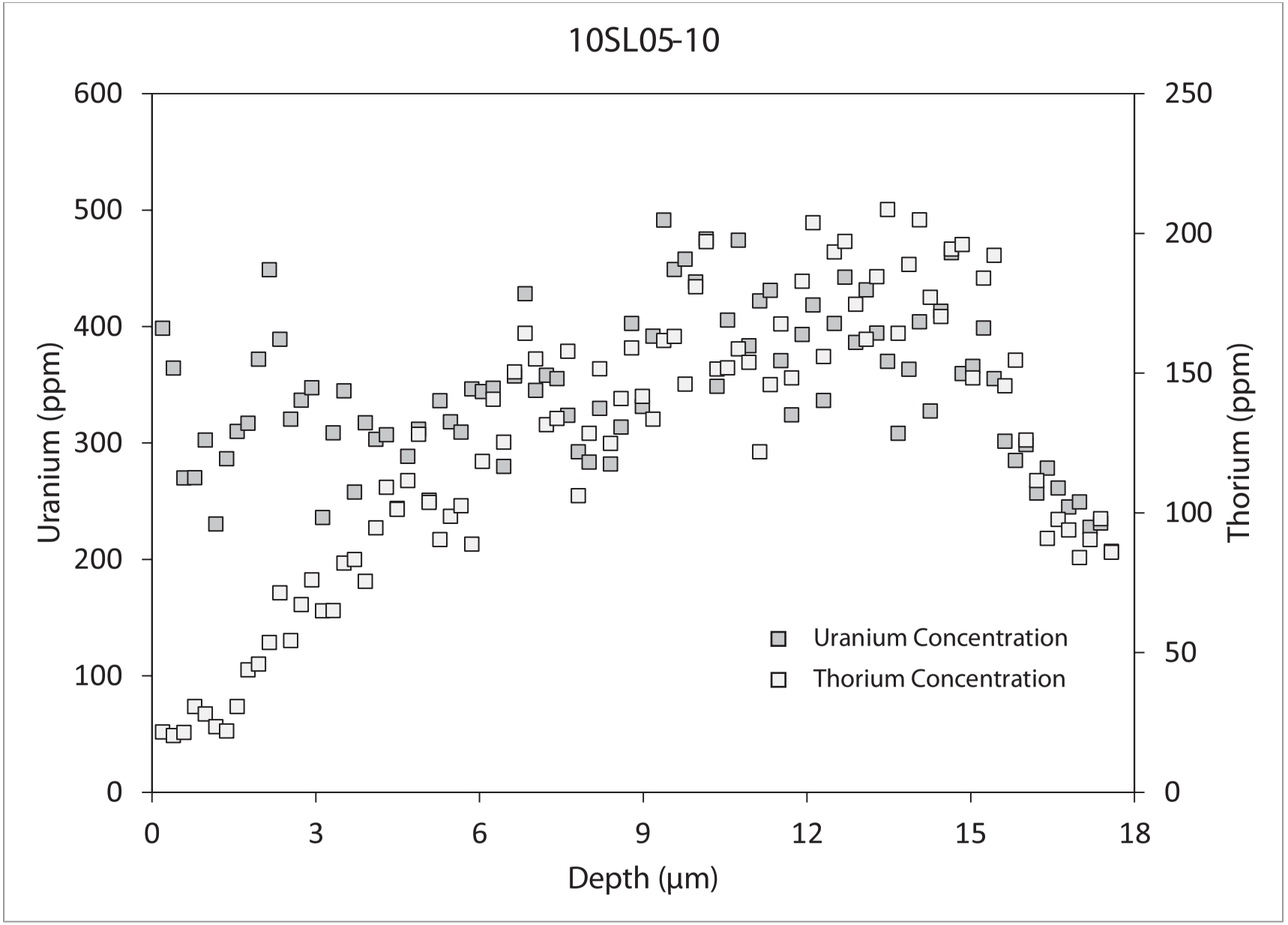
10SL05-10
600
500
400
300
200
100
0
Uranium (ppm)
250
200
150
100
50
0
Thorium (ppm)
0
3
6
9
12
15
18
Depth (µm)
Uranium Concentration
Thorium Concentration

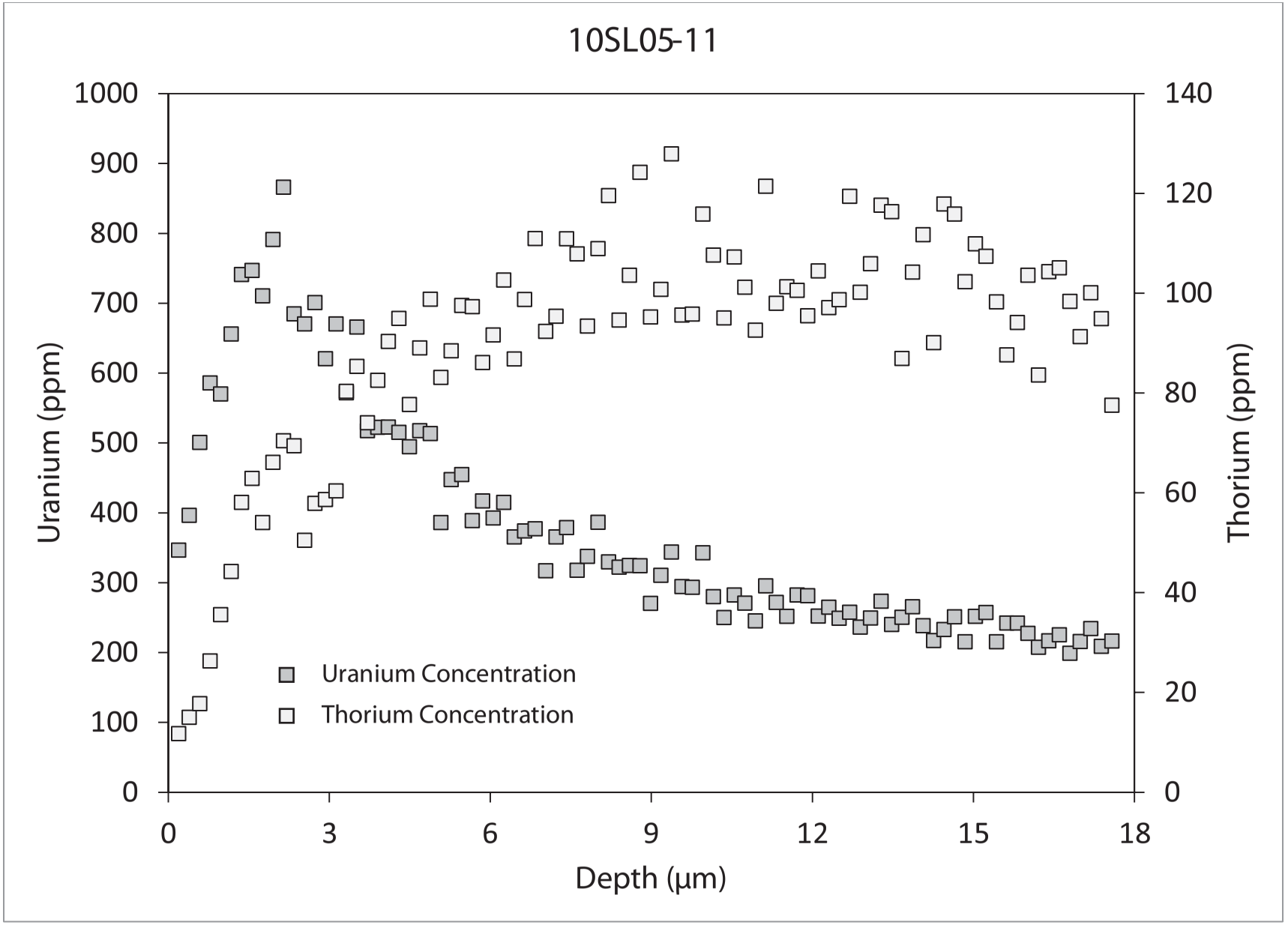
10SL05-11
Uranium (ppm)
Thorium (ppm)
Depth (µm)
Uranium Concentration
Thorium Concentration
0
100
200
300
400
500
600
700
800
900
1000
0
20
40
60
80
100
120
140
0
3
6
9
12
15
18

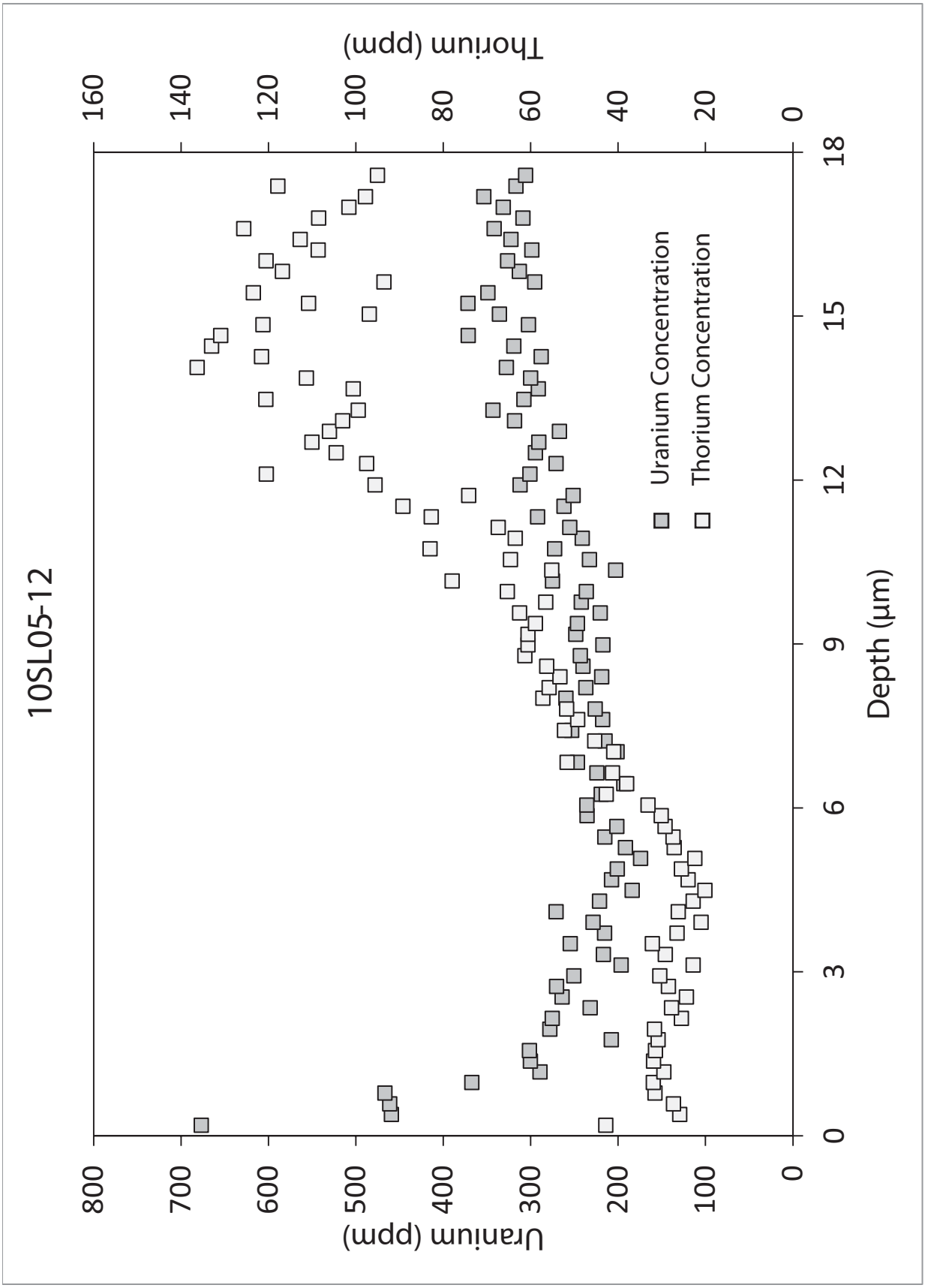
10SL05-12
Uranium (ppm)
Thorium (ppm)
Depth (µm)
Uranium Concentration
Thorium Concentration
0
100
200
300
400
500
600
700
800
0
20
40
60
80
100
120
140
160
0
3
6
9
12
15
18

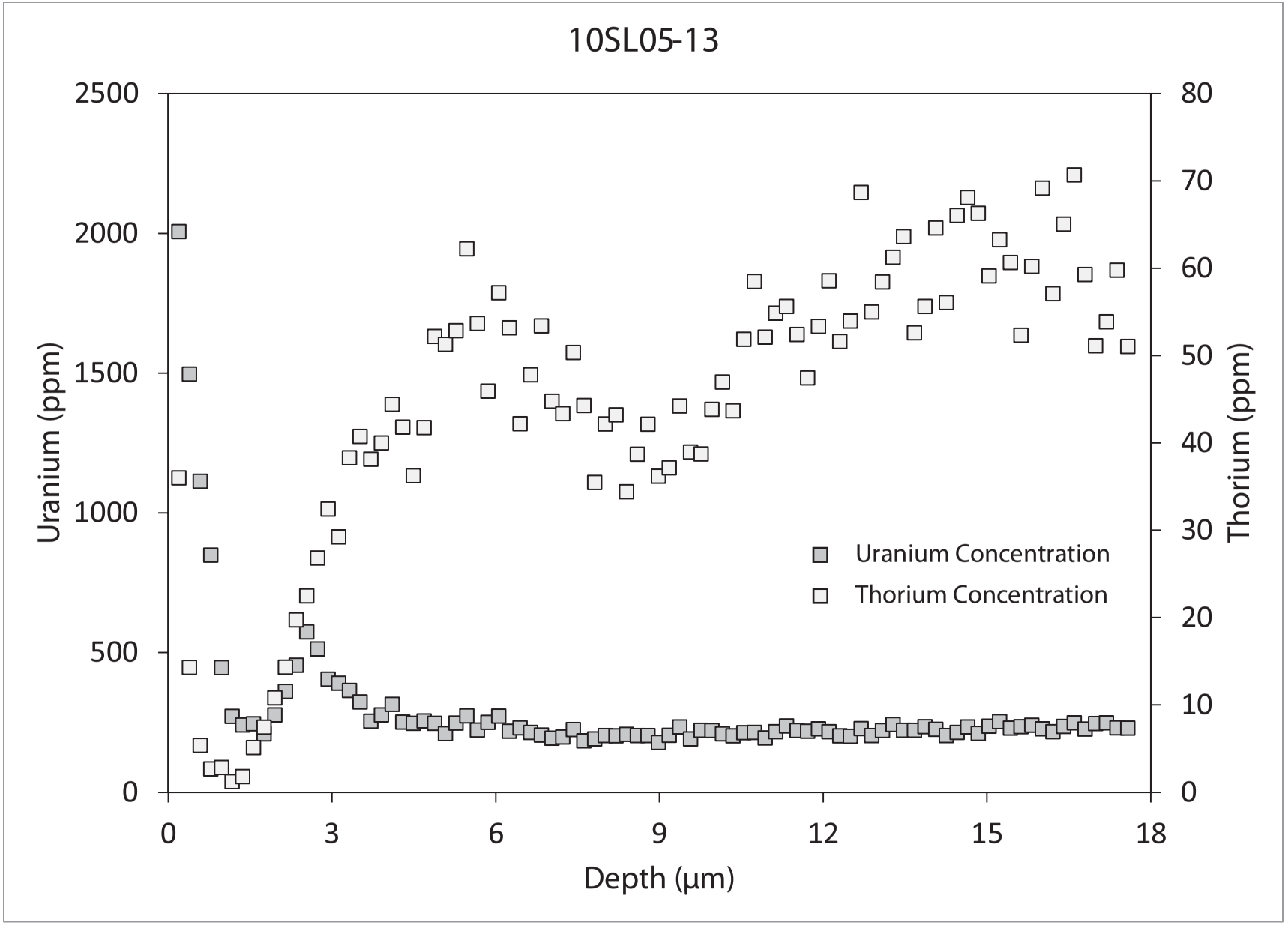
10SL05-13
Uranium (ppm)
Thorium (ppm)
Depth (µm)
Uranium Concentration
Thorium Concentration
2500
2000
1500
1000
500
0
80
70
60
50
40
30
20
10
0
0
3
6
9
12
15
18

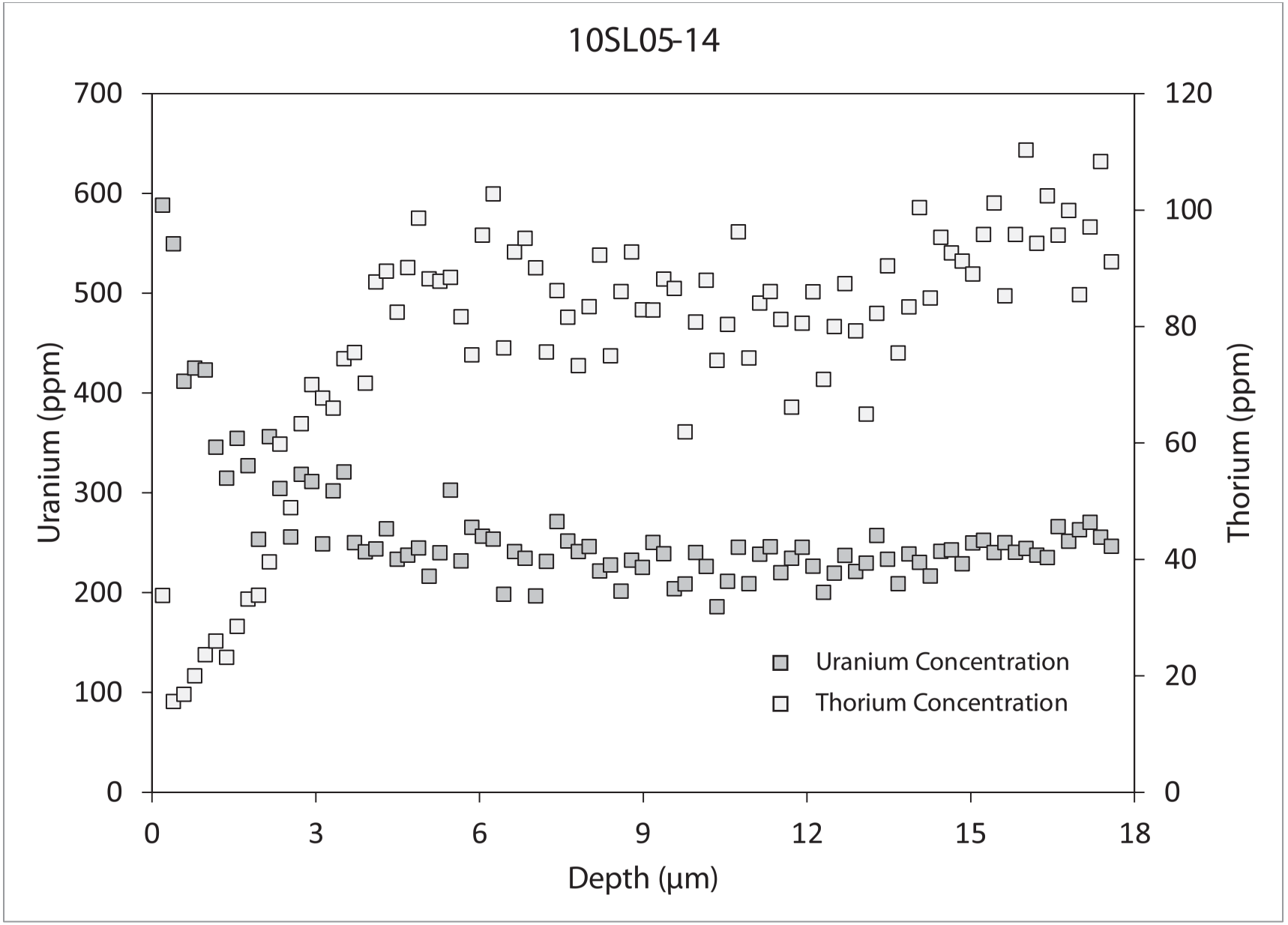
10SL05-14
Uranium (ppm)
Thorium (ppm)
Depth (µm)
Uranium Concentration
Thorium Concentration
0
100
200
300
400
500
600
700
0
20
40
60
80
100
120
0
3
6
9
12
15
18

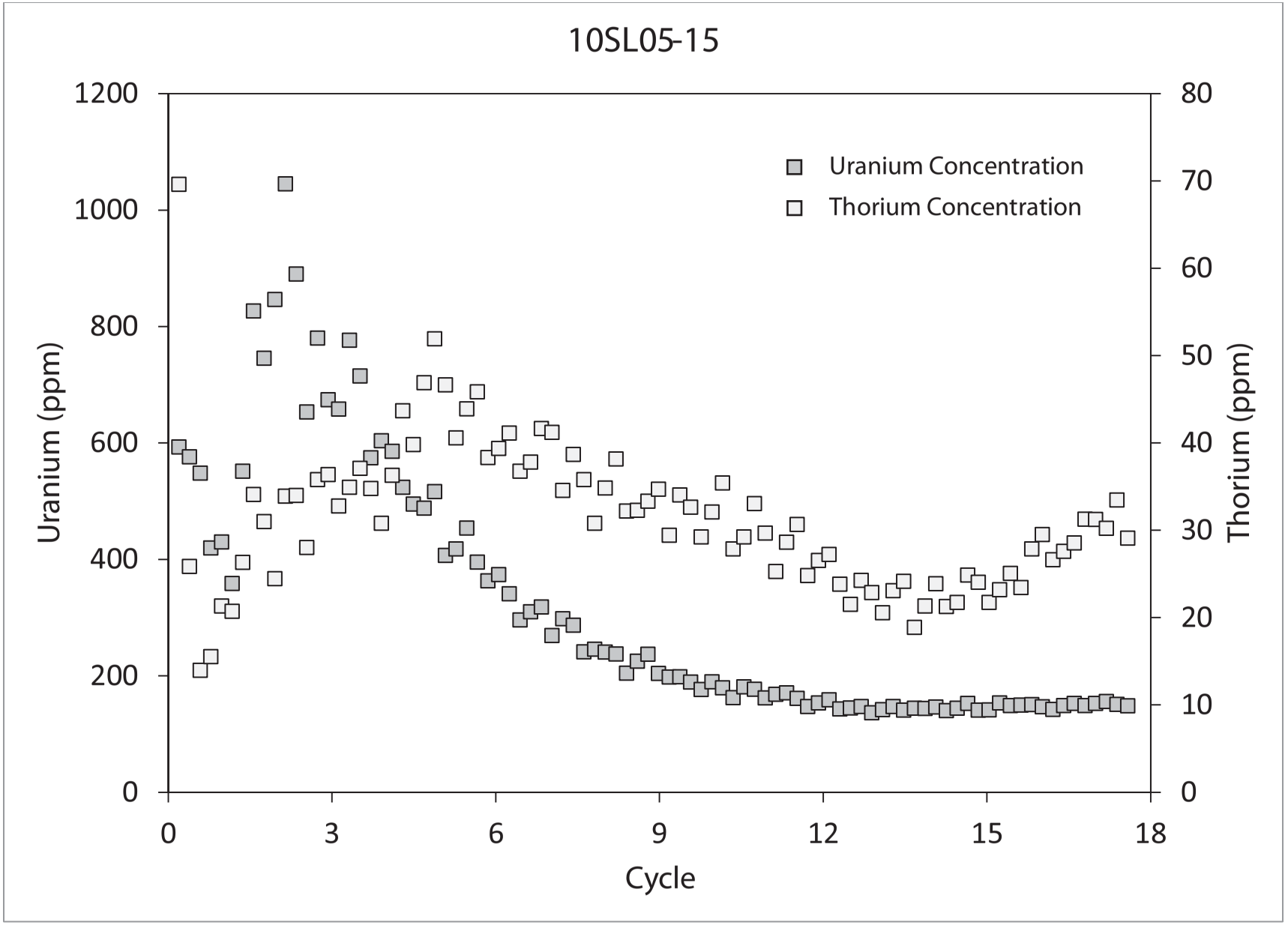
10SL05-15
Uranium Concentration
Thorium Concentration
Uranium (ppm)
Thorium (ppm)
Cycle
0
200
400
600
800
1000
1200
0
10
20
30
40
50
60
70
80
0
3
6
9
12
15
18

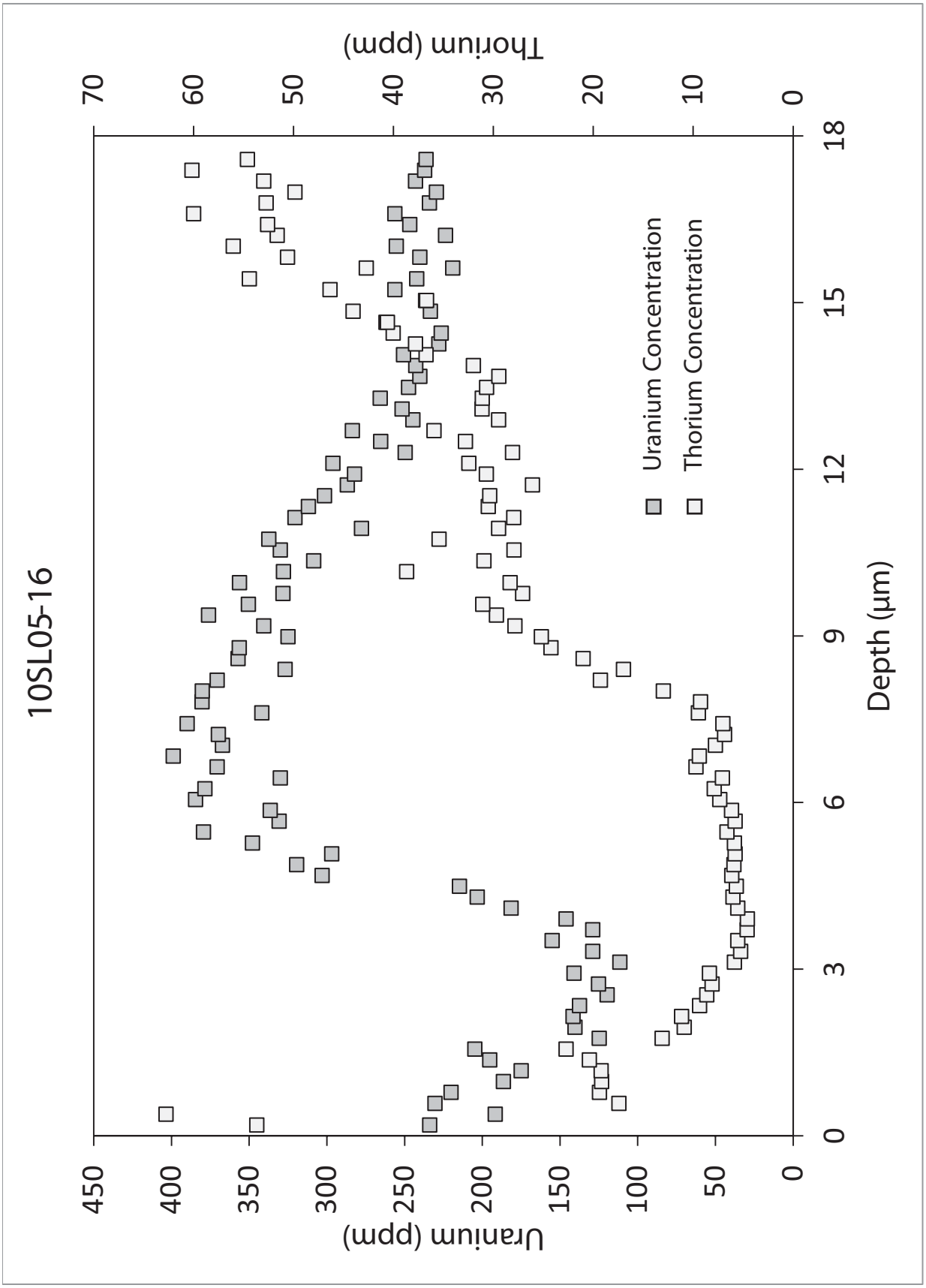
10SL05-16
Uranium (ppm)
Thorium (ppm)
Depth (µm)
Uranium Concentration
Thorium Concentration
0
50
100
150
200
250
300
350
400
450
0
10
20
30
40
50
60
70
0
3
6
9
12
15
18

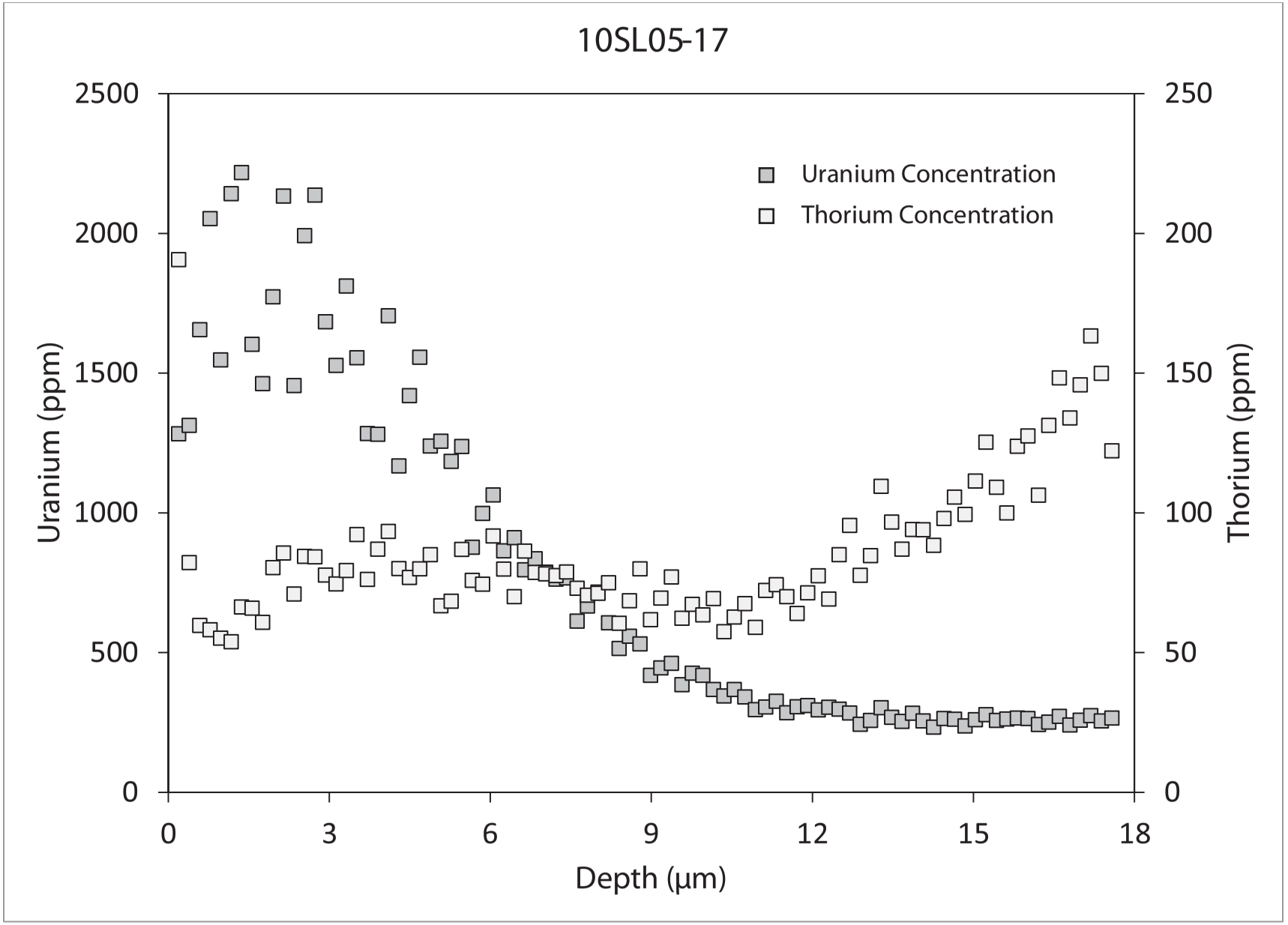
10SL05-17
Uranium Concentration
Thorium Concentration
Uranium (ppm)
Thorium (ppm)
Depth (µm)
2500
2000
1500
1000
500
0
250
200
150
100
50
0
0
3
6
9
12
15
18

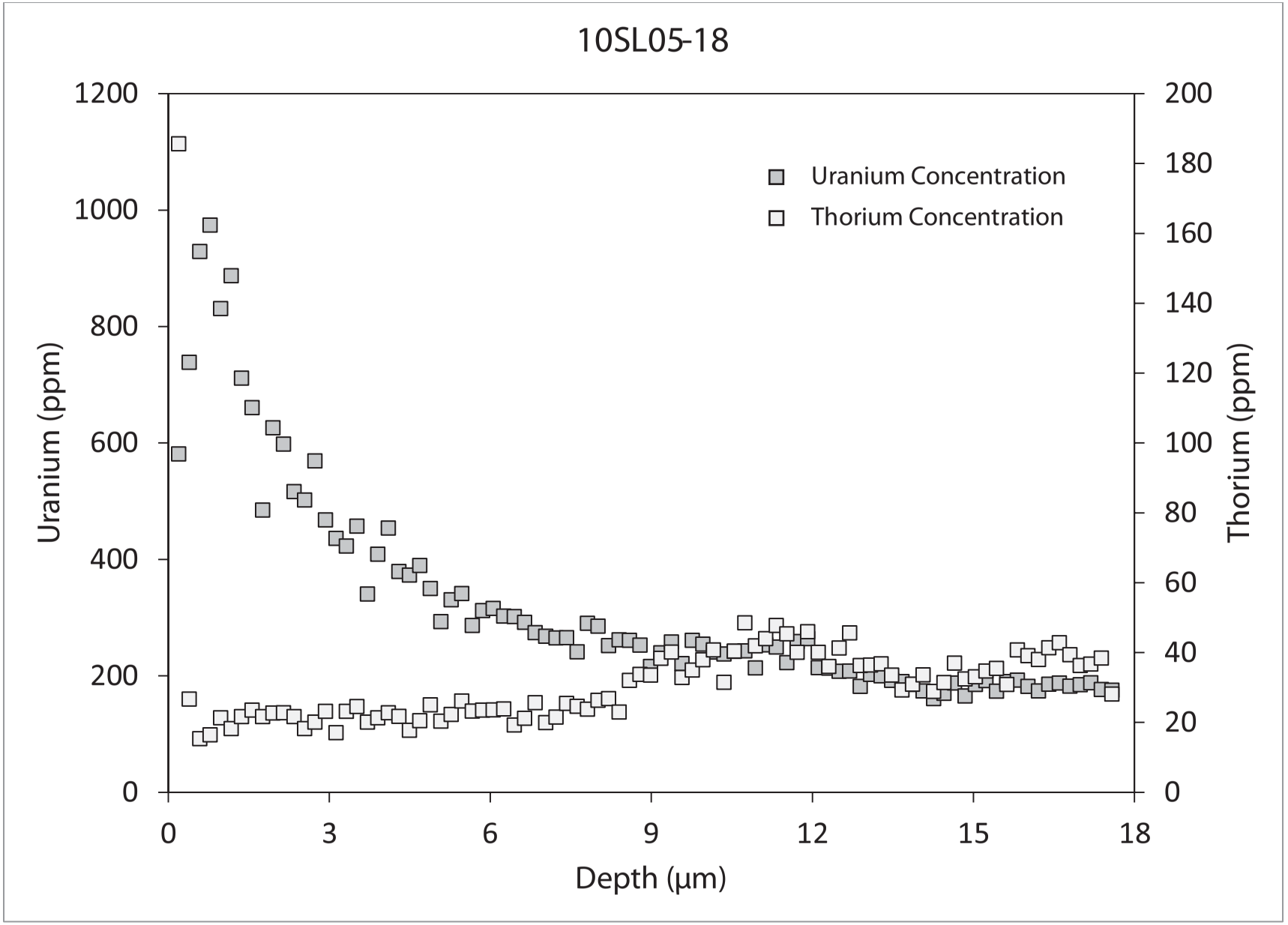
10SL05-18
Uranium Concentration
Thorium Concentration
Uranium (ppm)
Thorium (ppm)
Depth (µm)
0
200
400
600
800
1000
1200
0
20
40
60
80
100
120
140
160
180
200
0
3
6
9
12
15
18

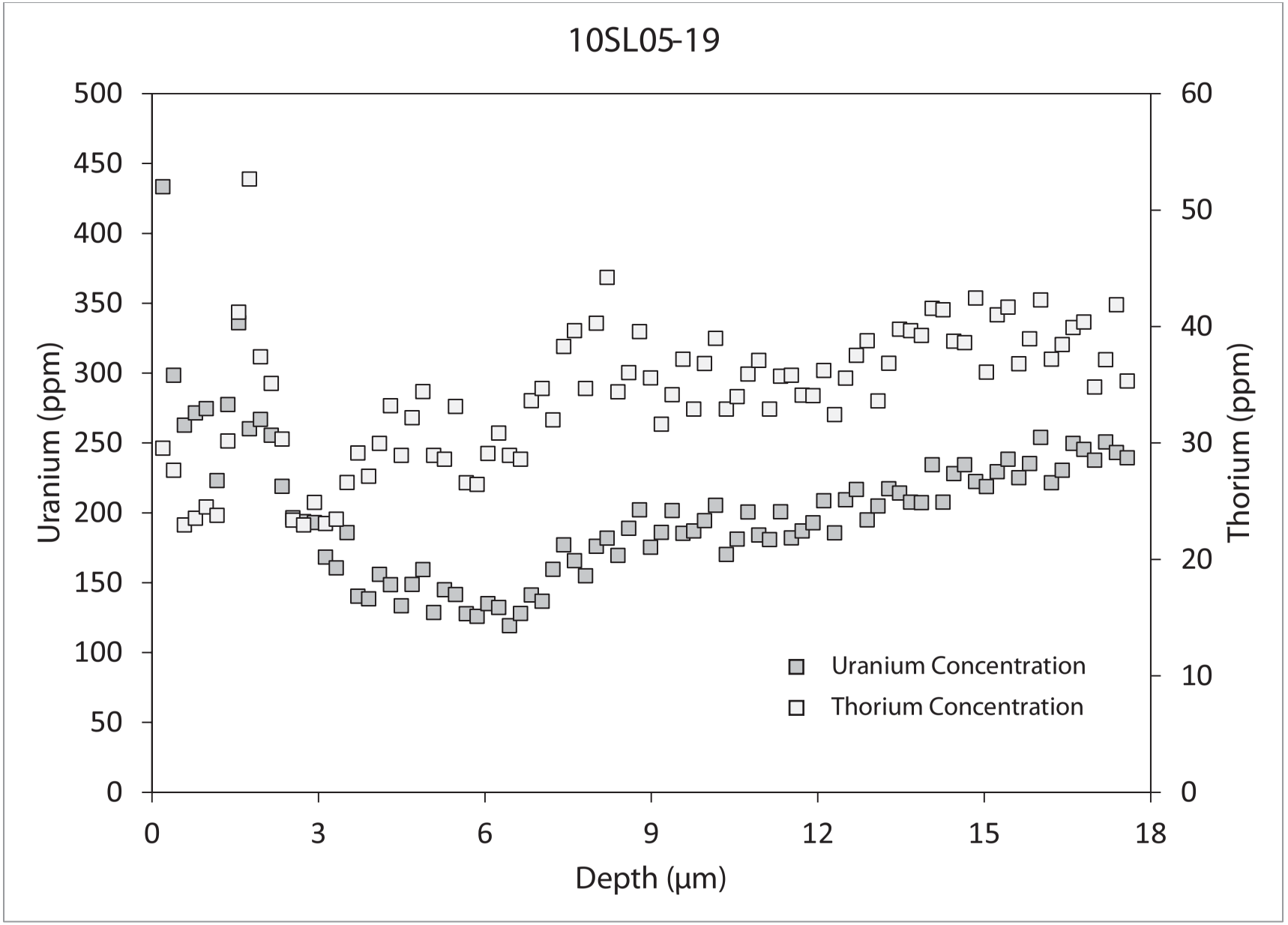
10SL05-19
Uranium (ppm)
Thorium (ppm)
Depth (µm)
Uranium Concentration
Thorium Concentration
0
50
100
150
200
250
300
350
400
450
500
0
10
20
30
40
50
60
0
3
6
9
12
15
18

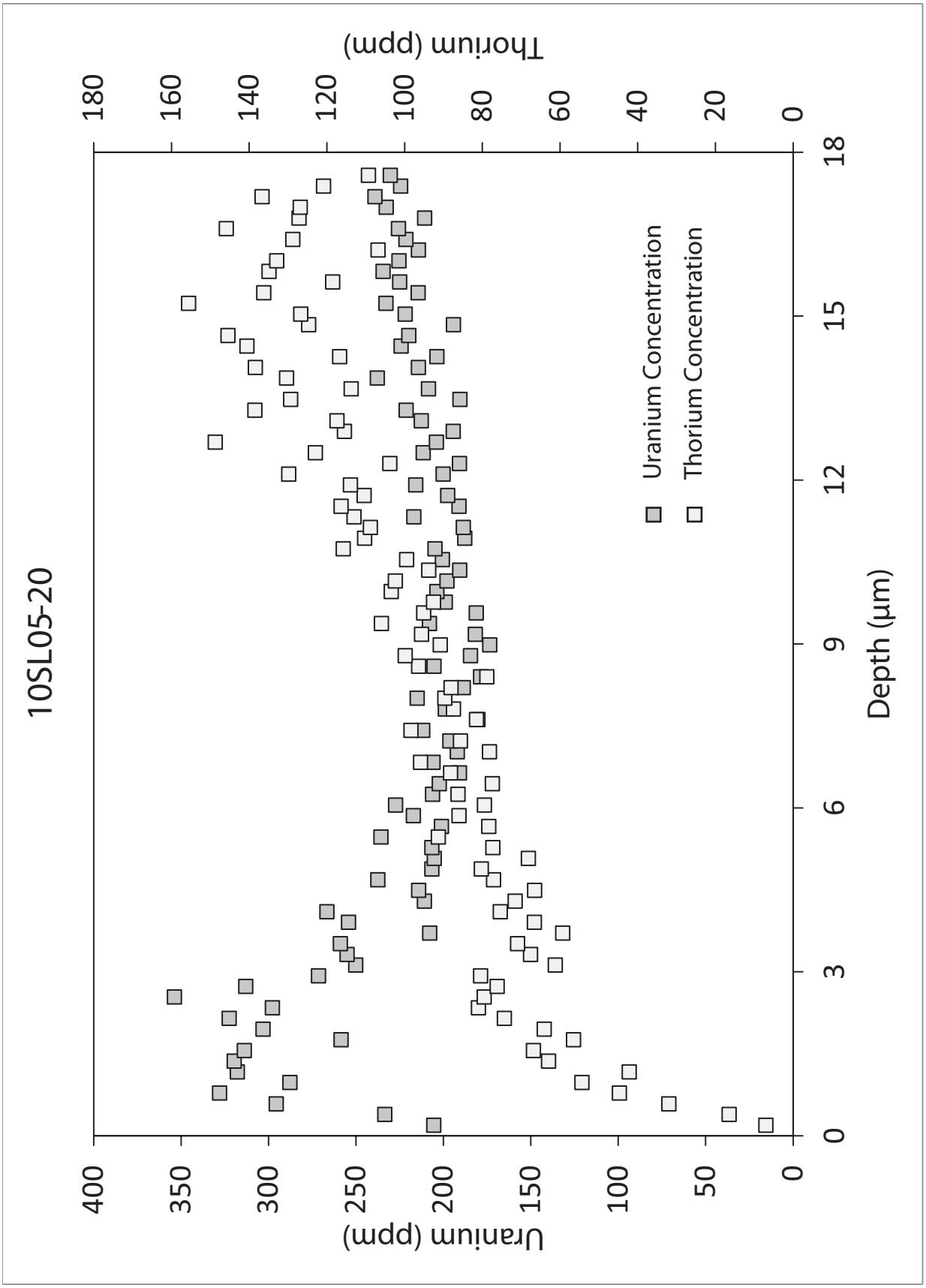
10SL05-20
Uranium (ppm)
Thorium (ppm)
Depth (µm)
Uranium Concentration
Thorium Concentration
0
50
100
150
200
250
300
350
400
0
20
40
60
80
100
120
140
160
180
0
3
6
9
12
15
18

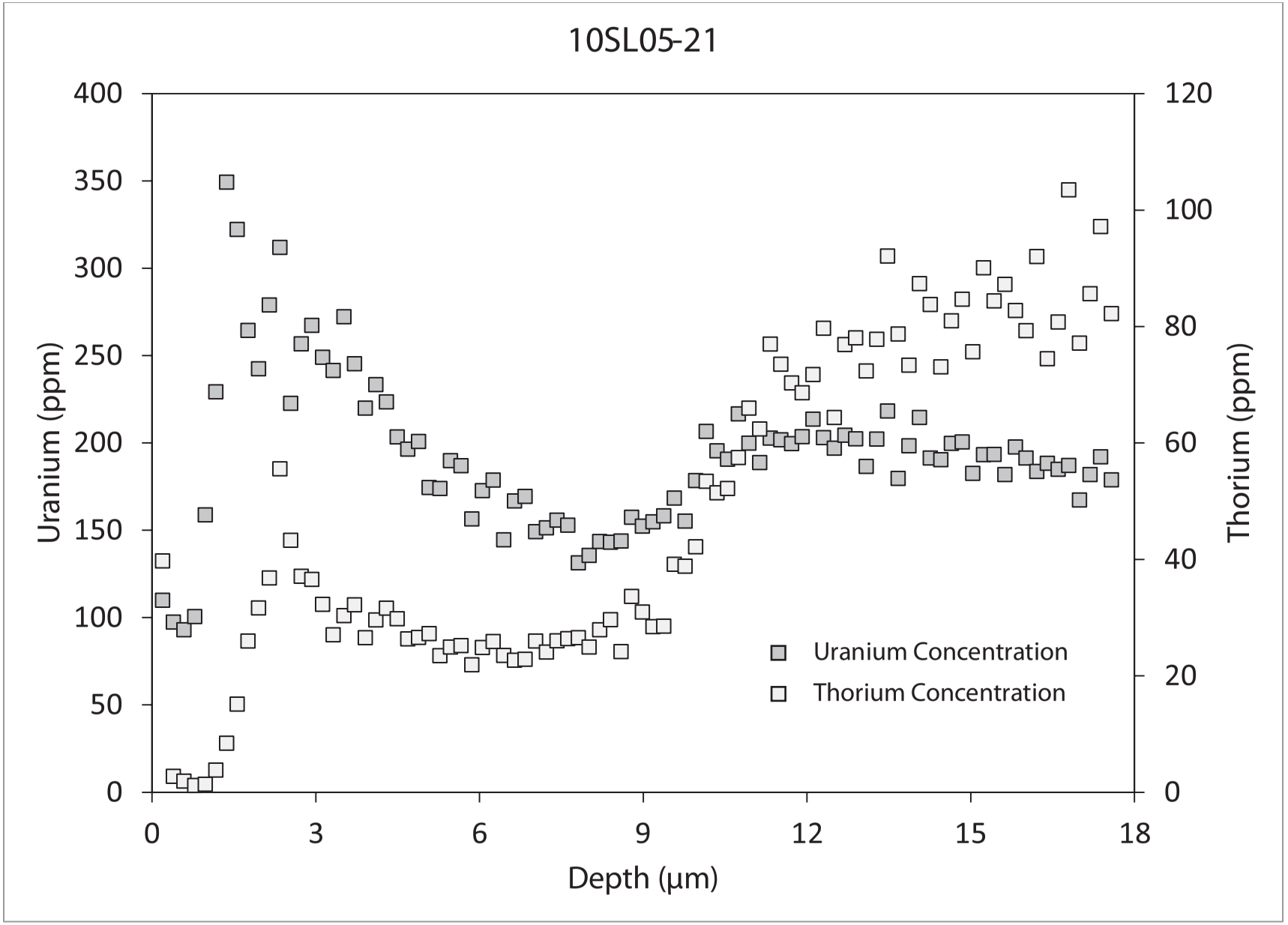
10SL05-21
Uranium (ppm)
Thorium (ppm)
Depth (µm)
Uranium Concentration
Thorium Concentration
400
350
300
250
200
150
100
50
0
120
100
80
60
40
20
0
0
3
6
9
12
15
18

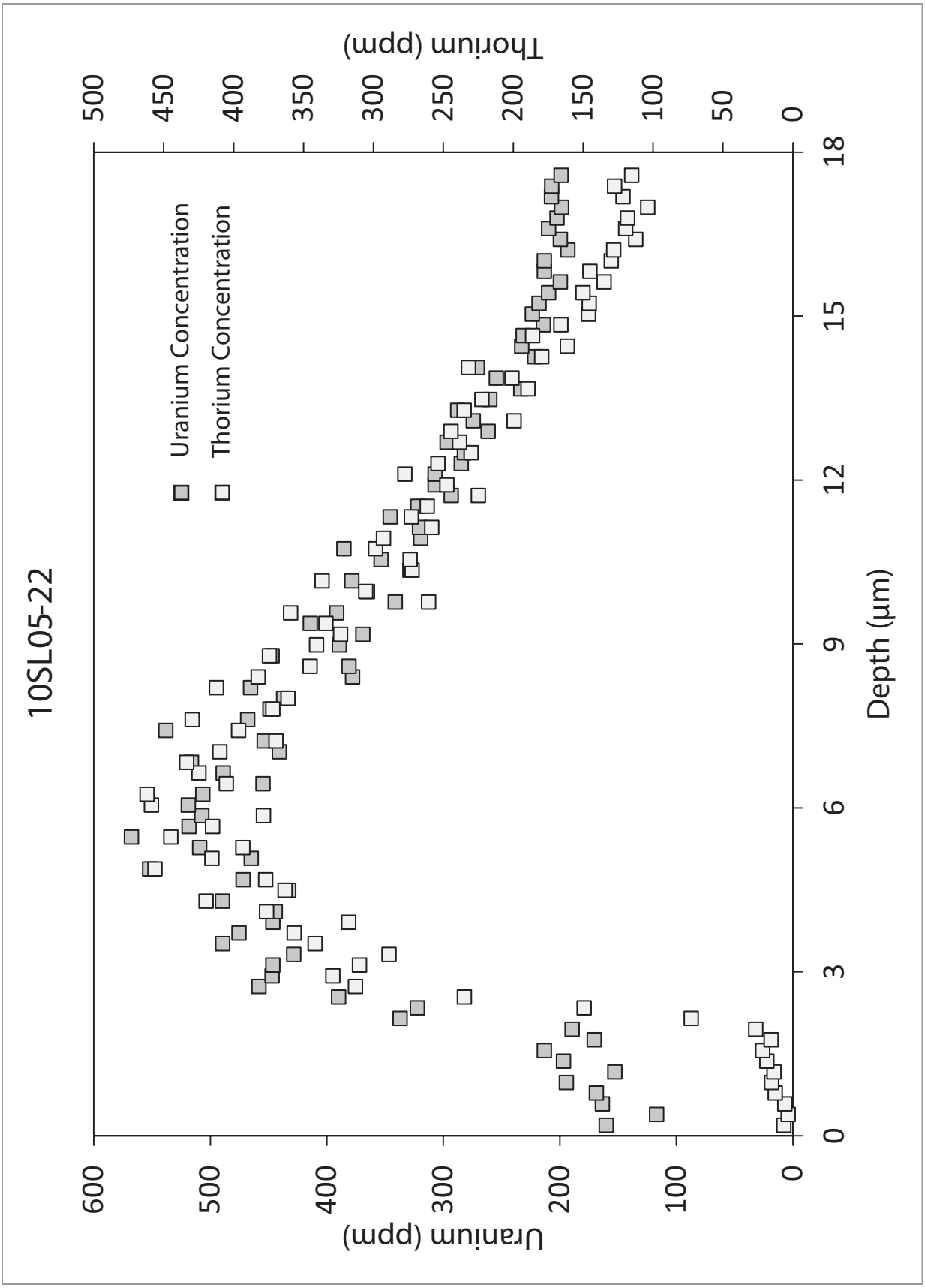
10SL05-22
Uranium Concentration
Thorium Concentration
Uranium (ppm)
Thorium (ppm)
Depth (µm)
0
100
200
300
400
500
600
0
50
100
150
200
250
300
350
400
450
500
0
3
6
9
12
15
18

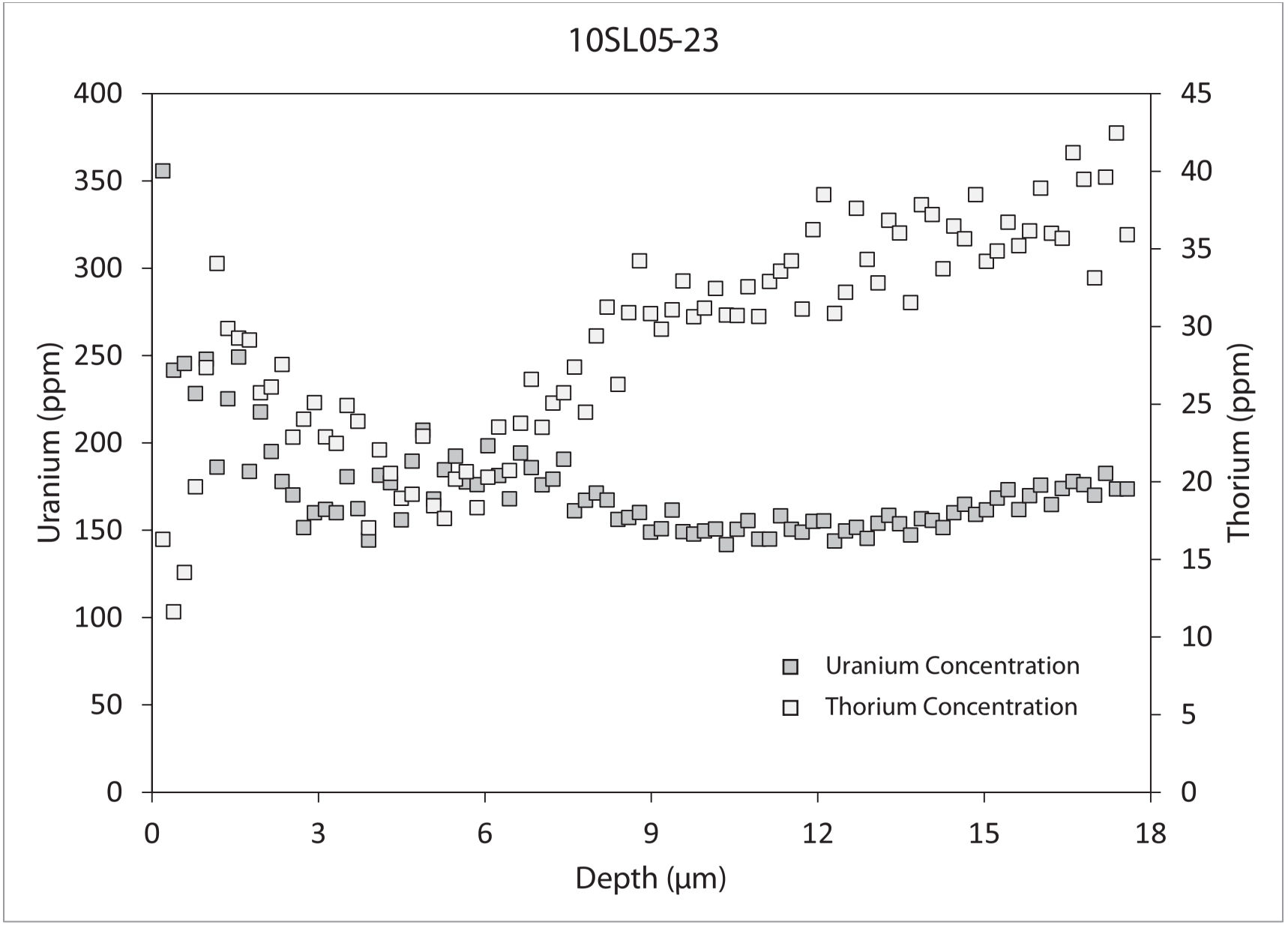
10SL05-23
Uranium (ppm)
Thorium (ppm)
Depth (µm)
Uranium Concentration
Thorium Concentration
400
350
300
250
200
150
100
50
0
45
40
35
30
25
20
15
10
5
0
0
3
6
9
12
15
18

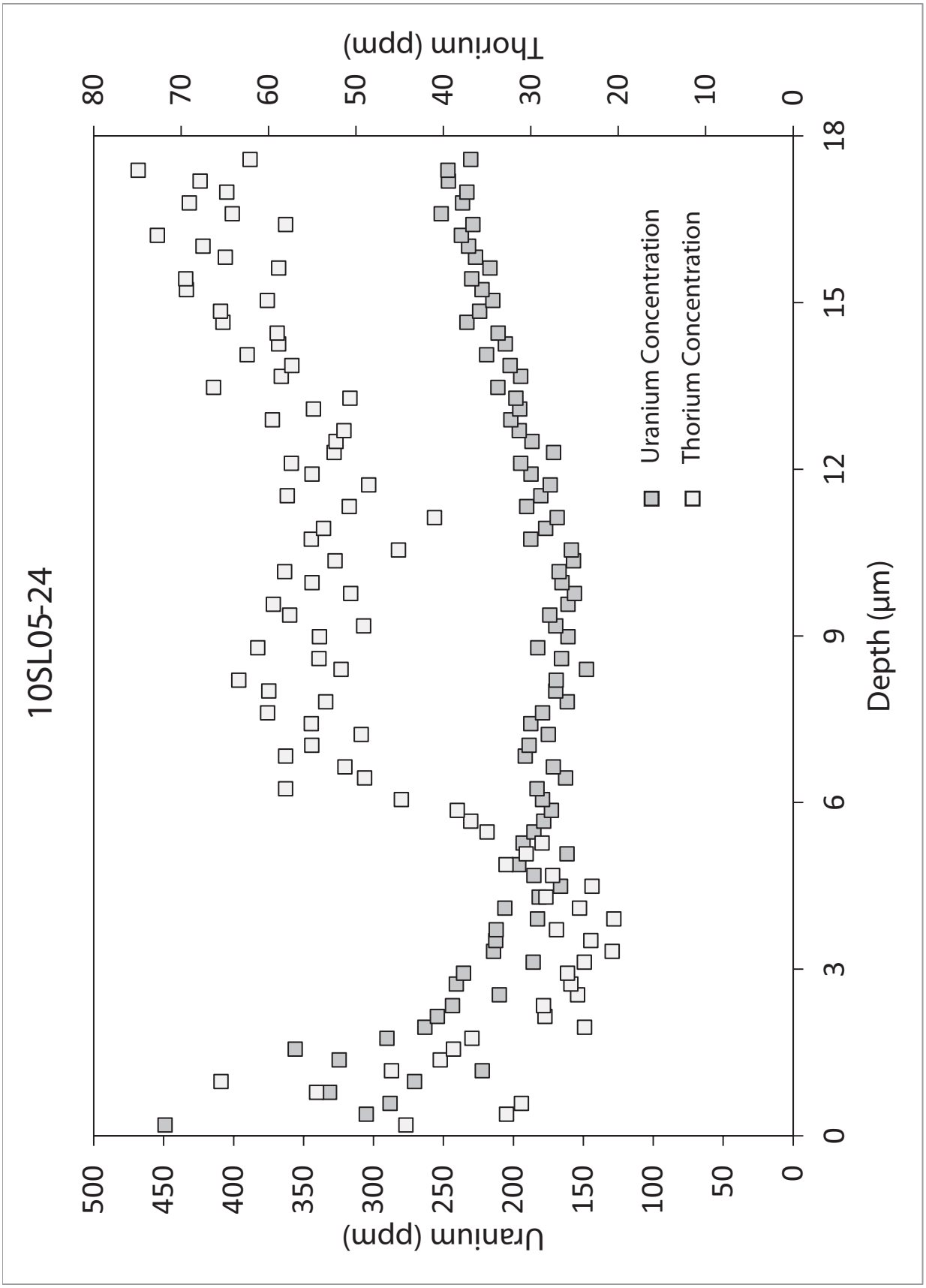
10SL05-24
Uranium (ppm)
Thorium (ppm)
Depth (µm)
Uranium Concentration
Thorium Concentration
0
50
100
150
200
250
300
350
400
450
500
0
10
20
30
40
50
60
70
80
0
3
6
9
12
15
18

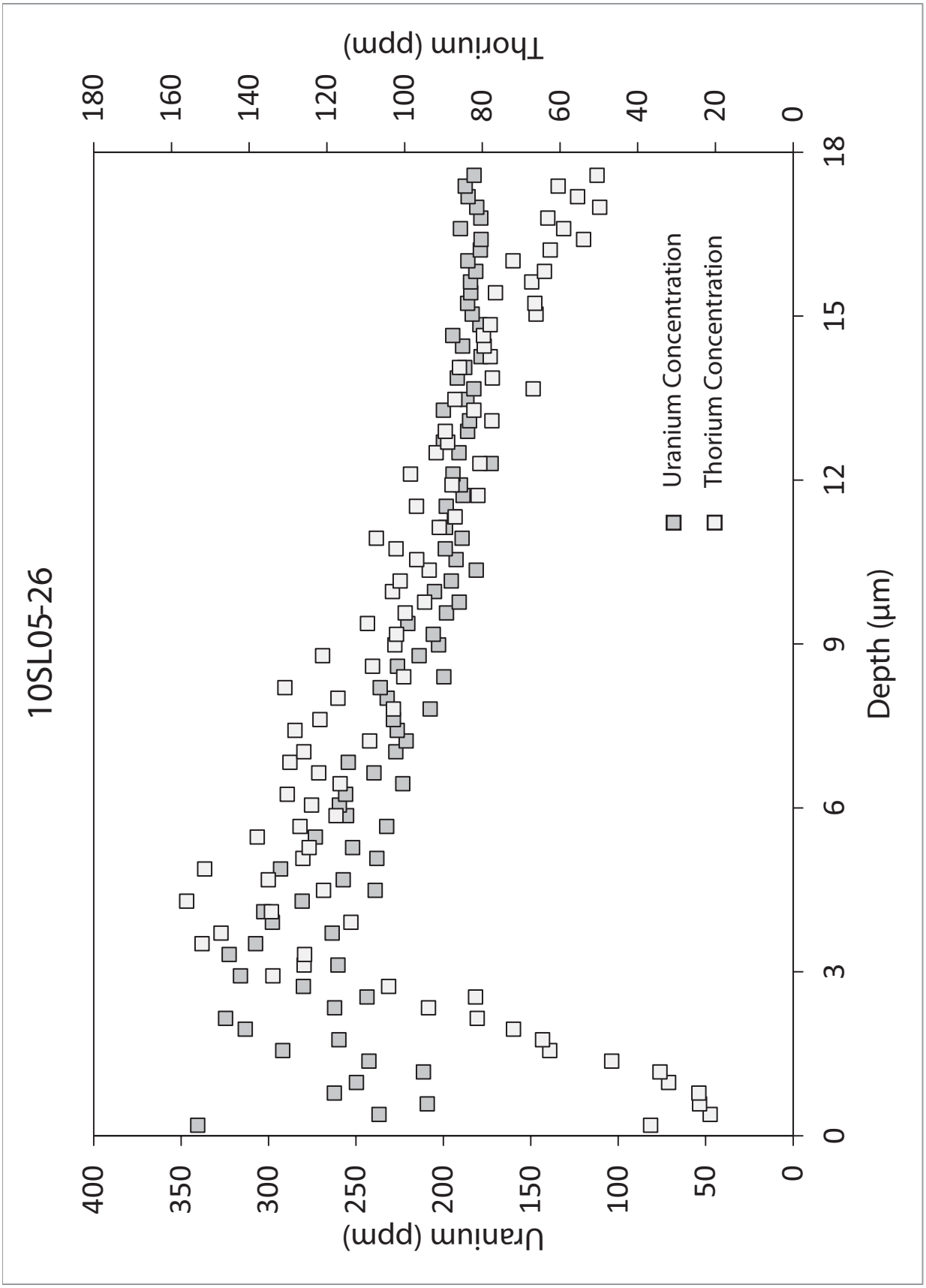
10SL05-26
Uranium (ppm)
Thorium (ppm)
Depth (µm)
Uranium Concentration
Thorium Concentration
0
50
100
150
200
250
300
350
400
0
20
40
60
80
100
120
140
160
180
0
3
6
9
12
15
18

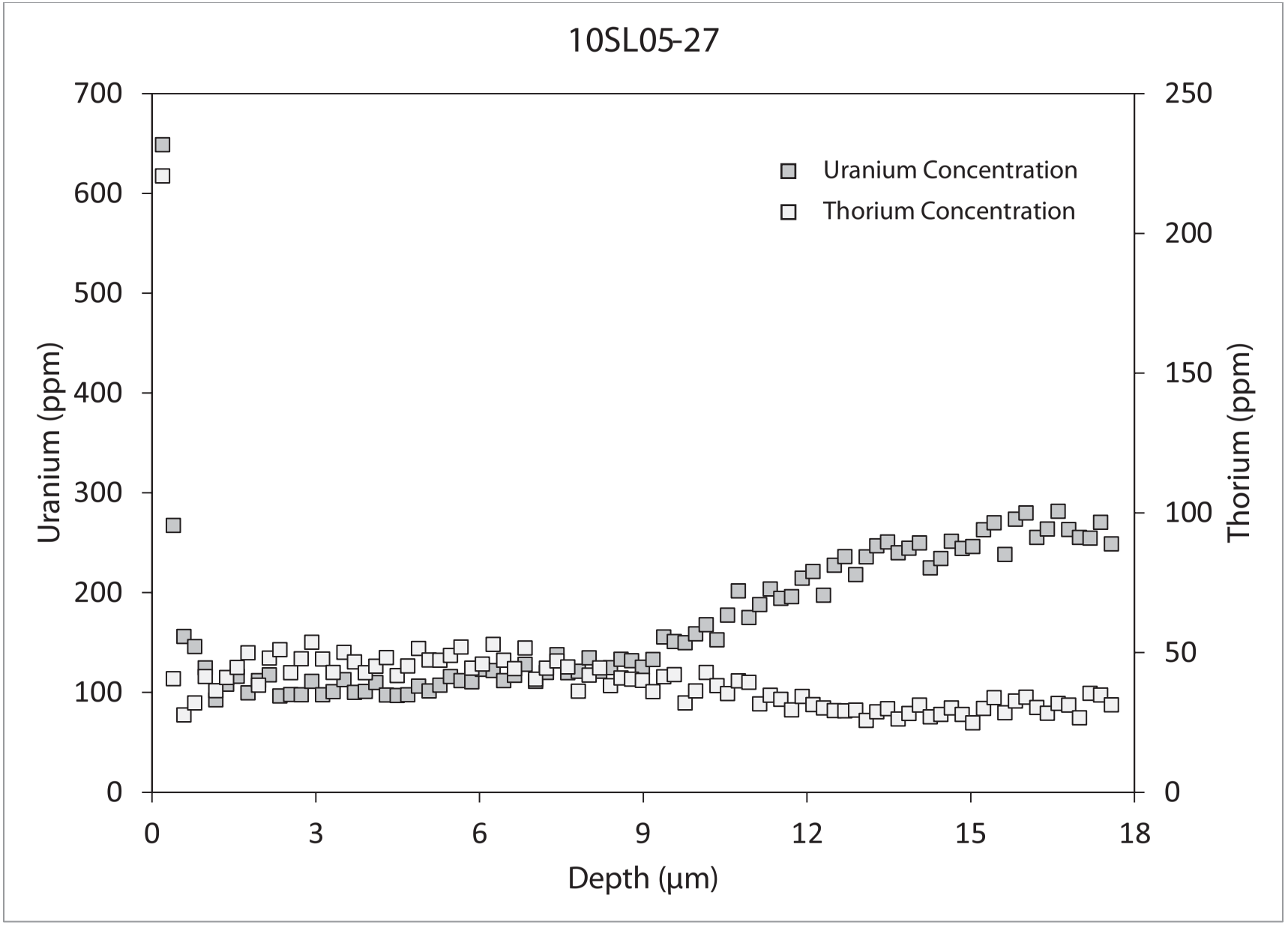
10SL05-27
Uranium Concentration
Thorium Concentration
Uranium (ppm)
Thorium (ppm)
Depth (µm)
0
100
200
300
400
500
600
700
0
50
100
150
200
250
0
3
6
9
12
15
18

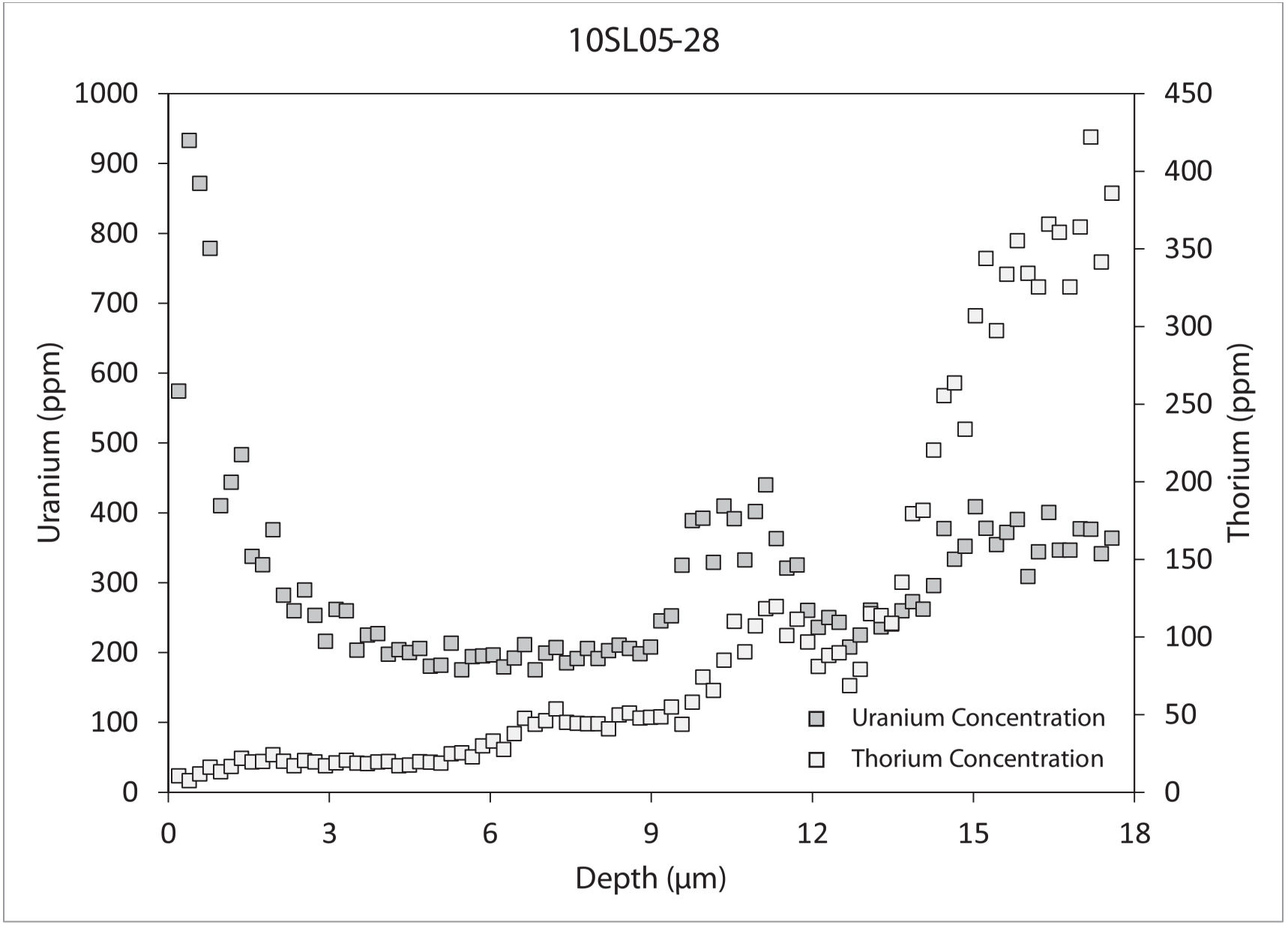
10SL05-28
Uranium (ppm)
Thorium (ppm)
Depth (µm)
Uranium Concentration
Thorium Concentration
0
100
200
300
400
500
600
700
800
900
1000
0
50
100
150
200
250
300
350
400
450
0
3
6
9
12
15
18

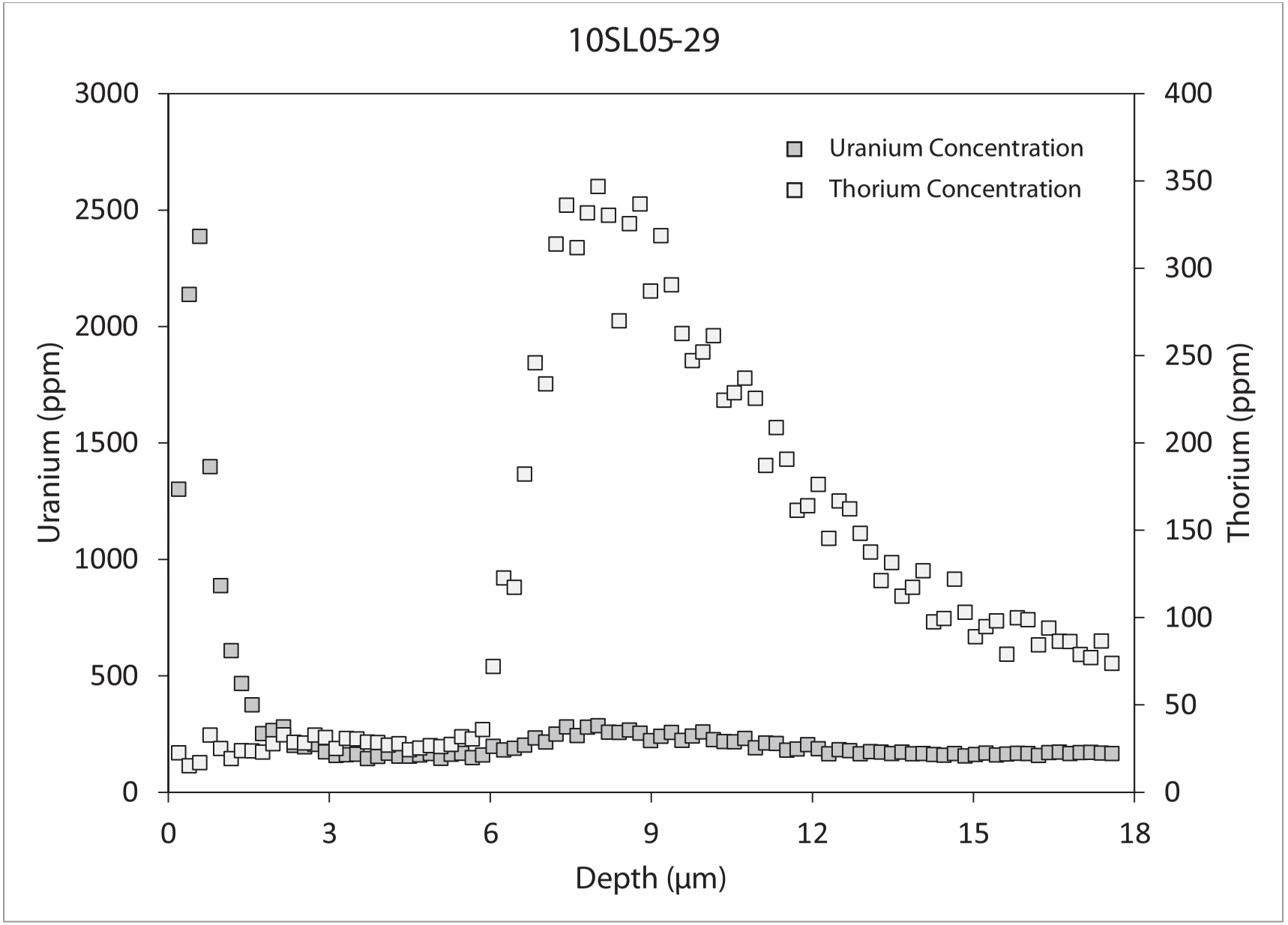
10SL05-29
Uranium Concentration
Thorium Concentration
Uranium (ppm)
Thorium (ppm)
Depth (µm)
3000
2500
2000
1500
1000
500
0
400
350
300
250
200
150
100
50
0
0
3
6
9
12
15
18

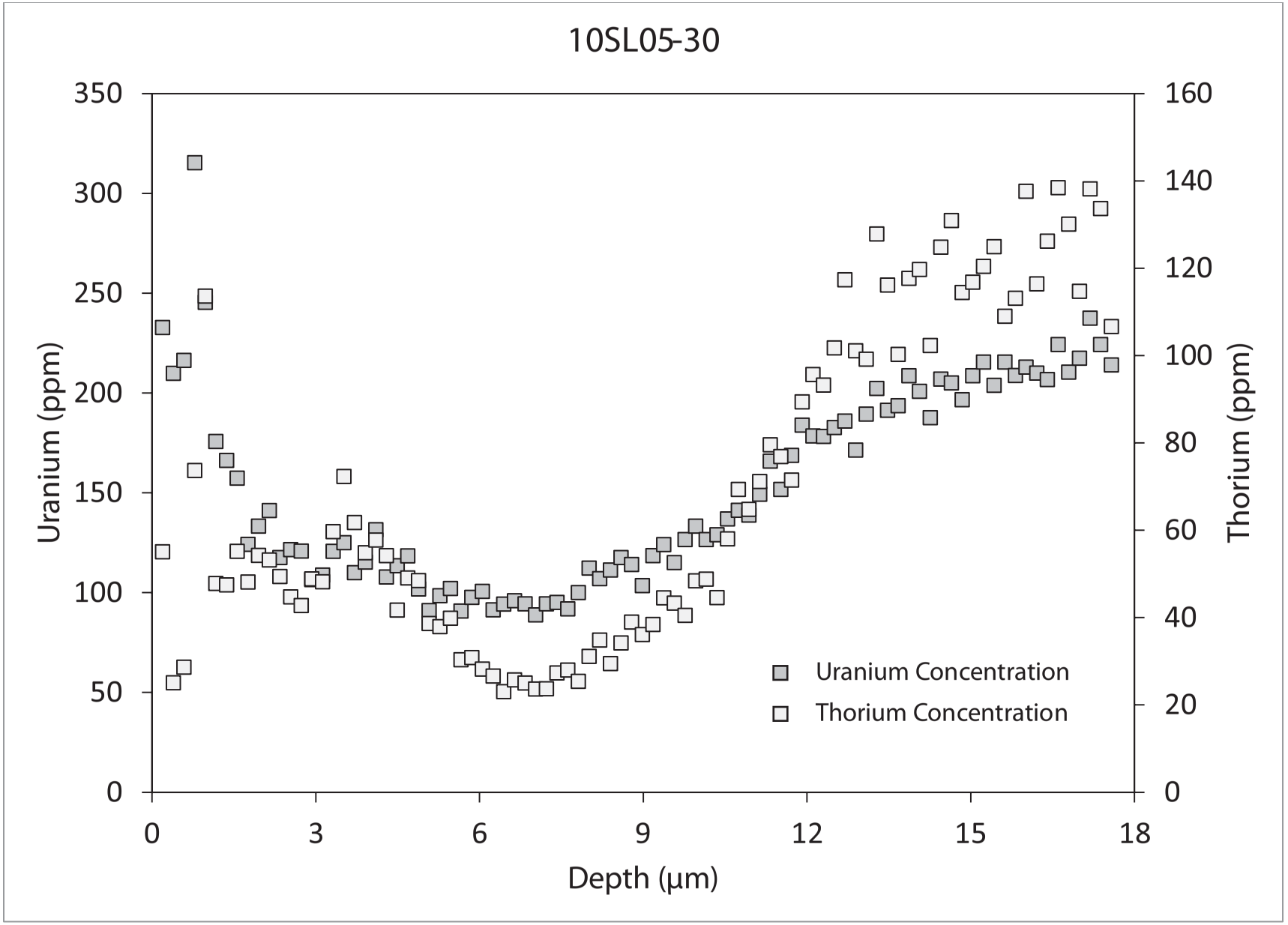
10SL05-30
Uranium (ppm)
Thorium (ppm)
Depth (µm)
Uranium Concentration
Thorium Concentration
0
50
100
150
200
250
300
350
0
20
40
60
80
100
120
140
160
0
3
6
9
12
15
18

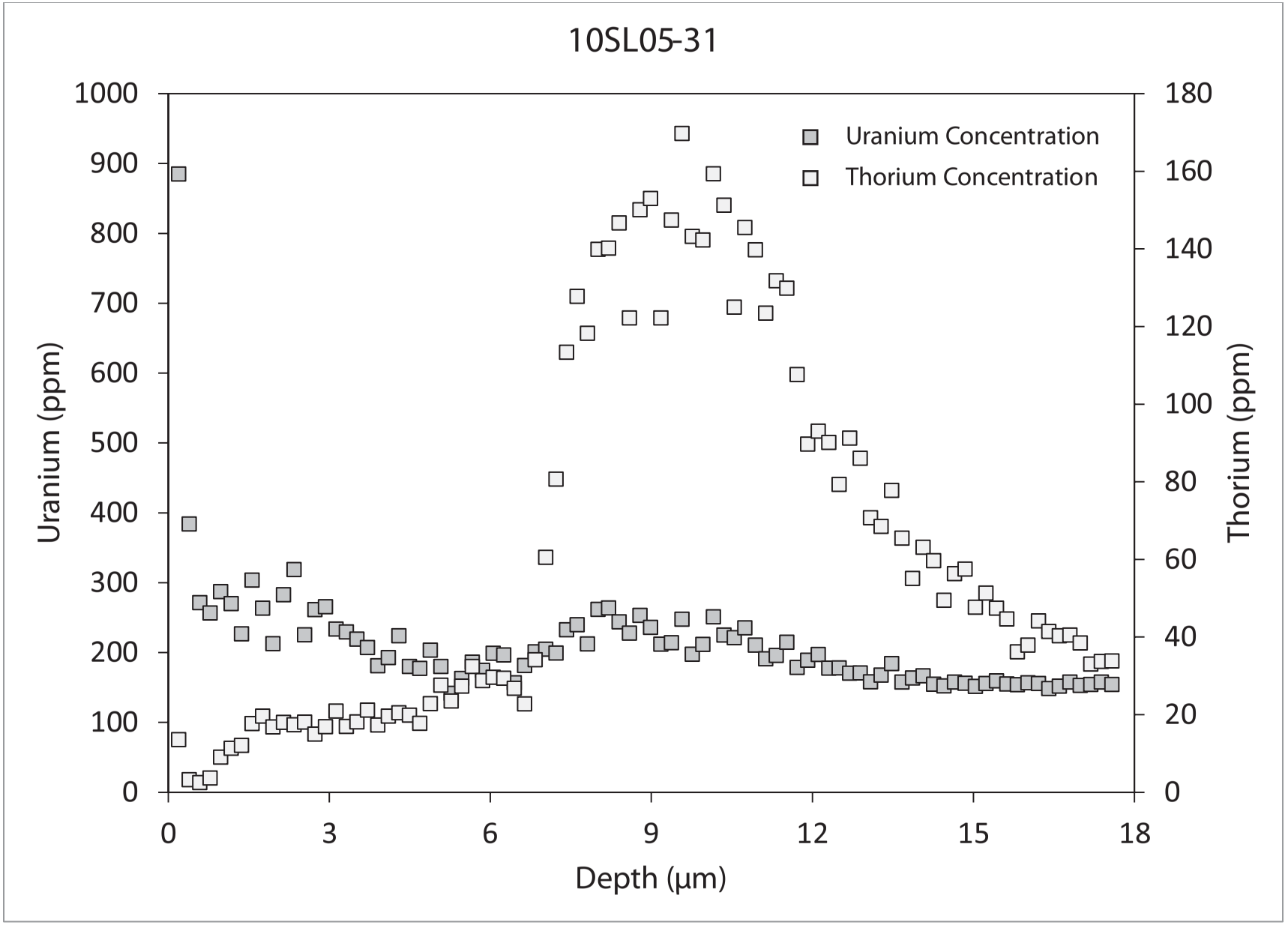
10SL05-31
Uranium Concentration
Thorium Concentration
Uranium (ppm)
Thorium (ppm)
Depth (µm)
0
100
200
300
400
500
600
700
800
900
1000
0
20
40
60
80
100
120
140
160
180
0
3
6
9
12
15
18

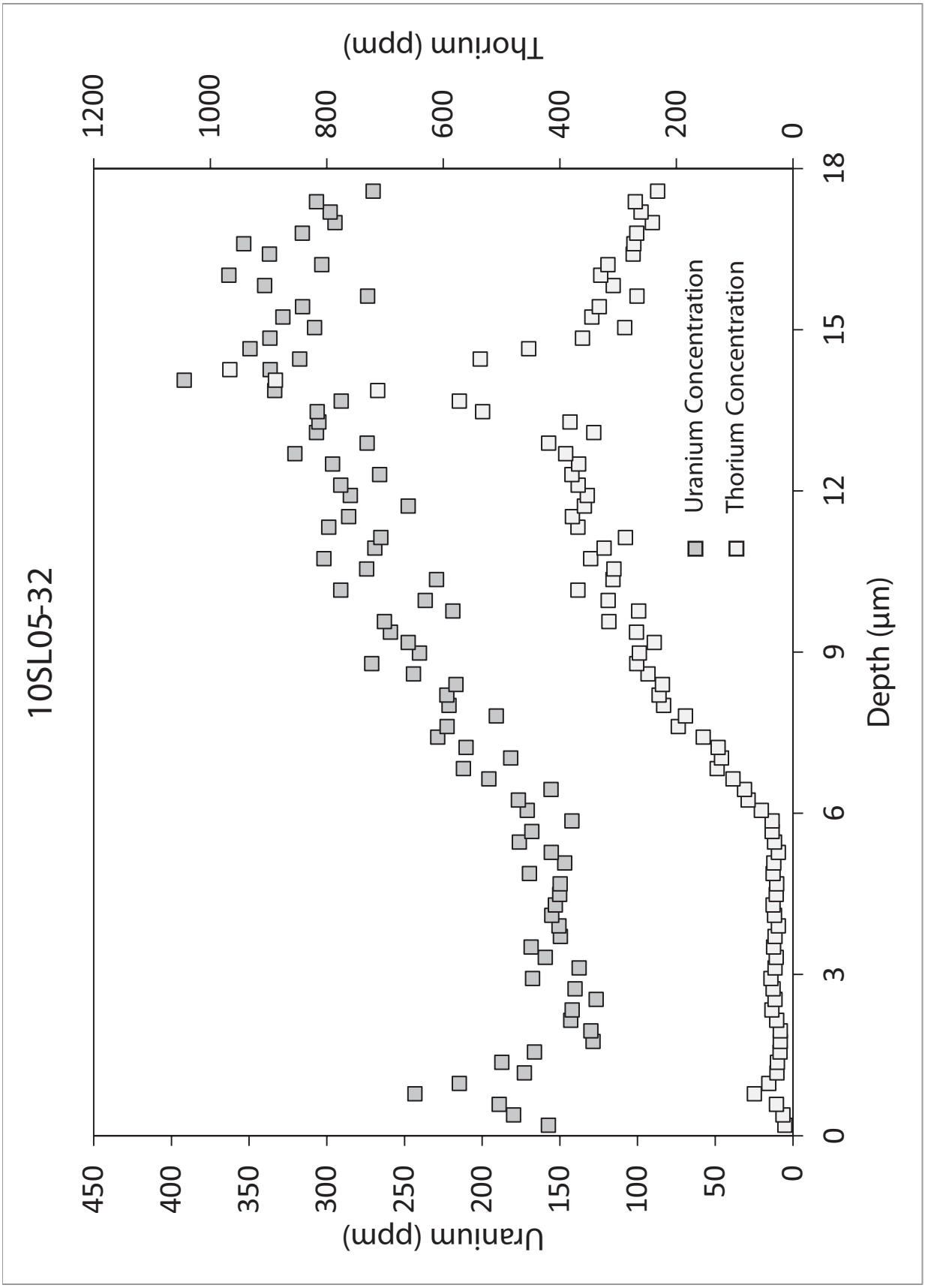
10SL05-32
Uranium (ppm)
Thorium (ppm)
Depth (µm)
Uranium Concentration
Thorium Concentration
0
50
100
150
200
250
300
350
400
450
0
200
400
600
800
1000
1200
0
3
6
9
12
15
18

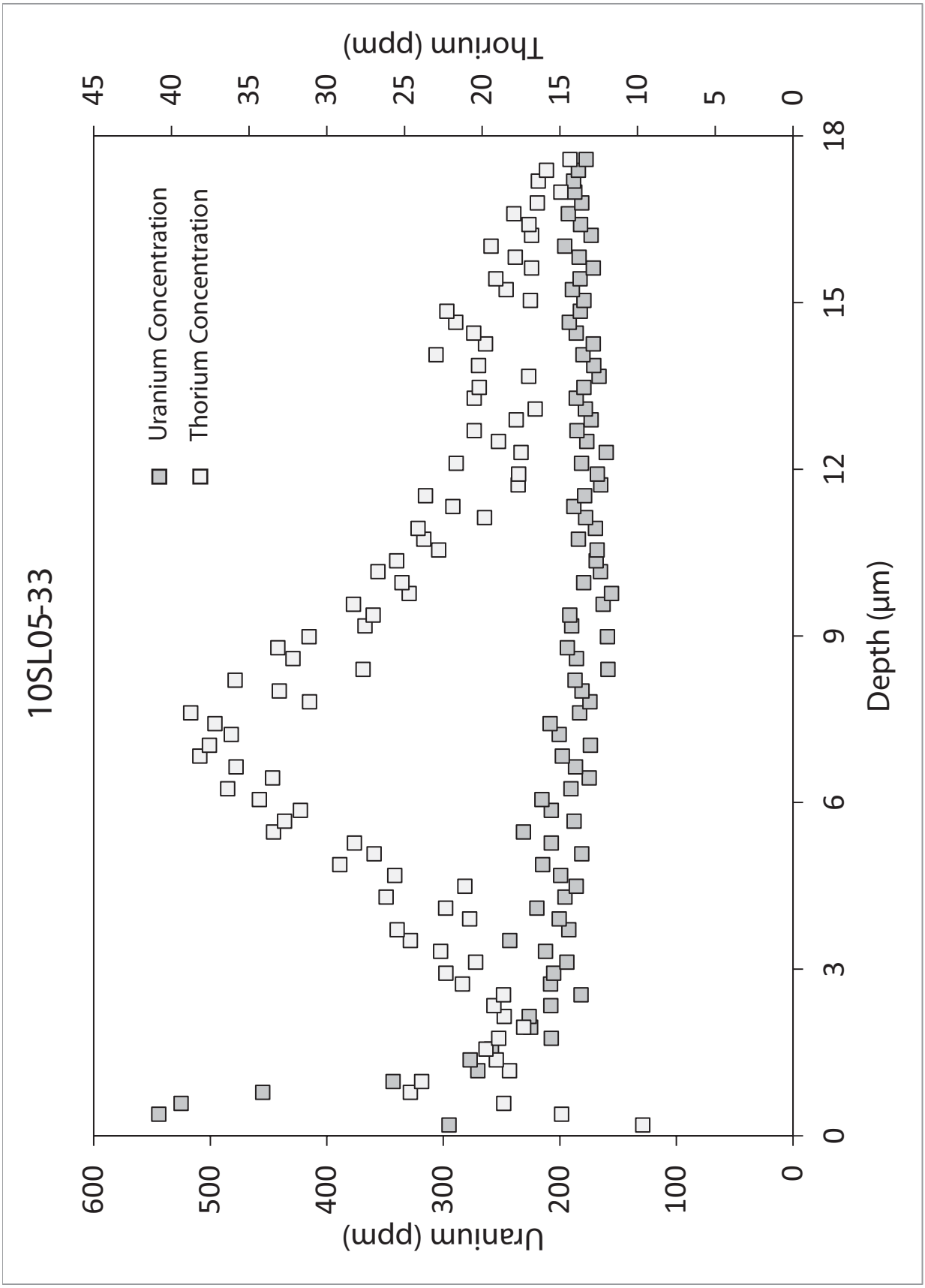
10SL05-33
Uranium Concentration
Thorium Concentration
Uranium (ppm)
Thorium (ppm)
Depth (µm)
0
100
200
300
400
500
600
0
5
10
15
20
25
30
35
40
45
0
3
6
9
12
15
18

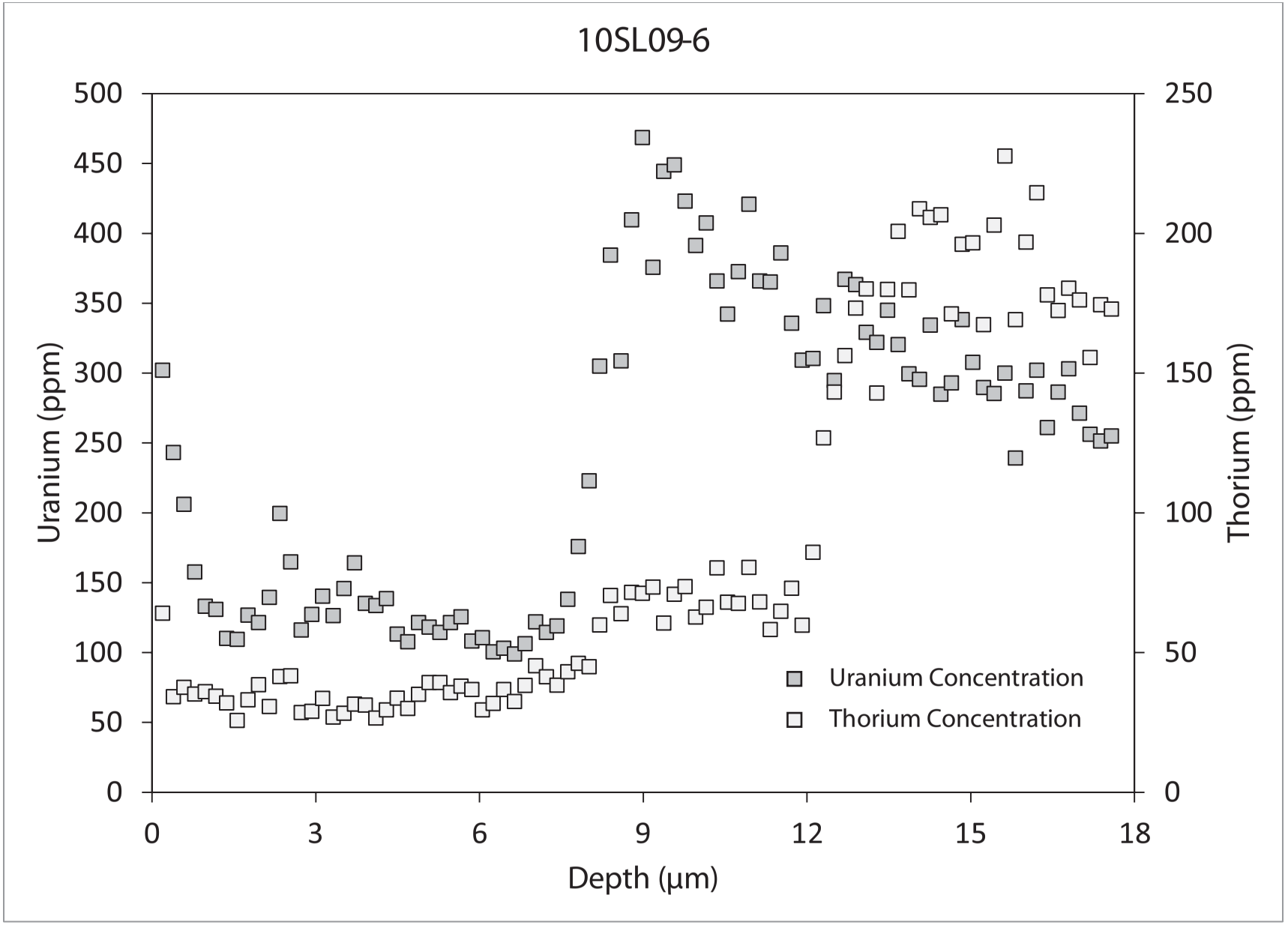
10SL09-6
Uranium (ppm)
Thorium (ppm)
Depth (µm)
Uranium Concentration
Thorium Concentration
0
50
100
150
200
250
300
350
400
450
500
0
3
6
9
12
15
18

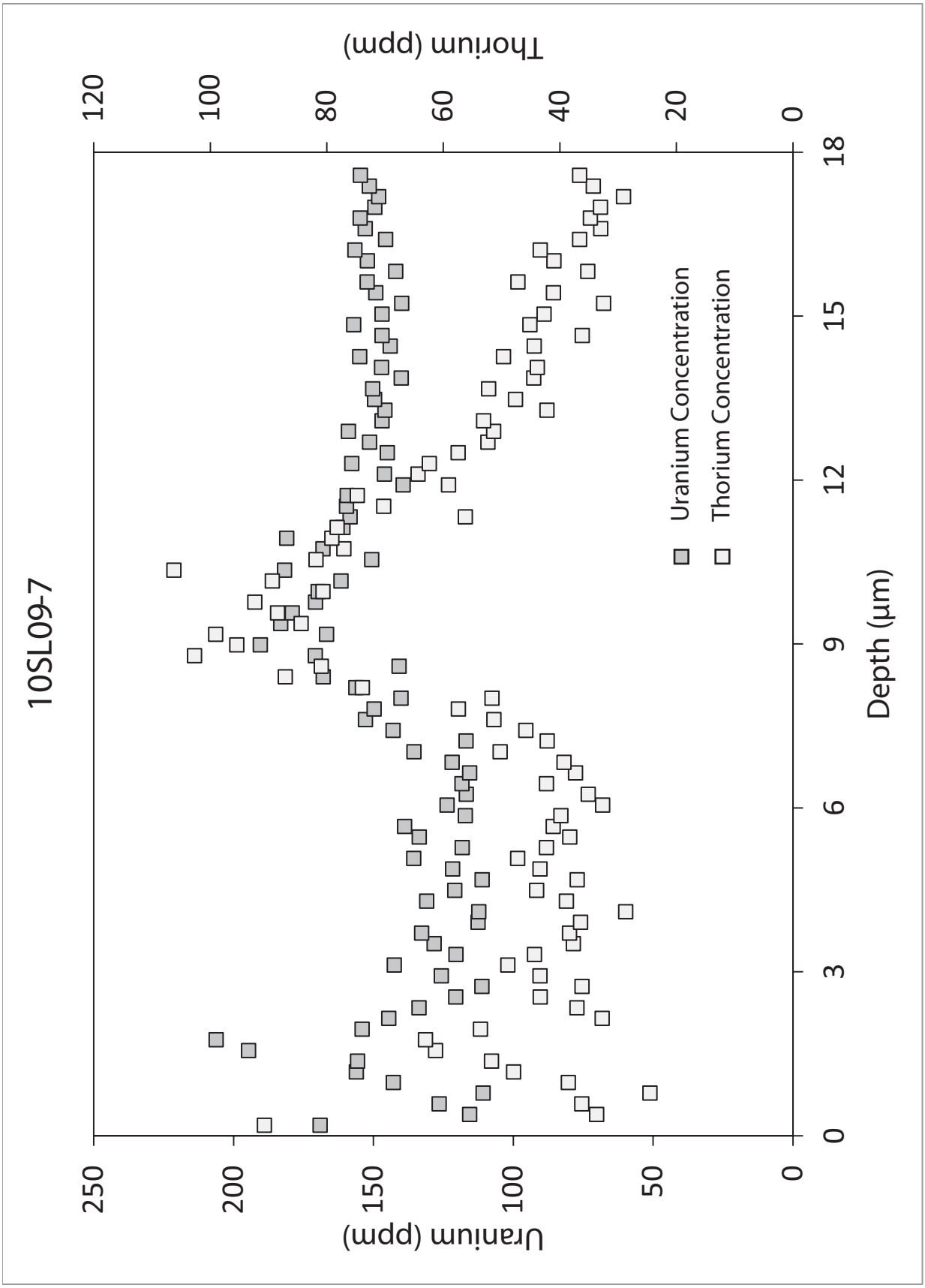
10SL09-7
Uranium (ppm)
Thorium (ppm)
Depth (µm)
Uranium Concentration
Thorium Concentration
0
50
100
150
200
250
0
20
40
60
80
100
120
0
3
6
9
12
15
18

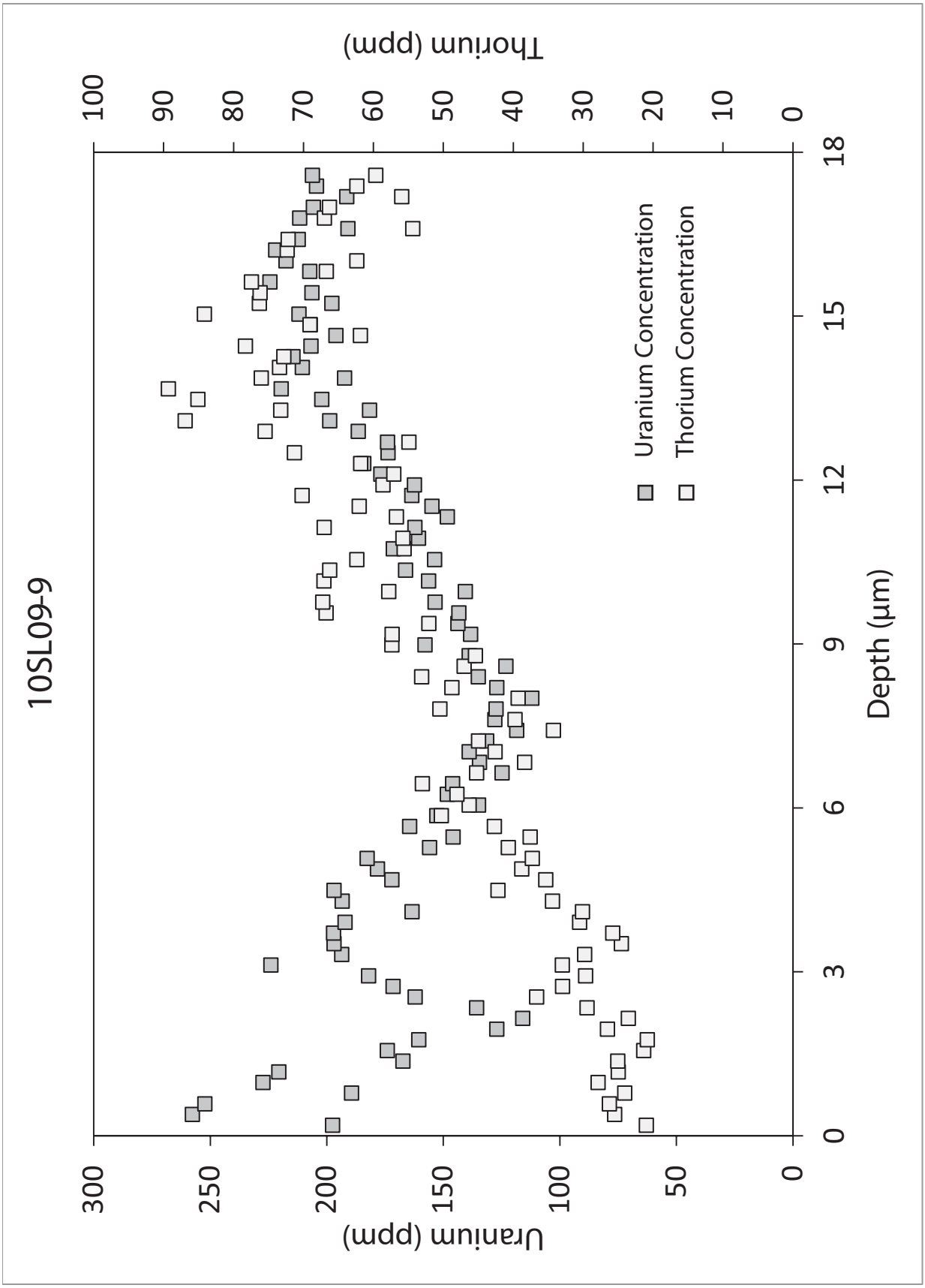
10SL09-9
Uranium (ppm)
Thorium (ppm)
Depth (µm)
Uranium Concentration
Thorium Concentration
0
50
100
150
200
250
300
0
10
20
30
40
50
60
70
80
90
100
0
3
6
9
12
15
18

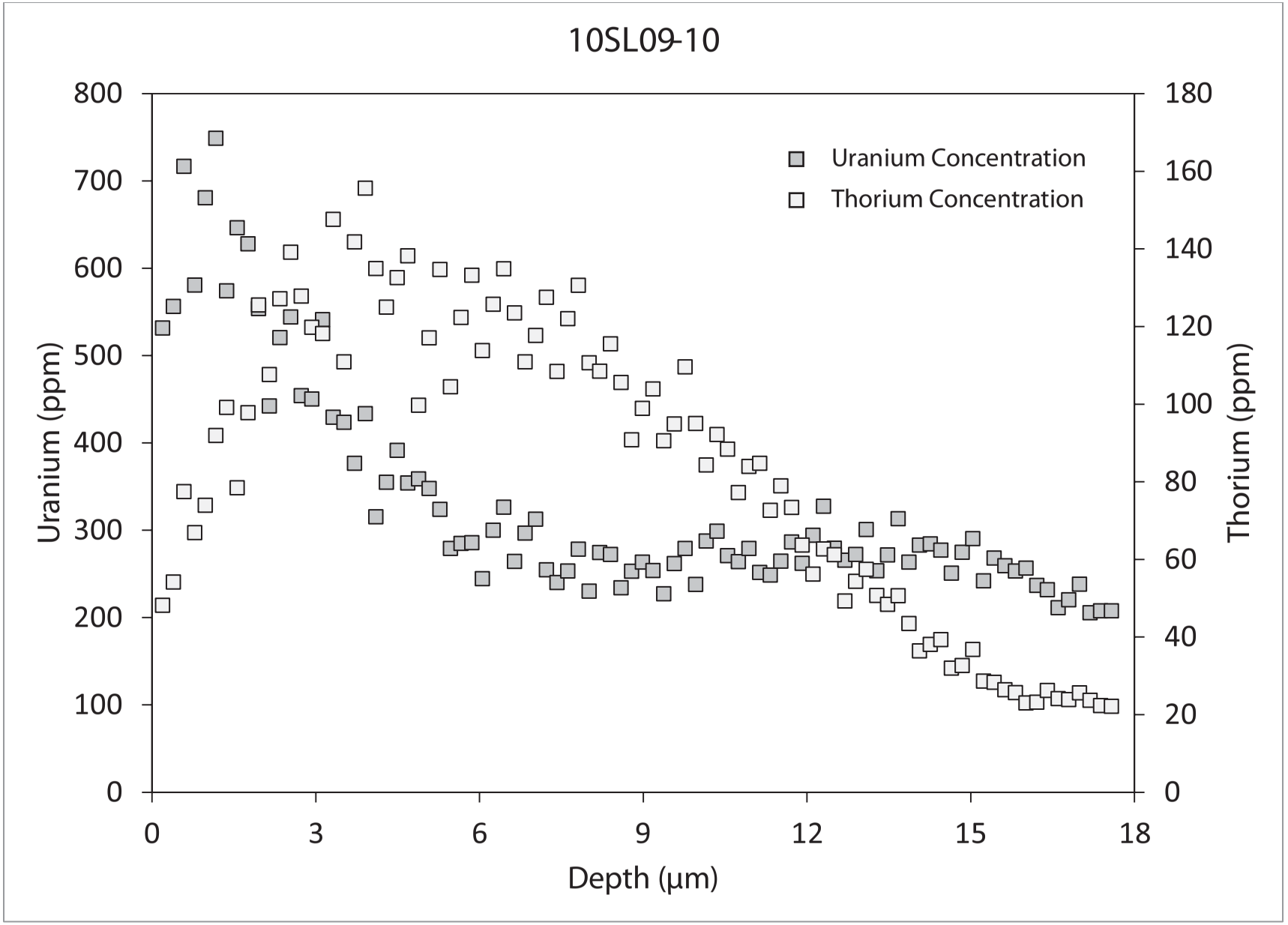
10SL09-10
Uranium Concentration
Thorium Concentration
Uranium (ppm)
Thorium (ppm)
Depth (µm)
0
100
200
300
400
500
600
700
800
0
20
40
60
80
100
120
140
160
180
0
3
6
9
12
15
18

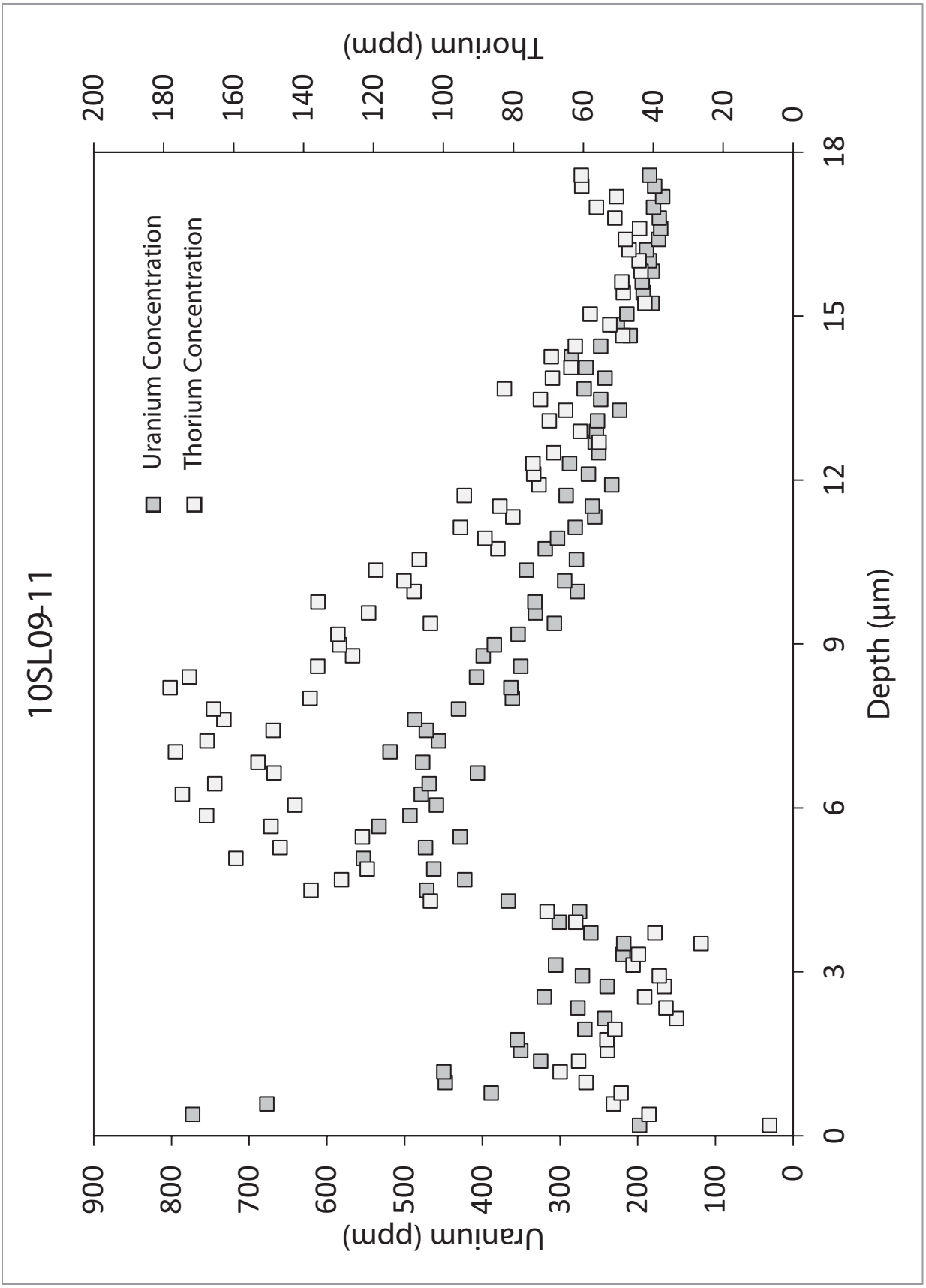
10SL09-11
Uranium Concentration
Thorium Concentration
Uranium (ppm)
Thorium (ppm)
Depth (µm)
0
100
200
300
400
500
600
700
800
900
0
20
40
60
80
100
120
140
160
180
200
0
3
6
9
12
15
18

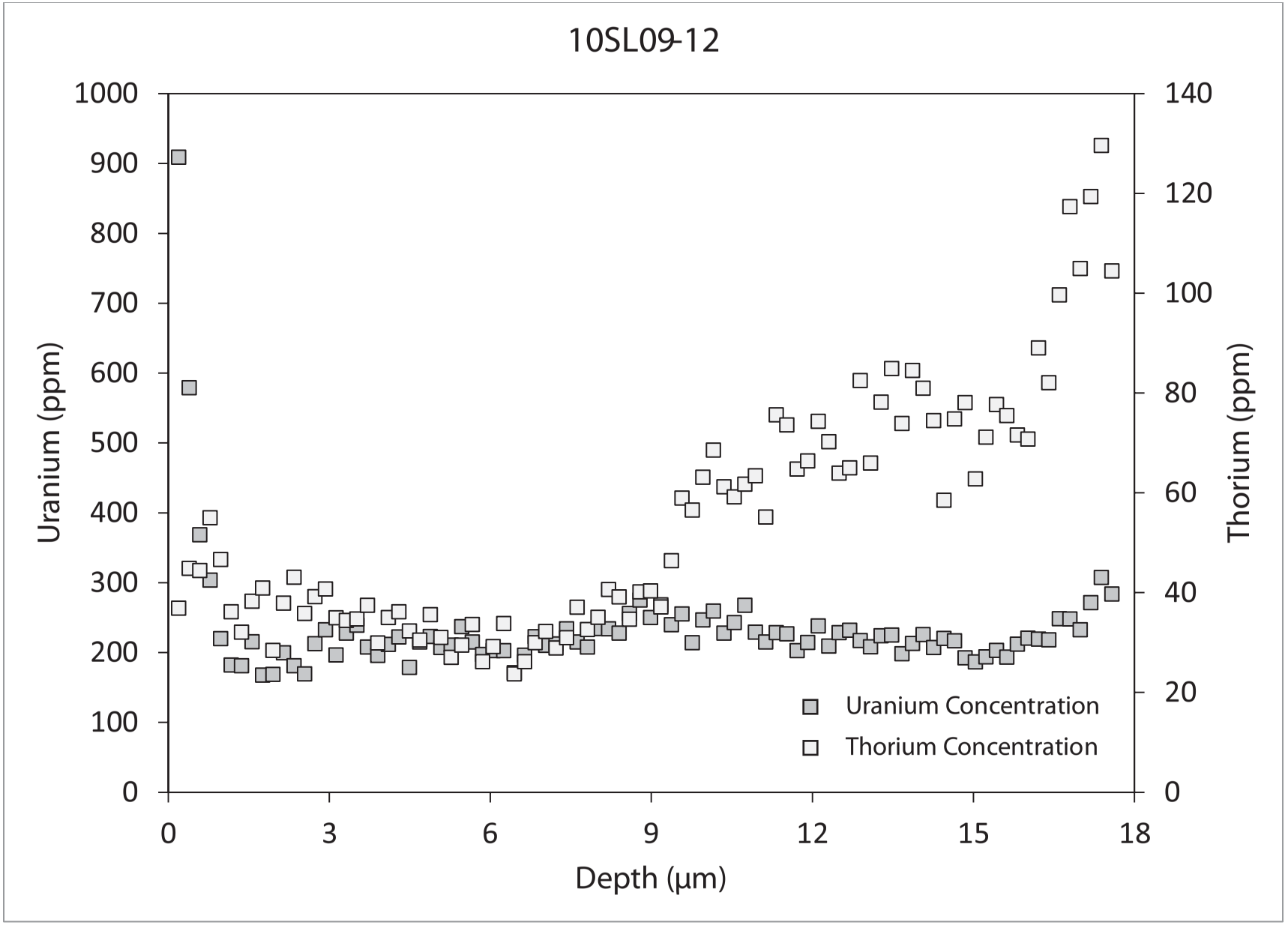
10SL09-12
Uranium (ppm)
Thorium (ppm)
Depth (µm)
Uranium Concentration
Thorium Concentration
0
100
200
300
400
500
600
700
800
900
1000
0
20
40
60
80
100
120
140
0
3
6
9
12
15
18

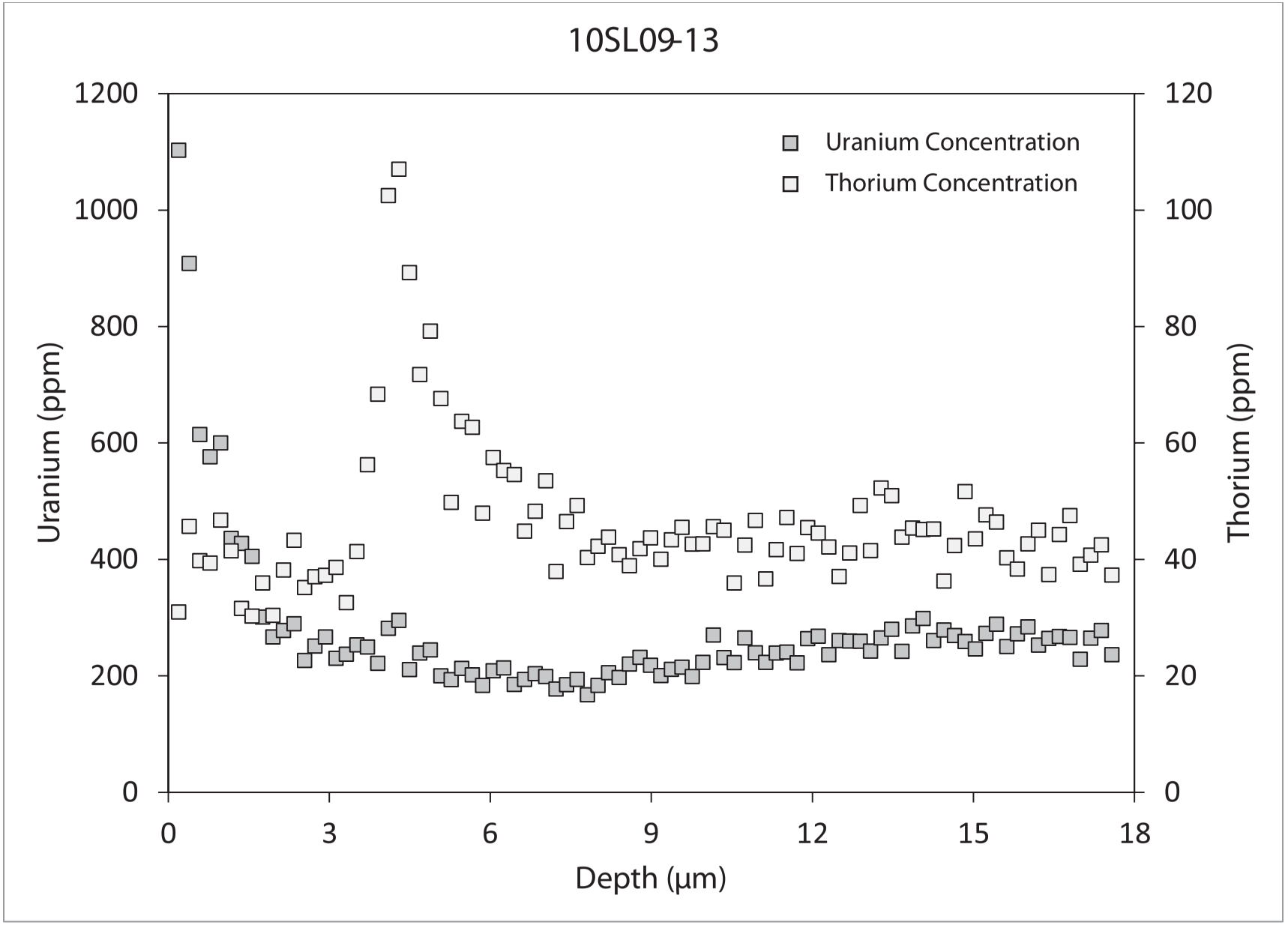
10SL09-13
Uranium Concentration
Thorium Concentration
Uranium (ppm)
Thorium (ppm)
Depth (µm)
0
200
400
600
800
1000
1200
0
20
40
60
80
100
120
0
3
6
9
12
15
18

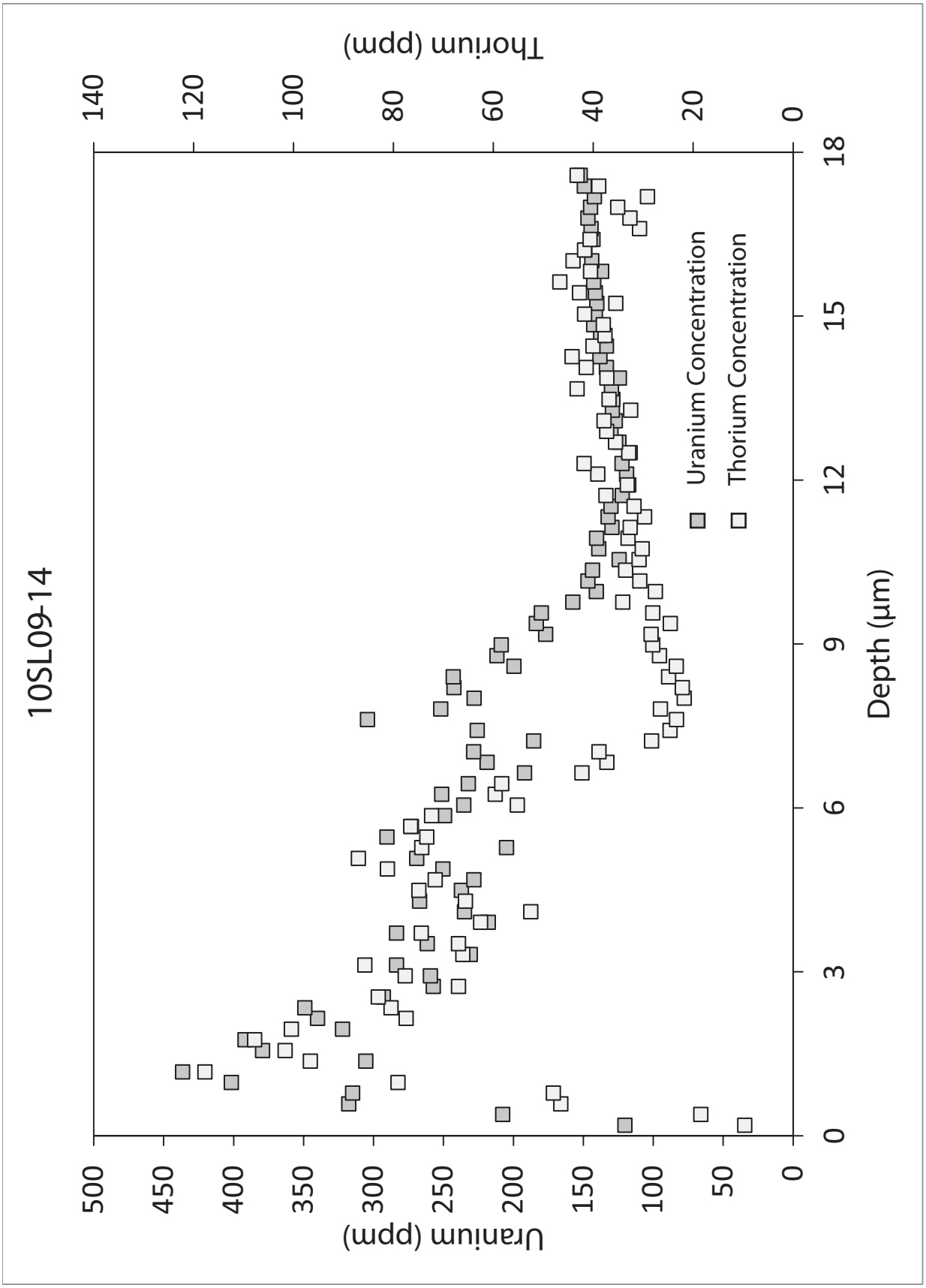
10SL09-14
Uranium (ppm)
Thorium (ppm)
Depth (µm)
Uranium Concentration
Thorium Concentration
0
50
100
150
200
250
300
350
400
450
500
0
20
40
60
80
100
120
140
0
3
6
9
12
15
18

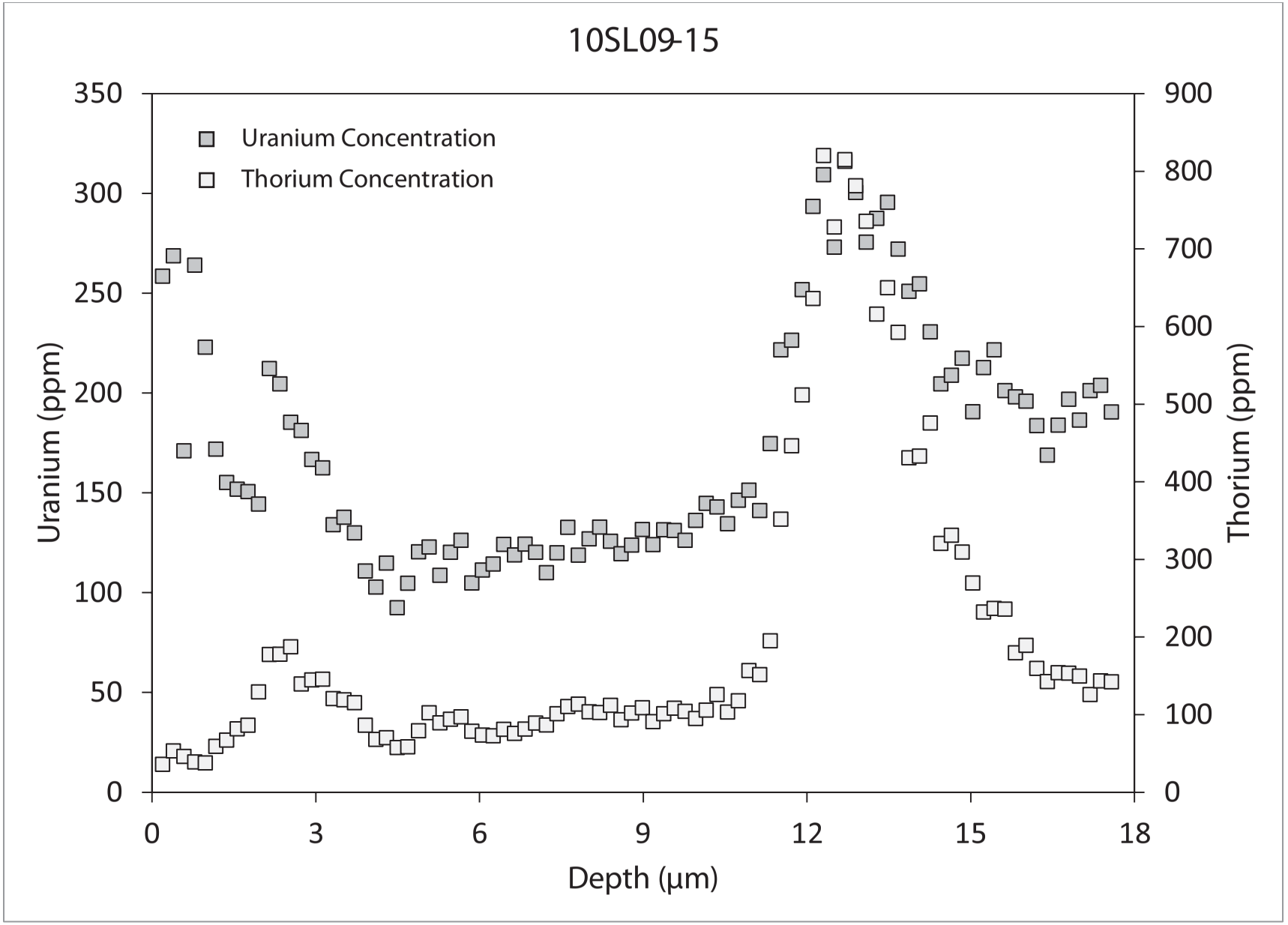
10SL09-15
Uranium Concentration
Thorium Concentration
Uranium (ppm)
Thorium (ppm)
Depth (µm)
0
50
100
150
200
250
300
350
0
100
200
300
400
500
600
700
800
900
0
3
6
9
12
15
18

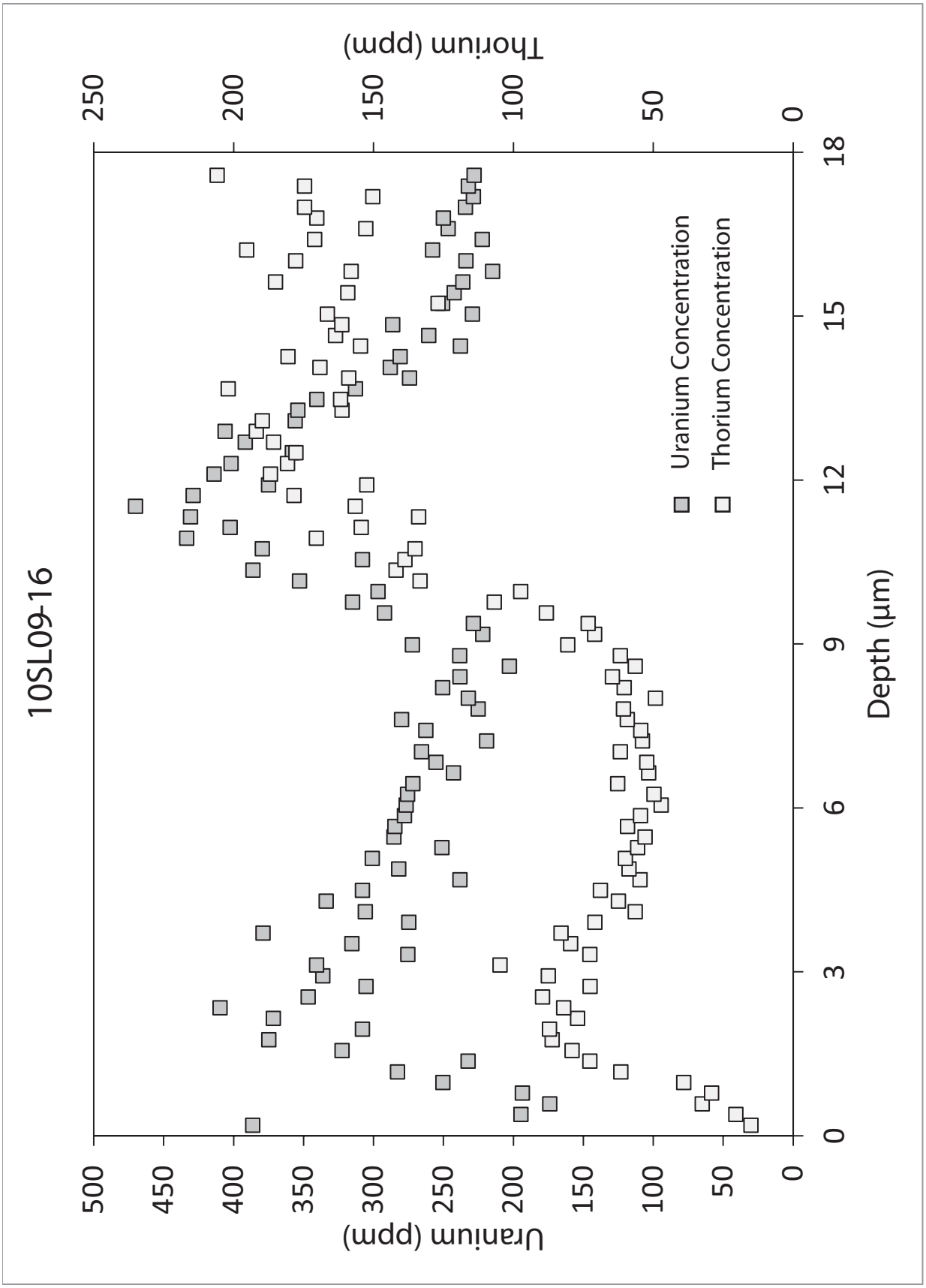
10SL09-16
Uranium (ppm)
Thorium (ppm)
Depth (µm)
Uranium Concentration
Thorium Concentration
0
50
100
150
200
250
300
350
400
450
500
0
50
100
150
200
250
0
3
6
9
12
15
18

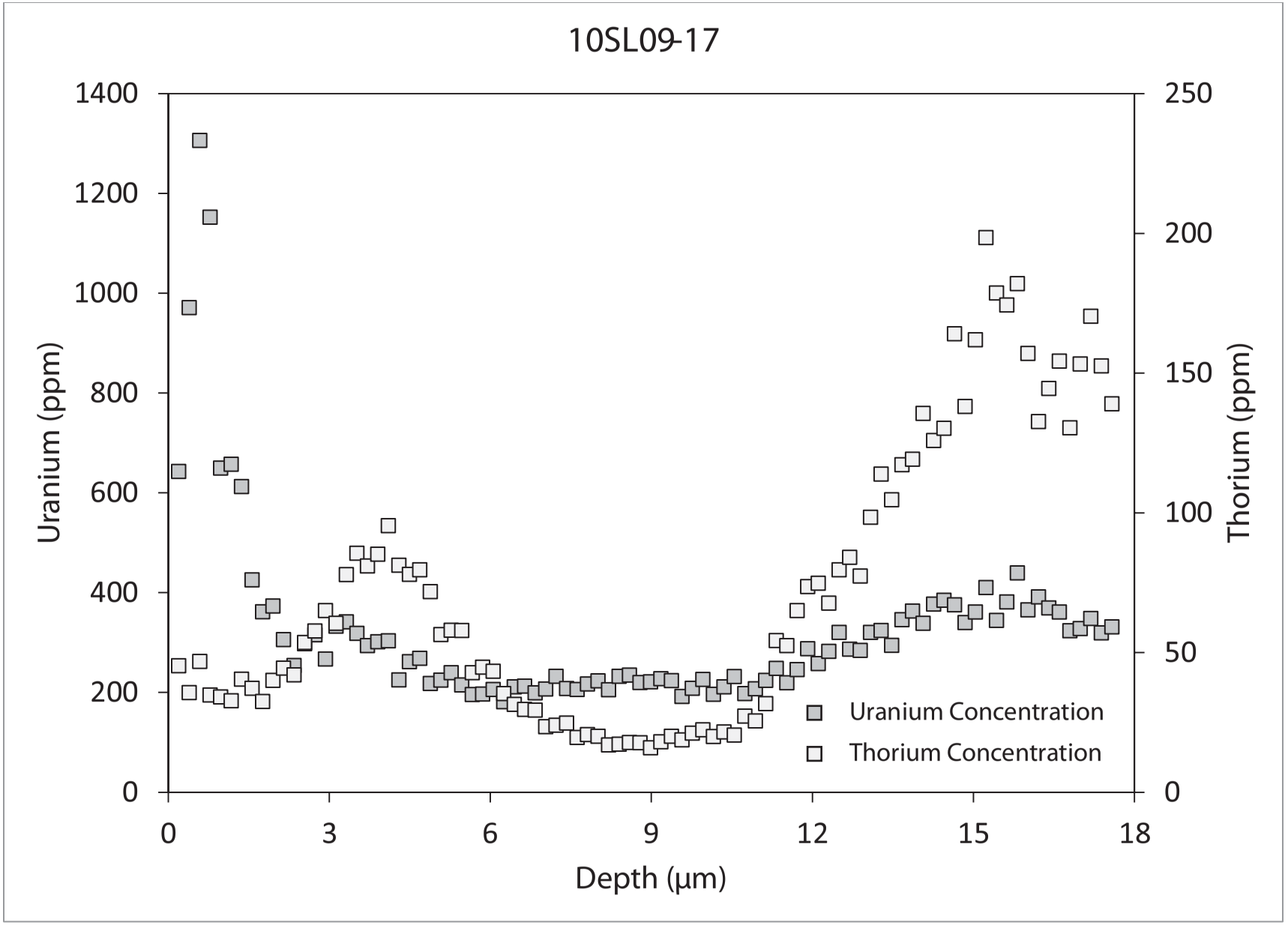
10SL09-17
Uranium (ppm)
Thorium (ppm)
Depth (µm)
Uranium Concentration
Thorium Concentration
0
200
400
600
800
1000
1200
1400
0
50
100
150
200
250
0
3
6
9
12
15
18

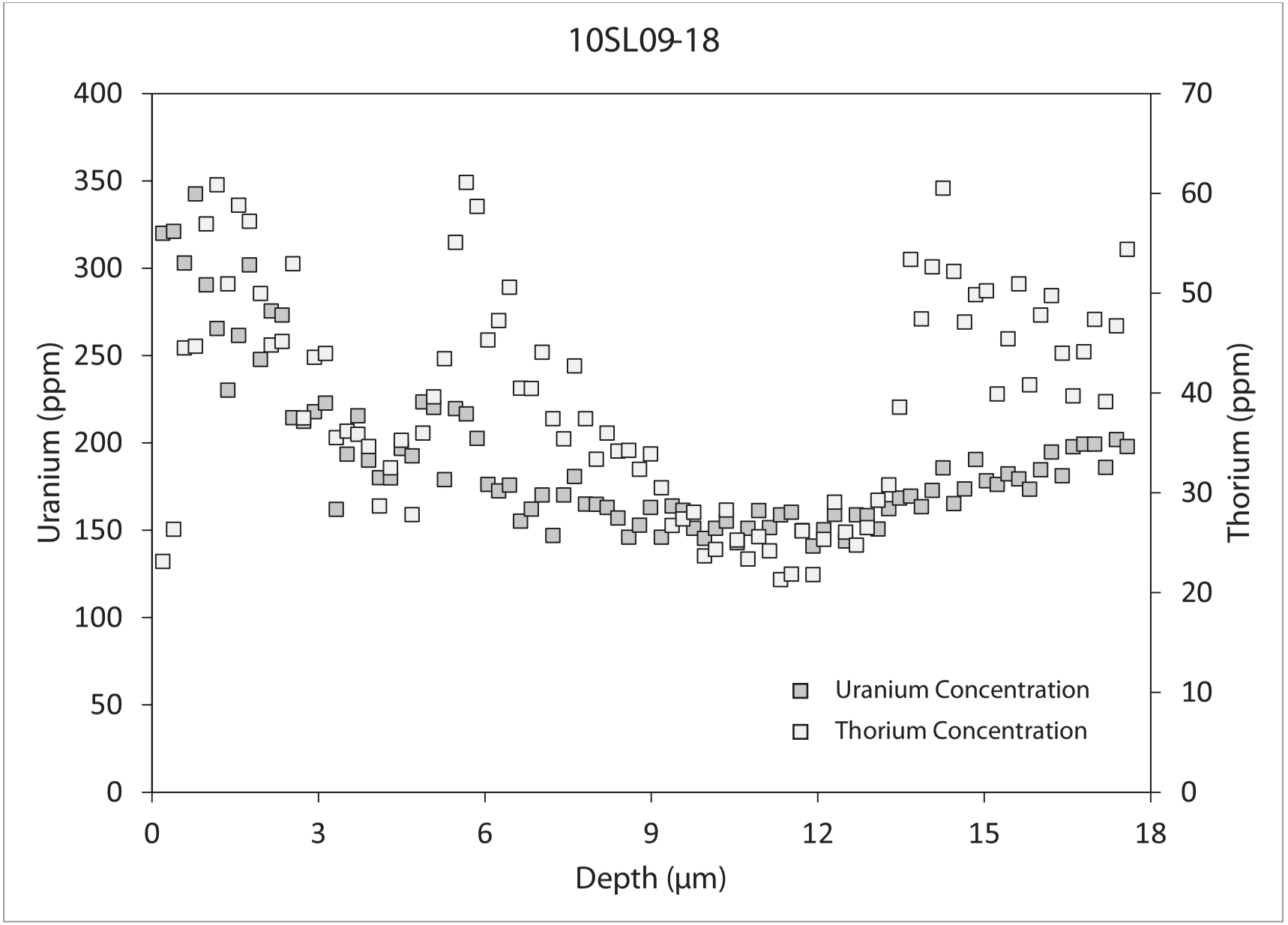
10SL09-18
Uranium (ppm)
Thorium (ppm)
Depth (µm)
Uranium Concentration
Thorium Concentration
400
350
300
250
200
150
100
50
0
70
60
50
40
30
20
10
0
0
3
6
9
12
15
18

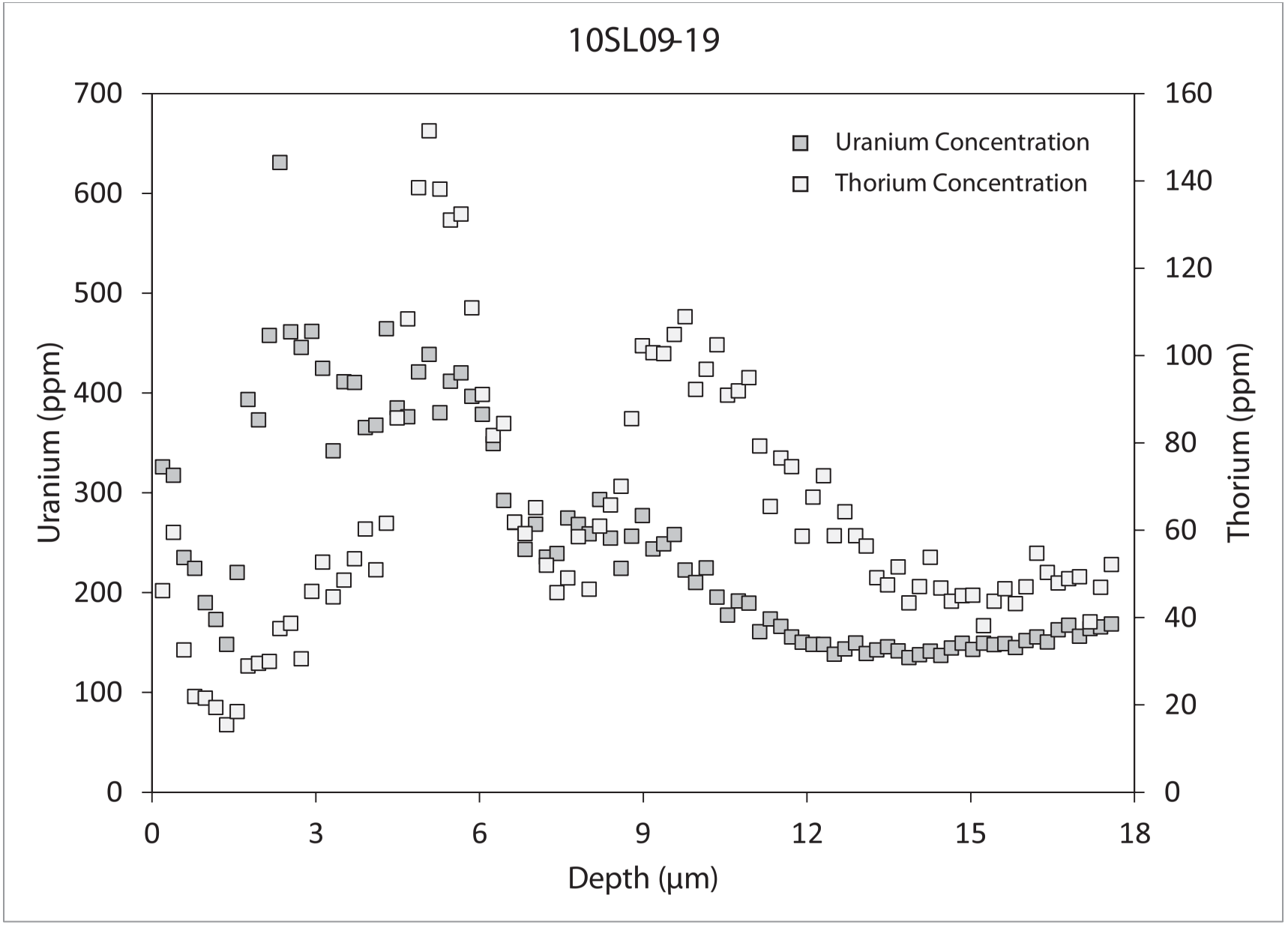
10SL09-19
Uranium Concentration
Thorium Concentration
Uranium (ppm)
Thorium (ppm)
Depth (µm)
0
100
200
300
400
500
600
700
0
20
40
60
80
100
120
140
160
0
3
6
9
12
15
18

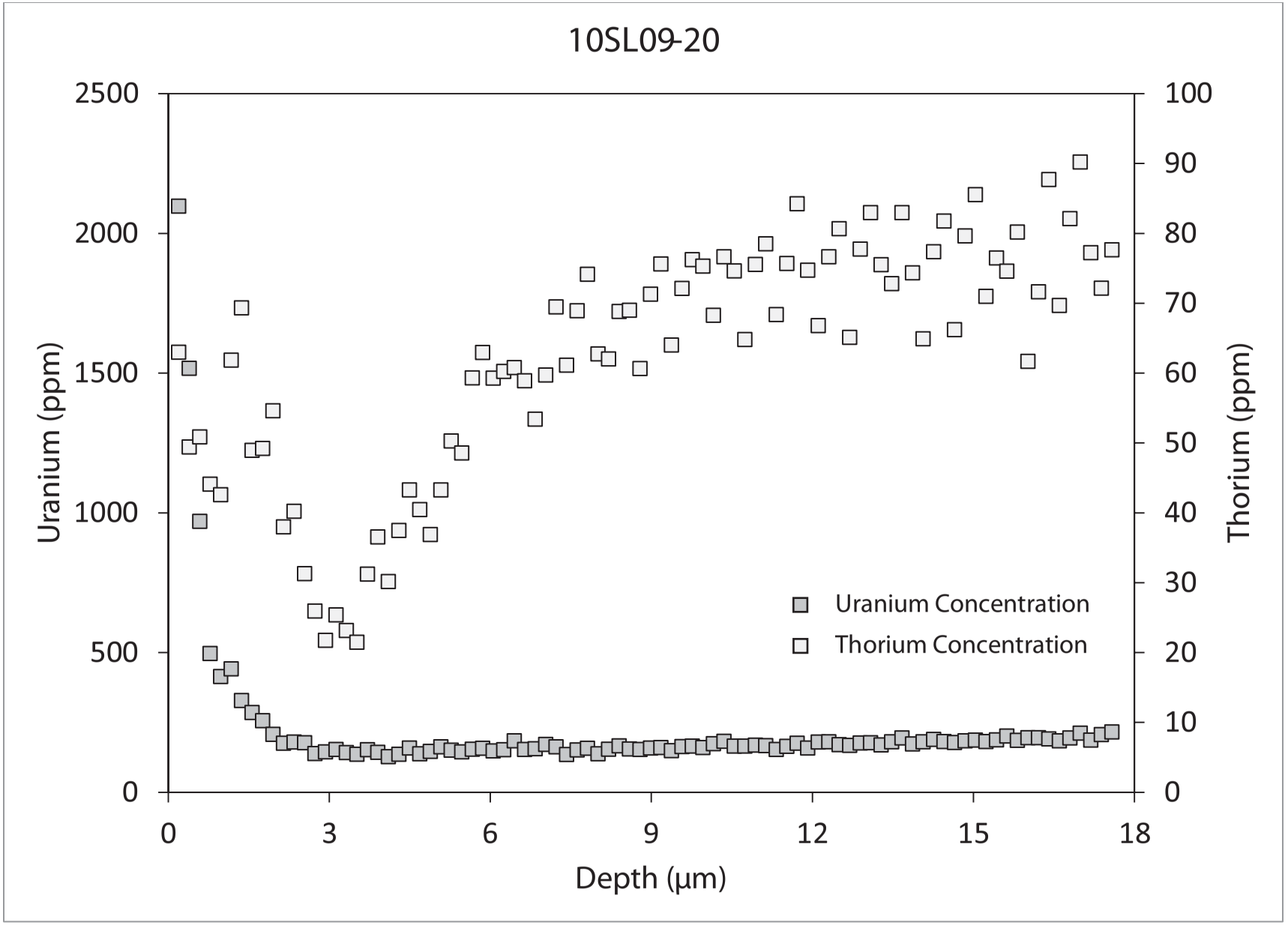
10SL09-20
Uranium (ppm)
Thorium (ppm)
Depth (µm)
Uranium Concentration
Thorium Concentration
2500
2000
1500
1000
500
0
100
90
80
70
60
50
40
30
20
10
0
0
3
6
9
12
15
18

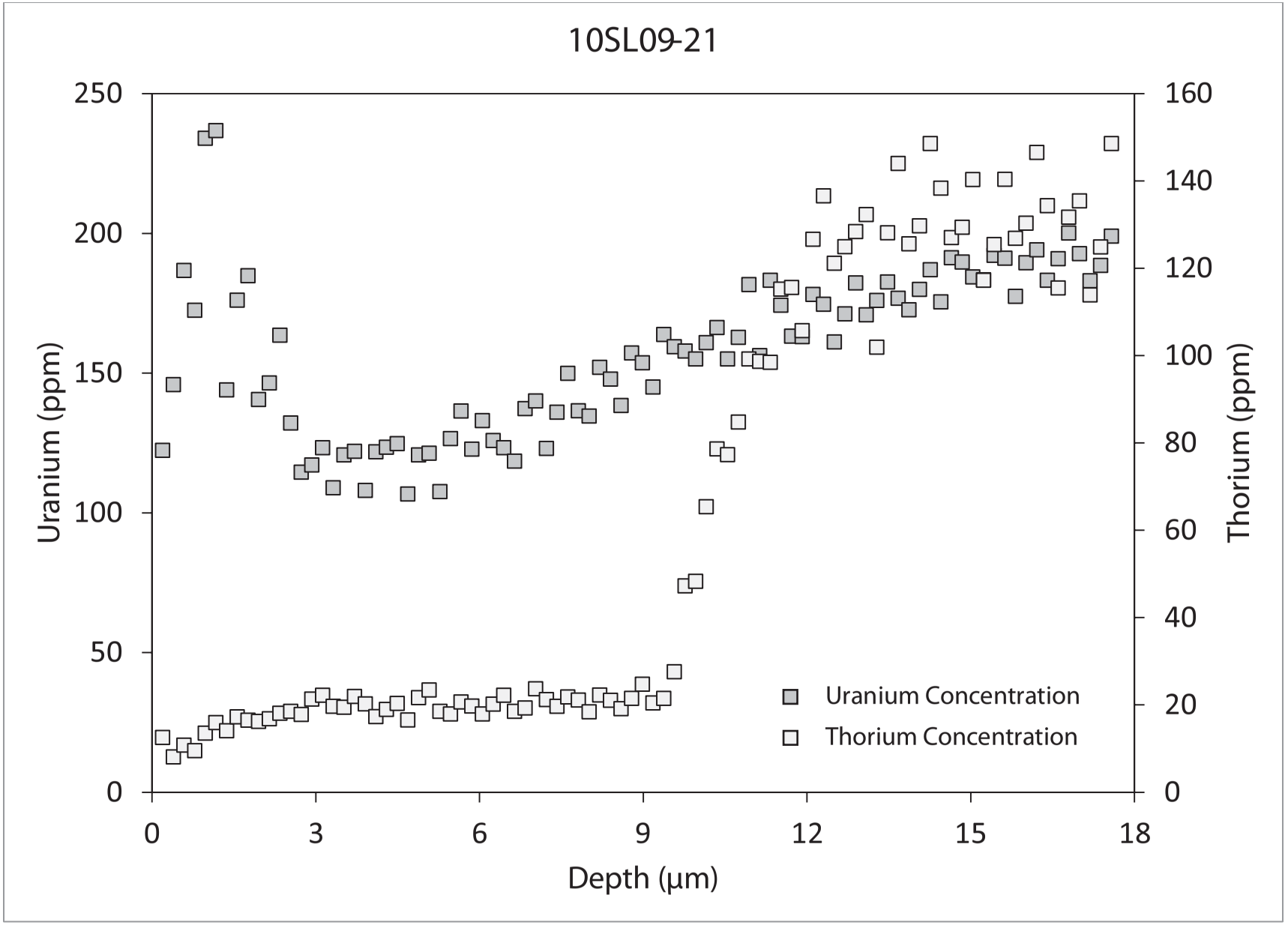
10SL09-21
Uranium (ppm)
Thorium (ppm)
Depth (µm)
Uranium Concentration
Thorium Concentration
0
50
100
150
200
250
0
20
40
60
80
100
120
140
160
0
3
6
9
12
15
18

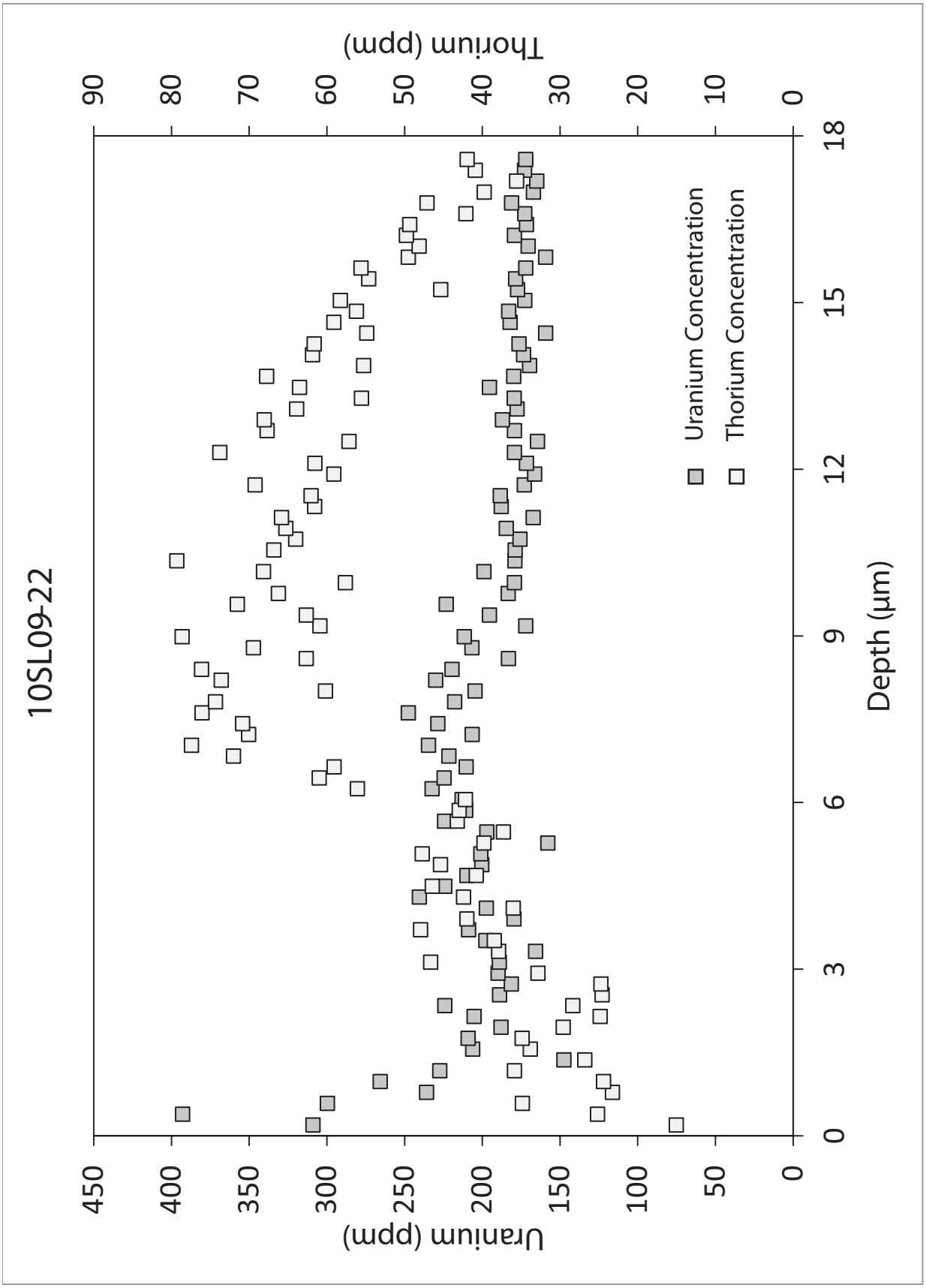
10SL09-22
Uranium (ppm)
Thorium (ppm)
Depth (µm)
Uranium Concentration
Thorium Concentration
0
50
100
150
200
250
300
350
400
450
0
10
20
30
40
50
60
70
80
90
0
3
6
9
12
15
18

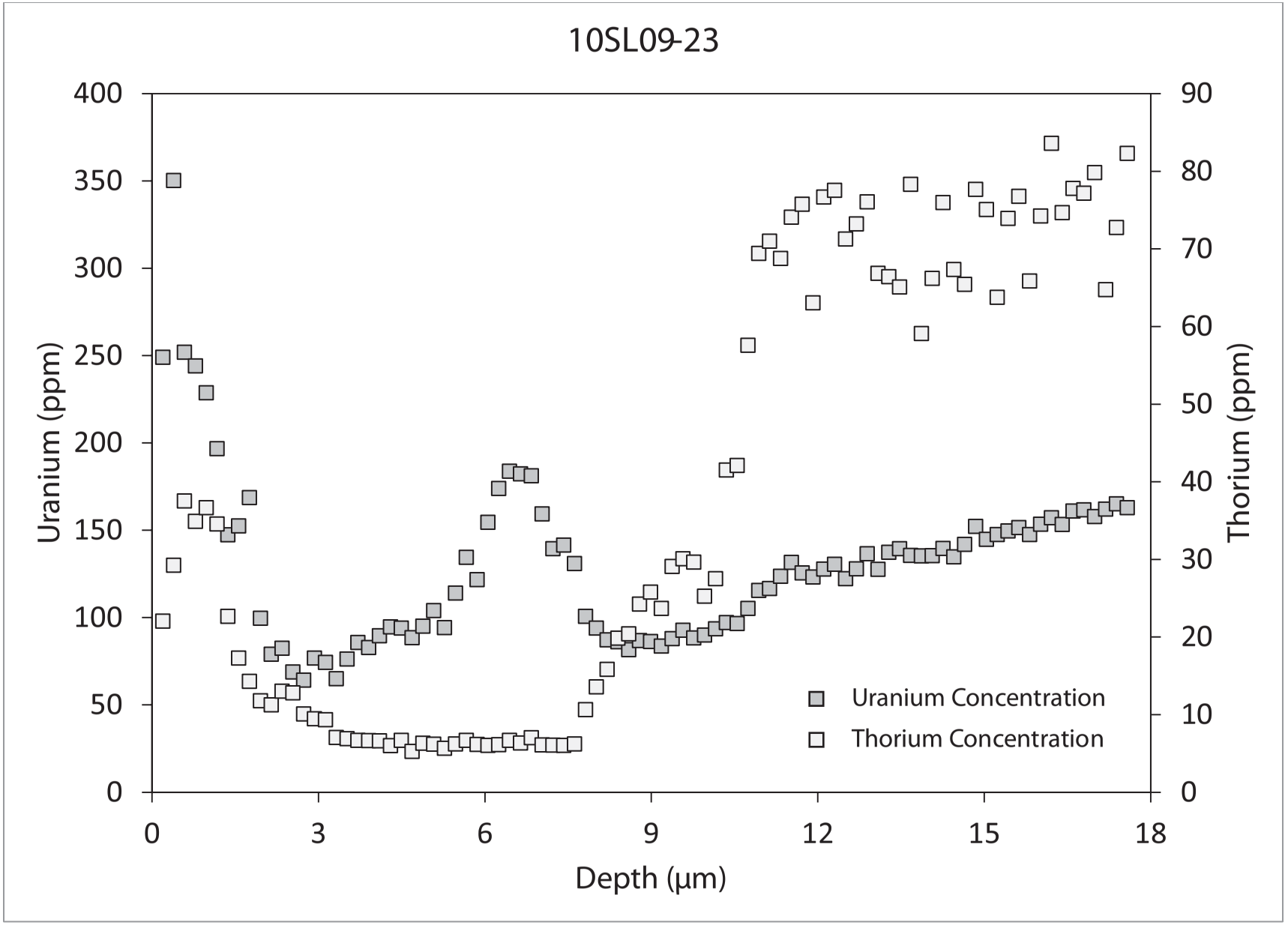
10SL09-23
Uranium (ppm)
Thorium (ppm)
Depth (µm)
Uranium Concentration
Thorium Concentration
0
50
100
150
200
250
300
350
400
0
10
20
30
40
50
60
70
80
90
0
3
6
9
12
15
18

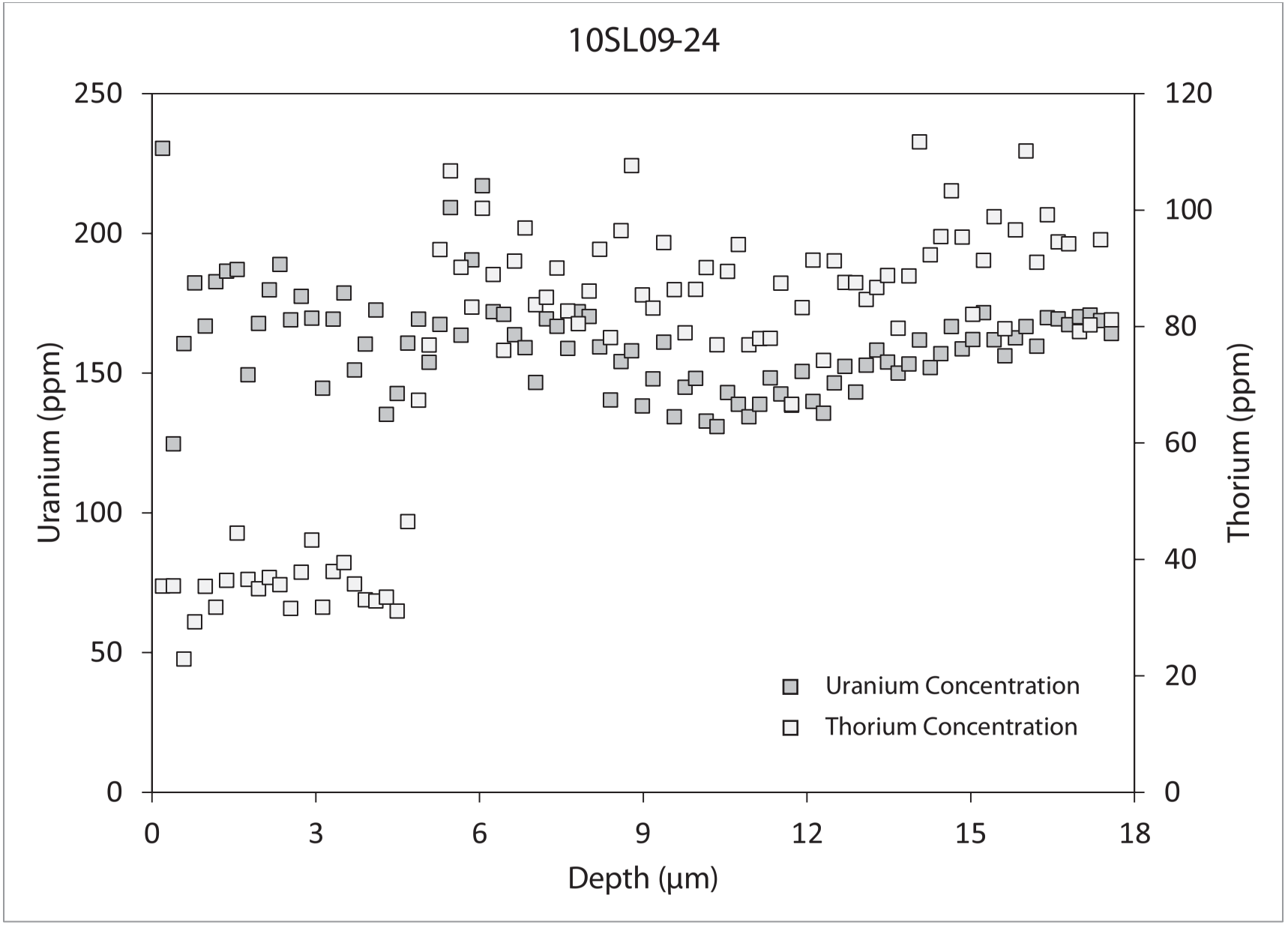
10SL09-24
Uranium (ppm)
Thorium (ppm)
Depth (µm)
Uranium Concentration
Thorium Concentration
0
50
100
150
200
250
0
20
40
60
80
100
120
0
3
6
9
12
15
18

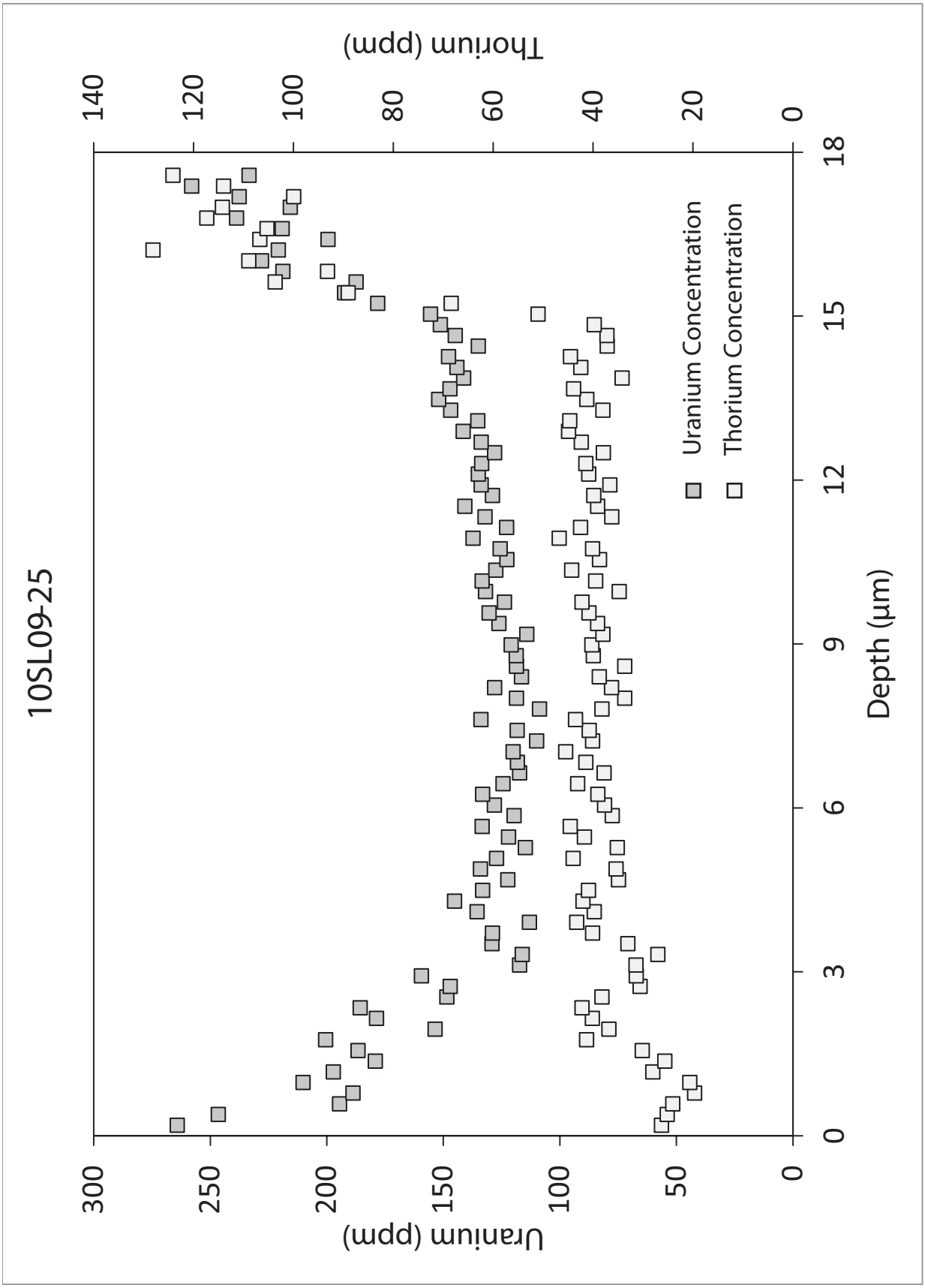
10SL09-25
Uranium (ppm)
Thorium (ppm)
Depth (µm)
Uranium Concentration
Thorium Concentration
0
50
100
150
200
250
300
0
20
40
60
80
100
120
140
0
3
6
9
12
15
18

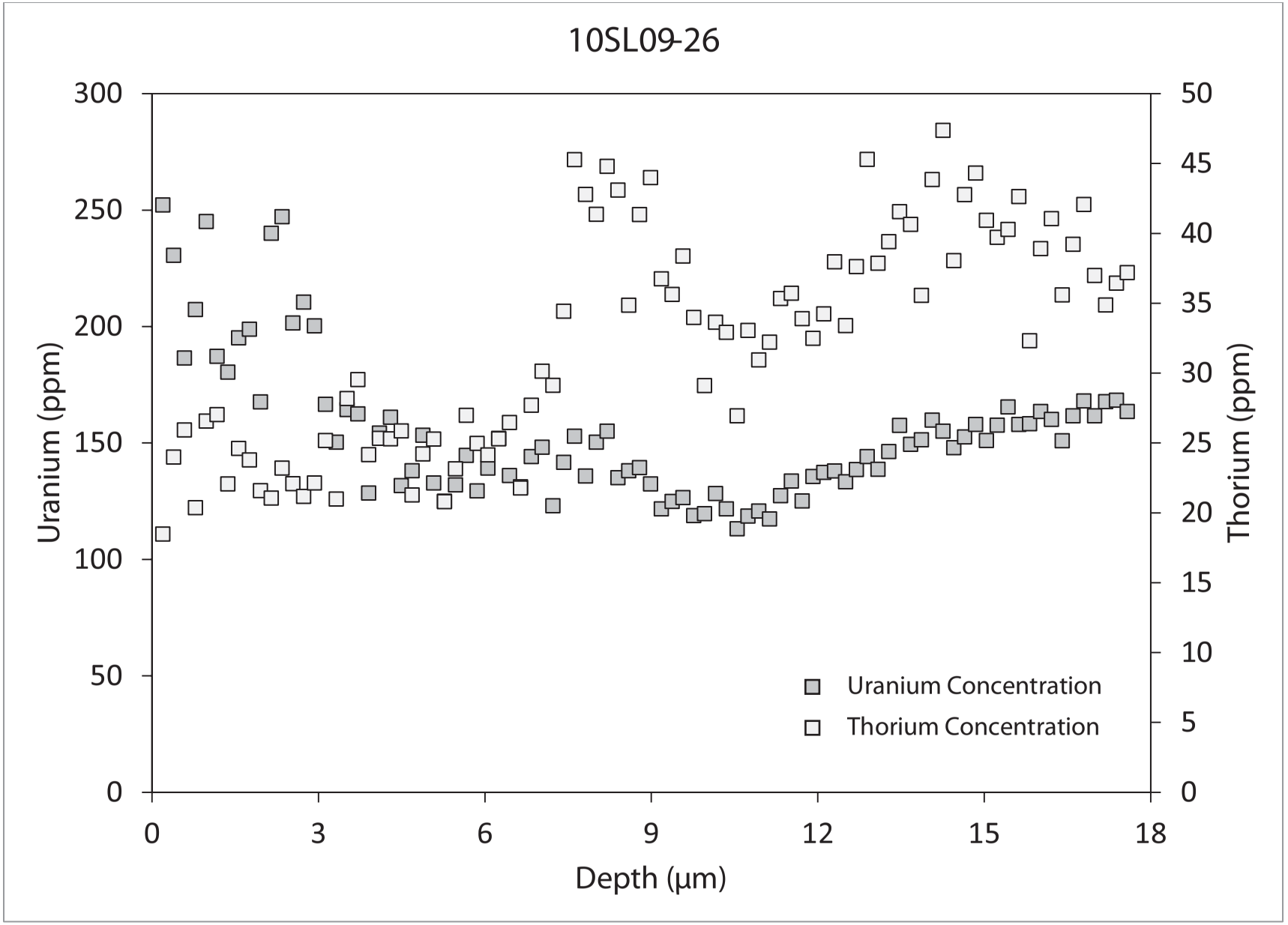
10SL09-26
Uranium (ppm)
Thorium (ppm)
Depth (µm)
Uranium Concentration
Thorium Concentration
300
250
200
150
100
50
0
50
45
40
35
30
25
20
15
10
5
0
0
3
6
9
12
15
18

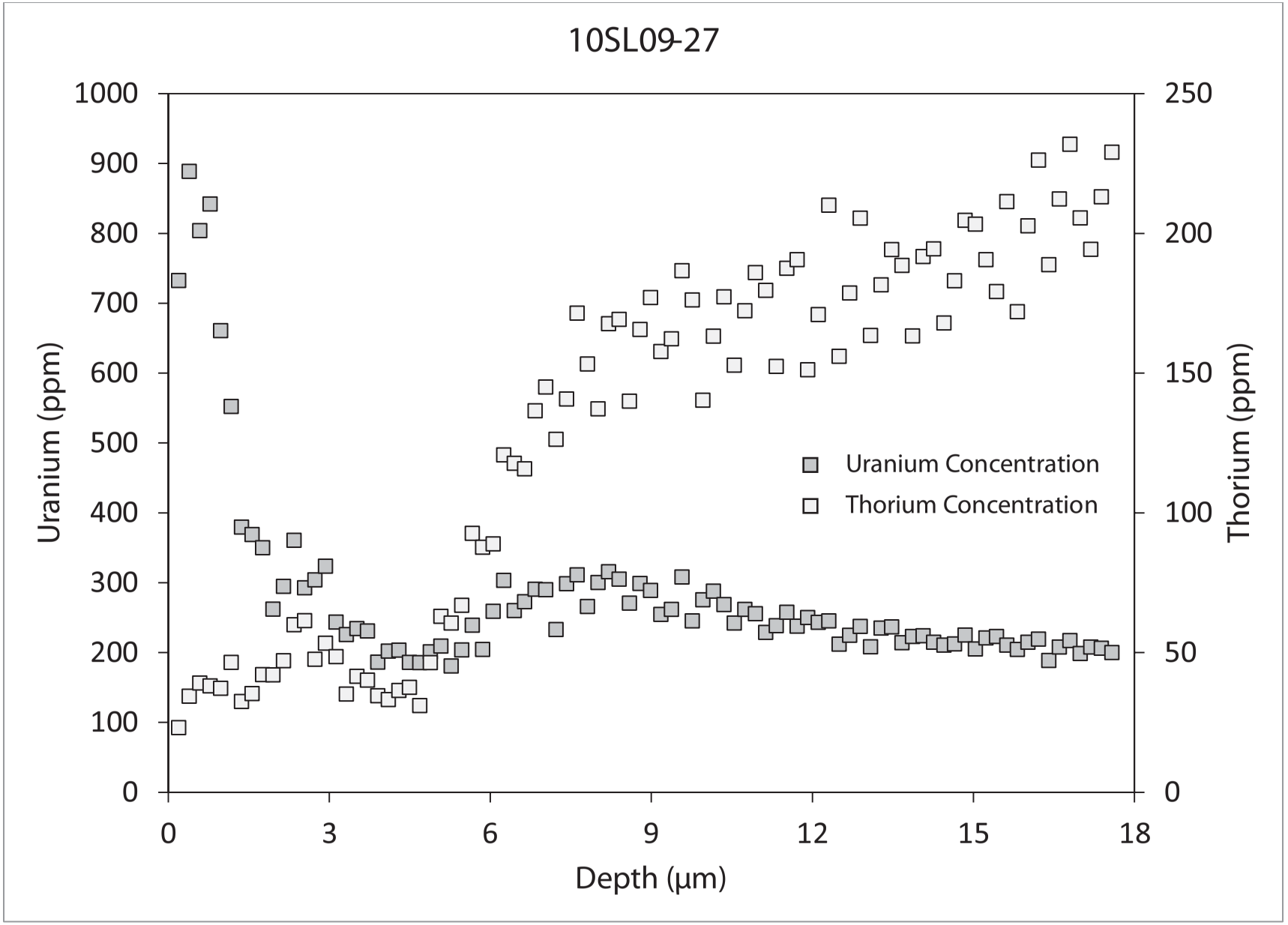
10SL09-27
Uranium (ppm)
Thorium (ppm)
Depth (µm)
Uranium Concentration
Thorium Concentration
0
100
200
300
400
500
600
700
800
900
1000
0
50
100
150
200
250
0
3
6
9
12
15
18

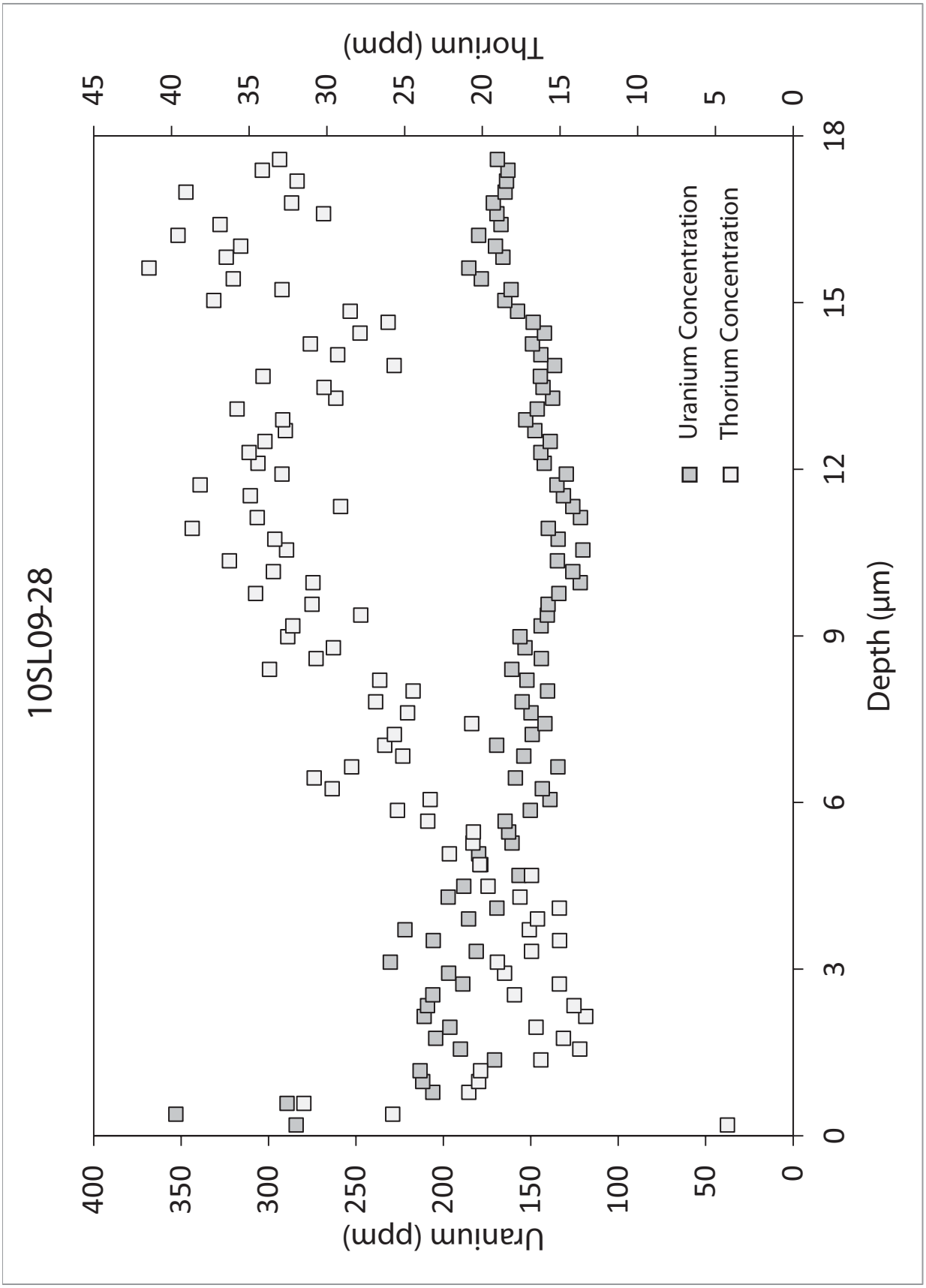
10SL09-28
Uranium (ppm)
Thorium (ppm)
Depth (µm)
Uranium Concentration
Thorium Concentration
0
50
100
150
200
250
300
350
400
0
5
10
15
20
25
30
35
40
45
0
3
6
9
12
15
18

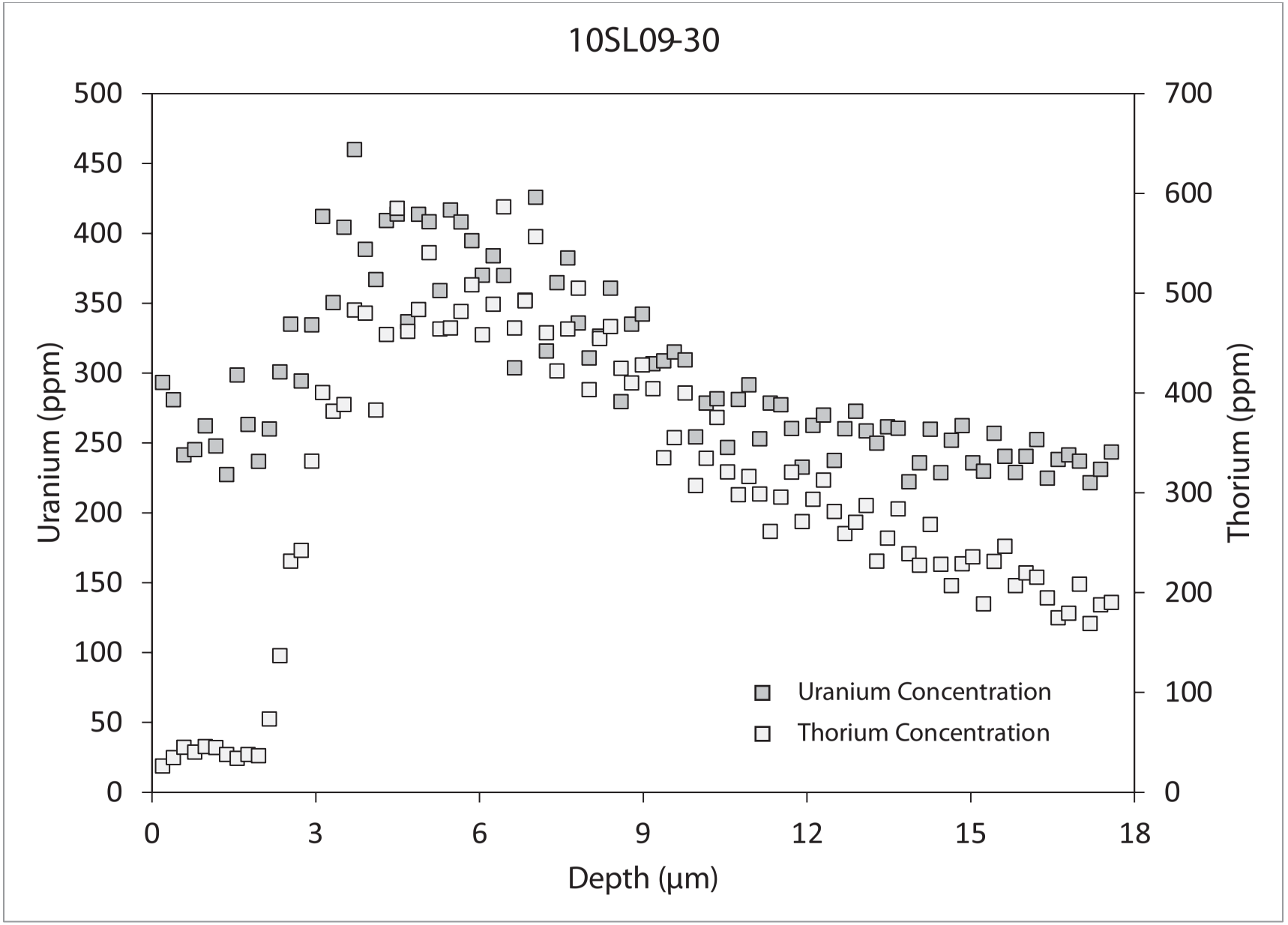
10SL09-30
Uranium (ppm)
Thorium (ppm)
Depth (µm)
Uranium Concentration
Thorium Concentration
0
50
100
150
200
250
300
350
400
450
500
0
100
200
300
400
500
600
700
0
3
6
9
12
15
18

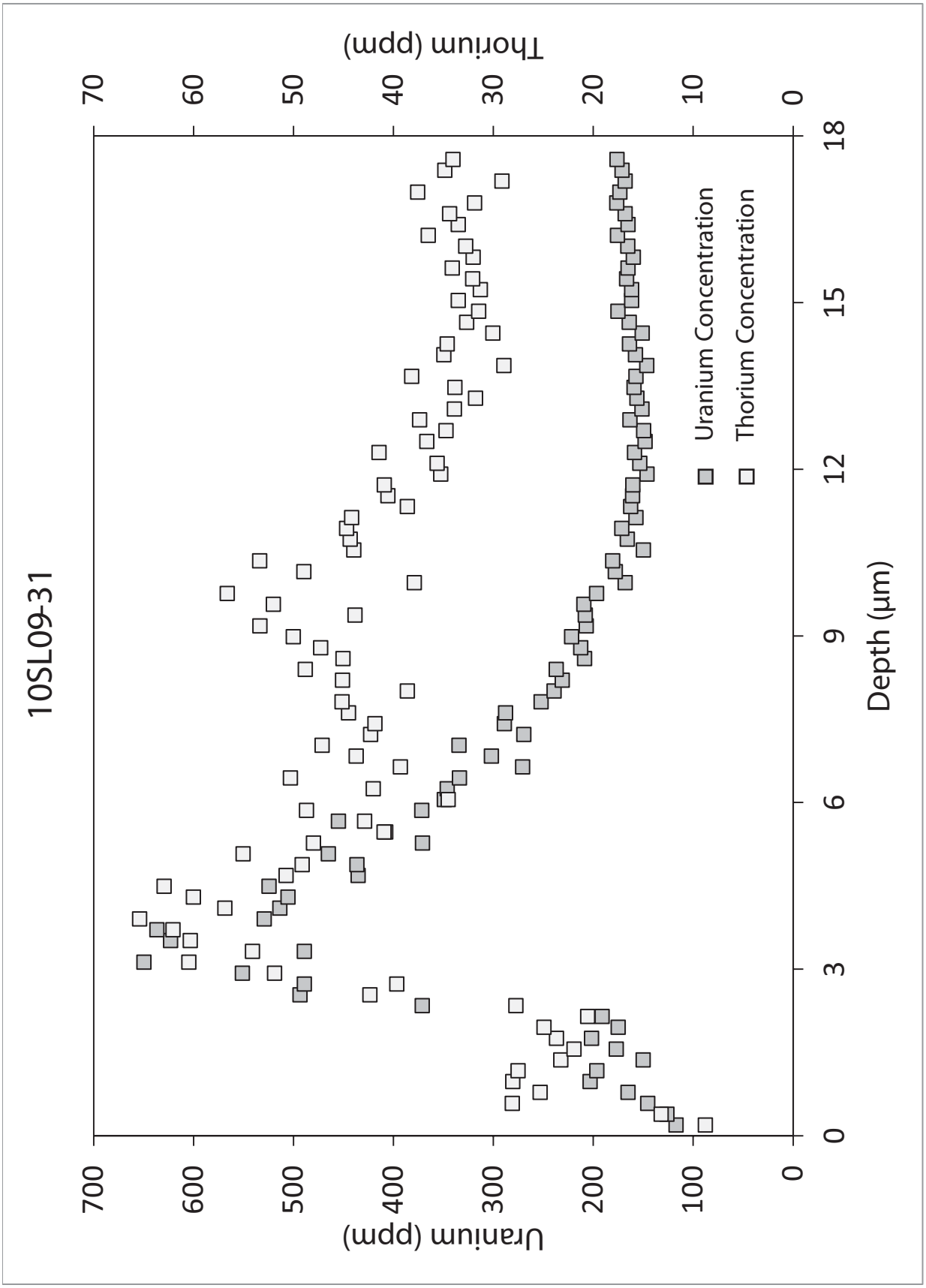
10SL09-31
Uranium (ppm)
Thorium (ppm)
Depth (µm)
Uranium Concentration
Thorium Concentration
0
100
200
300
400
500
600
700
0
10
20
30
40
50
60
70
0
3
6
9
12
15
18

Appendix C: Cathodoluminescence Images of Laser Ablated Zircon Grains

Zircon grains from three samples (10SL03, 05, 09) of the vertical transect through the Silvretta nappe were chosen for laser ablation-inductively coupled-mass spectrometry (LA-ICP-MS) depth-profiling to determine parent isotope concentrations (U and Th). Grey-scale cathodoluminescence (CL) imaging was also completed on about half of the laser ablated zircon grains, while the other half were dated using the (U-Th)/He method. The CL imaging was used to determine qualitatively the 2D pattern of parent isotope zonation within the laser ablated zircon grains. All CL imaging was performed at the Microscopy and Analytical Imaging Laboratory of the University of Kansas on the LEO 1550 Field Emission Scanning Electron Microscope. The following images were not published in the main body of text and are instead presented below; all grains are labeled by sample name in white. Corresponding U and Th concentration profiles are presented in Appendix B.

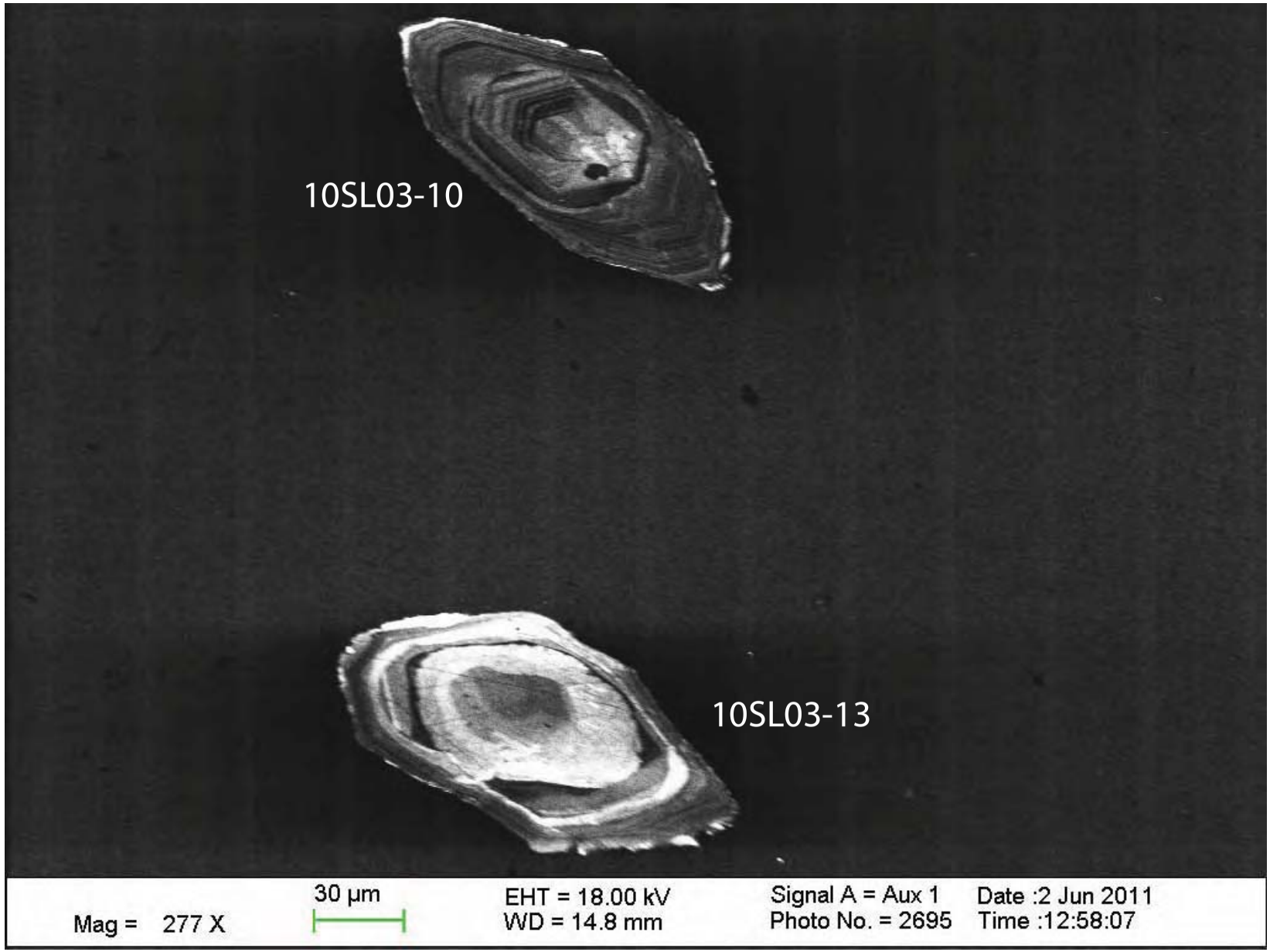
10SL03-10
10SL03-13
30 µm
Mag = 277 X
EHT = 18.00 kV
WD = 14.8 mm
Signal A = Aux 1
Photo No. = 2695
Date :2 Jun 2011
Time :12:58:07

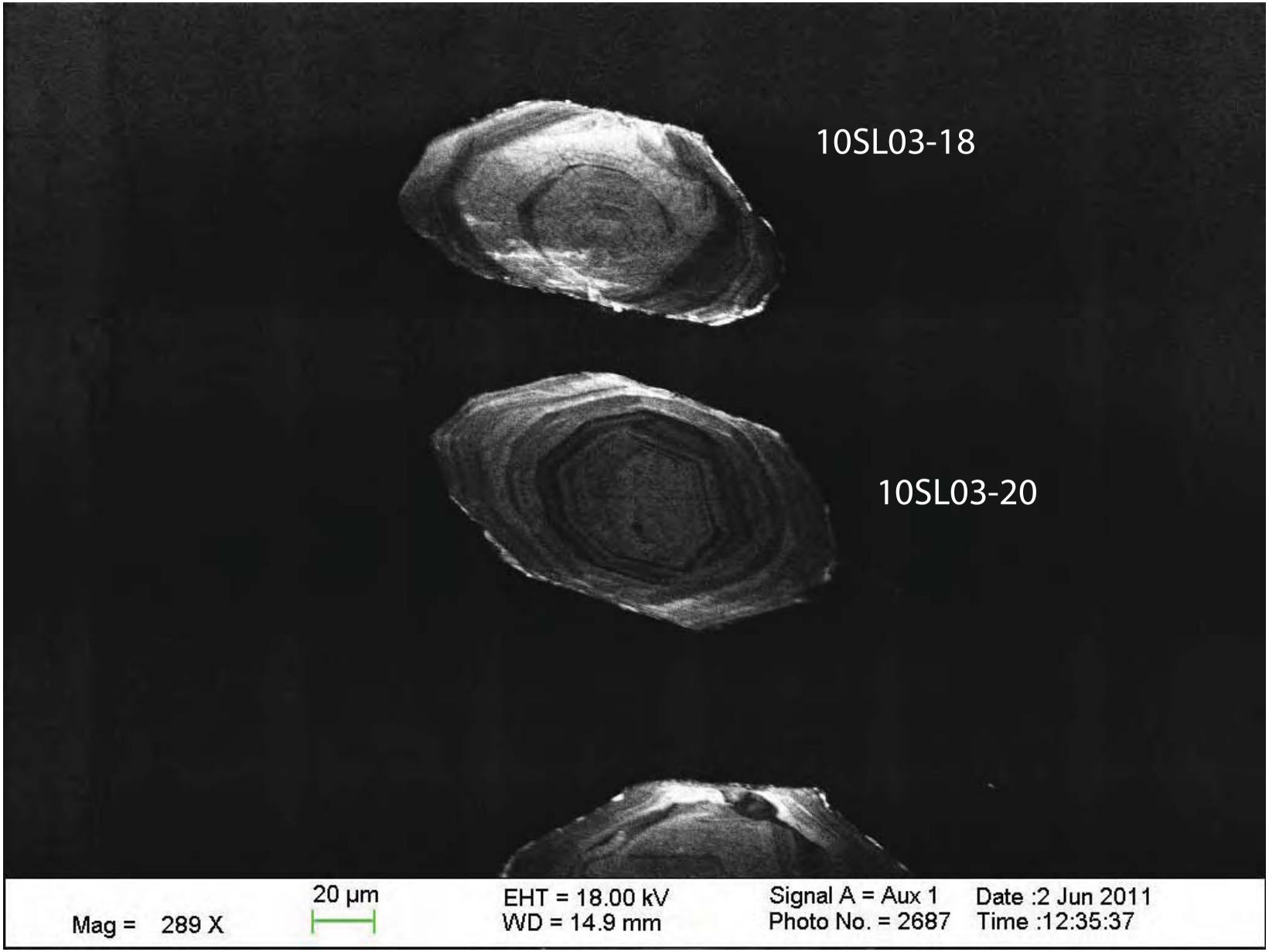
10SL03-18
10SL03-20
Mag = 289 X
20 µm
EHT = 18.00 kV
WD = 14.9 mm
Signal A = Aux 1
Photo No. = 2687
Date :2 Jun 2011
Time :12:35:37

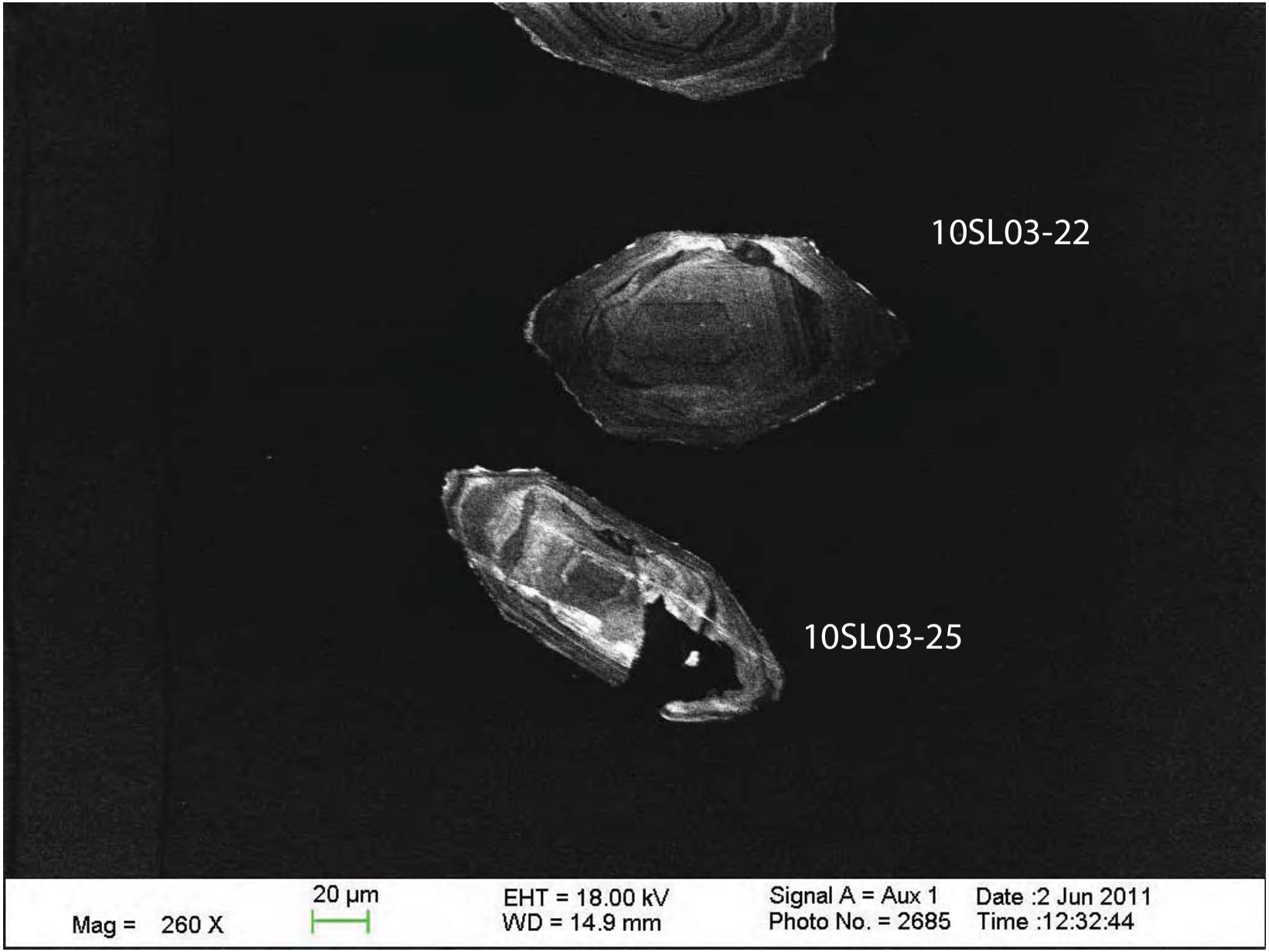
10SL03-22
10SL03-25
Mag = 260 X
20 µm
EHT = 18.00 kV
WD = 14.9 mm
Signal A = Aux 1
Photo No. = 2685
Date :2 Jun 2011
Time :12:32:44

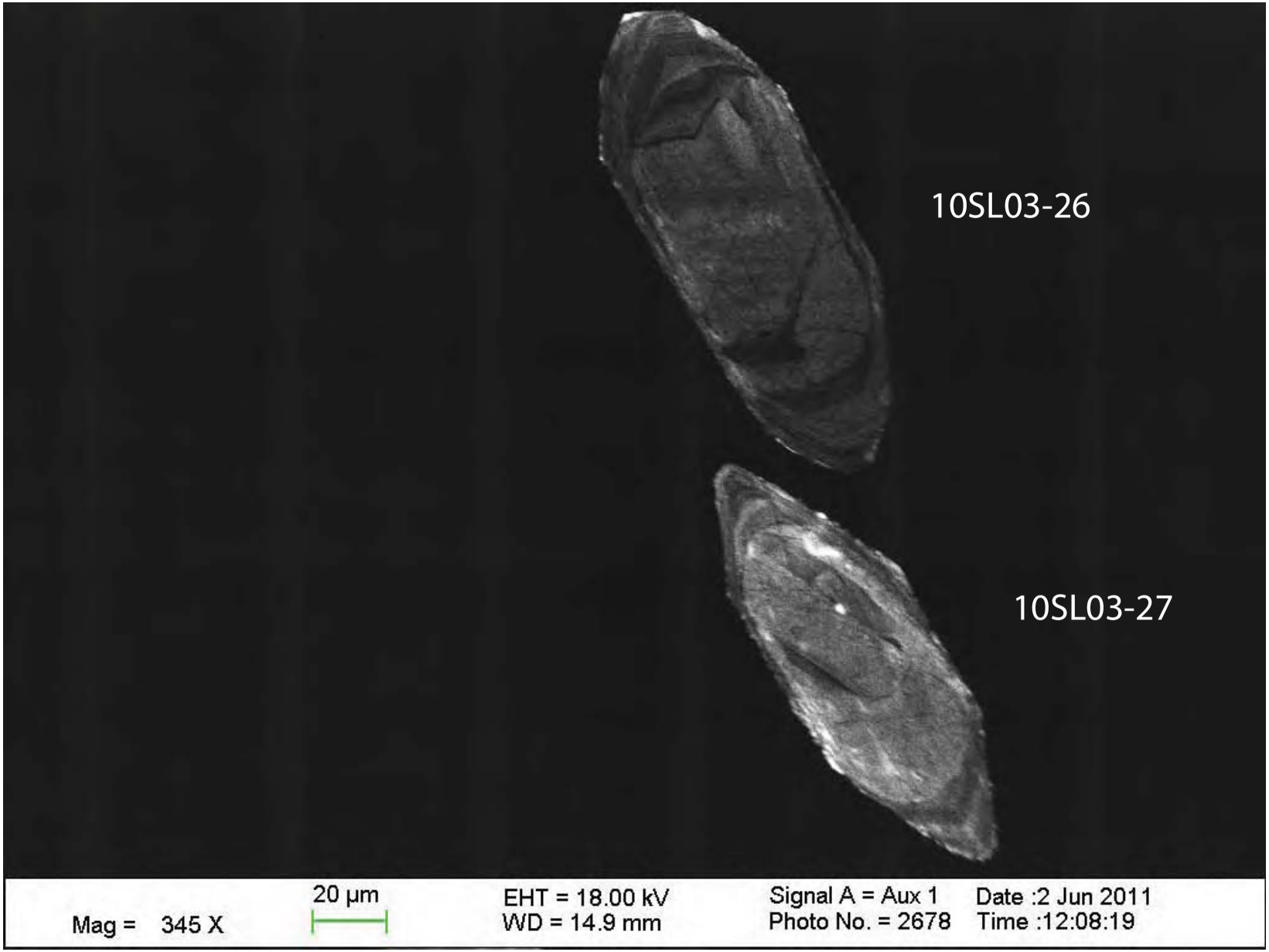
10SL03-26
10SL03-27
Mag = 345 X
20 µm
EHT = 18.00 kV
WD = 14.9 mm
Signal A = Aux 1
Photo No. = 2678
Date :2 Jun 2011
Time :12:08:19

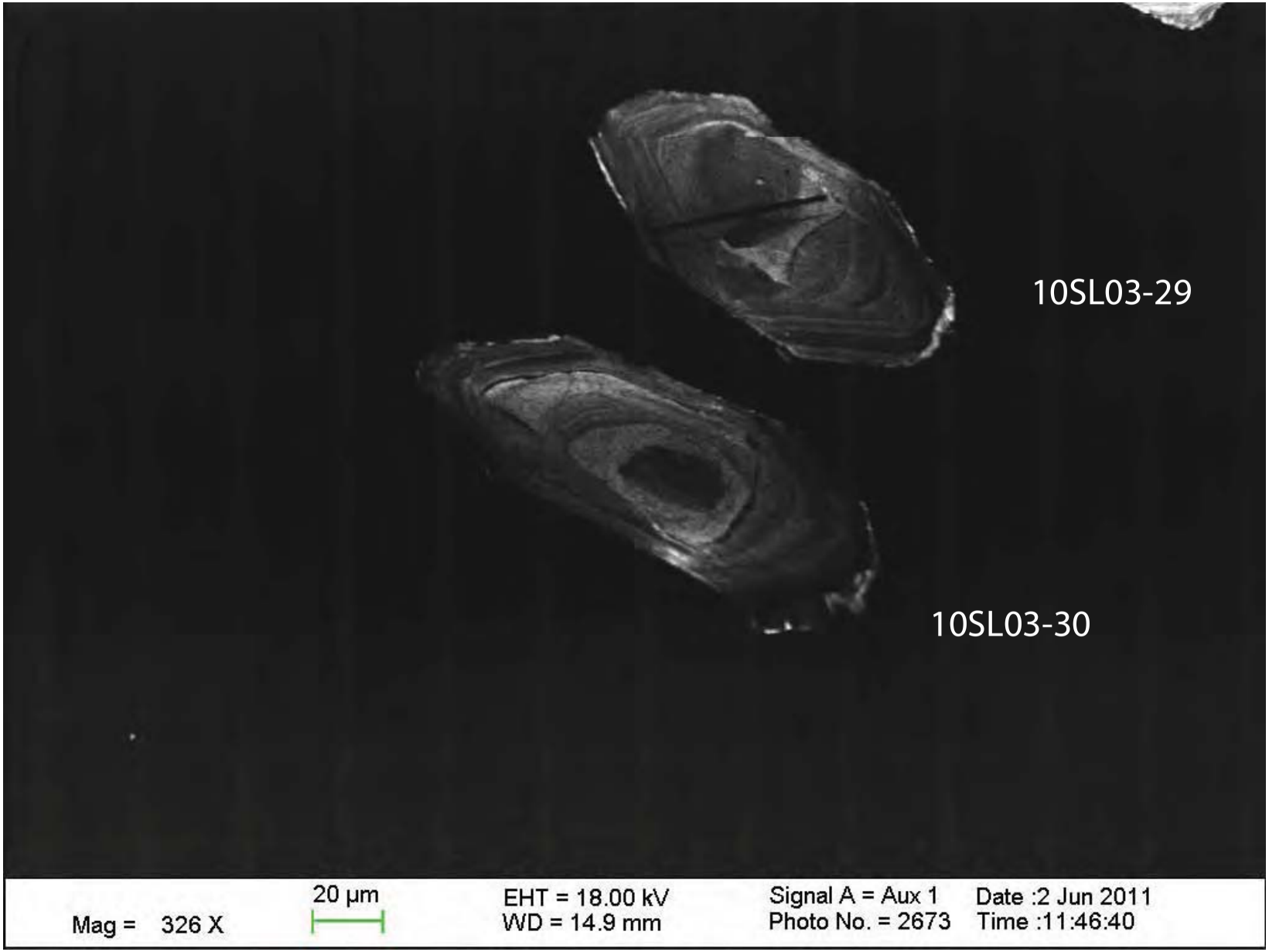
10SL03-29
10SL03-30
Mag = 326 X
20 µm
EHT = 18.00 kV
WD = 14.9 mm
Signal A = Aux 1
Photo No. = 2673
Date :2 Jun 2011
Time :11:46:40

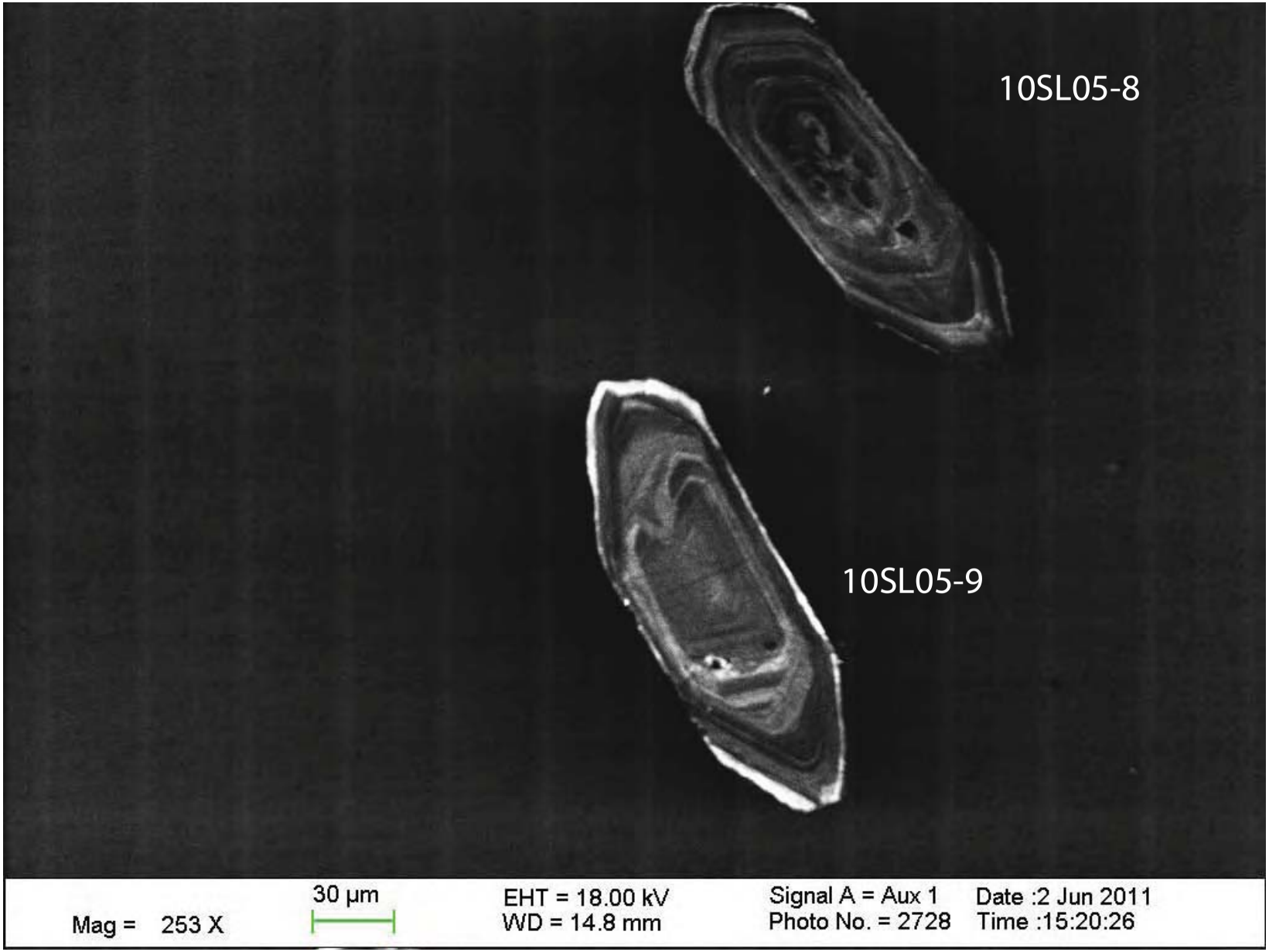
10SL05-8
10SL05-9
Mag = 253 X
30 µm
EHT = 18.00 kV
WD = 14.8 mm
Signal A = Aux 1
Photo No. = 2728
Date :2 Jun 2011
Time :15:20:26


10SL05-13
10SL05-12
10SL05-16
Mag = 253 X
30 µm
EHT = 18.00 kV
WD = 14.7 mm
Signal A = Aux 1
Photo No. = 2726
Date :2 Jun 2011
Time :15:13:42


10SL05-20
10SL05-17
Mag = 253 X
30 µm
EHT = 18.00 kV
WD = 14.7 mm
Signal A = Aux 1
Photo No. = 2725
Date :2 Jun 2011
Time :15:10:44

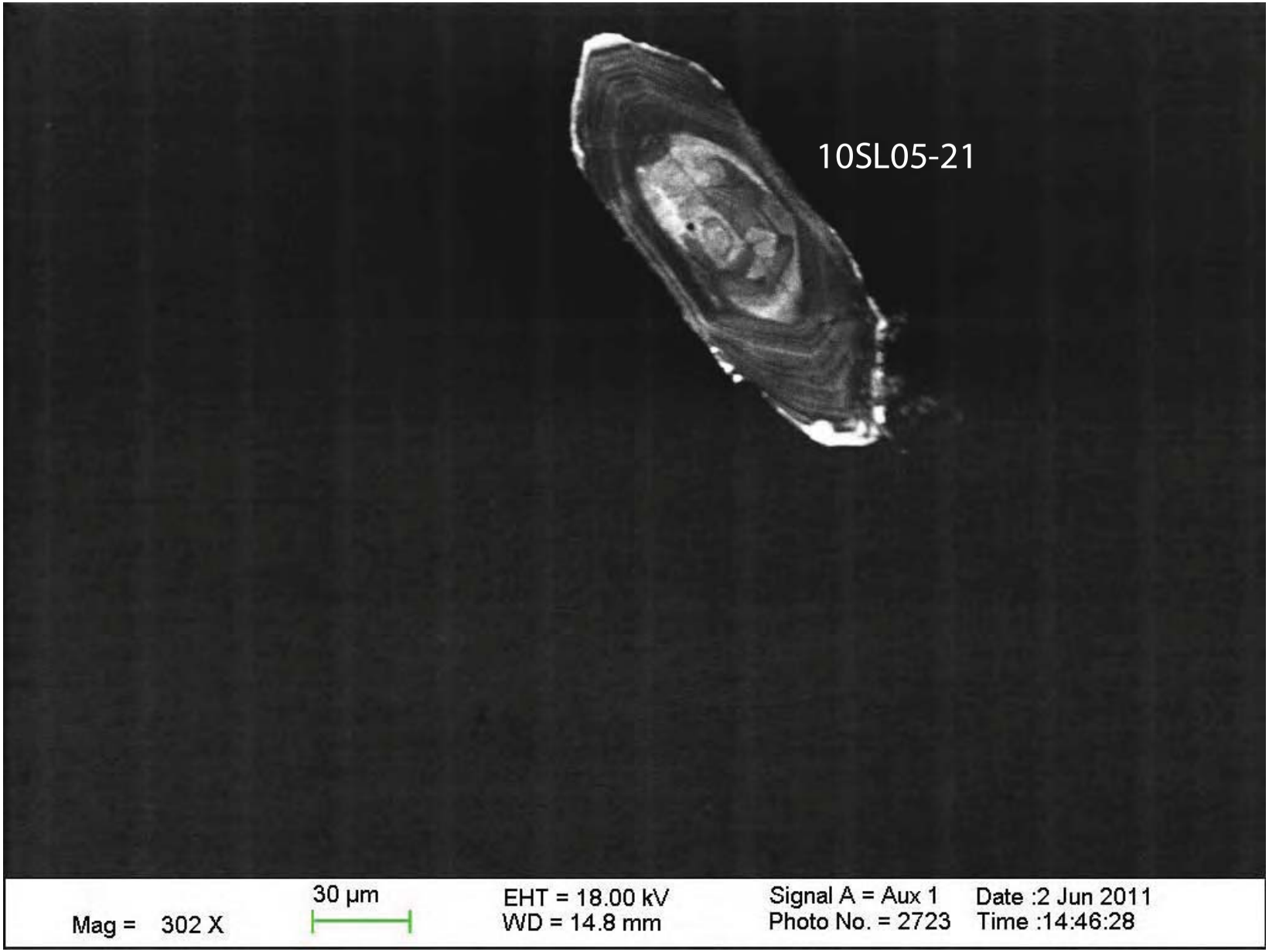
10SL05-21
30 µm
Mag = 302 X
EHT = 18.00 kV
WD = 14.8 mm
Signal A = Aux 1
Photo No. = 2723
Date :2 Jun 2011
Time :14:46:28

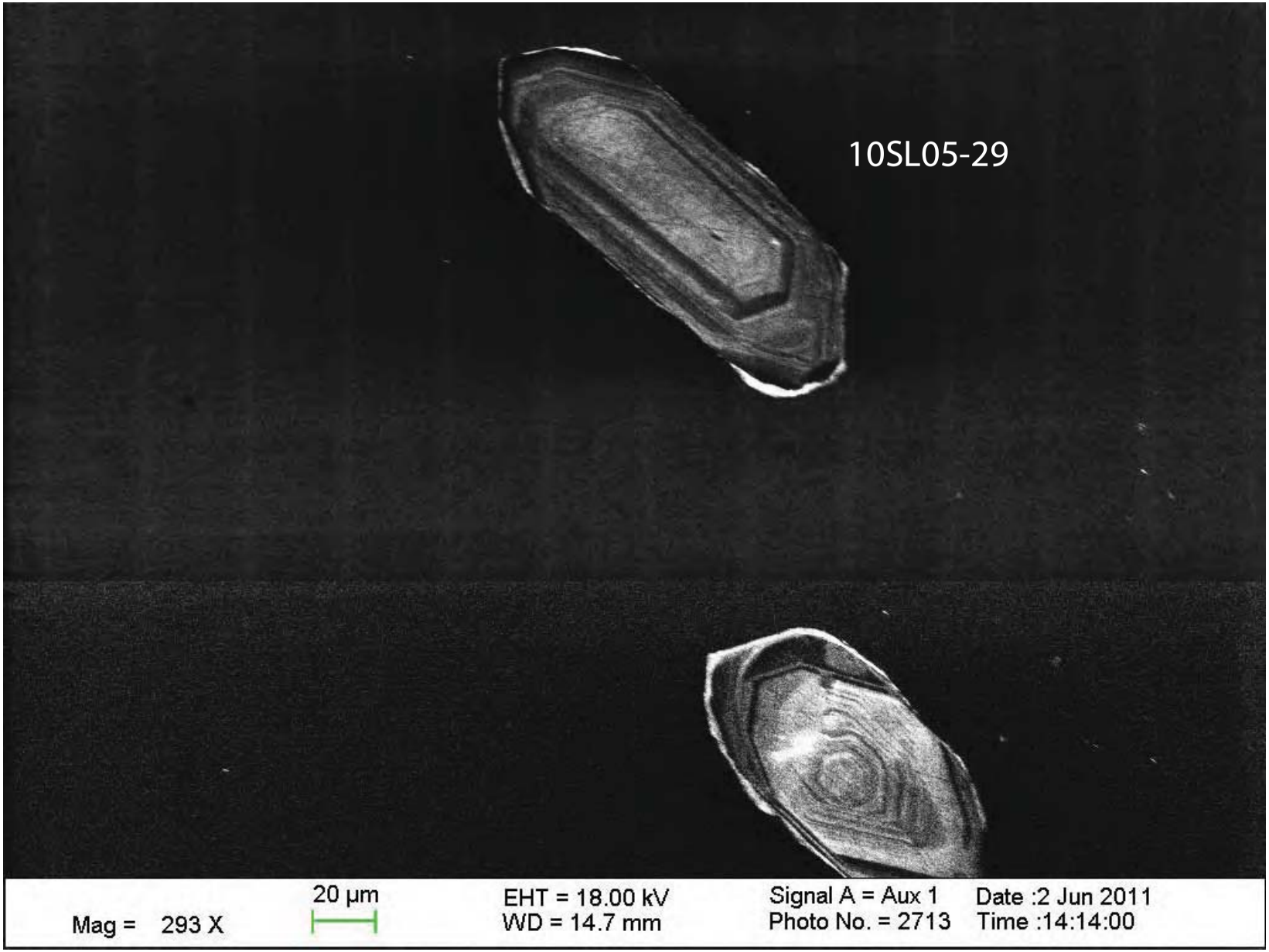
10SL05-29
Mag = 293 X
20 µm
EHT = 18.00 kV
WD = 14.7 mm
Signal A = Aux 1
Photo No. = 2713
Date :2 Jun 2011
Time :14:14:00


10SL05-30
10SL05-31
Mag = 297 X
20 µm
EHT = 18.00 kV
WD = 14.7 mm
Signal A = Aux 1
Photo No. = 2710
Date :2 Jun 2011
Time :14:05:25


10SL05-32
10SL05-33
Mag = 297 X
20 µm
EHT = 18.00 kV
WD = 14.7 mm
Signal A = Aux 1
Photo No. = 2708
Date :2 Jun 2011
Time :13:59:46

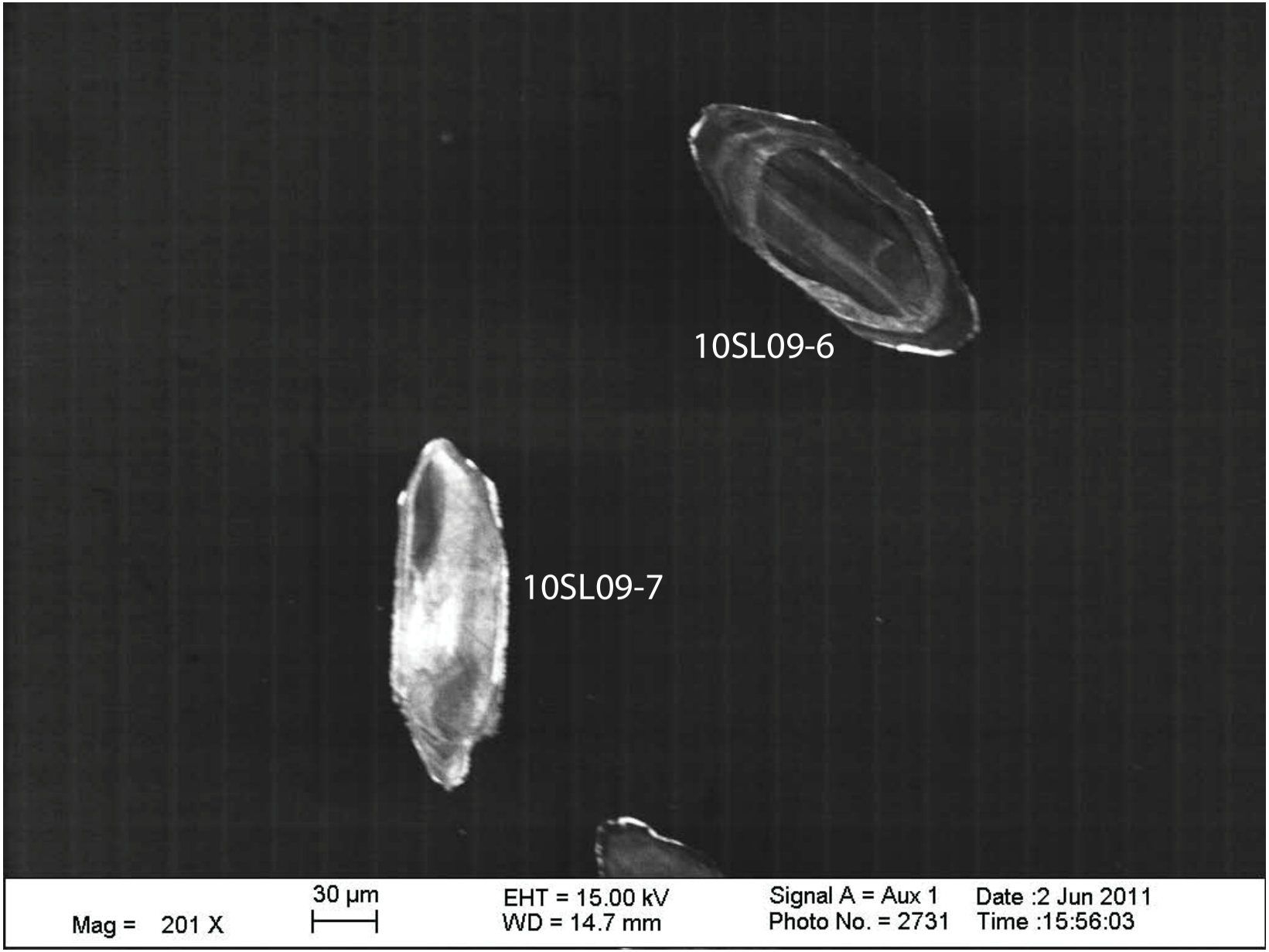
10SL09-6
10SL09-7
Mag = 201 X
30 µm
EHT = 15.00 kV
WD = 14.7 mm
Signal A = Aux 1
Photo No. = 2731
Date :2 Jun 2011
Time :15:56:03

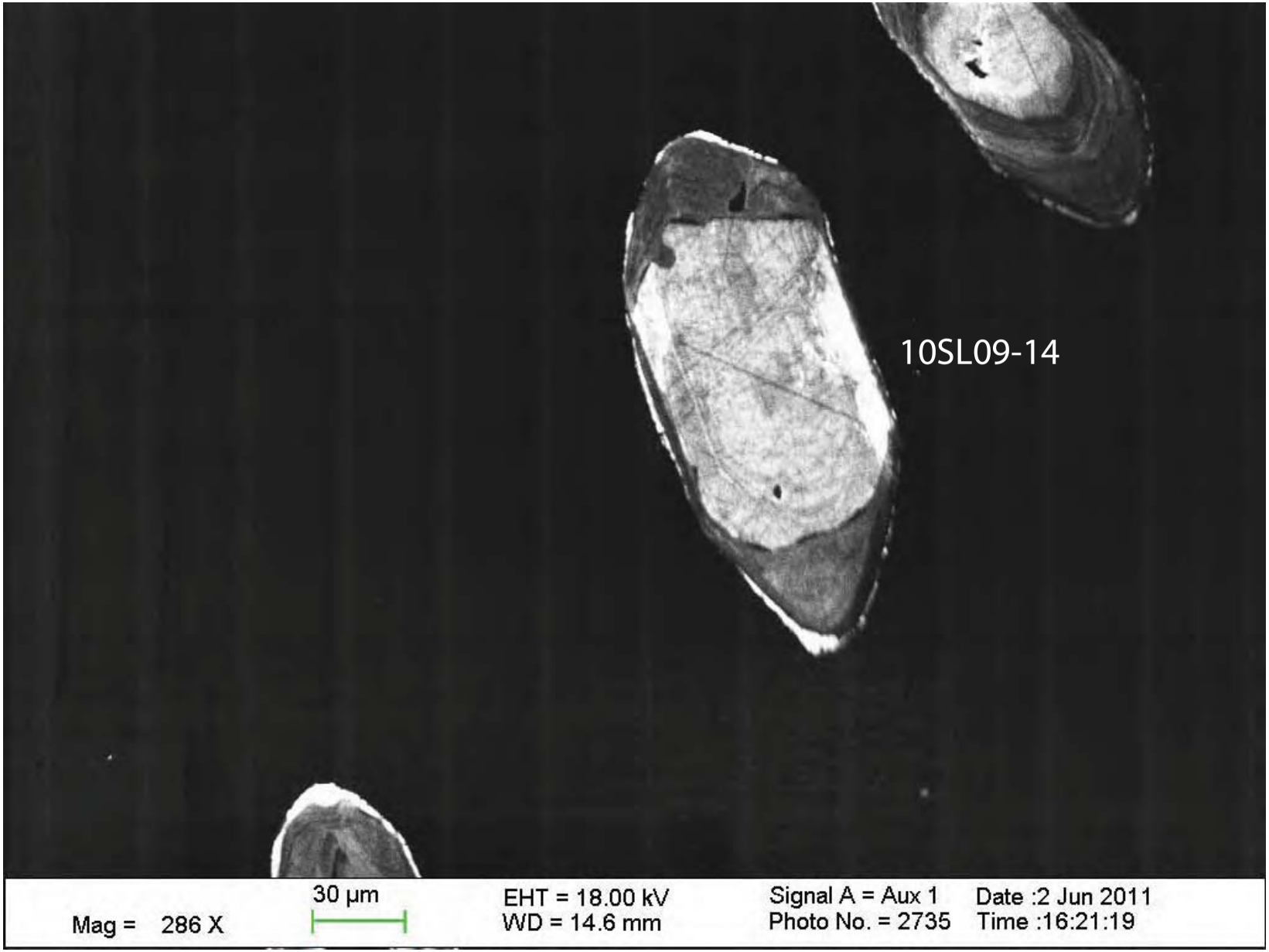
10SL09-14
30 µm
Mag = 286 X
EHT = 18.00 kV
WD = 14.6 mm
Signal A = Aux 1
Photo No. = 2735
Date :2 Jun 2011
Time :16:21:19


10SL09-17
30 µm
Mag = 305 X
EHT = 18.00 kV
WD = 14.6 mm
Signal A = Aux 1
Photo No. = 2737
Date :2 Jun 2011
Time :16:26:43


10SL09-19
30 µm
Mag = 262 X
EHT = 18.00 kV
WD = 14.6 mm
Signal A = Aux 1
Photo No. = 2738
Date :2 Jun 2011
Time :16:29:19


10SL09-21
10SL09-22
Mag = 262 X
30 µm
EHT = 18.00 kV
WD = 14.6 mm
Signal A = Aux 1
Photo No. = 2739
Date :2 Jun 2011
Time :16:31:34

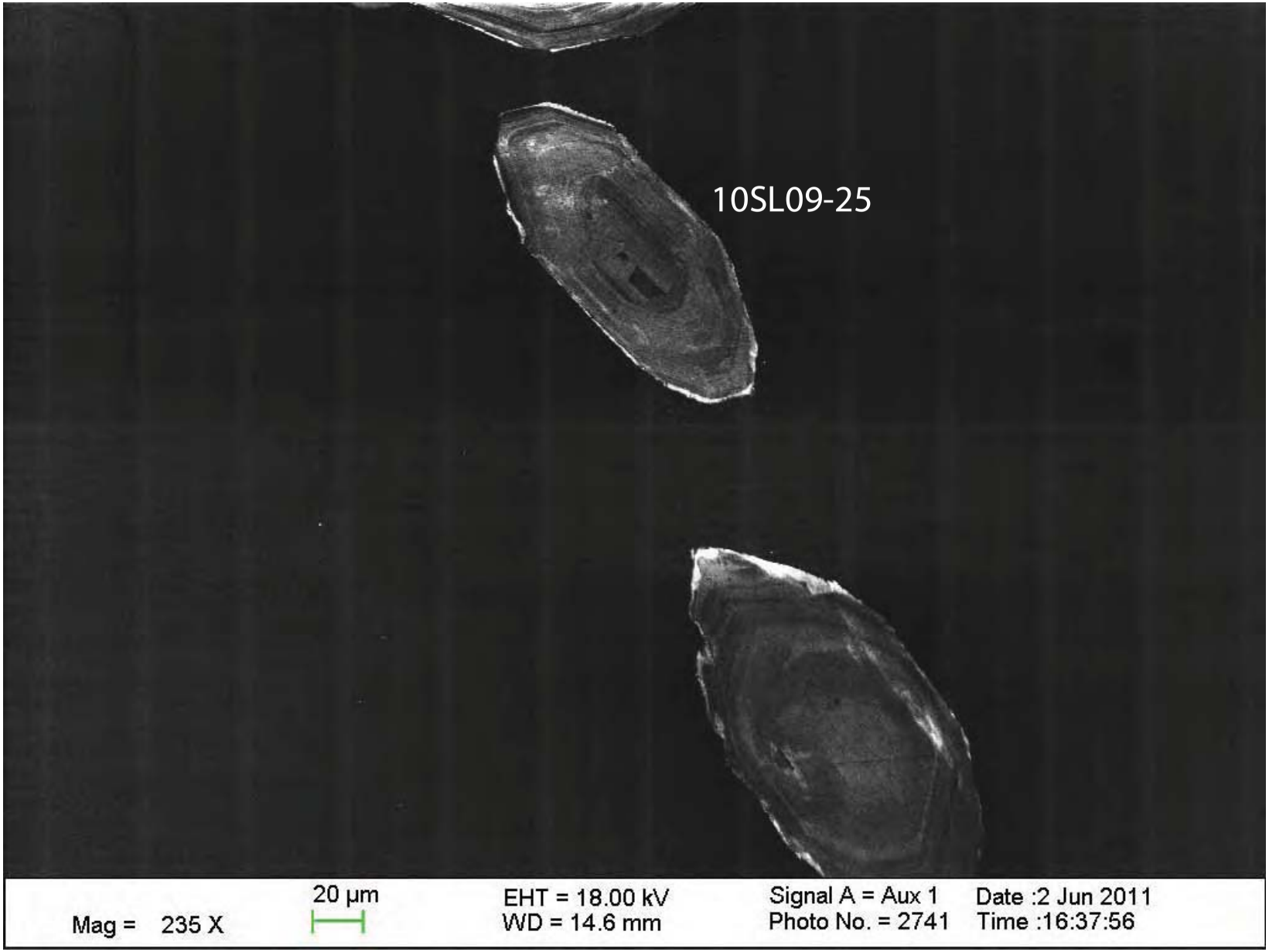
10SL09-25
Mag = 235 X
20 µm
EHT = 18.00 kV
WD = 14.6 mm
Signal A = Aux 1
Photo No. = 2741
Date :2 Jun 2011
Time :16:37:56

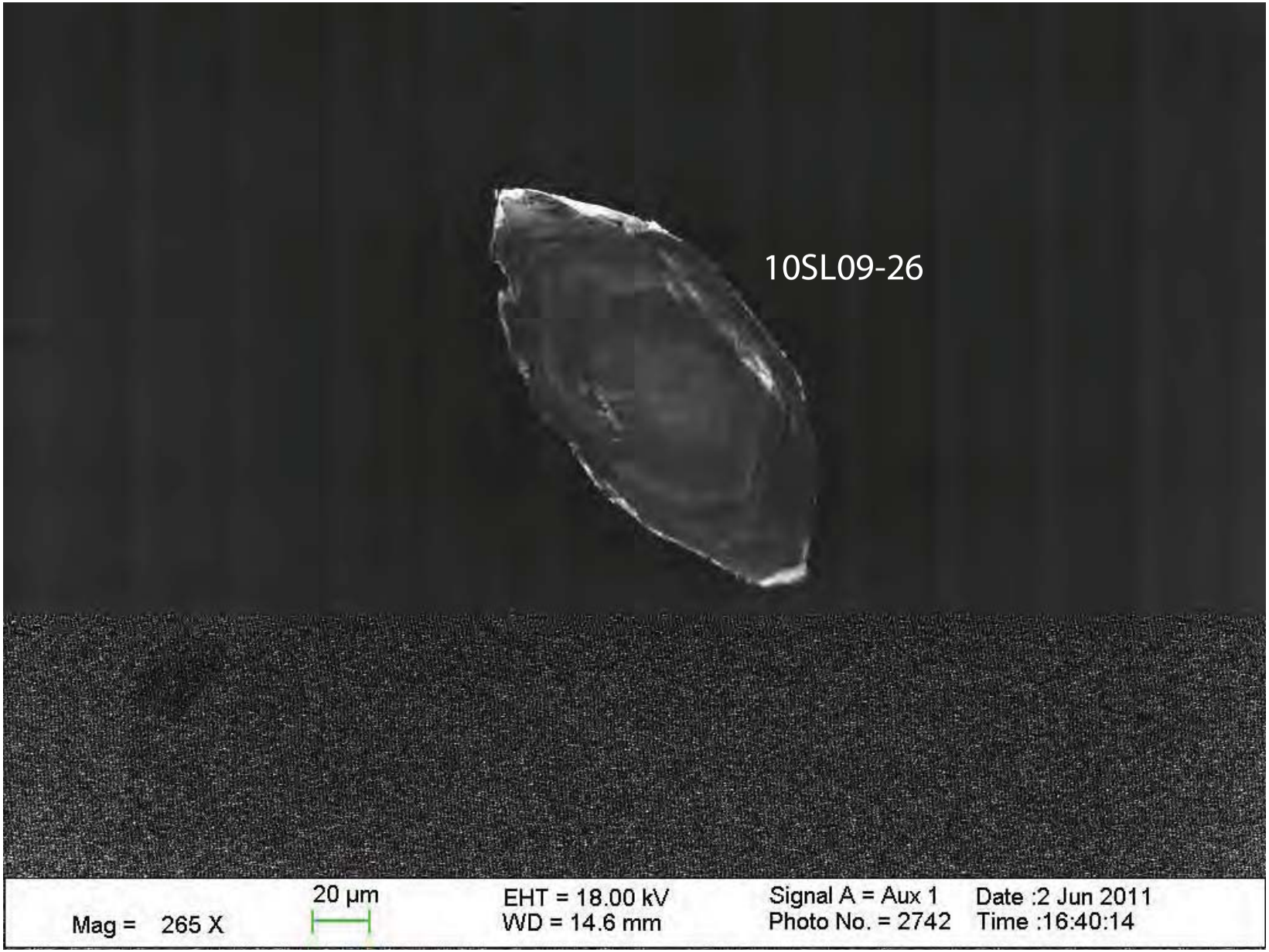
10SL09-26
Mag = 265 X
20 µm
EHT = 18.00 kV
WD = 14.6 mm
Signal A = Aux 1
Photo No. = 2742
Date :2 Jun 2011
Time :16:40:14

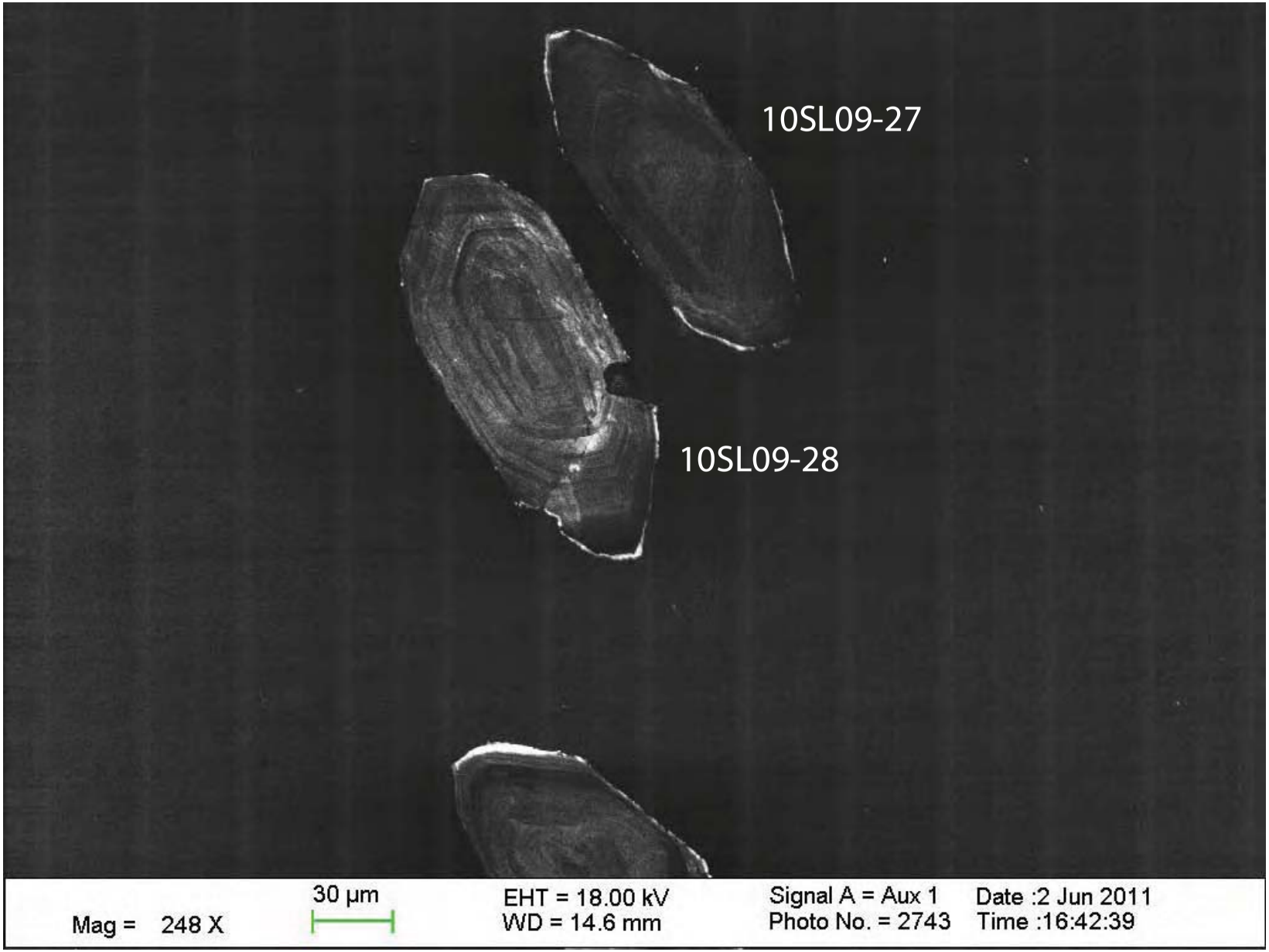
10SL09-27
10SL09-28
Mag = 248 X
30 µm
EHT = 18.00 kV
WD = 14.6 mm
Signal A = Aux 1
Photo No. = 2743
Date :2 Jun 2011
Time :16:42:39

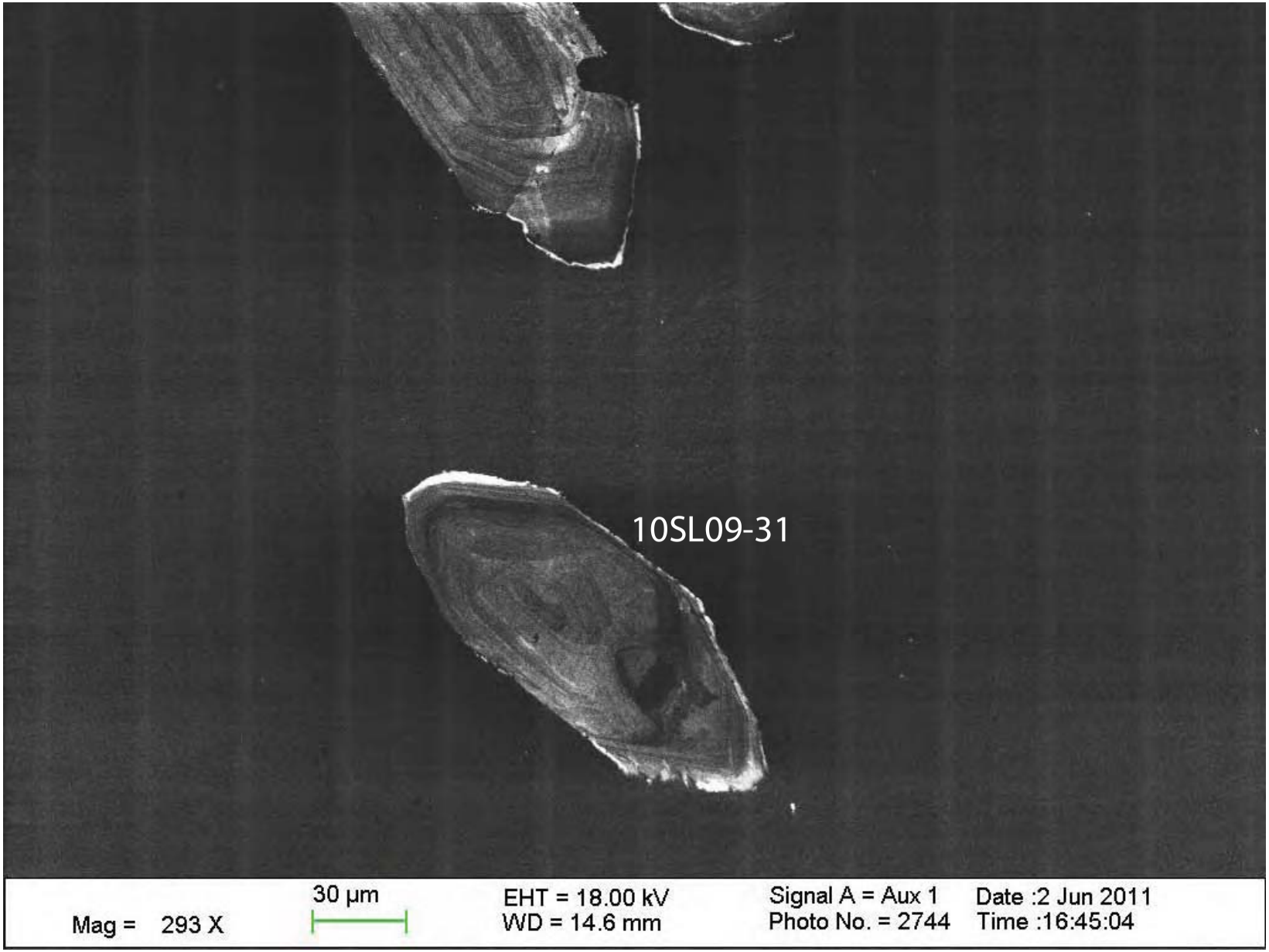
10SL09-31
Mag = 293 X
30 µm
EHT = 18.00 kV
WD = 14.6 mm
Signal A = Aux 1
Photo No. = 2744
Date :2 Jun 2011
Time :16:45:04

Appendix D: U-Pb Age Data of Silvretta nappe

Laser ablation depth-profiling was completed for three samples from the Silvretta nappe (10SL03, 05, 09). Depth-profiling provided a semi-quantitative method to establish parent isotope (U and Th) zonation within selected zircon grains, and also provided U-Pb ages for ablated unknown grains. The U-Pb ages are reported in this appendix in Table C; all ages were reduced using PepiAge v.1 (Dunkl et al., 2009). Drift corrections were performed using the internal standard GJ1 (e.g., Jackson et al., 2004), however the ages are not corrected for common Pb or Hg. Some ages were too discordant to produce ages and these have been indicated in Table C. A total of 73 U-Pb ages are reported for the Silvretta nappe and all are Paleozoic or older in age.

C. Table of U-Pb Ages of the Silvretta Nappe

Sample	$^{206}Pb/^{238}U$ Age (Ma)[a]	Error (±2σ, Ma)[b]	$^{207}Pb/^{235}U$ Age (Ma)[a]	Error (±2σ, Ma)[b]	$^{207}Pb/^{206}Pb$ Age (Ma)[a]	Error (±2σ, Ma)[b]	% U-Pb Discordance[c]	$^{206}Pb/^{238}U$ ratio[d]	$^{207}Pb/^{235}U$ ratio[d]	$^{207}Pb/^{206}Pb$ ratio[d]
10SL03; 46.9457°N, 10.0626°E; 1526 m										
10SL03-6	610.8	21.0	614.6	19.6	628.9	45.9	2.9	0.09684	0.81062	0.06071
10SL03-7	467.8	18.5	472.6	18.7	496	60.6	5.7	0.07225	0.56892	0.05711
10SL03-8	437.1	21.2	463.4	20.7	595.6	50.6	26.6	0.06998	0.57681	0.05978
10SL03-9	292.3	28.4	341.5	30.9	691.5	74.2	57.7	0.0476	0.41026	0.06251
10SL03-10	-	-	-	-	-	-	-	0.02318	1208623	378160
10SL03-11	41.9	24.7	89.4	52.2	1669.5	133.3	97.5	0.01772	0.25038	0.10248
10SL03-12	502.7	17.9	497.2	18.2	472.1	63.2	-6.5	0.07987	0.6222	0.0565
10SL03-13	134.4	33.1	228.2	53.5	1355	122.4	90.1	0.02612	0.31242	0.08675
10SL03-14	457.3	18.6	461.8	18	484.5	51.6	5.6	0.073	0.57191	0.05682
10SL03-15	197.1	50.1	299.1	70.5	1197.6	118.8	83.5	0.03131	0.34545	0.08002
10SL03-16	422.2	18.0	434.1	17.5	497.6	46.9	15.2	0.06912	0.54475	0.05716
10SL03-17	443	18.4	456.3	17.4	523.9	42.2	15.4	0.07019	0.55976	0.05784
10SL03-18	404	18.4	426.3	19	548.5	60.1	26.3	0.06562	0.52929	0.0585
10SL03-19	470.1	15.0	469.8	14.8	468.1	47.2	-0.4	0.07649	0.59482	0.0564
10SL03-20	345.1	24.6	393.4	26.1	688.5	63.1	49.9	0.05606	0.48248	0.06242
10SL03-21	485.2	15.4	498.5	15.1	559.8	39.7	13.3	0.07765	0.62954	0.0588
10SL03-22	169.8	100.8	336.3	188.2	1744.1	106.3	90.3	0.01831	0.2694	0.10671
10SL03-23	482.3	16.8	482.1	17.4	480.8	60.8	-0.3	0.07825	0.61196	0.05672
10SL03-24	439.3	14.9	448.6	14.6	496.8	44.7	11.6	0.07482	0.58947	0.05714
10SL03-25	378.1	28.3	415.1	28.3	626.6	63.8	39.7	0.0611	0.51086	0.06064
10SL03-26	437.9	15.3	449.3	14.6	507.9	37.8	13.8	0.06919	0.54778	0.05742
10SL03-27	222.3	55.7	487.5	110.3	2062.5	173.9	89.2	0.03972	0.69772	0.1274
10SL03-28	765.9	47.1	828.5	39.3	1000.3	41.2	23.4	0.12731	1.2728	0.07251
10SL03-29	435.1	17.3	450.2	16.1	527.8	37.7	17.6	0.07084	0.56602	0.05795
10SL03-30	471.8	20.0	488.5	18	568	30.8	16.9	0.0758	0.61684	0.05902
10SL05; 46.9109°N, 10.0401°E; 2152 m										
10SL05-6	483.6	17.7	487.6	18.4	506.7	60.5	4.6	0.07977	0.63121	0.05739
10SL05-7	553.1	23.9	563	22.3	603.3	55.1	8.3	0.08674	0.71746	0.05999
10SL05-8	472.5	17.3	469.9	17.1	457.1	54.1	-3.4	0.07626	0.59009	0.05612
10SL05-9	428.1	22.0	451.5	21.7	572.9	55.3	25.3	0.07065	0.57629	0.05916
10SL05-10	458.1	19.9	461.2	19.1	476.7	51.7	3.9	0.07028	0.54866	0.05662
10SL05-11	492.2	17.6	481.1	16.2	428.7	42.9	-14.8	0.07996	0.61089	0.05541
10SL05-12	-	-	-	-	2096	151.6	-	0.00067	0.012	0.12985
10SL05-13	470.7	19.1	466.9	18.1	448.3	54.3	-5.0	0.07674	0.59147	0.0559
10SL05-14	522	22.1	523.3	20.2	529.2	46.7	1.4	0.08154	0.65185	0.05798
10SL05-15	-	-	-	-	1528.1	177.7	-	-0.02248	-0.29446	0.095
10SL05-16	356.8	26.4	436.9	30.6	884.7	80.6	59.7	0.05856	0.55333	0.06853
10SL05-17	311.4	13.7	334.8	13.8	501.3	37.9	37.9	0.07224	0.57024	0.05725
10SL05-18	479.7	15.3	478	15.8	470	54	-2.1	0.07461	0.58071	0.05645
10SL05-19	482.4	15.8	485.8	15.6	501.7	46.9	3.8	0.07577	0.5982	0.05726
10SL05-20	120.7	44.0	296	100.9	2096.6	130.3	94.2	0.02557	0.45797	0.1299
10SL05-21	348.3	23.8	378.1	23.6	565	50.9	38.4	0.0595	0.48354	0.05894
10SL05-22	503	17.0	510.3	15.4	542.9	33.2	7.3	0.08107	0.65223	0.05835
10SL05-23	479.2	17.1	475.5	15.7	457.9	40.5	-4.7	0.07571	0.58604	0.05614
10SL05-24	512.6	14.3	505	13.6	470.7	38.1	-8.9	0.08309	0.64683	0.05646
10SL05-25	616.2	21.2	623.7	18.8	651.2	39.1	5.4	0.1021	0.86352	0.06134
10SL05-26	471.6	15.0	473.4	14.5	481.9	40.3	2.1	0.07602	0.59483	0.05675
10SL05-27	379.3	25.1	416	25.2	625	57.1	39.3	0.05957	0.49774	0.0606
10SL05-28	479.5	19.0	483.3	17.5	501.3	42.4	4.3	0.07618	0.60134	0.05725
10SL05-29	512.8	15.3	505.2	15.2	470.7	49.4	-8.9	0.08166	0.6357	0.05646
10SL05-30	537.9	18.6	526.9	17.4	479.5	49.3	-12.2	0.08477	0.6626	0.05669
10SL05-31	442	23.1	459.3	21.7	546.5	44.3	19.1	0.0689	0.55518	0.05844
10SL05-32	473.7	22.9	490.3	21.6	568.6	50.8	16.7	0.0766	0.62356	0.05904
10SL05-33	446.1	20.3	490.1	23.2	701.3	76.3	36.4	0.07258	0.62836	0.06279
10SL09; 46.8935°N, 10.0308°E; 2715 m										
10SL09-6	442.3	18.8	457.9	18.6	537.1	53.4	17.7	0.0722	0.57928	0.05819
10SL09-7	483.2	18.2	482.1	18.6	476.6	63.1	-1.4	0.07688	0.60008	0.05661
10SL09-8	484.8	18.2	489.5	18.4	511.6	60.5	5.2	0.07264	0.5761	0.05752
10SL09-9	487.1	16.9	493.8	17	525.5	53.5	7.3	0.07714	0.61562	0.05788
10SL09-10	469.3	16.8	474	16.8	497.3	53.8	5.6	0.07507	0.59154	0.05715
10SL09-11	491	23.2	511.4	22.3	603.6	52.8	18.7	0.07452	0.61649	0.06
10SL09-12	430.3	19.2	456.3	19.7	589.7	57.4	27.0	0.07173	0.58965	0.05962
10SL09-13	466.7	18.5	464	18	450.5	56.5	-3.6	0.07504	0.57889	0.05595
10SL09-14	342.5	25.7	373.9	26	573.5	64.3	40.3	0.05535	0.45157	0.05917
10SL09-15	552.4	23.3	563.2	22.3	607.1	55	9.0	0.08921	0.73925	0.0601
10SL09-16	462.7	21.0	469.2	20.1	501	56.1	7.6	0.07019	0.55396	0.05724
10SL09-17	446.7	22.5	473.2	21.4	603.8	48.4	26.0	0.07134	0.59018	0.06
10SL09-18	489.7	17.9	489.9	16.9	491	44.7	0.3	0.07643	0.60046	0.05698
10SL09-19	489.2	16.0	481.1	15.4	442.4	47.4	-10.6	0.07999	0.61487	0.05575
10SL09-20	212.2	75.6	490.5	154.3	2159.2	137.1	90.2	0.03314	0.61512	0.13462

C. Table of U-Pb Ages of the Silvretta Nappe, cont.

Sample	$^{206}Pb/^{238}U$ Age (Ma)[a]	Error (±2σ, Ma)[b]	$^{207}Pb/^{235}U$ Age (Ma)[a]	Error (±2σ, Ma)[b]	$^{207}Pb/^{206}Pb$ Age (Ma)[a]	Error (±2σ, Ma)[b]	% U-Pb Discordance[c]	$^{206}Pb/^{238}U$ ratio[d]	$^{207}Pb/^{235}U$ ratio[d]	$^{207}Pb/^{206}Pb$ ratio[d]
10SL09 cont.										
10SL09-21	396.9	18.9	412.6	18.5	501.1	51.4	20.8	0.06525	0.51506	0.05725
10SL09-22	491.6	18.5	484.8	17.9	452.9	56.5	-8.5	0.07637	0.58978	0.05601
10SL09-23	633.1	30.2	656.6	27.4	738.3	56	14.2	0.10201	0.89876	0.0639
10SL09-24	478.1	22.6	483.8	21.4	511.2	58.2	6.5	0.07603	0.60288	0.05751
10SL09-25	476.4	17.9	482.6	17.4	512.4	51.4	7.0	0.07712	0.61184	0.05754
10SL09-26	483.6	18.7	483.7	18.2	484.2	56.2	0.1	0.07567	0.59272	0.05681
10SL09-27	476.8	17.5	477.7	16.1	481.7	42.6	1.0	0.0774	0.60552	0.05674
10SL09-28	474.4	16.9	500.6	19.1	622.1	66	23.7	0.0766	0.63919	0.06052
10SL09-29	287.1	33.2	337.1	35.9	698.3	76.4	58.9	0.0452	0.39076	0.0627
10SL09-30	589.4	29.4	614.7	26.2	708.9	47.5	16.9	0.093	0.8081	0.06302
10SL09-31	495.4	16.7	495.4	16.2	495.5	46.9	0.0	0.0785	0.61803	0.0571

[a] Calculated age using PepiAge v. 1 (Dunkl et al., 2009) without Hg or common Pb correction, and Steiger and Jäger (1977) decay constant

[b] Propogated analytical error

[c] Discordance calculated as (1-($^{206}Pb/^{238}U$ age/$^{207}Pb/^{206}Pb$ age))*100

[d] Isotope ratios corrected for mass drift and background based on the zircon standard GJ1

No age calculated for samples indicated by (-) as a result of extreme discordance